UNIVERSITAT POLITÈCNICA
DE CATALUNYA
BARCELONATECH

A machine learning based material homogenization technique for masonry structures

Philip Kalkbrenner

Universitat Politècnica de Catalunya

A Machine Learning based Material Homogenization Technique for Masonry Structures

Doctoral Thesis by:
Philip Kalkbrenner

Supervised by:
Luca Pelà
Riccardo Rossi

Barcelona, September 29, 2021

Departament d'Enginyeria Civil i Ambiental
Programa de Doctorat en Enginyeria de la Construcció

A Machine Learning based Material Homogenization Technique for Masonry Structures

Doctoral Thesis submitted in fulfillment of the requirements for the
Degree of Doctor of Philosophy in Construction Engineering
by

PHILIP KALKBRENNER

Barcelona, September 2021

Escola de Camins
Escola Tècnica Superior d'Enginyeria de Camins, Canals i Ports
UPC BARCELONATECH

Thesis Supervisors:
Luca Pelà
Riccardo Rossi

Board of Examiners:
Hiram Badillo - Universidad Autónoma de Zacatecas
Pere Roca - Universitat Politècnica de Catalunya
Savvas Saloustros - École Polytechnique Fédérale de Lausanne

External Reviewers:
Hiram Badillo -Universidad Autónoma de Zacatecas
Savvas Saloustros - École Polytechnique Fédérale de Lausanne

Acknowledgment

This thesis has only been achieved due to the help and assistance of many people. Therefore, I dedicate the following pages to the ones that always believed in me and did the possible to support me.

The research presented in this thesis has been carried out at the Department of Civil and Environmental Engineering of the Technical University of Catalonia (UPC). It has only been possible thanks to the financial support of the FI-AGAUR predoctoral scholarship awarded to me by the Secretaria d'Universitats i Investigació de la Generalitat de Catalunya. Furthermore I would gratefully acknowledge also the financial support from the Ministry of Science, Innovation and Universities (MCIU) of the Spanish Government, the State Agency of Research (AEI) and the European Regional Development Fund (ERDF) through the SEVERUS project ("Multilevel evaluation of seismic vulnerability and risk mitigation of masonry buildings in resilient historical urban centres", ref. num. RTI2018-099589-BI00).

Writing a thesis requires scientific guidance. Therefore, I would like to express my thanks to both my supervisors Luca Pelà and Riccardo Rossi. Luca, thank you for giving me the chance to widen my professional skills as civil engineer by having given me the possibility to start a PhD at the UPC. You have spent many hours of introducing me to the complex science field of masonry structures and seismic engineering. Your ideas and comments have significantly contributed to the success of this thesis. Riccardo, thank you for your amazing analytic skills. Your guidance and ideas have helped me a lot through the numerical part of the thesis. You knew the challenges very well and have always proposed the right things.

Also technical guidance is indispensable for a thesis. Hence, I would like to thank the entire KRATOS MULTIPHYSICS team. Special thanks in the team go to Carlos Roig, Rubén Zorilla and Alejandro Cornejo. Carlos and Rubén thanks for helping with several compilations of the software. Alejandro thank you for introducing and

supporting me with the C++ implementation of constitutive laws. Furthermore I would also like to thank David Ortin for his support while using the Titani cluster of the Escola de Camins.

Writing a doctoral thesis is time consuming, but life is not only about that. Thanks to my PhD colleagues, I know you share these thoughts: Chiara for also tackling the DIANA FEA challenge, Naveen for your interest in topics aside research, Albert for teaching me the Catalan culture, Savvas for your fruitful discussions about research communication, Camilla for being the person with the biggest smile at UPC, Belén for the deep talks, Sara for being the most communicative colleague, Francesco for always gathering us to enjoy life, Larisa for having time at any moment, Jorge for your amazing understanding about what drives others and Nirvan for sharing your philosophical ideas about life. You have all become my friends.

Great thanks go to my mother Annette, thanks for making me the person who I am, and my father Andreas for always thinking many steps beyond and showing this important skill to me. Big thanks also go to my brother Michael for understanding my monologues.

My final thanks go to the two persons that have accompanied me through the last years: Daniela and Lucía. Lucía, thanks for giving me several attempts to be a good dad and for showing me that learning something new is all about having fun. Daniela, thank you for being the only person able to charge my batteries. You helped me to overcome my despair about PhD research. Thanks for showing me that problems only exist in order to be solved. This work is also your achievement.

Abstract

Cutting-edge methods in the computational analysis of structures have been developed over the last decades. Such modern tools are helpful to assess the safety of existing buildings. Two main finite element (FE) modeling approaches have been developed in the field of masonry structures, i.e. micro and macro scale. While the micro modeling distinguishes between the masonry components in order to accurately represent the typical masonry damage mechanisms in the material constituents, macro modeling considers a single continuum material with smeared properties so that large scale masonry models can be analyzed. Both techniques have demonstrated their advantages in different structural applications. However, each approach comes along with some possible disadvantages. For example, the use of micro modeling is limited to small scale structures, since the computational effort becomes too expensive for large scale applications, while macro modeling cannot take into account precisely the complex interaction among masonry components (brick units and mortar joints).

Multi scale techniques have been proposed to combine the accuracy of micro modeling and the computational efficiency of macro modeling. Such procedures consider linked FE analyses at both scales, and are based on the concept of a representative volume element (RVE). The analysis of a RVE takes into account the micro structural behavior of component materials, and scales it up to the macro level. In spite of being a very accurate tool for the analysis of masonry structures, multi scale techniques still exhibit high computational cost while connecting the FE analyses at the two scales.

Machine learning (ML) tools have been utilized successfully to train specific models by feeding big source data from different fields, e.g. autonomous driving, face recognition, etc. This thesis proposes the use of ML to develop a novel homogenization strategy for the in-plane analysis of masonry structures, where a continuous

nonlinear material law is calibrated by considering relevant data derived from micro scale analysis. The proposed method is based on a ML tool that links the macro and micro scales of the analysis, by training a macro model smeared damage constitutive law through benchmark data from numerical tests derived from RVE micro models. In this context, numerical nonlinear tests on masonry micro models executed in a virtual laboratory provide the benchmark data for feeding the ML training procedure. The adopted ML technique allows the accurate and efficient simulation of the anisotropic behavior of masonry material by means of a tensor mapping procedure. The final stage of this novel homogenization method is the definition of a calibrated continuum constitutive model for the structural application to the masonry macro scale.

The developed technique is applied to the in-plane homogenization of a Flemish bond masonry wall. Evaluation examples based on the simulation of physical laboratory tests show the accuracy of the method when compared with sophisticated micro modeling of the entire structure. Finally, an application example of the novel homogenization technique is given for the pushover analysis of a masonry heritage structure.

Keywords: *Masonry · Finite Element Method · Macro Scale Modeling · Micro Scale Modeling · Multi Scale Modeling · Material Homogenization · Heterogeneous Material· Machine Learning · Continuum Damage Mechanics · Pushover Analysis*

Resumen

En las últimas décadas se han desarrollado diversos métodos avanzados para el análisis computacional de estructuras. Estas herramientas modernas son también útiles para evaluar la seguridad de los edificios existentes. En el campo de las estructuras de la obra de fábrica se han desarrollado principalmente dos técnicas de modelizacón por elementos finitos (FE): la modelización en escala micro y en escala macro. Mientras que en un micromodelo se distingue entre los componentes de la obra de fábrica para representar con precisión los mecanismos de daño característicos de la misma, en un macromodelo se asignan las propiedades a un único material continuo que permite analizar modelos de obra de fábrica a gran escala. Ambas técnicas han demostrado sus ventajas en diferentes aplicaciones estructurales. Sin embargo, cada enfoque viene acompañado de algunas posibles desventajas. Por ejemplo, la micromodelización se limita a estructuras de pequeña escala, puesto que el esfuerzo computacional que requieren aumenta rápidamente con el tamaño de los modelos, mientras que la macromodelización, por su parte, es un enfoque promediado que no puede por tanto tener en cuenta precisamente la interacción compleja entre los componentes de la fábrica (unidades de ladrillo y juntas de mortero).

Hasta el momento, se han propuesto algunas técnicas multiescala para combinar la precisión de la micromodelización y la eficiencia computacional de la macromodelización. Estos procedimientos aplican el análisis de FE vinculado a ambas escalas y se basan en el concepto de elemento de volumen representativo (RVE). El análisis de un RVE tiene en cuenta el comportamiento microestructural de los materiales componentes y lo escala hasta el nivel macro. A pesar de ser una herramienta muy precisa para el análisis de obra de fábrica, las técnicas multiescala siguen presentando un elevado coste computacional que se produce al conectar los análisis de FE de dos escalas. Además, diversos autores han utilizado con éxito herramientas de aprendizaje automático (machine learning (ML)) para poner a punto modelos específicos

alimentados con grandes fuentes de datos de diferentes campos, por ejemplo, la conducción autónoma, el reconocimiento de caras, etc.

Partiendo de los anteriores conceptos, este tesis propone el uso de ML para desarrollar una novedosa estrategia de homogeneización para el análisis en plano de estructuras de mampostería, donde se calibra una ley de materiales continua no lineal considerando datos relevantes derivados del análisis a microescala. El método propuesto se basa en una herramienta de ML que vincula las escalas macro y micro del análisis mediante la puesta a punto de una ley constitutiva para el modelo macro a través de datos producidos en ensayos numéricos de un RVE micro modelo. En este contexto, los ensayos numéricos no lineales sobre micro modelos de mampostería ejecutados en un laboratorio virtual proporcionan los datos de referencia para alimentar el procedimiento de entrenamiento del ML. La técnica de ML adoptada permite la simulación precisa y eficiente del comportamiento anisotrópico del material de mampostería mediante un procedimiento de mapeo tensorial. La etapa final de este novedoso método de homogeneización es la definición de un modelo constitutivo continuo calibrado para la aplicación estructural a la macroescala de mampostería.

La técnica desarrollada se aplica a la homogeneización en el plano de un muro de obra de fábrica construido con aparejo flamenco. Ejemplos de evaluación basados en la simulación de pruebas físicas de laboratorio muestran la precisión del método en comparación con una sofisticada micro modelización de toda la estructura. Por último, se ofrece un ejemplo de aplicación de la novedosa técnica de homogeneización para el análisis pushover de una estructura patrimonial de obra de fábrica.

Palabras claves: *Obra de fábrica · Método de los elementos finitos · Macromodelización · Micromodelización · Modelización multiescala · Homogeneización de materiales · Material heterogéneo · Aprendizaje automático · Mecánica del daño continuo · Análisis pushover*

Zusammenfassung

In den letzten Jahrzehnten wurden modernste numerische Methoden zur Simulation von Bauwerken entwickelt. Diese Werkzeuge sind hilfreich, um auch die Standsicherheit von Bauwerken des Bestands zu beurteilen. Speziell im Bereich des Mauerwerkbaus wurden zwei Finite-Elemente (FE) basierte Techniken entwickelt: Mikro- und Makromodellierung. Während bei der Mikromodellierung zwischen den Mauerwerkskomponenten unterschieden wird - um typische Schadensmechanismen im Mauerwerk genau abzubilden - werden bei der Makromodellierung die Eigenschaften auf ein einziges Festkörpermaterial gemittelt, damit komplette Mauerwerksbauten analysiert werden können. Beide Techniken haben ihre Vorteile. Allerdings überwiegen die jeweiligen möglichen Nachteile: Die Mikromodellierung ist auf kleine wandartige Mauerwerksstrukturen beschränkt, da der Rechenaufwand zu groß wird, je größer die Modelle sind. Andererseits ist die Makromodellierung ein verschmierter Ansatz, der die Interaktion der Mauerwerkskomponenten (Ziegelsteine und Mörtelfügen) nicht korrekt berücksichtigen kann.

Um die Genauigkeit der Mikromodellierung mit der Recheneffizienz der Makromodellierung zu kombinieren, wurden Mehrskalenverfahren entwickelt. Solche Verfahren berücksichtigen die direkte Verknüpfung der FE-Berechnungen auf beiden Skalen und beruhen auf dem Konzept eines repräsentativen Volumenelements (RVE). Die Berechnung eines RVE repräsentiert das mikrostrukturelle Verhalten von Bauteilmaterialien und skaliert es auf die Makroebene. Obwohl es sich um ein sehr genaues Werkzeug für die Analyse von Mauerwerksbauten handelt, verursachen Mehrskalenverfahren immer noch hohe Rechenkosten während sie die FE Berechnungen auf beiden Skalen miteinander verbinden.

Verschiedenste Bereiche der Wissenschaften bedienen sich dem Werkzeug des maschinellen Lernens. Beispiele aus der Wissenschaft zeigen, dass solche Modelle durch das Einspeisen von großen Datenmengen erfolgreich trainiert werden konnten,

z.B. autonomes Fahren, Gesichtserkennung, usw. Diese Dissertation schlägt eine neuartige Homogenisierungsstrategie für die Simulation von Mauerwerk (im ebenen Spannungszustand) vor, bei der ein kontinuierliches, nichtlineares Materialgesetz kalibriert wird, indem relevante Daten aus der Simulation im Mikrobereich berücksichtigt werden. Die vorgeschlagene Methode basiert auf einem maschinellen Lernwerkzeug, das die Makro- und Mikroskalen miteinander verbindet, indem ein Materialgesetz auf Makroebene trainiert wird. Die dabei einzuspeisenden Benchmark-Daten werden aus numerischen Tests an RVE-Mikromodellen generiert.

In diesem Zusammenhang liefern numerische nichtlineare Tests an Mauerwerksmikromodellen, die in einem virtuellen Labor durchgeführt werden, die Benchmark-Daten für das ML-Trainingsverfahren. Das angewandte ML-Verfahren ermöglicht die genaue und effiziente Simulation des anisotropen Verhaltens von Mauerwerk mit Hilfe eines Tensor-Mapping-Verfahrens. Der letzte Schritt dieser neuartigen Homogenisierungsmethode ist die Definition eines kalibrierten konstitutiven Materialgesetzes für die Anwendung auf die Simulation von Mauerwerk auf der Makroebene.

Die entwickelte Technik wird auf die Homogenisierung einer Mauer aus flämischem Verbundmauerwerk in der Ebene angewendet. Bewertungsbeispiele, die auf der Simulation physikalischer Labortests basieren, zeigen die Genauigkeit der Methode im Vergleich zu einer ausgefeilten Mikromodellierung der gesamten Struktur. Abschließend wird ein Anwendungsbeispiel der neuartigen Homogenisierungstechnik für die Pushover-Analyse eines historischen Mauerwerkes gegeben.

Stichwörter: *Mauerwerk · Finite Element Methode · Makromodellierung · Mikromodellierung · Mehrskalen Modellierung · Homogenisierung von Materialien · Heterogene Festkörper · Maschinelles Lernen · Bruchmechanik · Pushover Analyse*

Contents

List of Figures

List of Tables

List of abbreviations and symbols

Acronyms

	Definition	1^{st} Appearance
ANN	Artificial neural network	Sec. 2.3
APA	Adaptive pushover analysis	Sec. 3.2.2
CMM	Continuous micro modeling	Sec. 2.2.1
CQC	Complete quadratic combination	Sec. 3.2.2
DMM	Detailed micro modeling	Sec. 2.2.1
$EC8$	Eurocode 8	Sec. 3.2.1
FE	Finite element	Sec. 1.1
$LVDT$	Linear variable differential transformer	Sec. 4.7.2.1
$MDOF$	Multi degree of freedom	Sec. 3.3.2
$MDPA$	Multi directional pushover analysis	Sec. 3.1
MPA	Modal pushover analysis	Sec. 3.2.2
NDA	Nonlinear dynamic analysis	Sec. 3.1
NSA	Nonlinear static analysis	Sec. 3.1
PP	Performance point	Sec. 3.3.2
RC	Reinforced concrete	Sec. 3.2.2

RSE	Representative single element	Sec. 5.3.4
RVE	Representative volume element	Sec. 2.2.3
$SDOF$	Single degree of freedom	Sec. 3.3.2
SMM	Simplified micro modeling	Sec. 2.2.1
$SRSS$	Square root of the sum of squares	Sec. 3.2.2
$TLBCPB$	Tension Lubliner Bézier Compression Petracca Bézier	Table 4.2
$TLECPB$	Tension Lubliner Exponential Compression Petracca Bézier	Table 4.2
$TRBCPB$	Tension Rankine Bézier Compression Petracca Bézier	Table 4.2
$TRECPB$	Tension Rankine Exponential Compression Petracca Bézier	Table 4.2
URM	Unreinforced masonry wall	Sec. 4.7.2.1
VL	Virtual laboratory	Sec. 5.3

Greek Symbols

Symbol	**Description**	1^{st} **Appearance**
α	Scalar value used for the computation of the equivalent stress	Eq. (4.8, 4.9)
$\alpha^{\star}$	Scalar values for the computation of the closest isotropic matrix	Eq. 5.41
$\bar{\boldsymbol{\sigma}}$	Effective stress tensor	Eq. (4.1)
$\bar{\boldsymbol{\sigma}}^{\pm}$	Positive/negative part of the effective stress tensor	Eq. (4.2)
$\bar{\sigma}_i$	The i-th principal stress of the effective stress tensor	Eq. (4.5)
$\bar{\sigma}_{max}$	Maximum value of the principal stresses	Eq. (4.8, 4.9)
$\bar{\sigma}_{min}$	Minimum value of the principal stresses	Eq. (4.8, 4.9)

β	Scalar value used for the computation of the equivalent stress	Eq. (4.8, 4.9)
β_N	Newmark-beta constant	Section 3.4.4
$\beta_{1/2}$	Scalar values during optimization procedure	Eq. (5.6),(5.7), (5.8)
$\boldsymbol{\epsilon}$	Strain tensor	Eq. (4.1)
$\boldsymbol{\epsilon}_{pert,j}$	j-th perturbation strain vector	Sec. 4.5.2
$\boldsymbol{\epsilon}_{true}$	Input strain vector for the machine learning model	Sec. 5.2.3
$\boldsymbol{\sigma}$	Cauchy stress tensor	Eq. (4.2)
$\boldsymbol{\sigma}_{pert,j}$	j-th perturbation stress vector	Sec. 4.5.2
$\boldsymbol{\sigma}_{pred}$	Predicted stress vector	Sec. 5.2.3
$\boldsymbol{\sigma}_{true}$	Input stress vector for the machine learning model	Sec. 5.2.3
$\boldsymbol{\Theta}$	Container of trainable parameters of a machine learning model	Sec. 5.2.1
$\boldsymbol{\Theta}^\star$	Container of finally optimized model parameters	Eq. (5.14)
$\boldsymbol{\Theta}^\star$	Container of finally optimized model parameters	Sec. 5.2.3
χ_{adap}	Scalar value to ensure optimization stability	Eq. 5.5
χ_{pert}	Perturbation factor	Eq. (4.40)
$\epsilon^{\pm}_{0/i/p/j/k/r/u}$	Scalar values to define damage evolution in compression or tension, Bézier control strains 0,i,j,p,j,k,r,u	Fig. 4.2
η	Learning rate	Eq. 5.2
Γ	Transformation factor of the N2 method	Eq. (3.1)
γ_N	Newmark-beta constant	Section 3.4.4

$\hat{\boldsymbol{\epsilon}}$	Placeholder strain of the machine learning model	Fig. 5.2
$\hat{\boldsymbol{\sigma}}$	Placeholder stress of the machine learning model	Fig. 5.2
κ	Scalar value to better control the shear behavior in the compression yield surface	Eq. (4.9)
$\kappa^{\star}$	Scalar values for the computation of the closest isotropic matrix	Eq. 5.41
λ	Scalar parameter for boundary strain generation	Eq. 5.24
$\mu^{\star}$	Scalar values for the computation of the closest isotropic matrix	Eq. 5.41
ν	Poisson's ratio of an isotropic material	Table 3.1
Ω_{RVE}	Volume of the representative volume element	Fig. 5.6
ω_t	Correction factor for gradient descent optimization	Eq. 5.5
ϕ	Angle for boundary strain generation	Eq. 5.24
$\Phi^{\pm}$	Damage criteria for tension/compression behavior	Eq. (4.15)
Φ_i	Normalized displacement of the i-th mode	Eq. (3.1)
ρ	Density of a material	Table 3.1
$\tau^{\pm}$	Equivalent stress tension(+)/compression(-)	Sec.4.2 and Eq. (4.8. 4.9)
$\tau_n^{\pm}$	Value of the tension/compression equivalent stress at the analysis step n	Eq. (4.14)
τ_{max}	Maximum shear strength	Section 3.4.2
θ	Angle for boundary strain generation	Eq. 5.24
$\tilde{\boldsymbol{\epsilon}}$	Arbitrary strain vector	Eq. (5.14)

Υ	Scalar value to compute the damage variable	Eq. (4.16)
φ_n	Angle of multi directional pushover variation	Sec. 3.3.2
$\xi^{\pm}$	Strain-like counterpart for tension or compression	Eq. (4.16)
ζ	Scalar factor for the splitting of the machine learning input data	Eq. (5.19)

Roman Symbols

Symbol	Description	1^{st} Appearance
$\bar{I}_1$	First invariant of the effective stress tensor	Eq. (4.8, 4.9)
$\bar{J}_2$	Second invariant of the deviatoric effective stress tensor	Eq. (4.8, 4.9)
$\boldsymbol{A}_\epsilon$	Strain transformation matrix	Eq. 5.46
$\boldsymbol{A}_\sigma$	Stress transformation matrix	Eq. 5.46
$\boldsymbol{C}$	Linear elasticity tensor	Eq. (4.1)
$\boldsymbol{C}_s$	Secant constitutive tensor	Eq. (4.37)
$\boldsymbol{C}_t$	Tangent constitutive tensor	Eq. (4.39)
$\boldsymbol{C}_{ortho}$	Orthotropic elasticity tensor	Eq. 5.35
$\boldsymbol{C}_{raw}$	Raw elasticity tensor	Eq. 5.30
$\boldsymbol{c}_{t,j}$	j-th column vector of the tangent constitutive matrix	Sec. 4.5.2
$\boldsymbol{D}$	Fourth order tensor for damage compuation	Eq. (4.37)
$\boldsymbol{I_4}$	Constant matrix for the computation of the closest isotropic matrix	Eq. 5.41
$\boldsymbol{I}$	Identity tensor	Eq. (4.6)

$\boldsymbol{J}$	Constant matrix for the computation of the closest isotropic matrix	Eq. 5.41
$\boldsymbol{K}$	Constant matrix for the computation of the closest isotropic matrix	Eq. 5.41
$\boldsymbol{n}_i$	Eigenvector of the i-th principal stress σ_i	Sec. 4.1
$\boldsymbol{P}^{\pm}$	Positive/negative projection tensor	Eq. (4.3 and 4.4)
$\boldsymbol{p}_{ii}$	Vector to compute the projection tensor	Eq. (4.5)
$\boldsymbol{T}$	General transformation tensor	Eq. 5.50
$\mathcal{B}$	Function to compute the Bézier curve	Eq. (4.26)
$\mathcal{G}$	Computation graph of the machine learning model	Fig. 5.2
$\mathcal{G}$	Function to compute the area beneath a Bézier defined curve	Eq. (4.26)
$\mathcal{L}$	Loss function of a machine learning model	Sec. 5.2.1
$\mathcal{P}$	Optimization node of the machine learning model	Fig. 5.2
$\mathcal{S}$	Stretching factor for energy regulation	Eq. (4.30)
Ψ	Function that contains the constitutive law	Sec. 5.2.3
$\triangle t$	Step size of a numerical analysis	Section 3.4.4
A, B, C, D	Scalar variables to compute the compression damage	Eqs. (4.18, 4.21)
$a_{0/1}$	Factors for computation of Rayleigh damping	Sec. 3.4.4
A_j	Area of the j-th element of the representative volume element	Eq. 5.27
a_{max}	Maximum horizontal pushover acceleration	Sec. 3.4.3
a_{PP}	Pushover acceleration at performance point	Table 3.2

A_{RVE}	Total area of the representative volume element	Eq. 5.27
$c^{\pm}_{1/2/3}$	Scalar values to control better the post peak part of the compression or tension damage evolution	Sec. 4.3.1
C_{Ray}	Rayleigh damping matrix	Sec. 3.4.4
$d^{\pm}$	Positive/negative damage variable	Eq. (4.2)
$d^{\star}$	Control node displacement of the equivalent SDOF	Eq. (3.3)
d_n	Control node displacement of the MDOF system	Eq. (3.3)
d_u	Ultimate displacement of control node	Sec. 3.4.3
$d^{\pm}_{eq}$	Equivalent damage variable	Eq. 5.56
$d^{\pm}_{eq}$	Equivalent damage variable	Eq. 5.57
d_{PP}	Control node displacement at performance point	Table 3.2
E	Young's modulus of an isotropic material	Table 3.1
$e_{0x/y}$	Structural eccentricity in x/y direction	Sec. 3.4.1
$F^{\star}$	Base shear force of the equivalent SDOF	Eq. (3.2)
f^{+}_{0}	Damage onset stress in tension behavior	Eq. (4.14)
f^{-}_{0}	Damage onset stress in compression behavior	Eq. (4.14)
F_b	Base shear force of the MDOF system	Eq. (3.2)
f^{+}_{p}	Uniaxial tensile strength	Table 3.1
f^{-}_{p}	Uniaxial compressive strength	Table 3.1
$f_{c,bi}$	Biaxial compression strength	Eq. (4.11)

$f_{c/t,r}$	Compressive and tensile residual strengths	Table 3.1
$f^{\pm}_{i/j/k/u}$	Scalar values to define damage evolution in compression or tension, Bézier control stresses i,j,k,u	Fig. 4.2
$G^{\pm}$	Compressive and tensile fracture energy	Table 3.1
$g^{\pm}$	Specific fracture energy	Eq. (4.31)
$g^{\pm}_{1/2/3}$	Scalar values to compute the area beneath the Bézier defined curves for compression or tension	Fig. 4.2
$g^{\pm}_{calc}$	Specific fracture energy calculated from Bézier functions	Eq. (4.28)
$g_{n,i}$	Gradient of optimization procedure	Eq. 5.3
H_{dis}	Discrete softening parameter in tension	Eq. (4.34)
I_{true}	Inputs of machine learning model	Sec. 5.2.1
K	Stiffness matrix in order to compute Rayleigh damping	Sec. 3.4.4
k_b	Scalar value to compute the equivalent stress	Eq. (4.11, 4.12)
k_i	Number of Gauss points of the i-th element of the representative volume element	Eq. 5.27
l_{dis}	Size of the energy dissipative zone	Eq. (4.33)
l_{mat}	Material length	Eq. (4.35)
M	Mass matrix in order to compute Rayleigh damping	Sec. 3.4.4
$m^{\star}$	Mass of the equivalent SDOF system	Eq. (3.1)
m_i	Mass of the i-th node of the finite element model	Eq. (3.1)
$m_{n,i}$	Gradient during optimization procedure	Eq. 5.5

n	Scalar that indicates the actual step of a numerical analysis	Sec. 4.3)
O_{pred}	Predicted output of a machine learning model	Sec. 5.2.1
O_{true}	Outputs of machine learning model	Sec. 5.2.1
p	Scalar variable to compute the compression damage	Eq. (4.17)
$r^{\pm}$	Damage threshold in tension/compression	Eq. (4.14)
$r_0^{\pm}$	Initial value of the tension/ compression damage threshold	Eq. (4.14)
$r_{x/y}$	Torsional radius in x/y direction	Sec. 3.4.1
t_0	Start time of a numerical analysis	Sec. 4.3)
T_1	Period of first mode	Section 3.4.4
t_e	End time of a numerical analysis	Sec. 4.3)
$v_{n,i}$	Gradient during optimization procedure	Eq. 5.5

Part I

Introduction

Chapter 1

Introduction

1.1 Background and motivation

Humans have been using masonry structures to build their surrounding environment since very ancient times. It all started with rocks put together in order to be protected from natural or social hazards. Humans could construct from small walls passing to houses and up to large structures (e.g. temples, palaces, fortresses) by developing their own techniques that severely improved the use of masonry. It has always been one of the prioritized construction materials. At the end of the industrialization age the invention of reinforced concrete provoked an important reduction of the use of masonry in construction. Engineers started to think in other dimensions and tried to reflect this in their architecture. High rise buildings scratching the sky were only possible when constructing out of concrete or steel. The workmanship required less manpower and machines facilitated the construction with new building materials. This has led to a debatable use of resources that was anything else but sustainable. However, the generation of the 21^{st} century is tackling climate change and the construction world must take action. More sustainable materials must be found, recycled and brought into a circular economy that does not allow ignorance anymore. Constructing out of masonry plays an important role for this change. Bricks can be reused and also produced from other recycled materials. Furthermore, bricks are available locally and short transport routes reduce carbon emissions. Therefore, investigating in the field of masonry is much more than the preservation of architectural heritage, as it is part of the story about how humans tackle environmental issues in their built environment.

Masonry is an assembly of many different materials - a conjunction of rocks/stones or bricks usually bound together with mortar. There is no unique definition of how to allocate the units in order to obtain masonry, as it depends on the explicit knowledge developed by each cultural group in order to construct. Inside these cultural groups, the knowledge of how to construct masonry has been passed on from one generation to the other. Furthermore, each technique has been improved over time through the application of the latest technological developments.

Today's world contains a collection of many different masonry construction techniques. In any region, masonry features the local and traditional way of constructing. This collection must be saved by the present society. Many of the still existing structures around the globe belong to instances that represent our social values, e.g. churches, temples and mosques represent our religious values while palaces represent the administrative institutions that have allowed the development of our society. Up to now, people have endeavored to communicate these social values in their architecture. The master builders of past times knew that their built environment also represents cultural values and consequently they tried to design to perfection. Since there was no other possibility than to construct from timber or stones at that time, the architects and engineers had to invent the best structures out of these limitations. And the master builders trained themselves in using materials for complex structures, such as masonry arches, as can be observed in many churches from the Gothic and Baroque age. They knew about the properties of masonry, i.e. the weak strength in tension and strong strength in compression. Thus, they minimized the occurrence of tensile stresses by optimizing the geometry of structures. At that time the builders used simple analysis approaches in order to build their masterpieces. Each generation - and thanks to the age of masonry many former generations already existed - has always improved its construction techniques and assessment tools so that large structures could be built.

Nowadays, demanding mathematical tasks are done by computers. Great effort has been put into the development of computer hardware in order to increase computation capacities. Modern software is continuously improved in order to facilitate the work of all. Nowadays, structural engineers also employ these tools in order to assess the stability of structures. The finite element (FE) method is one of the most renowned approaches employed to perform structural analysis. Computer aided design tools allow the detailed modeling of large structures. The FE method can then

be utilized in order to compute the stress/deformations corresponding to particular loading and boundary conditions. A great visualization of the results is given by post processing software. The availability of such numerical tools has also brought the structural analysis of masonry structures to a next level.

The availability of numerical analysis for masonry structures is a fundamental step towards overcoming the limitations faced by the master builders of ancient times. In the past decades, several numerical modeling techniques for the assessment of existing masonry buildings have been developed. Masonry structures are more vulnerable when exposed to horizontal loading. Such loads can be induced by strong winds or earthquake actions. Under such conditions, masonry's poor strength in tension can be exhausted easily and large cracks can lead to total collapse of structures. Numerical analyses simulating these loading scenarios can help to assess the vulnerability of historical structures and to identify weak parts that require structural intervention. However, conventional procedures include assumptions and are very often restricted to regular structures. Especially historical structures are characterized by irregularities in plan and elevation and when exposed to horizontal actions, conventional assessment methods are not representative anymore. Therefore, further improved procedures that also take irregularities into account should be developed.

The more accurate way of modeling masonry is the renowned micro modeling approach. Masonry is modeled by differing between the material components. Broadly spoken, the geometrical model consists of brick units and mortar joints. Distinct constitutive models assigned to each component are able to represent its respective natural material behavior. The numerical simulation of such micro modeled structures is able to represent the damage and cracks very accurately when compared to experimental data. However, this approach requires a large computational cost and restricts its application to small-scale structures. Large investigative effort was put into a technique that assumes masonry to be a continuum material with smeared material properties. This technique is called macro modeling. The major advantages are less modeling and computational effort. Thus, large-scale structures can be analyzed through simulations of earthquakes, wind loads, soil settlements, etc. Many different types of simulations have been carried out and are still being developed in order to investigate the causes of a wide variety of potential structural problems. However, masonry is a composite material and averaging its properties

makes each analysis strongly dependent on the assumptions made by the analyst while defining the homogenized constitutive model. Therefore, the simulation of damage might give either correct or false assessments. In order to overcome this inaccuracy, multi-scale approaches have been investigated as they are able to combine the micro and macro modeling. These approaches have shown to be able to connect the advantages of both techniques, even though the computational cost is still too expensive (Petracca (2016)).

It becomes clear from the previous considerations that novel tools must be considered for the numerical analysis of masonry structures in order to minimize computational effort and optimize the assumed material properties at the same time. K.C. Park, a renowned Professor Emeritus from University of Colorado at Boulder, mentioned in a keynote speech given at the International Centre for Numerical Methods in Engineering (CIMNE Barcelona) that *"Paradigm Changes in Engineering Modeling"* are taking place. He motivated young researchers in the field of mechanics to utilize directly processed data in order to identify system parameters, and he talked about the convenience of skipping analytic model construction stages when practical and reliable alternative solutions can be achieved through data models. He refers to keywords like big data, artificial intelligence, machine learning etc. Those approaches have been pushed forward in many scientific and industrial fields. In fact, large amounts of data are nowadays utilized to train machine learning models and artificial neural networks that have applications in almost every field. Such models establish patterns in large data training sets that enable predictions on data that are not part of the training set. The most famous application of such models is face recognition in photos. So why not use this strong contemporary tool of learning from data in the research field of masonry?

Considering the above, two challenges in the numerical analysis of masonry structures are evolving. On the one hand, advanced numerical simulation techniques applied to large structures must be developed in order to correctly assess the diverse structural response of masonry structures. On the other hand, constitutive models utilized in macro modeling approaches must be defined in order to correctly represent the peculiar material behavior of masonry.

Consequently, this research addresses both these challenges. Firstly, it evaluates the opportunities of macro modeling by developing a novel nonlinear simulation technique for the seismic analysis of irregular masonry structures. The technique is

applied to a complex case study. Based on this application, the conventional approach of defining macro model properties is explored and its limitations are demonstrated. Secondly, the use of machine learning to overcome some of these limitations is investigated. The main motivation of this work is to utilize the modern tool of machine learning to develop well-trained constitutive models based on data derived from small-scale micro modeling results. This procedure leads to the development of a novel homogenization strategy based on machine learning, allowing the reliable calibration of relevant parameters for the macro modeling of masonry structures.

1.2 Scope and objectives

The primary objective of this thesis is to develop a machine learning based homogenization technique for the non-linear numerical analysis of masonry structures in order to provide more representative homogenized properties for the analysis at the masonry macro scale. The research is performed within the scope of non-linear advanced simulations of masonry at the macro scale, the definition of nonlinear continuum damage models and the elaboration of machine learning tools. The study focuses on two-dimensional structures which can be simulated as being in the state of plane stress. In order to accomplish the primary goal of the studies, several specific objectives have been defined. These are summarized in the following.

(a) To generate a comprehensive state-of-the-art collection including investigative results with objectives similar to the one of this study, including the improvement of nonlinear numerical simulation techniques and the optimization of homogenization techniques for masonry.

(b) To demonstrate the importance of macro modeling techniques for the analysis of masonry structures by developing an advanced novel nonlinear analysis tool for the seismic assessment of irregular masonry structures. This step of the research allows the understanding of possible limitations of conventional macro model material definitions.

(c) To analyze and improve constitutive continuum damage models for the nonlinear analysis of masonry by means of a calibration procedure based on machine learning.

(d) To facilitate macro scale analysis by utilizing a machine learning based homogenization technique. The development of the technique includes the following objectives:

- To define a set of constitutive models eligible for machine learning models and representative for masonry material behavior.
- To compile a suitable numerical computation graph inside the machine learning model.
- To generate large data sets in a virtual laboratory as training input for the machine learning model.
- To derive a post machine learning constitutive model suitable for numerical macro scale analysis of masonry.

(e) To apply the machine learning based homogenization technique to a real scale masonry wall in order to evaluate the trained post homogenization macro scale model, and compare its performance with that of sophisticated micro modeling.

(f) To run seismic nonlinear analyses on a large scale structure by utilizing the machine learning based material homogenization technique, and comparing the results with a continuum FE homogenization approach.

1.3 Outline of the thesis

This document is separated into four parts. Part I is an introduction to the topic and consists of three chapters.

Chapter 1 presents the author's motivation to develop a machine learning homogenization technique for masonry and defines the research background. It also depicts the objectives and the scope of the research, and gives an outline of the thesis document.

Chapter 2 introduces the research of this thesis by presenting a literature review on the underlying topics. Firstly, it gives an overview of numerical analysis of masonry structures and specifies it into three modeling strategies. Special attention is given to the currently available multiscale and homogenization techniques by also

including the ideas behind micro and macro modeling. Secondly, it presents a short summary of available numerical tools for the seismic analysis of masonry. Finally, deep insights are given into the history of machine learning techniques and its use in the field of structural engineering.

Chapter 3 includes an advanced numerical simulation technique for masonry in order to demonstrate the advantages and limitations of macro scale modeling. This chapter presents a novel multi directional pushover approach applicable to the seismic analysis of irregular masonry structures. The novel method is compared with conventional nonlinear seismic analyses approaches in order to investigate the method's performance on seismic vulnerability analyses. This chapter also highlights the limitations and drawbacks of macro scale analysis by discussing its conventional approach of defining homogenized material properties for masonry. A case study of an existing masonry heritage structures allows the development of a detailed discussion.

Part II summarizes the investigations made on the machine learning homogenization technique. It consists of two chapters.

Chapter 4 details the theoretical backgrounds of the constitutive models utilized for the nonlinear analysis of masonry. The adopted continuum damage law is based on two damage variables indicating the state of damage in tension or compression, respectively. The damage variables have separate damage evolution laws. Numerical benchmark examples illustrate its functionality and versatility of the approach, while the application of the constitutive model to a masonry wall demonstrates the accuracy of numerical analysis results when compared with experimental tests.

Chapter 5 proposes the novel machine learning based homogenization technique, including fundamental background information, e.g. numerical software tools, gradient descent operators, loss functions and the computation graph. Chapter 5 also introduces the concept of a virtual laboratory. Numerous micro scale analyses on masonry representative volume elements generate large data sets of coupled strain and stress pairs. The data then serve as training input for the machine learning model. In order to utilize the data for training, a previous step of data isotropization prepares them for the constitutive machine learning model. This procedure includes least square fitting, parameter optimization and transformations by using the tensor mapping concept in order to define anisotropic and isotropic linear elas-

tic parameters of the homogenized masonry material. The post machine learning constitutive model is defined. Each step of presented procedure is accompanied by depicting the numerical implementation algorithm.

Part III presents some meaningful application examples of the machine learning based homogenization technique and discusses the results derived from the given methodology.

Chapter 6 presents the structural application of the machine learning based homogenization technique to a masonry wall built in Flemish bond. A numerical virtual laboratory campaign by considering 26 micro model analyses is performed in order to generate the training set of the machine learning model. The machine learning model takes into account an advanced constitutive model in order to analyze the prediction results. Optimization results of the model are compared by analyzing the results of post machine learning macro scale analysis and micro scale analysis.

Chapter 7 presents the application example of the machine learning based homogenization technique for the pushover analysis of a real masonry structure. For this purpose, an analogous procedure as presented for the Flemish bond wall is applied in order to define the macro constitutive model of the considered case study. The case study is the Palacio Pereira, an heritage building located in Santiago de Chile. In this context, the post machine learning constitutive model is assigned to the FE models of the two principal facades of the structure. Both models are subject of nonlinear pushover analyses. In order to discuss the results of the novel homogenization technique compared with available standard methods, the same nonlinear pushover analyses are applied to the facade models by using a conventional macro scale approach. A final presentation of the results compares and discusses both the methodologies.

Part IV includes the closing Chapter 8 of the dissertation discussing the performed research, presenting the main conclusion, defining the main contributions and discussing suggestions for future works on machine learning based homogenization techniques.

Chapter 2

Literature review

2.1 Introduction

This chapter presents a literature review about the numerical finite element analysis of masonry. Masonry is a heterogeneous component material that requires proper techniques when modeled via FE analysis. In this context, the review includes a general overview of numerical modeling techniques and their respective field of application. Modern data driven models are also introduced as they have been applied to the analysis of masonry structures, as well as the topic of machine learning based constitutive modeling for material homogenization.

Section 2.2 presents previous research insights about numerical modeling of masonry. In this context, two modeling techniques are presented: micro and macro modeling. After having presented the advantages and drawbacks, an introduction is given to multi scale techniques. Such approaches aim to profit from the advantages of both micro and macro techniques and connect them within a sophisticated computational framework. Its applicability to large scale masonry structures is discussed.

Section 2.3 gives an introduction on modern numerical machine learning applications in the field of civil engineering. In this context, a first general overview is given in order to show its wide ranging fields of application in the structural engineering world. Furthermore, this section presents specific examples for machine learning in the numerical analysis of masonry structures. A closing subsection proposes a discussion regarding the use of artificial neural networks for constitutive modeling. A recent work presenting the use of machine learning for material homogenization

is presented.

The chapter finalizes with a summary given in Section 2.4.

2.2 Numerical analysis of masonry structures

In the last decades numerical analysis has become an established tool to evaluate the structural behavior of buildings in the entire field of civil engineering. The large efforts made in order to improve the FE method were essential for this growth. A strong contribution has also been the development of technical devices, such as processor speed and memory size of computers. Nowadays, large numerical three dimensional models of bridges, high rise buildings, soil foundation interactions, etc. with an unimaginable amount of finite elements can be build up and solved in the scope of the FE method. These achievements did not pass by to the structural analysis of masonry buildings.

Since always the research on structural behavior of masonry aims to capturing its heterogeneous behavior. The heterogeneity comes from its composition of brick units and mortar joints. The geometrical allocation of both the components made modeling of masonry to a difficult task. Having the FE numerical analysis by hand, the geometrical arrangement of the masonry components could be respected in detailed micro models. Page (1978) made the first scientific achievements into this direction. Being micro modeling a very detailed and time intense analysis method, its results can now be compared with less effortless tools such as macro modeling. As a consequence macro modeling can be applied to the analysis of large scale structures.

Apart from FE modeling of masonry, there exist numerical analysis tools like the discrete element method, discontinuous modeling, limit analysis, etc. Insights on these procedures and other analytic approaches are given by the review papers of Lourenço (2002); Roca et al. (2010); Theodossopoulos and Sinha (2013); D'Altri et al. (2019)

The literature review of this thesis only summarizes a small part of available numerical analysis methods for masonry structures. In the following of this section an introduction to the micro mechanical and the macro mechanical modeling of masonry is made. Both these techniques represent the masonry material in a more or a less detailed model, respectively. The consideration of the advantages and

drawbacks of micro and macro modeling of masonry, made in the last decades, led to multi-scale approaches. The efforts made in this direction are also summarized in the following.

2.2.1 Micro modeling

From an intuitive point of view, the heterogeneous component material masonry cannot be modeled as a single smeared homogeneous material with just one continuum constitutive law. The reasons are obvious. Masonry consists of brick units that are arranged following a geometrical ordered pattern or a random allocation. A mortar joint, usually made of a cement or clay mixture, serves as glue to ensure the geometrical allocation of the brick bond. Both these materials have differing linear elastic properties, such as the elasticity or the lateral strain behavior. Apart from the linear behavior, the brick and the mortar point out distinct post peak performance, e.g. the ductility. The noticeable differences in its behavior does then have the biggest effect when put together as a masonry structure. Then also the geometrical allocation of the components plays a significant role while modeling masonry. In order to be able to now numerically model masonry, the approach of micro modeling has won large interest in the last decades. This approach consists of distinguishing between the components and taking the spatial distribution of the components into account.

The main aim of masonry micro models is the ability to model all possible failure modes of masonry structures. These modes have been presented carefully in numerous investigations (Lourenço and Rots (1993), Lourenço and Rots (1997), Petracca (2016)) and will be summarizes here. The five basic types of masonry crack mechanisms are (Figure 2.1):

(a) cracking in the masonry joints

(b) diagonal tension cracking in the brick units

(c) splitting of brick units in tension caused by mortar dilatancy at high values of normal stresses

(d) sliding of brick units along the joints

(e) cracking of the brick units in direct tension

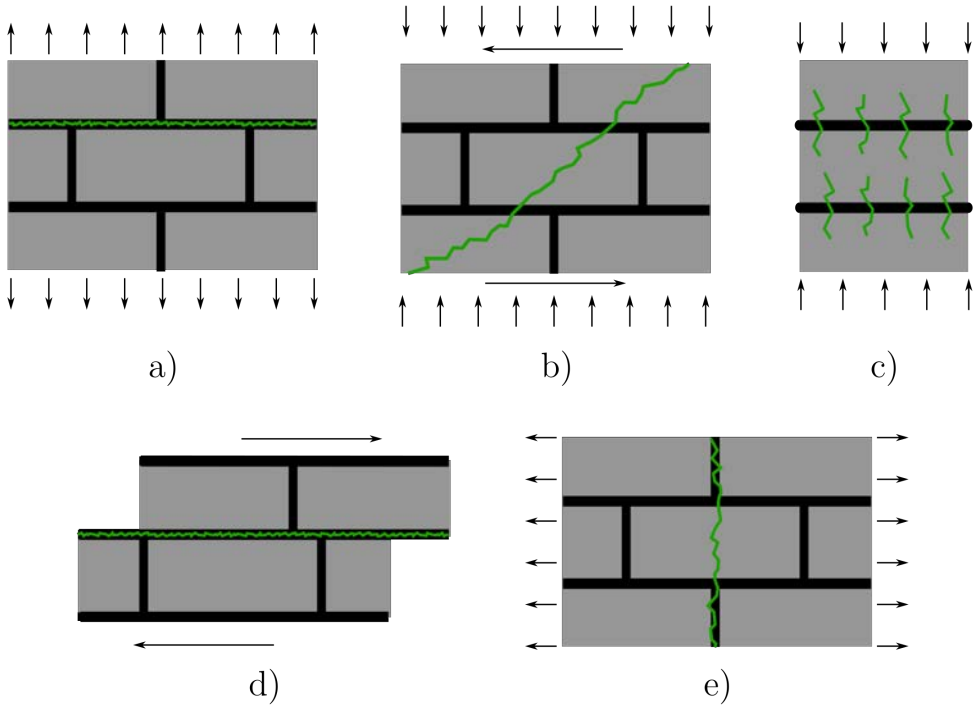

Figure 2.1: In-plane crack mechanisms of masonry: a) cracking in the joint, b) diagonal cracking of brick units, c) splitting of brick units due to dilatancy in the mortar joints, d) sliding of the bricks along the mortar joints, e) cracking of the bricks in direct tension

In the last decades, several researchers put huge effort in micro modeling of masonry in order to represent these mechanisms. Many different modeling techniques were elaborated. The main procedures in FE analysis range from detailed micro modeling (DMM) approaches to simplified (SMM) and continuous (CMM) ones. Figure 2.2 shows the most important micro modeling techniques applied to masonry structures. All these methods are based on assumptions made about the masonry components and its interaction. Their conceptional background and scientific applications will be presented in the following.

2.2.1.1 Detailed micro modeling

The detailed micro modeling of masonry is the most accurate one. This technique takes into consideration the components and an interaction of the bond between the components while setting up the micro model. The brick units and the mortar joints are then discretized with continuum elements. Additional interface elements

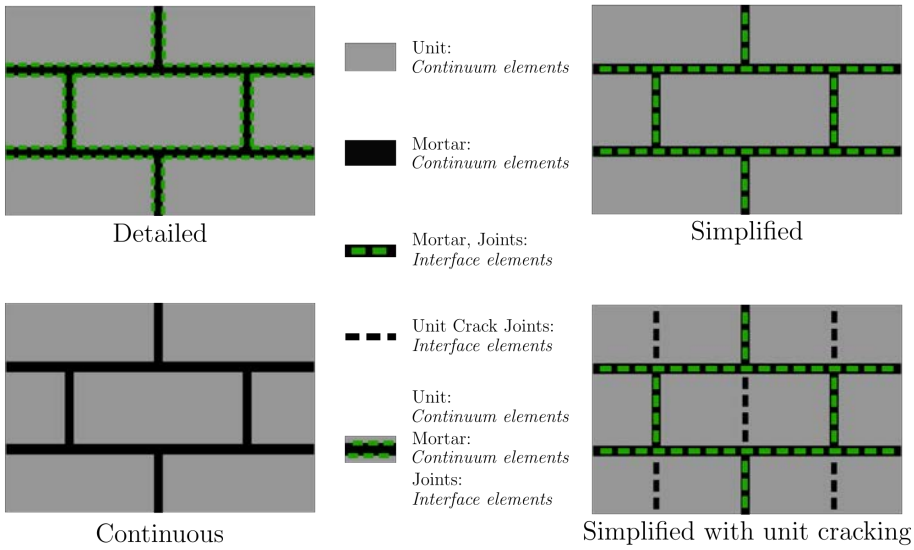

Figure 2.2: Overview of available micro modeling techniques for masonry. Showing the modeling background for the brick units, the mortar and a unit mortar joint interaction

represent the frictional behavior in between the two components. The detailed approach allows an accurate response of the FE analysis results. Nonetheless, is this procedure very time intense and highly expensive on computational cost. Thus the technique is only applicable to small scaled structures. As a result, researchers came up with simplified strategies to model the heterogeneity of masonry in means of FE analysis.

2.2.1.2 Simplified micro modeling

The simplified micro modeling (SMM) technique ranges back to investigations made by Page (1979). His motivation arose, since previous researchers considered the complex material behavior of masonry as a smeared linear elastic one. This approach did not consider masonry as a two-phased material. Thus Page (1979) assumed that the brickwork masonry consists of linear elastic brick units and inelastic mortar joint interactions. Back in the days, this procedure was not called SMM technique, since it was the first general approach to model masonry by distinction of the units and the joints.

Nowadays, more detailed models have been established in terms of SMM. However, the general modeling technique of considering the brick units as continuous

elements and the mortar joints as inelastic interfaces is still in use.

SMM considers the mortar joint as the weakest zone of the masonry material. As described above, this is taken into account by modeling the mortar joint and the unit-mortar interaction as a single lumped nonlinear interface. Thus a basic SMM FE model consists of continuous linear elastic brick elements allocated according to the masonry bond and are linked by non-linear mortar joint interface elements. The mortar joints then underlie the modeling concept of zero-thickness and the unit's dimensions are expanded in relation to the mortar thickness.

This technique is restricted to mortar joint cracking only and is not capable of representing all the mechanisms of masonry cracking shown in Figure 2.1. In order to also enable cracking in the brick units vertical discontinuous interface elements at the middle of the bricks have been introduced. Then vertical cracking of the brick units can be covered during an analysis. The SMM has been performed in several investigations (Lotfi and Shing (1994), Lourenço (1996), Lourenço and Rots (1997), Gambarotta and Lagomarsino (1997), Macorini and Izzuddin (2011), Petracca (2016), Minga et al. (2018), Chisari et al. (2018), Kumar and Barbato (2019)).

In the last decades a variety of constitutive models that is able to represent the unit/mortar interface have been introduced. Fortunately, many of the respective researchers have applied their numerical techniques to a benchmark experiment from the TU Eindhoven. In 1992, Raijmakers and Vermeltfoort (1992) performed shear compression tests on English bond masonry walls. Numerical analysis results applying the SMM approach in order to reproduce the experimental results are shown in Figure 2.3.

Instead of defining interface elements in the middle of the brick units, yet another possibility to respect cracking in the units, is to model them with a non-linear continuous material law that takes into account softening and cracking.

2.2.1.3 Continuous micro modeling

The continuous micro modeling approach is considering the components of the masonry as continuum elements being connected without any interface interaction. Both the components are then assigned with a respective linear-elastic or nonlinear damage material model. This approach is a simplification of the detailed micro modeling technique. All analyses further carried out in this thesis apply the CMM

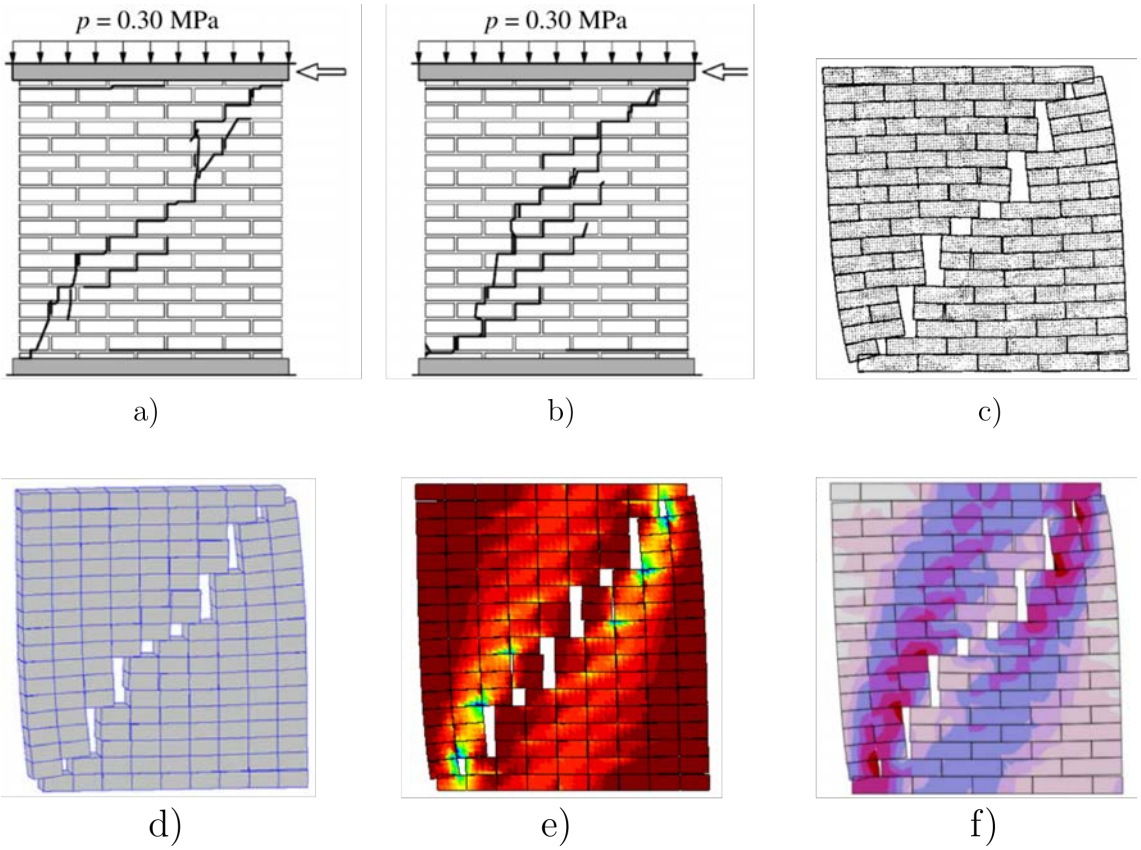

Figure 2.3: Schematic comparison of experimental and numerical shear compression test analysis of the TU Eindhoven experiment (Raijmakers and Vermeltfoort (1992)). Showing the crack patterns of two experimental tests (a) and b)) and the numerical results of different simplified micro modeling approaches: c) Lourenço and Rots (1997), d) Macorini and Izzuddin (2011), e) Petracca (2016) and f) Kumar and Barbato (2019)

technique for micro model analysis.

Some of the first continuous micro modeling approaches for masonry lead back to investigations made by Page (1988). This research discusses the behavior of a simple masonry wall subjected to concentrated loads. Therefore, a FE micro model has been constructed that differs clearly between the brick units and the mortar joints without taking into account any interface condition. By performing experimental tests, the material behavior of the respective component has been investigated very properly and resulted in the definition of continuum models for each component. Figure 2.4 shows a typical FE mesh that has been utilized in the research of Page (1988).

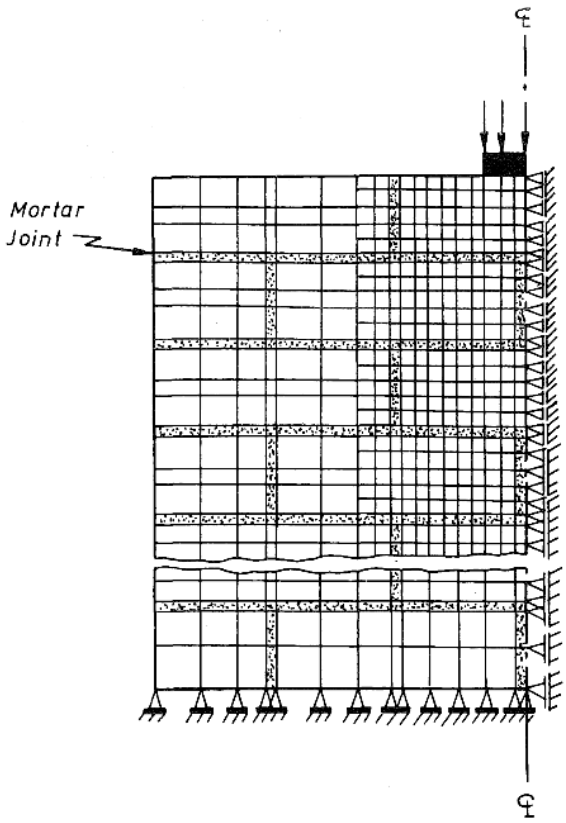

Figure 2.4: Continuous FE micro model elaborated in the research made in Page (1988)

Further investigations and applications of the CMM techniques have been carried out in Berto et al. (2004), Barbosa et al. (2010), Parisi et al. (2011), Drougkas et al. (2015), Petracca (2016), Petracca et al. (2017), Drougkas et al. (2019), Prakash et al. (2020). Figure 2.5 shows an overview of different fields of application of CMM extracted from these researches.

2.2.2 Macro modeling

Masonry macro modeling techniques consider masonry as a homogeneous material with average properties. No distinction is made between the brick units and the mortar joints. A single material model taking into account the linear elastic and the nonlinear inelastic behavior is assigned to all elements of the model. This technique is customized for the application to large scale structures and finds its use broadly in practice oriented industry. It is less suitable for the detection of local masonry

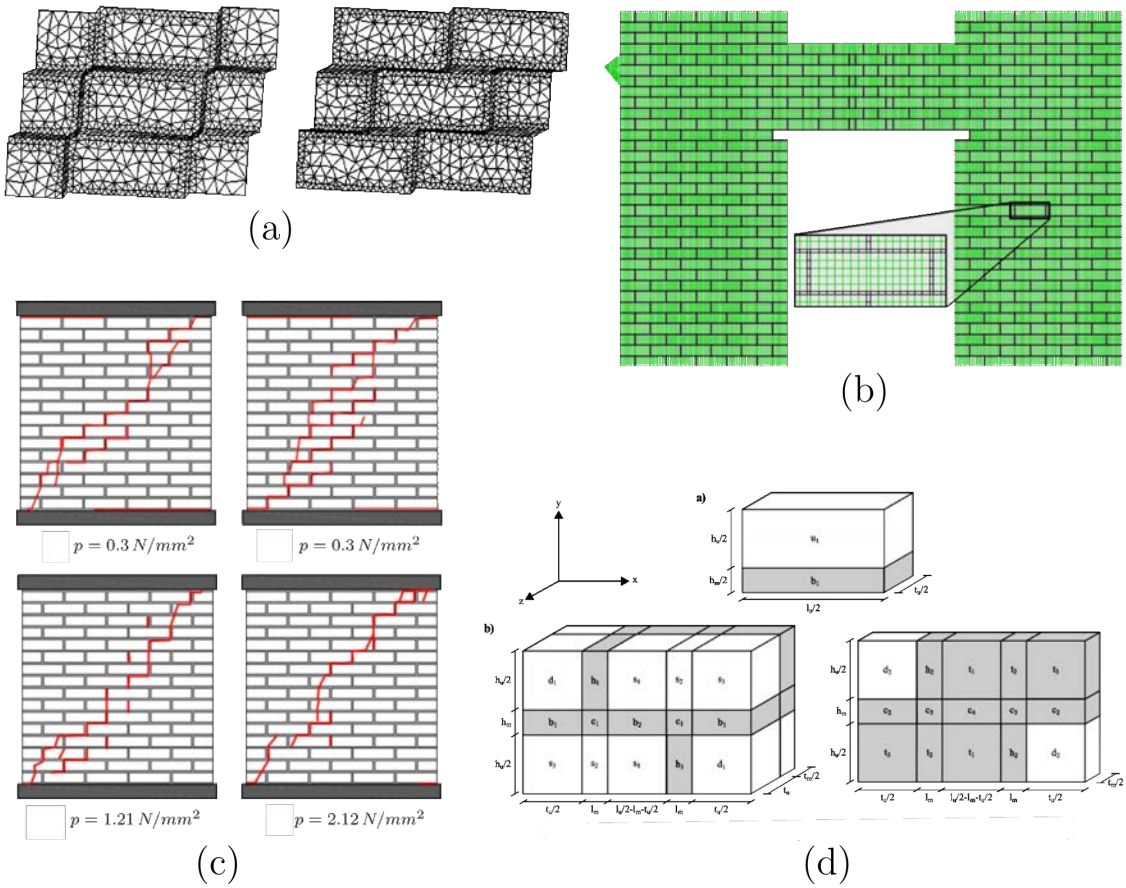

Figure 2.5: Continuous micro modeling: presentation of investigations using the continuous micro modeling approach for numerical analysis of masonry. Showing (a) micro model small wall model analysis from Berto et al. (2004), (b) large scale wall analysis with door opening Parisi et al. (2011), (c) continuous micro model analyses of TU Eindhoven shear wall Petracca et al. (2017) and (d) masonry micro model periodic cell analyses Drougkas et al. (2019)

failures such as described in Figure 2.1 than used for the structural assessment of entire masonry structures.

In this context, macro modeling approaches tremendously facilitate the geometrical modeling of masonry structures, since no specific masonry bond must be included to the FE models. That is also a reason why very few large scale structure analysis can be found in literature that apply the micro modeling technique.

Furthermore, the FE element mesh size can be chosen quite coarse when applying the macro modeling approach. Whereas micro models require the smallest element size to be at least the thickness of the mortar joint. Thus a huge FE model, in terms

of number of nodes and elements, and a even larger number of solvable numerical equations would arise. However, if modeling at the macro scale is considered, the smeared approach allows a FE mesh with elements of any thoughtful chosen size (engineering conscience).

However, the material models of macro scale masonry models must be chosen wisely. Usual models are smeared damage models that are able to represent damaged regions in the structures after nonlinear analysis. Such constitutive models should at least respect the material behavior of masonry. On the one hand a differentiation between tension and compression behavior should be made. Masonry belongs to the family of mineral building materials, which in general means that the compression strength is much higher than the tension one. In this context, proper yield criteria should be implemented that also respect this behavior. It has been also shown in previous research that such yield criteria do also serve in order to improve the model performance in terms of shear behavior (Petracca et al. (2017)). Masonry is also known to be an orthotropic material. Therefore proper approaches including orthotropy to the macro modeling have been elaborated (Lourenço (1995), Pelà et al. (2013)). Nonetheless, further improvements must be developed.

Generally spoken, macro modeling comes along with a tremendous decrease of computational effort. That is why many works have been presented in the last decades that consider numerical analysis of entire masonry structures. And macro modeling has become a preferred tool also in research. A huge amount of numerical linear and nonlinear analyses have been carried out that discuss the assessments of towers, churches, cathedrals, fortresses, bridges, etc. Each investigation has enhanced the numerical analysis of masonry. Many research insights can be found here: Lourenço et al. (2011), Roca et al. (2013), Almac et al. (2013), Pelà et al. (2013), Saloustros et al. (2015), Torelli et al. (2019), Micelli and Cascardi (2019), Brunelli et al. (2021), Milani and Clementi (2021), etc. Nonetheless, the given investigation examples are only a small excerpt from the entire investigation catalog about numerical analysis of large scale masonry structures. Figure 2.6 shows some macro scale numerical analysis examples.

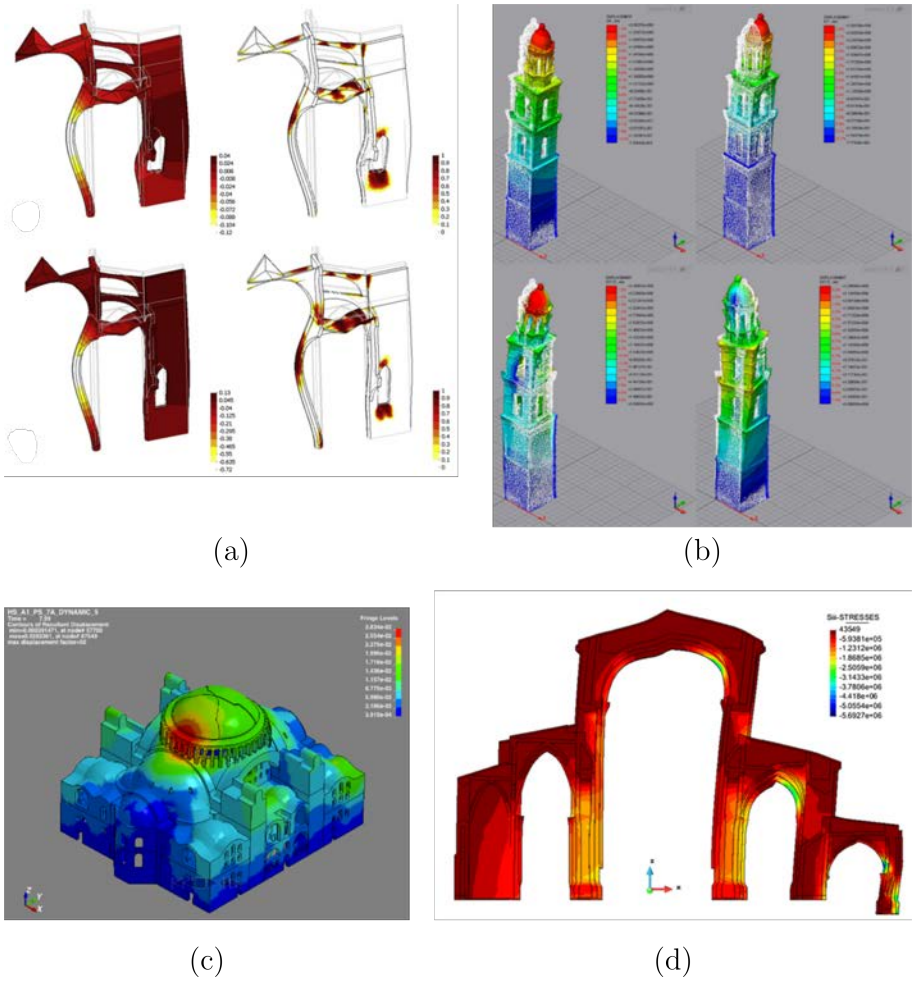

(a) (b)

(c) (d)

Figure 2.6: Large scale masonry analysis: presentation of investigations using the macro modeling approach for numerical analysis of masonry large scale structures. Showing (a) the numerical analysis of Mallorca cathedral Roca et al. (2013), (b) the structural assessment of a 14th century masonry tower Micelli and Cascardi (2019), (c) the seismic analysis of the Hagia Sofia in Istanbul Almac et al. (2013) and (d) the numerical analysis of the church of the Poblet Monastery Saloustros et al. (2015)

2.2.3 Multiscale modeling

Macro modeling implies a direct closed-form formulation of specific constitutive laws capable to represent the masonry material. However, applying such laws to homogenized geometrical models does not take into account the component interaction of bricks and mortar. It is hardly possible to study anisotropic behavior nor can stress redistribution or strain localization caused by damage be considered correctly in macro models. Nonetheless, macro modeling is the prior technique for numerical

analysis of large scale masonry structures. On the other hand, the micro modeling method most accurately represents the component material. In nonlinear analysis, damage propagation can be simulated with high precision by representing the typical masonry damage mechanisms shown in Figure 2.1. However, analyzing the masonry by distinctly modeling each component is time expensive on geometry construction and connected with a huge computational effort.

Given both the advantages and disadvantages of the modeling techniques macro and micro modeling, multi-scale modeling approaches have the aim to provide a direct relationship between both scales. The literature review of this thesis aims to present computational first order homogenization techniques. Such techniques are also known as FE^2 methods, since the boundary problem of the FE problem is solved at two scales with strongly differing sizes ($l << L$, where L is the size of the model at macro scale and l is the size of the micro scale). A general introduction to FE^2 methods is made in Schröder and Hackl (2014). In this context, several investigations have been made on applying first order multiscale techniques to the heterogeneous material masonry. A coarse overview is given in the following.

The general work flow of computational first order homogenization is the weak coupling of the micro and the macro scale. In this context, the large scale analysis takes place at the macro level where the strains at each Gauss point are computed. In order to now include the microscopic influence of the heterogeneous material to the macro scale, the strain field is scaled down to the micro scale. At this level the strains are applied as boundary conditions to a representative volume element (RVE). The RVE is modeled by clearly distinguishing between the material components. A numerical FE analysis calculates the corresponding stresses at the micro scale. In order to obtain the stress at the macro scale, a volume average of the micro scale RVE stress is computed. Then the so called up scaled stress can be mapped to the macro scale as the corresponding macro scale stress.

In this context, computational homogenization of masonry has been carried out in Massart (2003), Massart et al. (2007a), Massart et al. (2007b) for the in-plane analysis of small scaled masonry walls. The here applied multi scale scheme avoids the complex definition of macro scale constitutive laws by retrieving the response from computations carried out on micro model unit cells. These approaches have been later extended for the analysis of out-of-plane analysis of masonry walls (Mercatoris et al. (2009), Mercatoris and Massart (2011), Massart et al. (2011)). Figure

2.7 shows results from computational homogenization applied to an in plane loaded masonry wall. The plot is extracted from the investigations mentioned above. It demonstrates the damages computed at the unit cell level and the macro scale level, respectively.

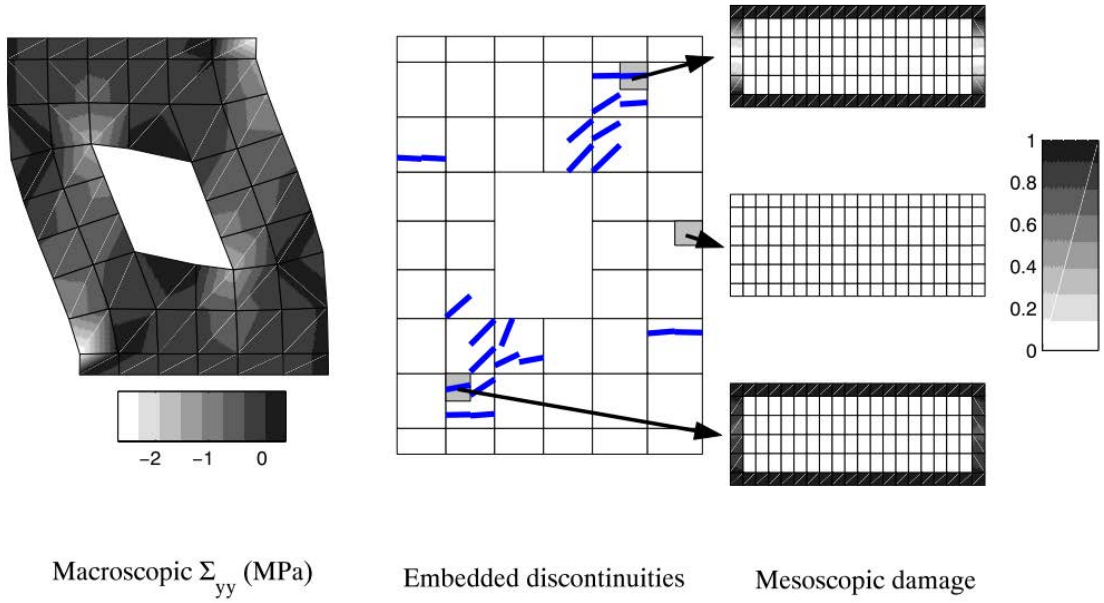

Figure 2.7: Masonry multi scale analysis of in-plane loaded masonry wall Massart (2003)

The insights obtained by the analyses presented have been further improved by defining more proper boundary fluctuation fields and implementing new constitutive modeling approaches for the analysis at micro scale in Petracca et al. (2016) and Petracca et al. (2017). Figure 2.8 shows the analysis results for the multi scale analysis of a large scale out-of-plane loaded masonry wall.

Such techniques have shown to very accurately represent experimental results performed on masonry walls. However, the presented techniques require the homogenization to be performed at each Gauss point of the macro scale model. This brings along a huge computational effort that makes the analysis of large scale masonry structures too expensive. Hence, appropriate alternatives to the classical computational homogenization have been presented, that disconnect the macro and micro scale analysis completely. Zaghi et al. (2018) have introduced an off-line technique that computes the RVE solutions of the micro scale separated from the macro analysis. In this context, the RVE was subjected to multiple numerical analyses, each

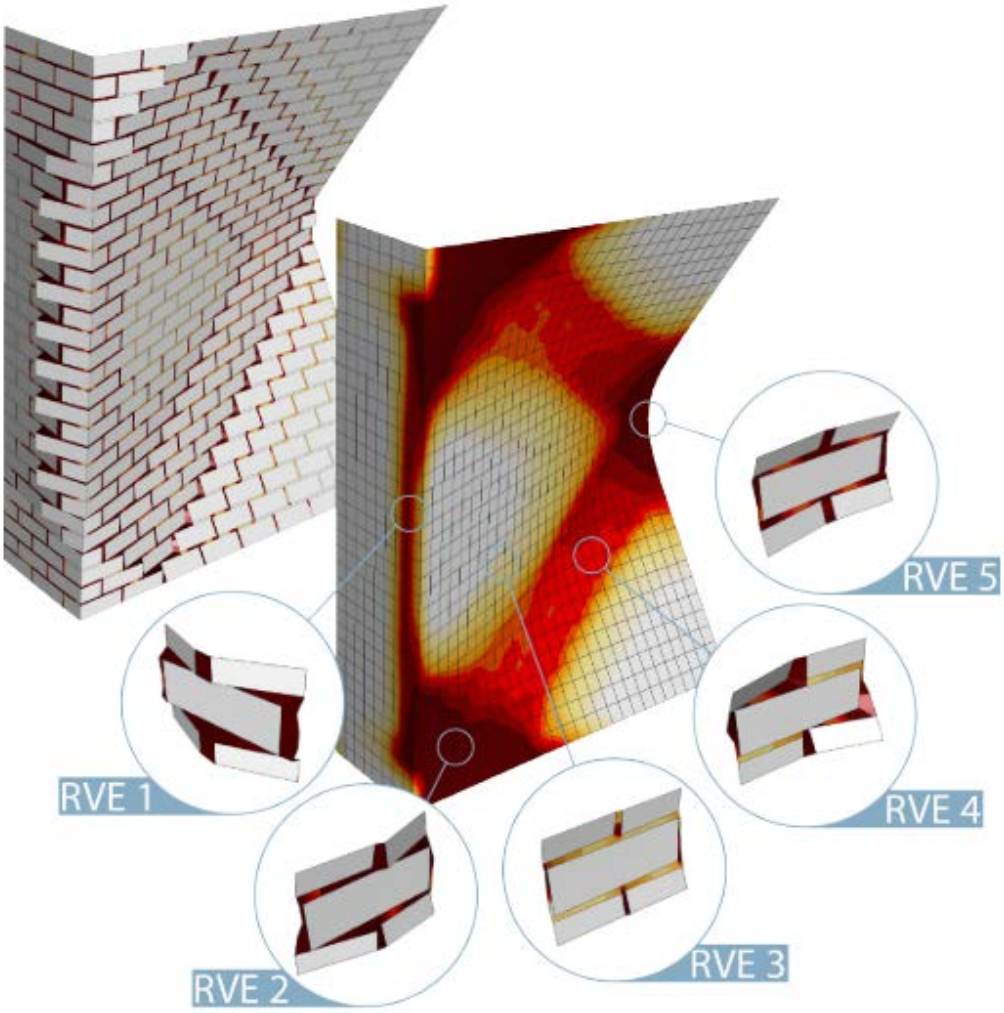

Figure 2.8: Masonry multi scale analysis: First order homogenization results of out-of-plane analysis of large scale masonry wall Petracca et al. (2017)

applying different boundaries, and the results were stored in a database. Consequently, the analysis at macro scale can now access to the database and is able to extract the suitable results by taking into account the strain field of the macro scale. The research made by Zaghi et al. (2018) has strongly influenced the present work since the idea of creating a virtual laboratory has evolved from the presented concept. Furthermore, utilizing processed data for homogenization has embarked the methodology of machine learning based homogenization for masonry.

2.3 Machine learning applications in civil engineering

Nowadays, data analysis, machine learning and artificial intelligence are technologies that are impacting almost every field in a significant way, e.g. techniques in face recognition Bhele and Mankar (2012), intelligent self driving networks Huang et al. (2020b), automatic translation systems Singh et al. (2017), modern medicine Sidey-Gibbons and Sidey-Gibbons (2019) or bio organic chemistry Panteleev et al. (2018), but also in the research on human behavior Ma and Peters (2020) in order to optimize marketing concepts Ma and Sun (2020). Such investigations, among many others, have significantly improved machine learning and artificial intelligence application to almost all research fields. Furthermore, this has been accelerated by the large computational capacity. Also in the field of civil engineering, machine learning and artificial neural network (ANN) models have gained importance. This section shall give a short overview of its impact to structural engineering, the research in the field of heritage masonry structures and homogenization techniques for component materials.

2.3.1 Application field: structural engineering

The use of machine learning for the structural design has been driven forward by Adeli and Yeh (1989). In this research a perceptron based machine learning model has been trained to design structural steel beams. At that time training set sizes were restricted due to computation power. Training such models with a set of 24 examples took 2400 *min* which is very time intense. And models predict better the more training examples they take into consideration. Nonetheless, has it been an impressive start for machine learning in structural design.

Very good insights of machine learning in structural engineering are given in several review papers: for research articles from 1989-2000 Adeli (2001), from 2001 - 2016 Amezquita-Sanchez et al. (2016) and the most recent investigations are summarized in Amezquita-Sanchez et al. (2020). Many of the actual investigations are made on structural system identification by machine learning and ANN (Jiang et al. (2016), Yongding and Zhang (2018), Yuen et al. (2019)). Other researchers investigate on structural health monitoring and use machine learning to analyze crack

propagation (Smarsly et al. (2016), Ibrahim et al. (2019)). A research proposed by Kostić and Gül (2017) has utilized machine learning for the damage detection of a bridge caused by complex temperature effects. The mentioned researches have shown that the use of ANNs can successfully determine the existence, location and severity of damage.

Another very specific review article on using machine learning for structural health monitoring of heritage buildings is given by Mishra (2021). The article presents a large amount of already carried out case studies of different kinds of heritage structures about the mentioned topic.

Furthermore, ANNs and machine learning have also been used in recent investigations in order to design and assess structures. Many of them consider seismic induced vibrations as main loading case of the investigations. Greco et al. (2017) have presented an automatic approach for the seismic collapse prediction of planar frame structures. It has been shown that this technique results in similar collapses when compared to nonlinear static procedures such as pushover analysis. At the same time, time savings are ranging from 55.0% to 96.0%. Another research carried out by Asteris (2019) has presented a bee-colony based ANN for the prediction of the fundamental vibration period of an infilled frame reinforced concrete structure.

Another recent investigation is using a machine learning optimization algorithm to improve finite element model updating of structures Naranjo-Pérez et al. (2020). It has been shown that, by using a multi-objective harmony search algorithm and a non-crowded Pareto front, a clear reduction of simulation time of FE model updating could be obtained. Furthermore a robust selection of the best updated model among all the possible optimal solutions was guaranteed. Figure 2.9 shows the modal analysis results of the method applied to a steel bridge.

Many investigations on engineering structures appeared in the last years and the research field is growing. Several investigations connecting machine learning with the research on heritage and masonry structures were already published. The following section shall give a short overview.

2.3.2 Application field: masonry structures

The research field of masonry and heritage structures has gained importance in the last decades. Therefore, novel numerical tools such as ANNs have been also applied to improve the assessment methods for masonry buildings.

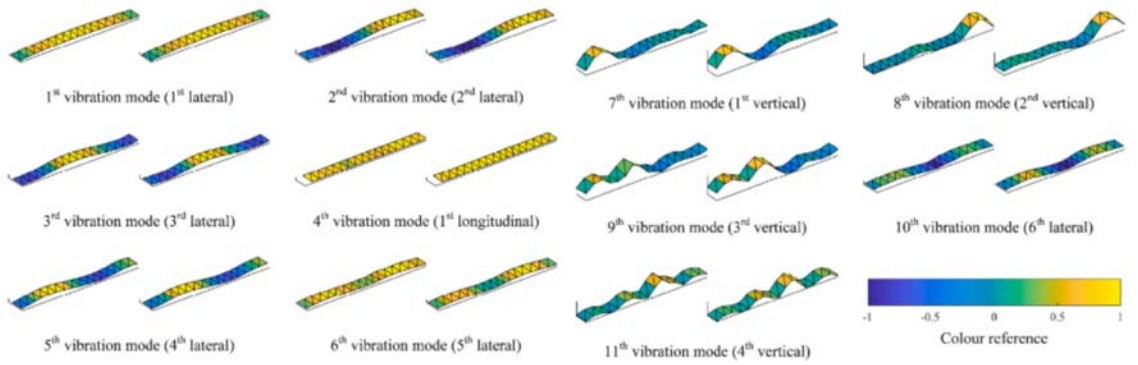

Figure 2.9: Machine learning technique utilized for FE model updating applied to the modal analysis of a steel bridge showing the experimental vibration modes and the updated vibration modes Naranjo-Pérez et al. (2020)

Garzón-Roca et al. (2013) have investigated the use of an ANN to determine the maximum axial load that can be withstood by a masonry wall. In this context, an advanced ANN based on sigmoid functions has been trained in order to predict the load reduction factor. 1944 data items, coming from a parametric study, have been used for the model training. The data includes walls with different geometry effects such as the slenderness ratio or load eccentricity, but also different stiffness and tensile strengths.

Another very interesting research goes further and directly addresses training a failure criteria curve for masonry. Firstly, Plevris and Asteris (2014) have developed a method to predict the yield criteria for compression only states. They further improved their technique by also considering tension and shear loading cases in Asteris and Plevris (2017). Their main objective was modeling the yield surface for masonry in a dimensionless form. So they trained an ANN with experimental data in order to obtain reliable and robust approximations for the anisotropic failure surface of masonry. Figure 2.10 shows the surfaces obtained by the approaches investigated in Plevris and Asteris (2014) and Asteris and Plevris (2017).

Aguilar et al. (2016) have also investigated the use of ANNs to predict the shear strength of reinforced masonry walls. The model has been trained by data obtained from experiments. The ANN model has shown to be able to accurately comply with evaluation data and at the same time it represents them less conservative.

Beside techniques, that aim to predict the structural material behavior, ANN have also been utilized to estimate the damage occurring in masonry buildings after

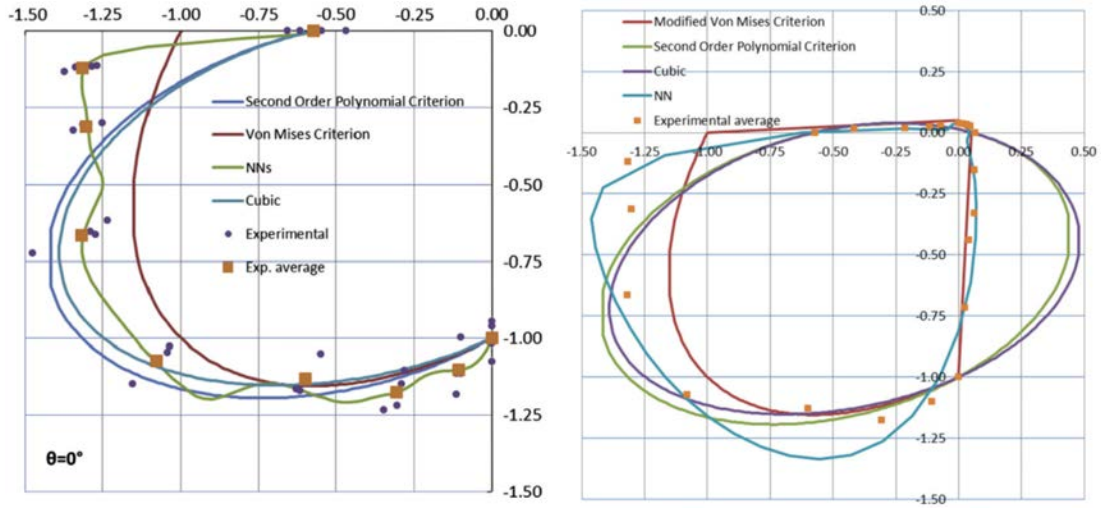

(a) (b)

Figure 2.10: Prediction of failure criteria for masonry using artificial neural networks, showing (a) the prediction of the compression only regiment by Plevris and Asteris (2014) and (b) the entire load case prediction for compression, tension and shear Asteris and Plevris (2017)

seismic actions. In this context, Ferreira et al. (2020) developed an ANN that has been trained with gathered damage data that was discovered after an earthquake. The ANN was elaborated in order to improve the precision of already established empirical methods, such as the widely used vulnerability index method. It has been shown that the ANN delivers more accurate results and complements the conventional method.

The here mentioned investigations on the use of machine learning in the research field of masonry have been extracted from academia and demonstrate the intense use of such techniques in many different fields. However, in order to also address masonry homogenization techniques based on machine learning, several approaches are going to be presented in the following.

2.3.3 Data-driven constitutive modeling and material homogenization

Liu et al. (2020) express the vision of using machine learning models for the use of composite materials as follows: *With the unprecedented growing data from experiments and computer simulations, rapid increasing computing power, and emerg-*

ing advanced algorithms, one should expect unforeseeable and revolutionary impacts across nearly the entire domain of design and analysis of composite materials and structures over the next two decades. This phrase tremendously motivates the research community working on material homogenization techniques and Liu et al. (2020) have published a rewarding review article on machine learning and composite structures. The work focuses on three important applications of ANN for composite materials. (i) *learning constitutive models* (ii) *accelerating multi scale* and (iii) *design optimization.*

The *learning constitutive models* application is summarized by Liu et al. (2020) as an approach postulating general polynomial functions that approximate the homogenized material. This method also includes the possibility to build a constitutive model by considering the respective constitutive models of the components. Such approaches connect the strains and stresses of composite materials by the construction of an ANN in between. These models are trained in order to accurately define a mathematical connection of strains and stresses inside the layers of a neural network. However, such techniques strongly depend on the amount of training data. Such constitutive models are generally trained by experimental data. Experiments usually result in one dimensional strain stress relations. Constitutive models on the other side are implemented to two or three dimensional analyses. Then the model trained by data coming from one dimensional analyses does not properly represent the spatial dependencies.

The *accelerating multi scale* approach has the basic idea of using ANN models to accelerate multi scale modeling by replacing the FE^2 based model with a model constructed from data. Liu et al. (2020) describe the conventional multi scale modeling process by the function $f(\boldsymbol{I}) = \boldsymbol{O}$, where $\boldsymbol{I}$ is the input coming from the macro scale and $\boldsymbol{O}$ is the output coming from the micro sub-scale (RVE-scale). The function f describes a mathematical connection, thus such descriptions can also be defined by ANN formulations. In this context, the idea of RVE based numerically simulated training data has evolved. However, Liu et al. (2020) determine these techniques as computational expensive, since large sets of data are required for training and additionally the trained ANN must be implemented to the analysis at the FE stage. Furthermore, the ANN models suffer the deficiency of physical interpretation. Engineers usually want to understand the mathematical relations that comprehensively describe the materials of their analyses.

The *design optimization* approach refers to tailoring the geometrical orientation of the constituents of composite materials so that their capabilities are mostly utilized, e.g. the orientation of reinforcement bars in concrete (named as a simplified problem in this context). However, such optimization procedures become more challenging the more complex the composite material. Performing design optimization then becomes numerically expensive. Advantages and drawbacks of ANN techniques substituting the optimization process are given in Liu et al. (2020).

The research of this thesis focuses on the composite material masonry that is already built in existing structures. Therefore design optimization procedures applying ANN are not purposeful. The numerical homogenization of masonry can be carried out much better by the given inspirations of *nonlinear constitutive models* and *accelerating multi scale* approaches. Therefore, this section continues the discussion by introducing some comparable techniques.

The classical approaches of defining mathematical constitutive models in order to describe the linear and non linear behavior of materials depends strongly on experimental data. The elaboration of constitutive laws by machine learning techniques also meets these requirements. However, data driven models have the advantage to improve model performance when additional data becomes available. Such models can be trained offline and later be used for online application. A recent investigation has developed a machine learning based plasticity model that follows this concept (Huang et al. (2020a)). In this context, a feed forward neural network utilizing proper orthogonal decomposition has been used in order to substitute analytic formulations of plasticity models. The trained ANN model has been applied as constitutive model for several 2D and 3D application examples. Figure 2.11 shows the application to the 3D Cook's membrane problem. The ANN model delivers very accurate results when compared to conventional plasticity model analysis.

Another related investigation has been made by Gorji et al. (2020) in order to study the potential of a recurrent neural network for the modeling of path dependent plasticity. In this context, uni and multi axial stress strain response have been investigated. While considering multi axial cases Gorji et al. (2020) have also discussed monotonic and arbitrary loading paths. Latter requires a specific training capacity of the ANN, since a strain value can be related to multiple stress values (due to loading - unloading and plastic deformations). Recurrent neural networks are able to take such effects into account. Therefore, Gorji et al. (2020) apply them

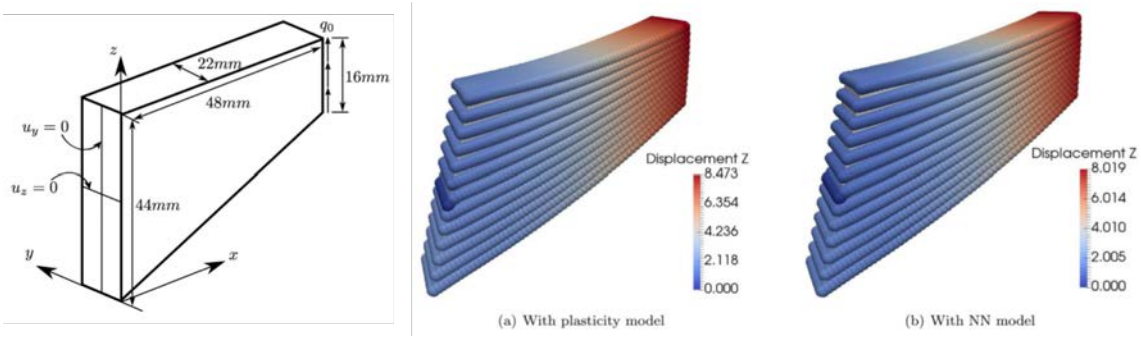

(a) With plasticity model (b) With NN model

Figure 2.11: Result comparison of the 3D Cook's membrane problem utilizing (a) a conventional plasticity model and (b) an artificial neural network based plasticity model from Huang et al. (2020a)).

for their needs.

A recent investigation made by Logarzo et al. (2021) steps further and introduces machine learning constitutive models for inelastic homogenization techniques, by developing so called *smart constitutive laws*. The research is motivated by the drawbacks connected with classical multi scale homogenization techniques, such as computational cost, and aims to tackle these by utilizing machine learning. In this context, a RVE based approach is considered that numerically produces training data at the micro scale of the considered heterogeneous material. Then a smart constitutive model architecture is defined. It consists of a recurrent neural network. Figure 2.12 shows the structure of the considered model. It depicts the three components of the 2D strain vector as the model inputs and the corresponding stress components and localized information as model outputs. The trained model has been implemented as smart constitutive model into the FE solver and application examples have underlined the ability of such models for material homogenization.

2.4 Summary

This chapter has presented the framework of the research performed in this thesis. The presented topics of this literature review have aimed to categorize the thesis into the topics of (i) numerical modeling of masonry, (ii) homogenization techniques for heterogeneous materials, and (iii) research on data driven models for engineering problems.

Firstly, an introduction to numerical modeling techniques for masonry structures

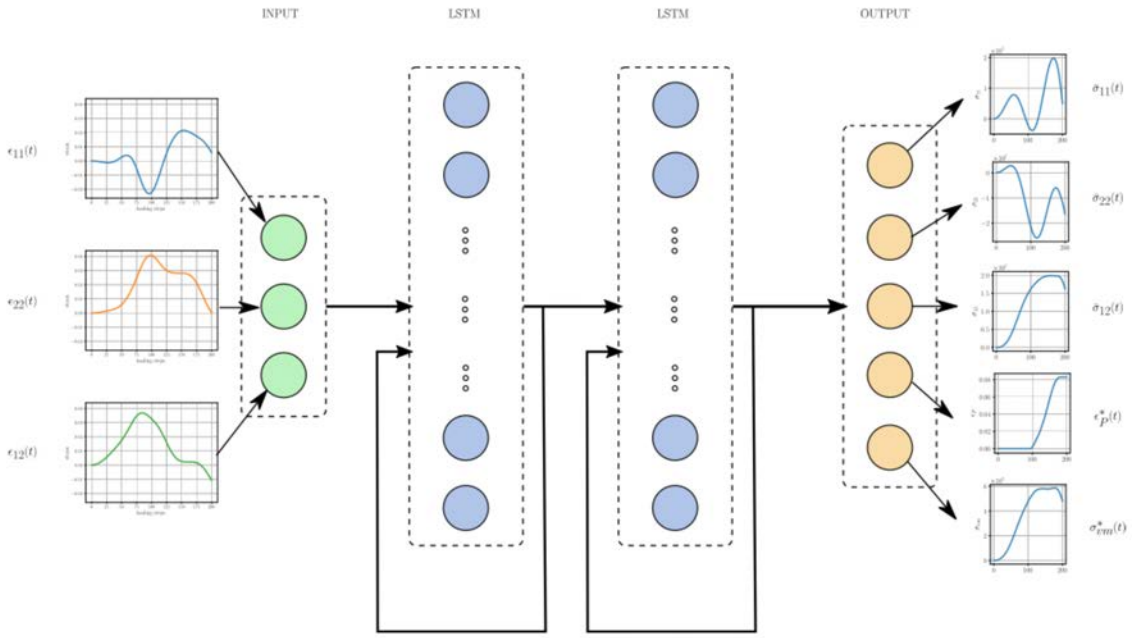

Figure 2.12: Architecture of the artificial neural network used as smart constitutive law in the investigations of Logarzo et al. (2021)

has been made. In this context, the micro modeling technique has been presented as the most accurate tool to model the nonlinear behavior of masonry. Several techniques have shown to represent typical masonry failure mechanisms at component scale. However, it has been proven that micro modeling is too expensive on computational cost, and therefore macro modeling of masonry has been presented as the tool for large scale numerical analysis. This approach smears the heterogeneous material masonry on a simplified continuum model. The presented references have underlined both the advantages and drawbacks of micro and macro modeling. These insights have led to the presentation of multi scale techniques. In this context, first order homogenization procedures have been discussed. The main drawback of these techniques is the huge computational effort that prevents the method from being applied to large scale masonry structures. In order to overcome this problem, the literature review has introduced the concept of off-line techniques that are able to decrease the computational effort substantially.

In the second part, data-based modeling approaches applied to the field of civil engineering have been presented. Therefore, an overview of research applications of machine learning tools to the field of structural engineering have been presented.

Further discussions have been also made on machine learning applications to the research field of masonry. These insights have shown extensive possibilities of data driven analysis for investigations in the field. A final section has further continued review by discussing the use of machine learning and artificial neural networks for constitutive model definition. In this context, general procedures utilizing recurrent neural networks for plasticity based modeling have been introduced. A recent research article presented the use of machine learning for the definition of smart constitutive laws that were trained by numerically produced data. The works done there have strongly motivated the research of this thesis facing the difficulties of masonry material homogenization.

Chapter 3

An advanced macro model seismic analysis of irregular masonry structures

3.1 Introduction

Masonry structures have shown to be very vulnerable to seismic actions. Several methods have been proposed to deal with the assessment of their seismic safety. The available approaches differ in the level of complexity based on the assumed fundamental hypotheses. Even though linear methods have been used in the past decades, nonlinear methods have been preferably applied to the seismic analysis of masonry structures.

Nonlinear analyses of masonry structures are advanced approaches that require a certain amount of expertise. Such advanced analyses have been enabled thanks to macro modeling approaches. Large structures would never be simulated in terms of micro models, since there computational effort is tremendous. Instead, macro modeling enables a quick geometry definition of large models, the material can be defined in terms of a single smeared constitutive model and the computational effort is minimized. These simplifications in numerical analyses led to a large number of modern and novel simulation methods. These approaches improved significantly the assessment of masonry heritage structures. Especially the vulnerability on seismic actions could be evaluated more effectively.

The nonlinear static analysis (NSA), also known as pushover analysis, models the

earthquake action as a system of seismic equivalent lateral forces increasing monotonically during the analysis. Another possibility is offered by nonlinear dynamic analysis (NDA) that can be performed by regarding complete earthquake acceleration time histories. This last approach is certainly very accurate but its computation time is higher than in the NSA. A recent study Endo et al. (2017) has shown that for simple symmetric masonry buildings, the capacity curve of the pushover analysis with mass proportional lateral loading pattern, expressed in terms of the relationship between the structure's base acceleration and top displacement, provides a good agreement with the envelope of the hysteretic loops from NDA. Another recent investigation Lagomarsino and Cattari (2015) has presented a discussion on the use of NSA and NDA for the performance based assessment of existing masonry buildings. Several recent works provide examples of applying pushover analysis to churches, fortresses and towers, e.g. Milani and Valente (2015); Endo et al. (2015); Torres et al. (2018); Degli Abbati et al. (2019). A parametric study of the important effect of material properties assumption on the results derived from nonlinear seismic analyses is reported in Mendes and Lourenço (2014).

Nonlinear static and dynamic methods have been employed to assess the seismic behavior of masonry buildings without box behavior (Mendes and Lourenço (2009); Lourenço et al. (2011)), i.e. presenting flexible floors and/or deficient floor-to-wall or wall-to-wall connections. These studies have shown limitations and possibilities for the different approaches to account for the lacking box behavior in the evaluation of the seismic response of the building.

Existing masonry structures often exhibit structural irregularities, as possible consequence of historical interventions and subsequent modifications to their layout. Such irregularities, which can be observed both in plan and in elevation, are frequent in historical masonry structures, especially in those of the urban centers. Static analysis methods present several limitations for this class of buildings, since they cannot represent properly the complex 3D dynamic response during the earthquake.

This chapter investigates the possibility to use multiple nonlinear static analyses to assess the seismic behavior of irregular masonry structures without a box behavior. The research proposes the use of a series of pushover analyses conducted by rotating the loading direction from 0° to 360°. This working strategy allows to evaluate the seismic response of the building along several directions, in addition to the two "principal" loading directions assumed in conventional pushover analysis

of regular buildings. The development of such novel nonlinear assessment methods demonstrates the wide range of possibilities given to the research world of masonry structures by macro modeling approaches.

The chapter is structured as follows. Section 3.2 gives an overview of available pushover procedures, such as conventional approaches and extended ones for the application to irregular buildings. Section 3.3 introduces the so-called multi directional pushover analysis (MDPA) and outlines the MDPA application procedure. Section 3.4 presents the application of the MDPA in a case example to a very complex building located in Santiago de Chile, the *Palacio Pereira*. This historical masonry building presents structural irregularity both in plan and in elevation, and exhibited structural deficiencies (flexible timber floors, inadequate floor-to-wall and wall-to-wall connections) when it was struck by 2010 Chile earthquake. The MDPA results are finally compared with the results made by a NDA. The chapter closes with a summary and a short discussion on the definition of homogenized macro model material properties for masonry.

3.2 Overview of available pushover procedures

3.2.1 Conventional approaches

The conventional NSA approach evaluates the seismic capacity by increasing monotonically an invariant lateral load pattern applied to the structural model. The gradual increase of horizontal loads leads to progressive damage, and thus to gradual decrease of the stiffness until reaching the collapse condition. The Eurocode 8 (EC8) European Committee for Standardization (2004) recommends the use of the "uniform" and "modal" loading patterns in NSA. The first consists in lateral forces proportional to mass regardless of elevation, while the second is proportional to lateral force distributions given by previous elastic (modal) analysis. The applicability of the conventional pushover approach is restricted to structures vibrating predominantly in the first mode and with time-independent deformation shape. For this reason, the N2 method Fajfar (2000), suggested by EC8 to determine the seismic demand, is applicable only to structures fulfilling specific requirements for plan and elevation regularity. A recent research Lagomarsino et al. (2018) suggests the application of a proper lateral load pattern in the pushover analysis of masonry buildings

with low participating mass in the first mode.

The evaluation of the seismic capacity in NSA refers to the relationship between the total base shear and the displacement of a representative control node. The choice of the control node is straightforward in buildings with rigid floors well connected to the walls. For such cases, the EC8 suggests the location of the control node to be at the center of mass at the top floor level. However, the choice of a suitable control node becomes difficult in NSA of irregular buildings with flexible diaphragms (Nakamura et al. (2017); Lagomarsino et al. (2018)) since the lack of box behavior leads to local damage and failure mechanisms (Mallardo et al. (2008); Lourenço et al. (2011); Avila et al. (2018); Palazzi et al. (2019)). Recent works propose the selection of different control nodes in NSA in order to follow the response of the most critical structural members during the analysis (Pelà et al. (2009); Endo et al. (2015); Lagomarsino et al. (2018)).

3.2.2 Extension to irregular buildings

The EC8 proposes a simplified procedure for the estimation of the torsional effects, also known as extended N2 method Fajfar et al. (2005), consisting in the definition of a proper amplification factor for the displacements, based on the results of an elastic modal analysis. The method combines the results from a NSA of a 3D structural model of the irregular structure with those from a linear dynamic (spectral) analysis, in order to estimate the torsional amplifications. The extended N2 method has been applied to the pushover-based seismic analysis of asymmetric reinforced concrete (RC) framed structures with rigid floors (Fajfar et al. (2005); G.P. Cimellaro, T. Giovine , D. Lopez-Garcia (2014)). Available standards are in need of improvement in order to provide practical specifications for the seismic analysis of irregular masonry buildings.

Several researches have addressed the possibility of extending the applicability of conventional pushover procedures by trying to overcome some of their intrinsic limitations (De Stefano and Mariani (2014)). The modal pushover analysis (MPA) (Chopra and Goel (2004)) considers the inertia force distributions for different modes with the aim of including also the contributions from higher vibration modes. These modal contributions are then combined by using the Square Root of the Sum of Squares (SRSS) or Complete Quadratic Combination (CQC) rules. The adaptive pushover analysis (APA) (Gupta and Kunnath (2000)) considers an adaptive force

distribution that is updated during the analysis according to the variable distribution of inertia forces given by the stiffness degradation and evolving damage. Recent works on seismic analysis of masonry buildings with flexible diaphragms have presented critical comparisons between the results from NDA and MPA or APA Lourenço et al. (2011); Endo et al. (2017); Nakamura et al. (2017) showing that these non-conventional pushover procedures should be used with caution since they may not provide meaningful improvements in terms of load-displacement diagrams and failure mechanisms.

3.3 Multi directional pushover analysis

3.3.1 Motivation

The NDA on spatial models of buildings considers the two horizontal components of the seismic action acting simultaneously. This allows NDA to evaluate in a direct manner the complex tridimensional response of structural systems subjected to multi directional earthquake ground motions.

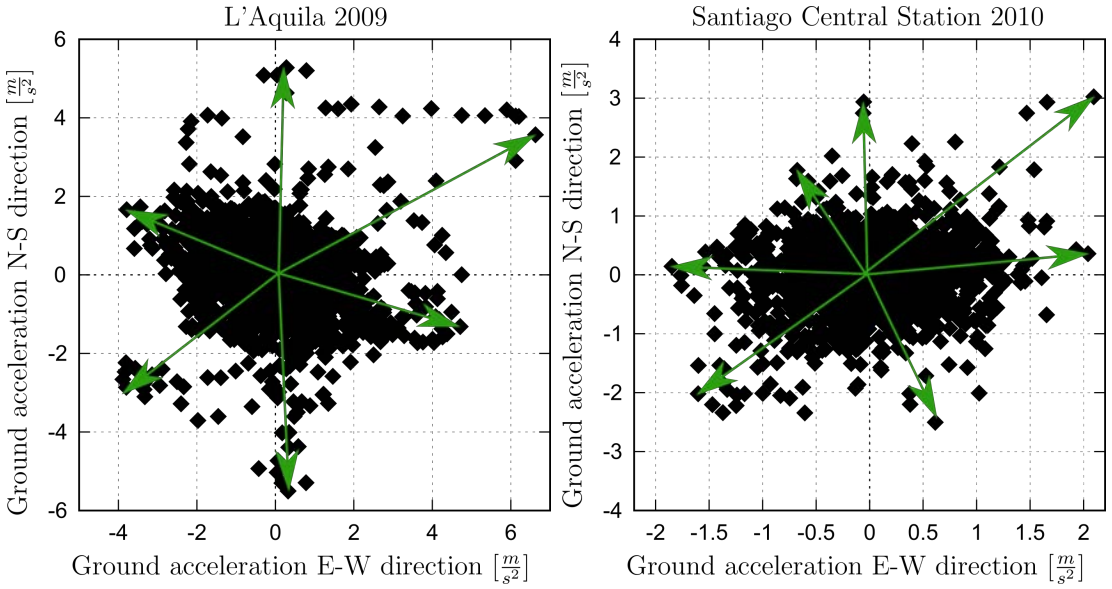

Figure 3.1: Examples of East-West vs. North-South acceleration relationship for the recorded earthquakes: L'Aquila 2009 recorded at Via Aterno - Centro Valle and Chile 2010 recorded at Santiago Central Station

Figure 3.1 shows the directional variability of the ground accelerations recorded

during the Mw 6.3 L'Aquila earthquake of 2009 (L. Luzi, F. Pacor, R. Puglia (2017)) and the Mw 8.8 Chile earthquake of 2010 (Sandoval et al. (2017); Boroschek et al. (2010)). The plot of the East-West versus the North-South acceleration values at the same time instant provides a point cloud, with some orientations characterized by larger responses, as shown by the arrows in Figure 3.1. This visual plotting shows the multi directional character of real earthquake ground motions and suggests how NDA can directly account for it in the evaluation of the seismic vulnerability.

The NSA procedures presented in Section 3.2 cannot address the aforementioned issue. The NSA of spatial models of buildings considers increasing horizontal loading patterns acting separately along the "principal" directions of the buildings, e.g. the longitudinal/transversal or North-South/East-West directions. This constitutes a strong limitation for the case of irregular buildings without box behavior, being not possible to include within the procedure the evaluation of the effect of bidirectional loading on structural members prone to local damage and failure mechanisms.

Recent works available in the literature have investigated the extension of the conventional NSA procedures to tridimensional analysis of structures subjected to bidirectional components of ground motions (Huang and Gould (2007); Reyes and Chopra (2011); Camara and Astiz (2012); G.P. Cimellaro, T. Giovine , D. Lopez-Garcia (2014)). These researches have carried out bidirectional NSA, i.e. by considering two simultaneous loading patterns along perpendicular horizontal directions, in the seismic assessment of RC chimneys, RC core wall tall buildings, irregular RC frames and cable-stayed bridges, respectively.

Two researches Cannizzaro et al. (2017) and Chácara et al. (2019) have recently addressed the topic of multi directional pushover-based seismic assessment applied to masonry buildings. Both investigations have considered a discrete macro-element modeling technique for the analysis of an historical palace damaged by L'Aquila earthquake, and a brick masonry structure prototype tested in the laboratory. The first case study is a building that underwent seismic retrofitting interventions before L'Aquila earthquake and thus exhibited a global box behavior with overall resisting response after the earthquake, as also confirmed by the numerical analyses. The second case study is a laboratory specimen including a main gable wall with two returns, i.e. an experimental prototype of a structural member with a predominant out-of-plane failure response.

3.3.2 Proposed procedure

The present research aims to contribute to further developments on multi directional pushover procedures for the seismic analysis of masonry buildings. This section presents the description of the different stages of the proposed methodology, while the following section will present its practical application to an irregular historical masonry building without box behavior. The considered real building has been chosen purposely in order to present a novel challenging case study of MDPA of a complex structure with prevailing out-of-plane mechanisms in case of earthquake. The working steps of the proposed MDPA are listed in the following.

Step 1: A spatial 3D FE model is developed with nonlinear constitutive laws for the materials. The modeling of diaphragms has to account for the actual stiffness of roofs and floors. In case that their rigidity is negligible and floor-to-wall connection is weak, the in-plane tying effect can be neglected and the floors may be modeled as lumped masses at the level of stories in order to simplify the FE model.

Step 2: The MDPA is applied to the spatial 3D FE model to determine the seismic capacity of the structure. The method considers multiple NSAs executed along different directions with respect to the plan of the building, after establishing an angle of variation φ_n between subsequent orientations. This work, as a first approach to the topic, suggests to consider at least eight NSAs, i.e. to assume $\varphi_n = 45°$ (Figure 3.2), with horizontal loading patterns proportional to the distribution of the masses in the FE model (constant accelerations along the height). Future works may consider $\varphi_n = 22.5°$ or $\varphi_n = 30°$, depending on the complexity of the investigated case study until achieving a good compromise between computation cost and accuracy of results.

Step 3: The control nodes to draw the load-displacement capacity diagrams are selected by carefully analyzing the most vulnerable structural members of the masonry building. For the case of irregular systems, the typical existence of different failure mechanisms leads to the choice of different control nodes. Out-of-plane displacements have to be controlled with caution in overturning walls of masonry buildings without box behavior.

Step 4: The nonlinear force-displacement relationship of the multi-degree of freedom (MDOF) system is plotted for the selected control node corresponding to the

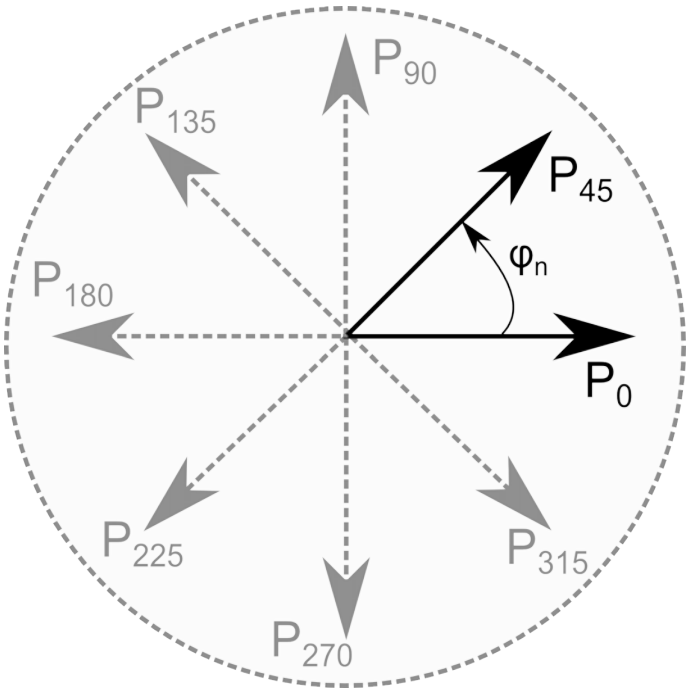

Figure 3.2: Proposal of basic directions to be considered in the multi directional pushover analysis

failure mechanism. The pushover curve of the MDOF system is transformed into the capacity curve of an equivalent single-degree of freedom (SDOF) system, by evaluating the transformation factor Γ according to the N2 method:

$$\Gamma = \frac{\sum m_i \Phi_i}{\sum m_i \Phi_i^2} = \frac{m^\star}{\sum m_i \Phi_i^2} \tag{3.1}$$

where $m^\star$ is the mass of the equivalent SDOF system, m_i is the mass of the i-th node of the FE model and Φ_i is the normalized displacement of the i-th node. Since this factor shows to be very sensitive to the applied load pattern in NSA and the related deformed shape, this work considers the displacement shape Φ_i derived from the initial elastic stage of a pushover analysis with mass-proportional horizontal loading pattern and without gravity loads applied (Cattari et al. (2015); Lagomarsino et al. (2018)). The displacement shape is normalized to the highest control displacement. Within the framework of the proposed MDPA, different transformation factors Γ are calculated for different NSA loading orientations, and this constitutes a novel contribution to the approach compared to previous studies considering a unique transformation factor for all the considered directions (Cannizzaro et al. (2017)). In

particular, for a specific NSA loading orientation, the direction for the calculation of the transformation factor Γ is that of the largest horizontal component (X or Y) of the control displacement. For the specific case of masonry buildings without box behavior, e.g. the case study investigated in this paper, if the overturning mechanisms of walls are the most vulnerable, the out-of-plane displacement directions are considered for the calculation of the transformation factors Γ, see Section 3.4.3. The capacity curve of the equivalent SDOF system is expressed eventually in terms of its force $F^\star$ and displacement $d^\star$:

$$F^\star = \frac{F_b}{\Gamma} \tag{3.2}$$

$$d^\star = \frac{d_n}{\Gamma} \tag{3.3}$$

where F_b and d_n are the base shear force and the control node displacement of the MDOF system. The capacity curve of the equivalent SDOF system is evaluated only along the direction of the largest horizontal component (X or Y) of the control displacement. However, its shape is affected by the orientation of the loading direction with respect to the plane of the wall. Finally, the capacity diagram is expressed in the acceleration-displacement format by dividing the forces in the $F^\star$-$d^\star$ curve by the mass $m^\star$ of the equivalent SDOF system.

Step 5: The capacity curve showing the relationship between the base shear force and the displacement of the SDOF equivalent system is idealized by a bilinear method. The simplified elastic perfectly-plastic bilinear capacity curve for the equivalent SDOF system can be evaluated by engineering judgment and guidelines available in regulatory documents (Ministero delle Infrastrutture e dei Trasporti. Circolare 21 gennaio 2019 (2019)). The ultimate displacement is identified in correspondence to a decrease of 20% of the maximum load capacity of the structure (European Committee for Standardization (2005); Ministero delle Infrastrutture e dei Trasporti. Circolare 21 gennaio 2019 (2019)). However, the execution of pushover analysis in the softening range is usually not straightforward in continuum FE models of masonry structures within the smeared crack approach, due to convergence problems related to the brittleness of the elements. For this reason, it is important to identify properly the ultimate displacement as the condition corre-

sponding to the full development of the collapse mechanism in the FE structural model. The yield displacement is given by an energy equivalence criterion, i.e. by assuming that the areas under the actual and idealized force-displacement curves are equal (European Committee for Standardization (2004)).

Step 6: The performance point (PP) is obtained by comparing the seismic capacity of the SDOF system with the demand expressed by an inelastic response spectrum, as indicated in the procedure of the N2 method Fajfar (2000); European Committee for Standardization (2004). The displacement demand for the equivalent SDOF system is finally transformed into that of the MDOF system, using Equation 3.3.

3.4 Application example

3.4.1 The Palacio Pereira

In the era of Chile's economic boom in the 1870s, rich mine magnates bought properties in the center of the city of Santiago and constructed "Haciendas" which due to their imposing and neoclassical style more or less appeared like palaces ("Palacios"). One of these buildings is the *Palacio Pereira* which was commissioned by *Luis Pereira*, designed by the French architect *Lucien Ambroise Hénault* and constructed in 1872. Figure 3.3 shows the building from the exterior in 2013.

Figure 3.3: Exterior view of the *Palacio Pereira* in 2013 before the works of restoration

The *Palacio Pereira* is a two-story building made of unreinforced masonry composed of traditionally produced clay bricks with dimensions $0.40 \times 0.20 \times 0.06\, m^3$ and

lime mortar. Vertical loads are transmitted to the foundations by the 0.6 m thick load bearing walls, that act also as shear resisting elements in case of application of horizontal actions. The height of the complete building is approximately 10 m. The floor and roof structures are made of timber members.

Figure 3.4 shows a schematic view in plan of the wall layout in first and second floor of the *Palacio Pereira*. As shown, the building is remarkably irregular in plan with a L shape, and also presents irregularity in elevation due to the presence of 2-storey volumes along with 1-storey ones surrounding the interior courtyard.

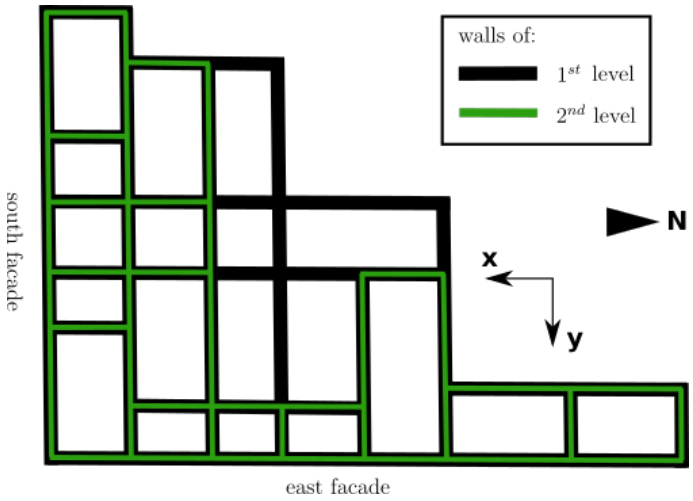

Figure 3.4: Plan view of the first and second floors' walls

Several geometrical criteria provided by the EC8 (European Committee for Standardization (2004)) for building regularity do not comply with the construction characteristics of the *Palacio Pereira*:

- Plan Irregularity (EC8, section 4.2.3.2). The *Palacio Pereira* is not symmetric in plan and does not present any rigid diaphragm at floor and roof levels, since these structural parts are made of timber. The structural eccentricities e_{0x} and e_{0y} exceed by more than 30% the torsional radii r_x and r_y, respectively. The eccentricities e_{0x} and e_{0y} are the distances between the barycenters of mass and stiffness along the x and y direction, respectively. The torsional radii r_x and r_y are the square roots of the ratio of the torsional and the lateral stiffness in y or x direction, respectively. (*Palacio Pereira*: $e_{0x} = 3.24\ m$, $e_{0y} = 1.79\ m$, $0.3\ r_x = 0.91\ m$ and $0.3\ r_y = 0.79\ m$).

- Elevation Irregularity (EC8, section 4.2.3.3). The difference of translation stiffness is about 75% between the first and second levels of the structure. This specifies an abrupt change in elevation. Setbacks are present and in several parts they do not comply with the specifications from the standard.

The *Palacio Pereira* suffered demanding seismic actions during its lifetime. Two strong earthquakes in 1985 and 2010 caused severe damage to the building. An overview of the present damages after the two earthquakes is given in Kalkbrenner et al. (2019). Even though many portions of the building were damaged, the entire structure has been restored to host cultural facilities and reopened in 2019.

3.4.2 Numerical modeling

A 3D FE model was built for the analysis of the *Palacio Pereira* before the recent restoration, i.e. in the structural configuration struck by 2010 earthquake. All computations were carried out by using the FE software DIANA FEA TNO (2017). Figure 3.5 shows the FE model of the building. All the walls of the *Palacio Pereira* were modeled by shell elements, i.e. the triangular three-noded element T15SH and the quadrilateral four-noded element Q20SH, with an average element size of 0.5 m. Three-point in-plane integration is used for triangular elements , while 2×2 in-plane integration is used for quadrilateral elements . The three-point Simpson rule is used for through-thickness integration in the shell elements. The total number of nodes and elements is 14144 and 12597, respectively. The FE model does not include any horizontal rigid diaphragm due to the flexibility of the roofs and floors existing in 2010. However, the corresponding masses of floors and roofs are added to the load bearing walls supporting the unidirectional floors. The model presents two horizontal levels of added masses in the form of distributed loads applied to the walls' nodes at the floor and roof levels. The distributed weight of the floors and the roof are 0.3 kN/m and 1.0 kN/m, respectively. All base nodes of the walls are fixed, with both translation and rotation constrained.

The total strain based rotating crack model implemented in the DIANA FEA software is chosen for the masonry material. This constitutive model considers an exponential softening curve under tension and a parabolic softening curve under compression. Table 3.1 shows the material properties applied in the FE model of the *Palacio Pereira*. Their values were calibrated through the numerical simulation

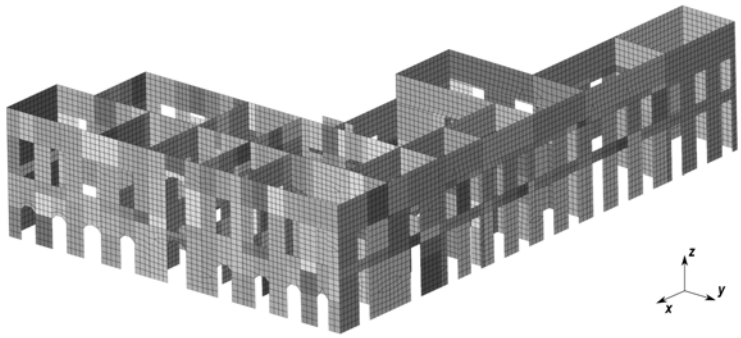

Figure 3.5: 3D Model of the *Palacio Pereira* for finite element analysis

of an in-situ shear test performed on a portion of an existing wall located at the first floor of the building Sandoval et al. (2017).

Table 3.1: Material properties of the smeared crack model for the finite element model of the *Palacio Pereira* in DIANA FEA

Material property	**Symbol**	**Value**	**Unit**
Density	ρ	1800	kg/m^3
Young's modulus	E	1.785	GPa
Poisson's ratio	ν	0.2	-
Compressive strength	f_p^-	2100	kN/m^2
Compressive fracture energy	G^-	15.7	kN/m
Tensile strength	f_p^+	120	kN/m^2
Tensile fracture energy	G^+	0.01	kN/m
Residual compressive strength	f_r^-	900	kN/m^2
Residual tensile strength	f_r^+	20	kN/m^2

Figure 3.6a shows the experimental setup of the in-situ shear test executed on a $1.00 \times 2.00\ m^2$ portion of the wall, reproducing two $1\ m^2$ specimens one upon the other. The loading was applied by a $600\ kN$ force-controlled hydraulic jack, while four displacement transducers were used to measure the diagonal shortening and lengthening in each specimen. Figure 3.6b shows the experimental cracking pattern obtained after the test, with two diagonal cracks going through the two specimens. The in-situ shear test provided a shear strength $\tau_{max} = 0.23MPa$ for the existing masonry. Figure 3.6d shows the shear stress vs. angular strain response for the two specimens. The observed experimental behavior was simulated numerically by means of a FE analysis of the in-situ experimental test. Conventional values were

assumed for density and Poisson's ratio in the FE model, whereas the compressive strength of 2.1 MPa was defined in accordance with the standard ASCE 41-06 ASCE (2007) for poor masonry. The remaining FE model parameters in Table 3.1 were evaluated in order to obtain a good agreement with the experimental evidence in terms of cracking pattern and stress-strain responses, see Figures 3.6c and 3.6d.

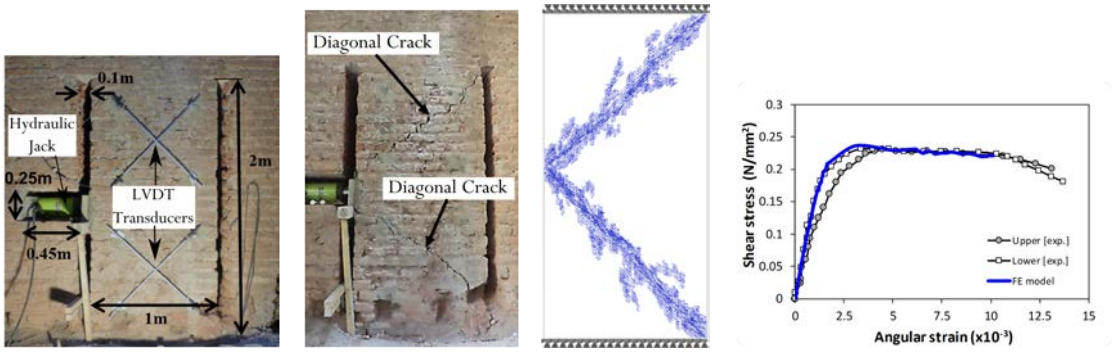

(a) (b) (c) (d)

Figure 3.6: In situ shear test campaign to calibrate the material properties of the *Palacio Pereira*: (a) Shear compression test-setup, (b) post-test crack pattern of the experiment, (c) crack pattern of the FE analysis and (d) experimental and numerical stress-strain curves

Appendix A.1 shows the summarized results of a linear modal and a response spectrum analysis.

3.4.3 Multi directional pushover analysis

The NSAs are carried out by considering a mass proportional distribution of horizontal forces. First, the pushover analyses are run along the four typical directions assumed in conventional NSA of regular buildings: *positive transversal* (P_0), *negative transversal* (P_{180}), *positive longitudinal* (P_{90}) and *negative longitudinal* (P_{270}). Second, supplementary NSAs are run along additional directions, according to the proposed MDPA approach, with the purpose of activating all the possible local collapse mechanisms around the building. The four additional pushover loading directions are P_{45}, P_{135}, P_{225} and P_{315}. Figure 3.7 shows the eight pushover directions considered in the MDPA of the *Palacio Pereira*.

Each NSA is carried out by considering a two-step procedure. In the first stage, the gravitational loading is applied to the model. In the second stage, the structure is

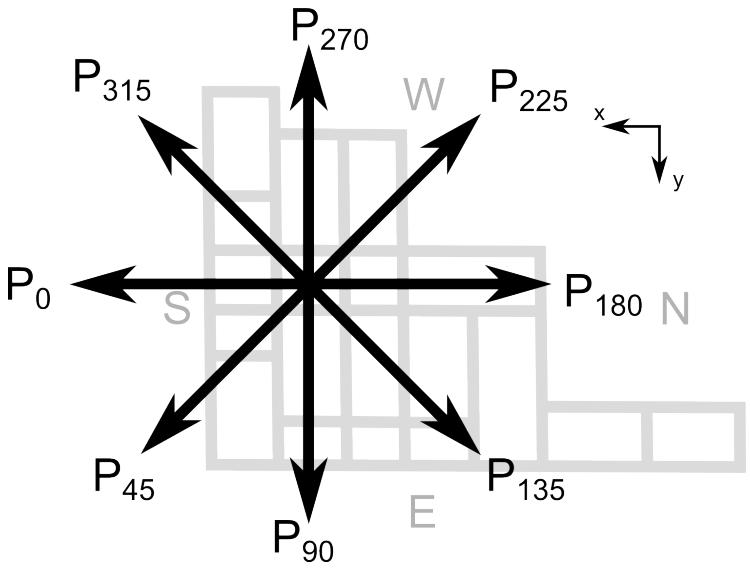

Figure 3.7: Loading directions assumed in the proposed multi directional pushover analysis of the *Palacio Pereira*.

horizontally pushed by a mass proportional horizontal loading pattern. The nonlinear numerical problem is solved by using an arc-length control and Newton-Raphson method.

Figure 3.8 shows the control nodes for NSA and NDA that have been chosen according to the collapse mechanisms observed in the eight pushover analyses. Large out-of-plane displacements occur in the walls during the MDPA, thus the control nodes are placed at their top.

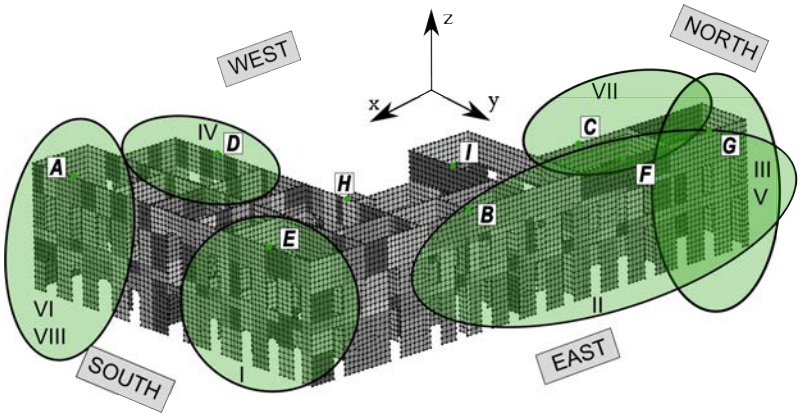

Figure 3.8: Overview of the locations of the failure mechanisms detected during the multi directional pushover analysis, and positions of the considered control nodes.

Table 3.2 shows the ultimate out-of-plane displacement values d_u of the chosen control nodes, and the maximum accelerations a_{max} derived from the eight MDPAs. The maximum acceleration values range between 0.154 g and 0.234 g.

Table 3.2: Maximum acceleration values derived from each pushover analysis and ultimate displacements of the control nodes in x- or y-direction. Seismic performance in terms of displacements and accelerations and transformation factors from MDOF to SDOF according to the N2 method

		Peak values		N2-method		
	node (dir.)	a_{max} [g]	d_u [m]	Γ [-]	d_{pp} [cm]	a_{pp} [g]
P_0	E (x)	0.193	0.254	2.68	6.69	0.177
P_{45}	E (x)	0.154	0.048	2.66	3.99	0.148
P_{90}	G (y)	0.216	0.116	3.16	2.68	0.167
P_{135}	G (y)	0.176	0.071	3.44	4.69	0.171
P_{180}	D (x)	0.234	0.042	2.68	4.11	0.233
P_{225}	A (x)	0.192	0.048	2.66	4.44	0.191
P_{225}	D (x)	0.192	0.062	2.66	5.24	0.189
P_{225}	G (y)	0.192	0.042	2.81	2.92	0.182
P_{270}	C (y)	0.225	0.292	3.16	2.92	0.176
P_{315}	A (x)	0.170	0.078	2.69	7.31	0.169

The elastic design spectra of the Chilean standards NCh433 (Kalkbrenner et al. (2019)) is used to evaluate the structural response at the performance point (PP). The PP is determined by considering the procedure presented in Section 3.3.2. Table 3.2 shows the transformation factor Γ, the acceleration a_{pp} and displacement d_{pp} at the performance point for the MDOF system corresponding to each NSA. As previously mentioned in Section 3.3.2, different transformation factors are calculated for different NSA loading orientations. Table 3.2 indicates the direction considered for their calculation (X or Y) for each pushover direction, according to the control displacement chosen to describe the obtained partial collapse mechanisms. It is worth noticing that NSA P_{225} is able to activate overturning mechanisms in three different walls and for this reason the results are detailed for the three cases (control nodes A, D and G).

The determination of the local failure mechanisms through the MDPA of the *Palacio Pereira* is carried out by considering the progressive damage appearing during each NSA. Figure 3.8 shows the locations of all the failure mechanisms detected

during the eight pushover analyses. As shown, the seismic response of the building is characterized by partial mechanisms, as expected in an irregular masonry building without box behavior. Figure 3.9 shows the total displacement contours at the PP for each pushover analysis. Figure 3.10 shows the capacity curves of each NSA for the out-of-plane displacement of the relevant control nodes. The description of each failure mechanism derived from MDPA is presented in detail in the following.

- **Pushover P_0** The mechanism in P_0 is an out of plane failure of the eastern part of the south facade along the positive x-direction. The global displacements at the PP are shown in Figure 3.9a. The first plateau of the capacity curve with control node **E** of Figure 3.10a is produced by the cracks developing in the spandrels of the walls perpendicular to the overturning part of the south facade. Increasing lateral acceleration leads to large displacements of the wall and finally to out of plane collapse of the eastern part of the south facade. This failure is designated as **Mechanism I**.

- **Pushover P_{45}** The lateral acceleration activates the same failure observed in P_0, i.e. the **Mechanism I**. Figure 3.9b shows the global displacements of the structure at the PP. As in P_0, the lateral acceleration induces first the development of cracks in the spandrels of the wall transversal to the east portion of the south facade. This behavior can be detected by analyzing the capacity curve of control node **E** shown in Figure 3.10b. At an acceleration of approximately 0.12 g, the slope of the capacity curve flattens and then the increasing acceleration leads to the out of plane collapse.

- **Pushover P_{90}** A further rotation of 45° of the pushover angle activates a different mechanism than the previous one displayed by P_0 and P_{45}. The lateral acceleration leads to the out of plane failure of a big portion of the east facade along the positive y-direction (**Mechanism II**). Figure 3.9c shows the global displacements of P_{90} at the PP. Figure 3.10c presents the capacity curve of control node **G**. At an acceleration of approximately $0.18g$ the wall perpendicular to the east facade at location of control node **B** undergoes shear cracking. This causes a sudden drop of the structural capacity. Further cracks appear in the walls perpendicular to the east facade while increasing the acceleration, until reaching the overturning of the facade.

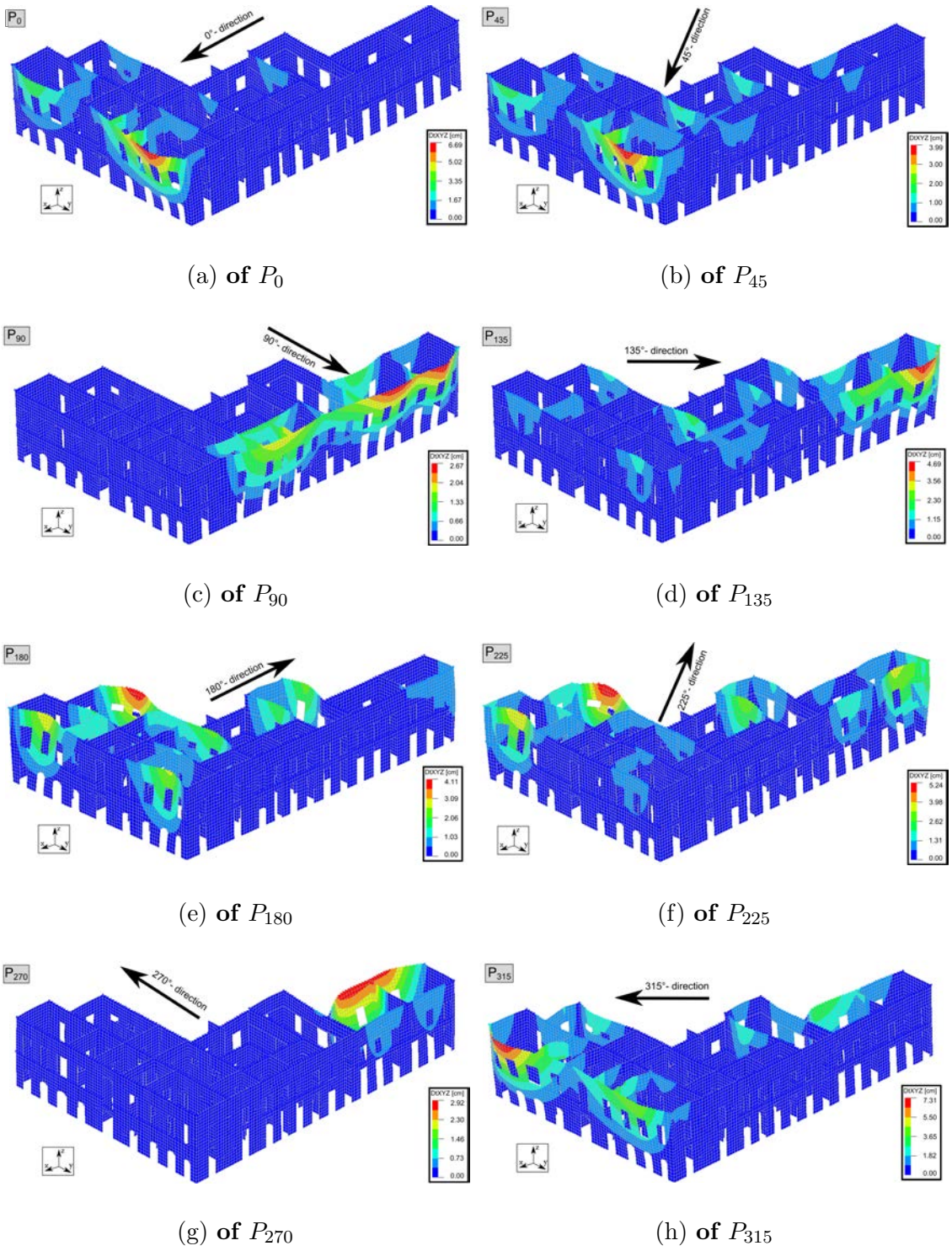

(a) **of** P_0 (b) **of** P_{45}

(c) **of** P_{90} (d) **of** P_{135}

(e) **of** P_{180} (f) **of** P_{225}

(g) **of** P_{270} (h) **of** P_{315}

Figure 3.9: Global displacements at the performance point for all the individual nonlinear static analyses of the proposed multi directional pushover approach

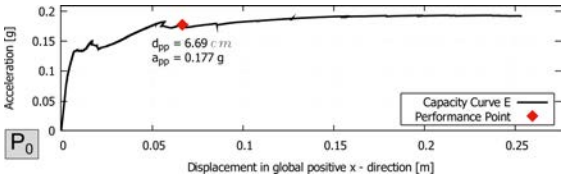

(a) Mechanism I: P_0 - node E

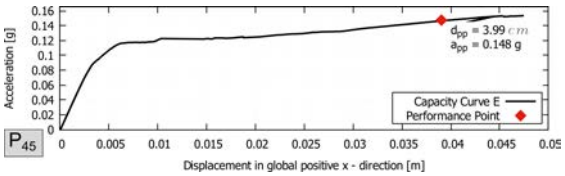

(b) Mechanism I: P_{45} - node E

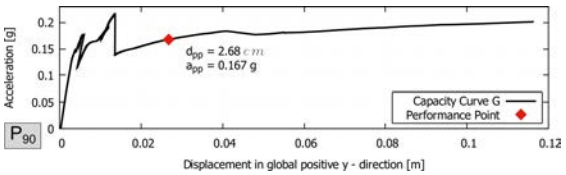

(c) Mechanism II: P_{90} - node G

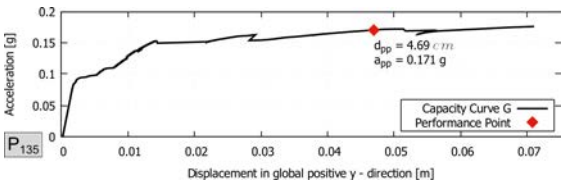

(d) Mechanism III: P_{135} - node G

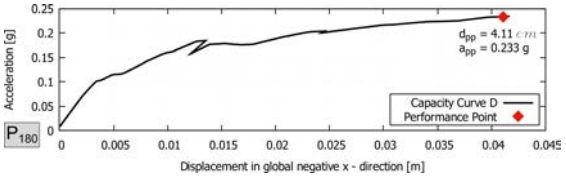

(e) Mechanism IV: P_{180} - node D

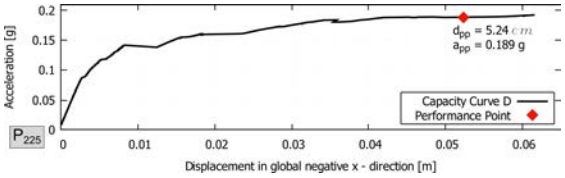

(f) Mechanism IV: P_{225} - node D

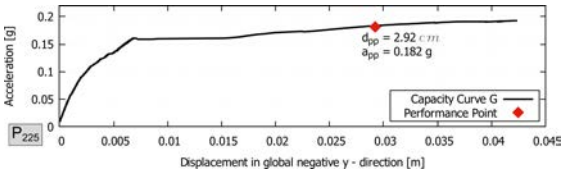

(g) Mechanism V: P_{225} - node G

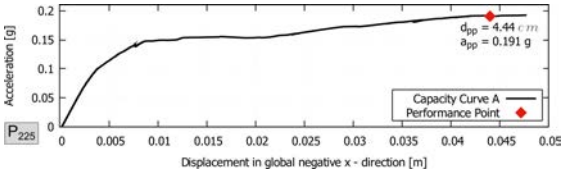

(h) Mechanism VI: P_{225} - node A

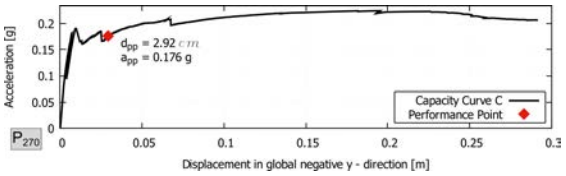

(i) Mechanism VII: P_{270} - node C

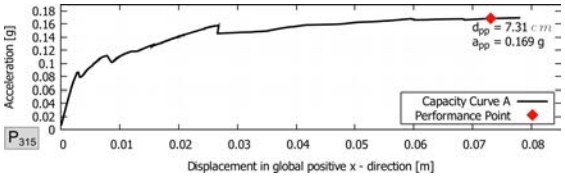

(j) Mechanism VIII: P_{315} - node A

Figure 3.10: Capacity curves and evaluation of the performance point for all the individual nonlinear static analyses of the proposed multi directional pushover approach

- **Pushover P_{135}** Figure 3.9d shows the global displacements of P_{135} at the PP, and depicts an out of plane failure of only the northern part of the east facade in positive y-direction (**Mechanism III**). Figure 3.10d shows the capacity curve of control node **G**. The first drop of stiffness of the capacity curve is caused by cracks in the spandrels of the facade. Further increase of the load results in cracks at the perpendicularly connected walls which activate the collapse.

- **Pushover P_{180}** Figure 3.9e shows the global displacements at the PP for **Mechanism IV**, that is the out of plane failure along the negative x-direction of the western part of the wall overlooking the courtyard parallel to the south facade. Figure 3.10e shows the capacity curve of P_{180} with the corresponding control node **D**. Cracks in one perpendicular wall cause a first change of stiffness at 0.11 g lateral acceleration. A sudden drop of capacity occurs at 0.18 g due to cracks in the corner and at the connection of the walls. The cracks grow further and lead to the out of plane failure at control node **D**.

- **Pushover P_{225}** Figure 3.9f shows that the NSA along this direction activates several mechanisms. First, there is the out of plane failure at node D which has already been introduced as **Mechanism IV**. This mechanism leads to total collapse of the FE model. However, two further large displacements of walls can be detected, such as the out of plane displacements in negative x-direction of the western part of the south facade at node **A** (**Mechanism V**). Further large displacements occur at the northern part of the east facade in negative y-direction and activate **Mechanism VI**. Figure 3.10f, 3.10g and 3.10h show the capacity curves of the three nodes corresponding to the mechanisms. Large cracks at the connection to the perpendicular walls appear in **Mechanism IV**. Cracks in the spandrels of the perpendicular wall of **Mechanism VI** decrease the stiffness and the connection of the east facade cracks in **Mechanism VI**.

- **Pushover P_{270}** The pushover analysis along this direction activates **Mechanism VII**. Figure 3.9g shows large out of plane diplacements at the inner wall parallel to the east facade at node **C**. Figure 3.10i shows the capacity curve of control node **C** during P_{270} and demonstrates the beginning of the nonlinear range at a lateral acceleration value of approximately 0.19 g. This loading leads to large cracks in the connection to the perpendicular wall. Further increase of the lateral acceleration loads activate the out of plane collapse until total failure of the wall.

- **Pushover P_{315}** Figure 3.9h shows large deformations occurring at the most western part of the south facade. Figure 3.10j shows the capacity curve of the corresponding control node **A**. The formation of cracks in the lower spandrel of the perpendicular wall initiates the drop of capacity at around $0.09g$. At approximately $0.11g$ the crack in the upper spandrel of the same wall becomes larger and causes further yielding. Increase of the lateral acceleration leads to growing cracks. Finally, **Mechanism VIII** is activated and the wall fails out of plane.

Table 3.3 shows the maximum displacements of the control nodes A, C, D, E and G in x- and y-direction, respectively. Section 3.4.5 presents a careful comparison of their values with those derived from NDA in Section 3.4.4.

Table 3.3: Comparison among the maximum displacements derived from the nonlinear dynamic analyses (NDA) and the performance displacements of the pushover analyses (NSA). Calculation of relative errors of NSA displacements compared with NDA displacements.

		NDA		NSA (PP)		
Control Node	Direction	t [s]	d_{max} [cm]	Id	d_{pp} [cm]	χ_{NSA} [%]
A	x	29.10	7.45	P_{315}	7.31	1.9
		28.20	-6.65	P_{225}	-4.44	33.2
C	y	29.54	2.90	–	–	–
		19.71	-2.81	P_{270}	-2.92	3.91
D	x	29.06	5.51	–	–	–
		28.20	-9.45	P_{225}	-5.24	44.5
E	x	28.97	8.78	P_0	6.69	23.8
		28.22	-6.80	–	–	–
G	y	29.51	4.75	P_{135}	4.69	1.26
		28.17	-3.06	P_{225}	-2.92	4.58
					$\bar{\chi}_{NSA}$	16.2

3.4.4 Nonlinear dynamic analysis

This section presents the results of the NDA of the *Palacio Pereira*. The transient acceleration which acts on the FE model of the building is the time history of the 2010 earthquake recorded at the Santiago Central Station in the transversal

and longitudinal directions, respectively. Figure 3.11 shows the most significant time frame of 80 seconds of the time history of the 2010 earthquake acceleration in longitudinal (y) and transversal (x) directions.

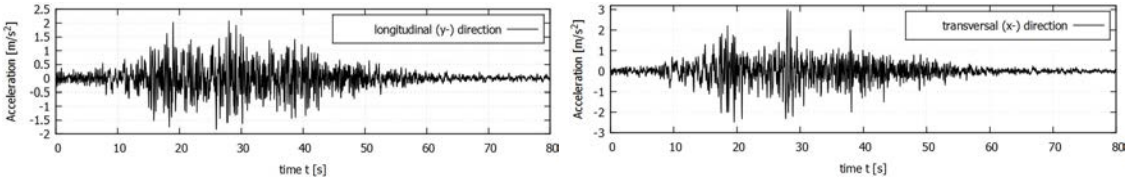

(a) **Longitudinal** ground acceleration (b) **Transversal** ground acceleration

Figure 3.11: Time history of the 2010 earthquake longitudinal and transversal accelerations recorded at the Central Station of Santiago

The NDA is performed by letting both the x and y components acting simultaneously. The time integration method is the Newmark-beta with $\gamma_N = \frac{1}{2}$ and $\beta_N = \frac{1}{4}$. An automatic time step actualization is used with maximum time step size $\triangle t_{max} = 0.025s$ and minimum step size is $\triangle t_{min} = 1.0 \cdot 10^{-9}$. The maximum time step size is based on the criterion of $\triangle t = 0.1 \cdot T_1$ suggested by Chopra Chopra (1995), being $T_1 = 0.268\ s$ the period of the first mode. However, since the contribution of the first mode is not predominant in this structure, as intensely discussed in the linear analyses shown in Appendix A.1.1, the automatic time step actualization has been controlled throughout all the analysis to ensure the proper accuracy of the results. The constitutive model is the total strain based crack model as for the NSA.

The classical Rayleigh damping matrix of type $C_{Ray} = a_0 M + a_1 K$ is used in NDA. The definition of the coefficients a_0 and a_1 can be obtained by regarding the method presented by Chopra Chopra (1995). The range of the modes not overdamped ranges from mode 2 to mode 18 for the *Palacio Pereira*. The corresponding eigenfrequencies are shown in Appendix A.1.1. The coefficients for the implementation of the damping model are $a_0 = 0.2365\ s^{-1}$ and $a_1 = 0.009852\ s$. Figure 3.12 shows the obtained values for the damping ratios versus the frequency.

The NDA of the *Palacio Pereira* is performed until the end of the 80 seconds of the earthquake excitation. This is in agreement with the real behavior of the *Palacio Pereira* during the earthquake in 2010, because the collapse of the building did not occur, even though the structure was severely damaged.

Several initiating failure mechanisms can be detected by considering the analysis results. The results of the last step at 80 seconds show a significant amount

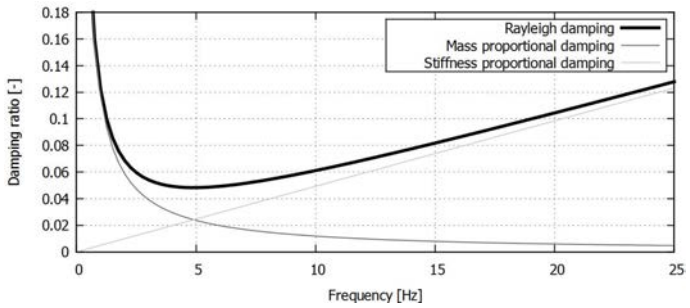

Figure 3.12: Rayleigh damping model

of accumulated hysteretic damage on the building, and the activated failure mechanisms are not sufficient to interrupt the NDA. The entire set of results is analyzed to identify possible failure mechanisms, as reported in the next section. The maximum displacements of the NDA and the PPs of the NSA are compared by considering the same control nodes. Table 3.3 shows the maximum displacements of the control nodes A, C, D, E and G directly compared with the performance displacements from the MDPA. The overall maximum displacement during the NDA is reached by control node D in the negative x direction with a value of 9.45 *cm*. Figure 3.13 shows the displacements in x direction at 28.20 seconds of the NDA, where the maximum displacement is reached.

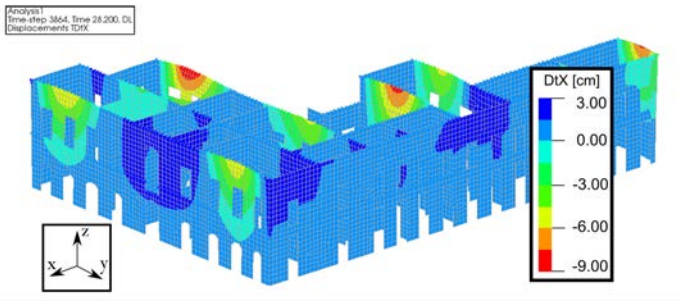

Figure 3.13: Contour plot of displacements in x direction provided by nonlinear dynamic analysis at 28.2 seconds.

Even though the base accelerations of the earthquake record reach similar maximum values in x and y directions, the displacements of the structure are bigger in x than in y direction. This is due to the intrinsic irregularity of the building. A similar behavior is obtained by the PP of the NSA results, where the displacements in x direction are bigger than the ones in y direction.

Table 3.3 shows the percentage relative errors of NSA displacements compared

with the NDA reference values, for the different control nodes and along both positive and negative directions. All these different relative errors are averaged for the NSA. The mean relative error $\bar{\chi}_{NSA}$ of the MDPA results 16.2%, showing a proper approximation of the MDPA results to the ones obtained by NDA. This important outcome shows the capability of the proposed MDPA to reproduce the overall seismic response of the irregular masonry building without box behavior.

3.4.5 Comparison and discussion

MDPA including eight pushover analyses provides useful information about various possible collapse mechanisms in the considered irregular structure without box behavior. The NDA, which considers simultaneously the two perpendicular time histories of the earthquake and accounts directly for nonlinear dynamic effects, can be compared with the overall results of the proposed MDPA. This kind of comparison is necessary in order to evaluate the capability of the MDPA to display all the damage and collapse mechanisms provided by the NDA and produced by the 2010 earthquake. The description of the failure mechanisms is based on the contour plots of crack width at meaningful steps of the analysis. Plots of each analysis are generated for both the MDPA at each PP and NDA at the step when the mechanism is clearly detectable. The smallest cracks plotted have a width of 1.0 mm. Figures 3.14 and 3.15 show all the local failure mechanisms mentioned in Section 3.4.3. The similarities of the mechanisms obtained by NDA and MDPA are analyzed in the following.

Mechanism I (Figure 3.14a and 3.14b) shows very similar crack patterns for both NDA and P_0 NSA. The spandrels of the perpendicular walls are cracked and the mechanism is produced by the out of plane deformation in the positive x direction.

Mechanism II (Figure 3.14c and 3.14d) presents the entire out of plane overturning of the east facade of the *Palacio Pereira*. It is caused by vertical cracks in all the walls perpendicularly connected to the facade. Both the NDA and the P_{90} NSA present this mechanism.

Mechanism III (Figure 3.14e and 3.14f) is identified by an out of plane overturning in positive y direction of the east facade with control node G. Large cracks in the walls connected perpendicularly to the facade are correctly displayed by both NDA and P_{135} NSA. Both the analyses present cracks in the spandrels close to node G.

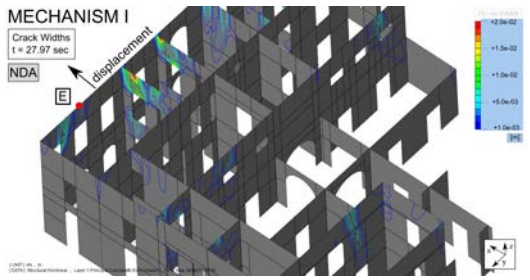

(a) NDA - mechanism I

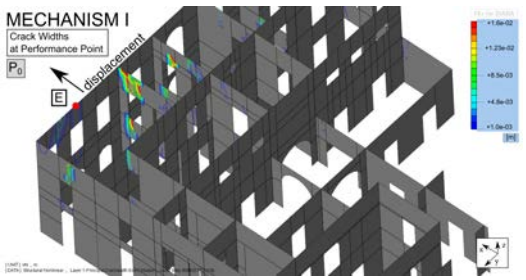

(b) NSA (P_0) - mechanism I

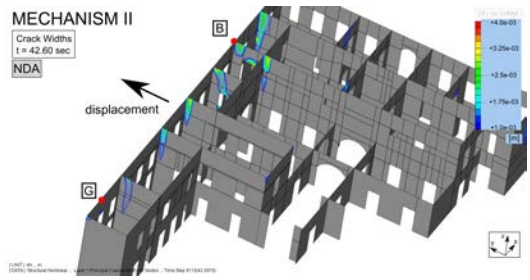

(c) NDA - mechanism II

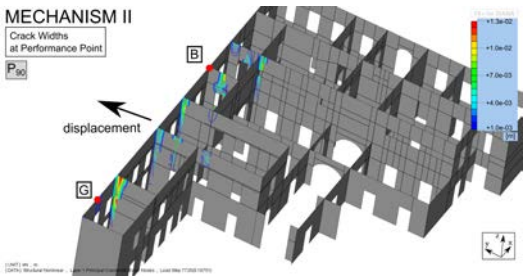

(d) NSA (P_{90}) - mechanism II

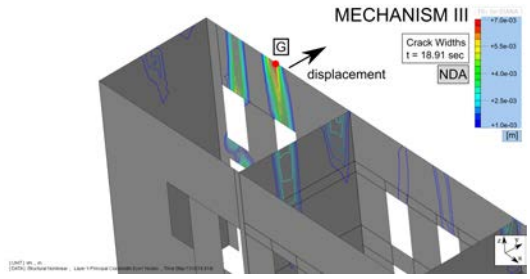

(e) NDA - mechanism III

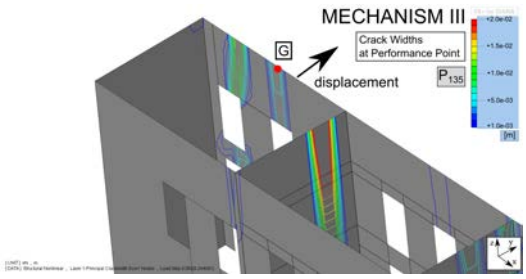

(f) NSA (P_{135}) - mechanism III

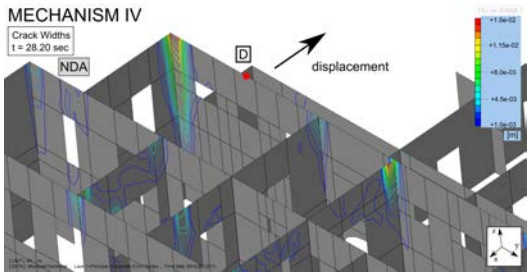

(g) NDA - mechanism IV

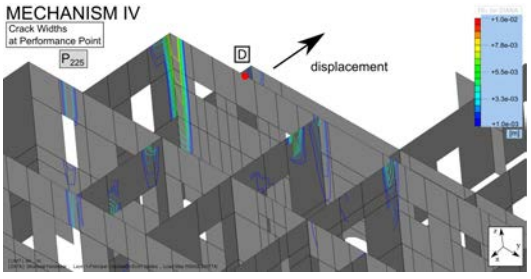

(h) NSA (P_{225}) - mechanism IV

Figure 3.14: Contour plots of the crack width larger than 1.0 mm for mechanisms I to IV provided by the nonlinear dynamic and static analyses (NDA and NSA)

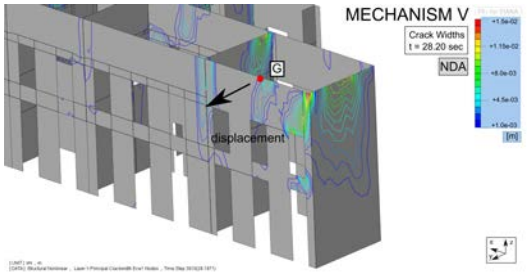

(a) NDA - mechanism V

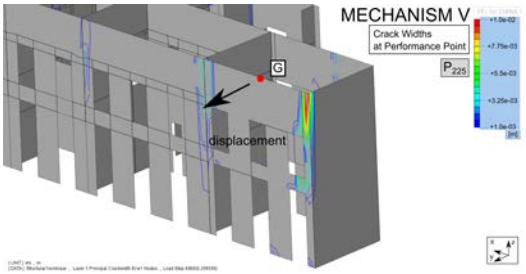

(b) NSA (P_{225}) - mechanism V

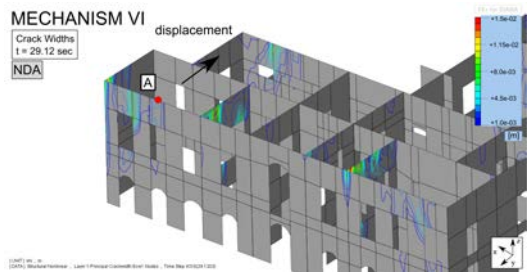

(c) NDA - mechanism VI

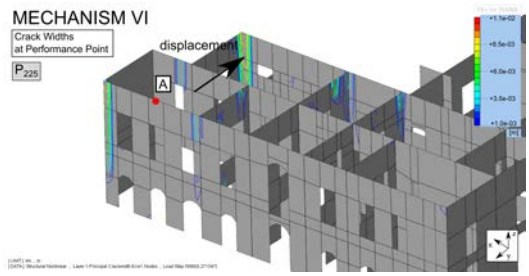

(d) NSA (P_{225}) - mechanism VI

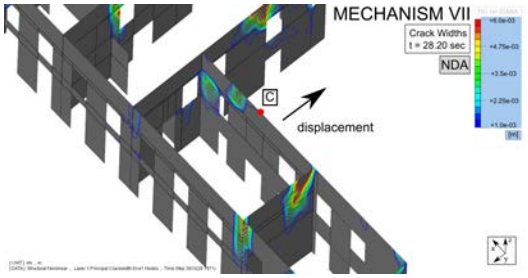

(e) NDA - mechanism VII

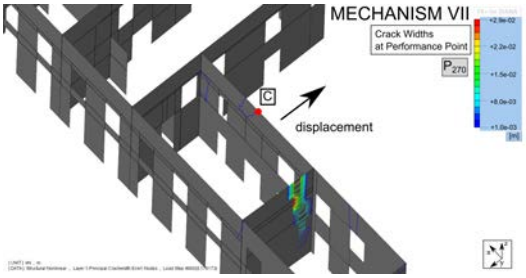

(f) NSA (P_{270}) - mechanism VII

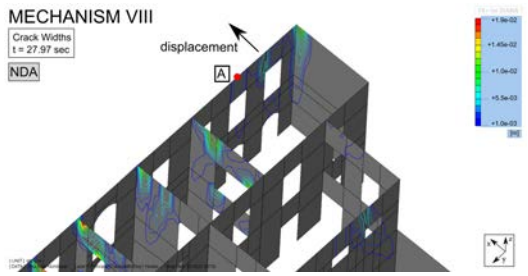

(g) NDA - mechanism VIII

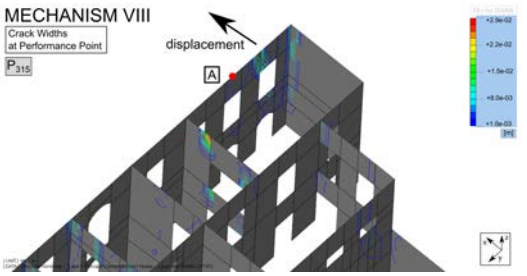

(h) NSA (P_{315}) - mechanism VIII

Figure 3.15: Contour plots of the crack width larger than 1.0 mm for mechanisms V to VIII provided by the nonlinear dynamic and static analyses (NDA and NSA)

Mechanism IV (Figure 3.14g and 3.14h) is the out of plane overturning in negative x direction with control node D. Both the NDA and the P_{225} NSA show cracks at the connections to the perpendicular walls.

Mechanism V (Figure 3.15a and 3.15b) displays an out of plane overturning in the negative y-direction of the facade at node G. For both the NDA and P_{225} NSA large cracks appear at the corners with the perpendicular walls.

Mechanism VI (Figure 3.15c and 3.15d) shows the out of plane overturning in negative x direction at node A. For both NDA and P_{225} NSA large cracks appear in the corner. The cracks occurring in the spandrels of the perpendicular connected walls are less pronounced in the NSA than in the NDA.

Mechanism VII (Figure 3.15e and 3.15f) presents the local out of plane overturning in negative y-direction of the wall with control node C and appears both in the NDA and P_{270} NSA. Large cracks in the perpendicular wall and the spandrels are correctly represented by both the analyses.

Mechanism VIII (Figure 3.15g and 3.15h) consists of large cracks in the corner and in the spandrels of the facade as well as in the perpendicular walls. The out of plane overturning of the wall is correctly provided by both the NDA and P_{315} NSA.

Table 3.4 shows a visual summary of which mechanisms are detected by the NDA and the MDPA, respectively. It illustrates that the results of the NDA and the overall results of the proposed MDPA with eight loading directions are in a very good agreement. In particular, there is an important advantage offered by the MDPA compared with the conventional NSA along only the principal directions of the building. In fact, the execution of P_0, P_{90}, P_{180} and P_{270} would exhibit only four different mechanisms (I, II, IV and VII), whilst the proposed MDPA displays a total of eight mechanisms. The novel MDPA approach allows to cover all the collapse mechanisms provided by the NDA.

Table 3.4: Failure mechanisms detected by nonlinear dynamic and multi directional static analyses

	I	II	III	IV	V	VI	VII	VIII
NDA	✓	✓	✓	✓	✓	✓	✓	✓
P_0	✓							
P_{45}	✓							
P_{90}		✓						
P_{135}			✓					
P_{180}				✓				
P_{225}				✓	✓	✓		
P_{270}							✓	
P_{315}								✓

3.5 Summary

This chapter has dealt with numerical simulation techniques for the assessment of masonry structures. It has strongly focused on the benefits of macro modeling strategies. Without macro modeling approaches, such advanced numerical analyses would not be possible, since more detailed computational strategies, e.g. micro or conventional multi scale modeling, would require larger computational resources. Macro modeling allows to run large scale analysis and facilitates significantly the development of novel simulation techniques that enable the assessment of the structural behavior of masonry.

In particular, this chapter has evidenced that such novel approaches are necessary in order to asses the seismic vulnerability of masonry structures. The macro modeling strategy has been utilized in order to discuss a novel approach for the seismic analysis through the application of the FE method to irregular masonry structures without box behavior. Nonlinear dynamic analysis (NDA) is currently the most adequate tool for this type of structure. To avoid the well-known large computational effort of nonlinear time history analysis, nonlinear static analysis (NSA) is usually carried out in seismic assessment. NSA generally exhibits significant limitations when dealing with irregular structures. This chapter has presented a novel multi directional pushover approach (MDPA) suitable to analyze existing buildings with plan and elevation irregularity, as well as without box behavior.

The proposed MDPA consists in performing sequentially a set of pushover analyses with mass proportional horizontal loading along eight directions with respect to the plan of the building. The approach breaks somehow one of the fundamental hypotheses of conventional NSA that consists in executing the pushover only along the principal directions of the masonry structure. The objective is to assess systematically the vulnerability of the structural members of the irregular building along a large set of lateral loading directions. This idea overcomes the limitations of conventional NSA that usually reveals to be unable to account for the multi directionality of the real earthquake motions. A masonry building with important irregularity in plan and elevation, and without box behavior, has been considered to show the advantages of the novel MDPA procedure. The case study has been the *Palacio Pereira* in Chile, an historical palace damaged by an earthquake in 2010.

The development of a MDPA has provided meaningful results about the assessment of the seismic behavior of the *Palacio Pereira*. The procedure has consisted in executing eight mass proportional pushover analyses by sequentially varying the loading direction of 45 degrees in plan. The overall results of the MDPA have shown eight possible local failure mechanisms consisting on out-of-plane overturning of partial portions of the facades. It is worth noticing that the conventional approach of executing pushover analyses along the principal axes of the building would provide only four collapse mechanisms. The application of the new MDPA approach has led to the detection of four more local failure mechanisms of the structure than the ones obtained from a classical NSA approach. In addition, the average relative error of MDPA performance displacements, compared with NDA reference values for the different failure mechanisms, results moderate (16.2%).

The NDA has been carried out by applying simultaneously the two perpendicular base accelerations of the 2010 Santiago de Chile earthquake. This analysis has shown several damage mechanisms in the structure during the base excitation. In particular, all the failure mechanisms provided by the NDA are equivalent to those reproduced by the MDPA.

The investigations made in this chapter have shown that a MDPA is a suitable procedure for the seismic analysis of irregular (in plan and in elevation) masonry buildings without box behavior. The main limitations of the standard pushover procedures applied to irregular structures can be overcome by considering the proposed MDPA since it shows to yield results more consistent with NDA. The selection

of a meaningful case-study of a masonry building hit by an earthquake in 2010 has demonstrated that the MDPA overall results are also in agreement with real damage observations (Kalkbrenner et al. (2019)).

This chapter has given deep insights to the analysis of masonry structures by using a macro modeling approach. One of the crucial points of the procedure has been the definition and calibration of the mechanical parameters for the homogenized material of the masonry macro model. The material properties of the here presented case study of the *Palacio Pereira* have been obtained by calibrating a numerical model that simulates a single in-situ shear test. This is a commonly established way of calibrating numerical models for large masonry structures, i.e. there are very few experimental tests available as reference for the determination of the macro model parameters. Those calibrated models are able to represent the correct behavior of a single calibration experiment, e.q. the in-situ shear test available in the specific case study examined. However, masonry is a complex anisotropic material, with both linear and nonlinear material responses strongly depending on the applied stress/strain state. The definition of material properties of a large structure by only taking into account one specific test loading condition, neglects all the other possible responses that the material might experience under different deformation/stress states. That is why the following chapters of the thesis investigate in detail a novel technique in order to reproduce multiple stress/strain states while calibrating the homogenized numerical constitutive law of masonry macro models.

Part II

Machine learning material homogenization

Chapter 4

Constitutive model

4.1 Constitutive law

An effective stress definition is adopted to distinguish between damaged/undamaged and loading/unloading stages. It is based on the principle of strain equivalence that assumes the comparison between damaged and undamaged configurations by strain consideration with reference to the elastic material behavior Woody Ju et al. (1998).

$$\bar{\boldsymbol{\sigma}} = \boldsymbol{C} : \boldsymbol{\epsilon} \tag{4.1}$$

Where $\bar{\boldsymbol{\sigma}}$ is the effective stress tensor, $\boldsymbol{\epsilon}$ the strain tensor and $\boldsymbol{C}$ is the fourth order elasticity tensor. The works of Cervera et al. (1995); Faria et al. (1998); Wu et al. (2006) introduce separated internal damage variables to use damage scalar models for tensile and compressive stress contributions and introduce the stress tensor as follows

$$\boldsymbol{\sigma} = (1 - d^{+})\, \bar{\boldsymbol{\sigma}}^{+} + (1 - d^{-})\, \bar{\boldsymbol{\sigma}}^{-} \tag{4.2}$$

In this expression, $\boldsymbol{\sigma}$ denotes the stress tensor. The internal damage variables d^{+} and d^{-} indicate the grade of damage in tension and compression, respectively. The values of d^{+}/d^{-} can range from 0 to 1, whereas the value 0 stands for no damage and the value 1 for complete damage. The tensors $\boldsymbol{\sigma}^{+}$ and $\boldsymbol{\sigma}^{-}$ are the

positive and negative parts of the effective stress tensor and account for different nonlinear behavior in tension and compression. The decomposition of the effective stress tensor $\bar{\boldsymbol{\sigma}}$ is performed according to Wu et al. (2006) as follows

$$\bar{\boldsymbol{\sigma}}^{+} = \boldsymbol{P}^{+} : \bar{\boldsymbol{\sigma}} \tag{4.3}$$

$$\bar{\boldsymbol{\sigma}}^{-} = \bar{\boldsymbol{\sigma}} - \bar{\boldsymbol{\sigma}}^{+} = \boldsymbol{P}^{-} : \bar{\boldsymbol{\sigma}}, \tag{4.4}$$

where $\boldsymbol{P}^{+}$ and $\boldsymbol{P}^{-}$ are fourth-order projection tensors expressed according to Faria et al. (2000)

$$\boldsymbol{P}^{+} = \sum_{i=1} H(\bar{\sigma}_i)\boldsymbol{p}_{ii} \otimes \boldsymbol{p}_{ii} \tag{4.5}$$

$$\boldsymbol{P}^{-} = \boldsymbol{I} - \boldsymbol{P}^{+}. \tag{4.6}$$

Where $\bar{\sigma}_i$ is the i-th principal stress or eigenvalue of the effective stress tensor $\bar{\boldsymbol{\sigma}}$. The symmetric tensor $\boldsymbol{p}_{ii}$ is the outer product of eigenvector $\boldsymbol{n}_i$ belonging to the i-th principal stress ($\boldsymbol{p}_{ii} = \boldsymbol{n}_i \otimes \boldsymbol{n}_i$). The Heaviside function $H(\bar{\sigma}_i)$ guarantees that the positive projection tensor $\boldsymbol{P}^{+}$ is only computed by positive values of the effective stress tensor. It is defined as follows

$$H(x) = \begin{cases} 0, & for\ x \leq 0 \\ 1, & for\ x > 0. \end{cases} \tag{4.7}$$

4.2 Yield criteria

Lubliner et al. (1989) introduce a proper yield criteria that considers two scalar values that respect different material behavior in tension and compression. The values τ^{+} (tension) and τ^{-} (compression) indicate the equivalent uni-axial stress of the respective parts $\bar{\boldsymbol{\sigma}}^{+}$ or $\bar{\boldsymbol{\sigma}}^{-}$ of the effective stress tensor. In this research the Lubliner yield criteria modified by Petracca et al. (2016) is considered. The scalars for tension (τ^{+}) and compression (τ^{-}) are then defined as follows.

$$\tau^{+} = H(\bar{\sigma}_{max})\left[\frac{1}{1-\alpha}\left(\alpha\bar{I}_1 + \sqrt{3\bar{J}_2} + \beta\bar{\sigma}_{max}\right)\frac{f_p^{+}}{f_p^{-}}\right] \tag{4.8}$$

$$\tau^{-} = H(-\bar{\sigma}_{min})\left[\frac{1}{1-\alpha}\left(\alpha\bar{I}_1 + \sqrt{3\bar{J}_2} + \kappa\beta\langle\bar{\sigma}_{max}\rangle\right)\right] \tag{4.9}$$

The modification of the formulation for τ^{-} from the definition in Lubliner et al. (1989) to the one presented here (Petracca et al. (2016)), is the introduction of κ in Equation 4.9. This constant better controls the effect of the compression surface on the shear strength of the model. It ranges from 0 (Drucker-Prager surface) to 1 (Lubliner surface).

$\bar{I}_1$ is the first invariant of the effective stress tensor, and $\bar{J}_2$ the second invariant of the deviatoric stress tensor. $\bar{\sigma}_{max}$ denotes the maximum principal stress and $\bar{\sigma}_{min}$ the minimum principal stress of the effective stress tensor. The application of the Heaviside function $H(x)$ guarantees the evolution of the tension yield surface if at least one positive principal stress value exists (analogous for the negative yield surface). $\langle\bullet\rangle$ are the Macaulay brackets so that

$$\langle x\rangle = \begin{cases} 0, & for\ \ x < 0 \\ x, & for\ \ x > 0. \end{cases} \tag{4.10}$$

The constants α and β are dimensionless scalar values and can be computed by the following expressions considering the yield values of tension and compression behavior of the material

$$\alpha = \frac{k_b - 1}{2k_b - 1} \tag{4.11}$$

$$\beta = (1-\alpha)\frac{f_p^{-}}{f_p^{+}} - (1+\alpha) \tag{4.12}$$

Where, k_b is a multiplier to respect the increasing strength under biaxial compression states, so that $k_b = {}^{f_{bi}^{-}}/_{f_p^{-}}$, with f_{bi}^{-} as the biaxial compression strength and f_p^{-} as the uni-axial peak strength in compression. f_p^{+} is the tension peak strength.

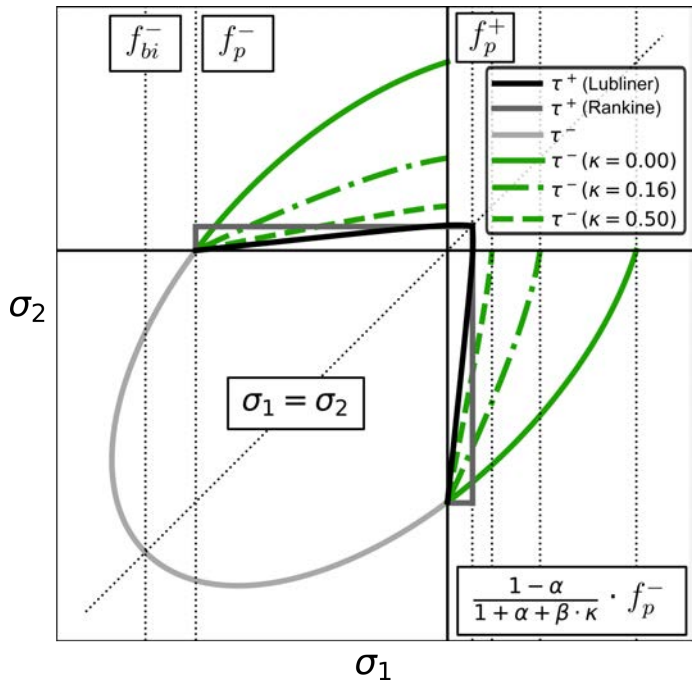

Figure 4.1: Yield surfaces for the tension equivalent stress τ^+ and the compression equivalent stress τ^- in the two dimensional principal stress state

Additional to the above introduced yield criteria in tension, a classic Rankine damage criteria is also applied in this thesis. For this case, the positive equivalent stress value is computed as follows

$$\tau^+ = \langle \bar{\sigma}_{max} \rangle \tag{4.13}$$

Figure 4.1 shows the yield surface of the Rankine and Lubliner model in tension and the modified Lubliner model in compression in the two dimensional principal stress state, respectively. The effect of a variation of κ, introduced by Petracca et al. (2016) in order to modify the surface in case of mixed stress states, is shown for three different values. The depicted yield surfaces are utilized in the application examples of this thesis. Deeper insights on the effect of κ are given in Petracca (2016).

Expressions 4.8 and 4.9 are valid for 2D analysis. In case 3D analysis are considered, the negative equivalent stress must be extended inside the brackets by a coefficient that accounts for three dimensional compression stress effects (Petracca (2016)).

4.3 Damage evolution

A threshold value must be introduced in order to distinguish between an undamaged and a damaged state of the material. Damage is an irreversible process and therefore the threshold must also indicate if the model undergoes loading/unloading or reloading. Thus, two additional scalar values $r_n^{\pm}$ are introduced as actual threshold values and defined as follows

$$r^{\pm} = \max\left\{r_0^{\pm}; \max_{t_0 \leq n \leq t_e} \tau_n^{\pm}\right\} \tag{4.14}$$

Where n indicates the actual step of an analysis going from a start time t_0 to an end time t_e with a step size $\triangle t$. Furthermore, $\tau_n^{\pm}$ is the actual uni-axial equivalent stress, $r_0^{\pm}$ is the initial threshold value, with $r_0^{+} = f_p^{+}$, if no hardening function in tension is considered and $r_0^{+} = f_0^{+}$, if a damage onset stress for tension behavior is considered. $r_0^{-} = f_0^{-}$ defines the elastic limit in compression. Observing the maximum value of the uni-axial equivalent stress ensures that during unloading and prospective reloading the maximum value remains the threshold. It follows the damage criteria

$$\Phi^{\pm}(\tau^{\pm}, r^{\pm}) = \tau^{\pm} - r^{\pm} \leq 0 \tag{4.15}$$

Petracca et al. (2017) came up with a valuable combination of damage evolution in tension and in compression. The research presented in detail that a combination of an exponential softening law in tension and a quadratic hardening and softening law in compression fits astonishingly good for the numerical analysis of masonry structures. Thus those damage evolution laws are also applied in the present research. Furthermore a novel extended model for the behavior in tension is presented in the following.

4.3.1 Compression behavior

To ensure hardening and softening in compression behavior, Petracca et al. (2017) established a novel hardening-softening law based on quadratic Bézier curves. Figure 4.2 shows the thoroughly developed post linear evolution behavior. It consists of

three Bézier splines and a final residual part. The computation of each part can be done as follows

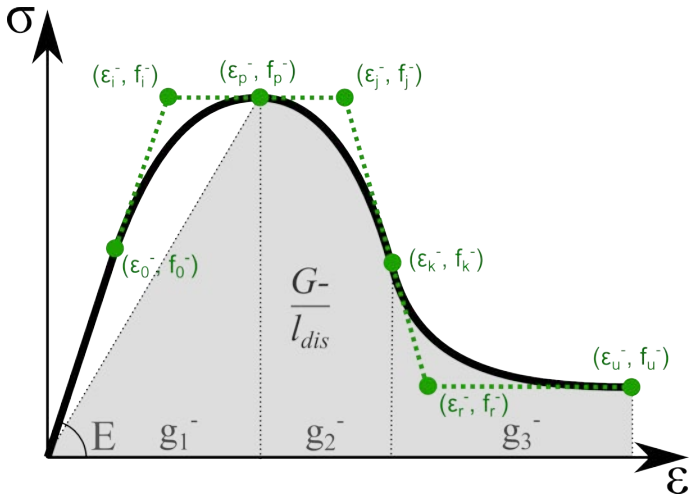

Figure 4.2: Uni-axial strain-stress curve of the material's compression behavior with Bézier control nodes

$$\Upsilon(\xi^-) = \begin{cases} \mathcal{B}(\xi^-, \epsilon_0^-, \epsilon_i^-, \epsilon_p^-, f_0^-, f_i^-, f_p^-) & \epsilon_{c,0} < \xi^- \leq \epsilon_p^- \\ \mathcal{B}(\xi^-, \epsilon_p^-, \epsilon_j^-, \epsilon_k^-, f_p^-, f_j^-, f_k^-) & \epsilon_p^- < \xi^- \leq \epsilon_k^- \\ \mathcal{B}(\xi^-, \epsilon_k^-, \epsilon_r^-, \epsilon_u^-, f_k^-, f_r^-, f_u^-) & \epsilon_k^- < \xi^- \leq \epsilon_u^- \\ f_u^- \end{cases} \tag{4.16}$$

Where $\mathcal{B}(\bullet)$ is a Bézier function that requires the coordinates of three control points and is defined as

$$\mathcal{B}(X, x_1, x_2, x_3, y_1, y_2, y_3) = (y_1 - 2y_2 + y_3)\, p^2 + 2p(y_2 - y_1) + y_1 \tag{4.17}$$

with

$$p = \frac{-B + \sqrt{D}}{2A} \tag{4.18}$$

and

$$A = x_1 - 2x_2 + x_3 \tag{4.19}$$
$$B = 2(x_2 - x_1) \tag{4.20}$$
$$C = x_1 - X \tag{4.21}$$
$$D = B^2 - 4AC \tag{4.22}$$

ξ^- is introduced as a strain-like counterpart to the current damage threshold r^- and is defined as the ratio of the damage threshold and the materials Young's modulus

$$\xi^- = \frac{r^-}{E} \tag{4.23}$$

Finally the damage variable d^- can be calculated as follows

$$d^-(r^-) = 1 - \frac{\Upsilon(\xi)}{r^-} \tag{4.24}$$

Following this procedure of computing the damage in compression also requires a fracture energy regularization which depends on the elemental size. The basics are explained in the following. However, a detailed discussion can be found in Petracca (2016) on fracture energy regularization.

The total specific fracture energy g^-_{calc} of the uni-axial damage evolution law can be calculated as follows

$$g^-_1 = \frac{f^-_p \epsilon^-_p}{2} \tag{4.25}$$
$$g^-_2 = \mathcal{G}\left(\epsilon^-_p, \epsilon^-_j, \epsilon^-_k, f^-_p, f^-_j, f^-_k\right) \tag{4.26}$$
$$g^-_3 = \mathcal{G}\left(\epsilon^-_k, \epsilon^-_r, \epsilon^-_u, f^-_k, f^-_r, f^-_u\right) \tag{4.27}$$
$$g^-_{calc} = g^-_1 + g^-_2 + g^-_3 \tag{4.28}$$

Where $\mathcal{G}$ is the area beneath the Bézier curves, that can be computed by taking into account the control nodes

$$\mathcal{G}(x_1, x_2, x_3, y_1, y_2, y_3) = \frac{x_2 y_1}{3} + \frac{x_3 y_1}{6} - \frac{x_2 y_3}{3} + \frac{x_3 y_2}{3} + \frac{x_3 y_3}{2} - x_1\left(\frac{y_1}{2} + \frac{y_2}{3} + \frac{y_3}{6}\right) \tag{4.29}$$

The energy regularization can now be performed by stretching the post peak part of the uni axial compression damage evolution. Then the following control nodes of the Bézier formulation must be adapted to

$$\bar{\epsilon}_i^- = \epsilon_i^- + \mathcal{S}(\epsilon_i^- - \epsilon_p^-) \tag{4.30}$$

Where $i = j, k, r, u$ and $\mathcal{S}$ is a stretching factor calculated as follows

$$\mathcal{S} = \frac{g^- - g_1^-}{g_{calc}^- - g_1^-} - 1 \tag{4.31}$$

with

$$g^- = \frac{G^-}{l_{dis}} \tag{4.32}$$

To avoid a sudden fall from the peak stress in compression to zero, the stretcher $\mathcal{S}$ must always be larger than -1.0. This leads to the condition

$$l_{dis} < \frac{2G^-}{\epsilon_p^- f_p^-} \tag{4.33}$$

Where l_{dis} is the size of the dissipative zone which is assumed to be equal to the characteristic length of the finite element. The effects of different elemental characteristic lengths can be observed in Petracca et al. (2017). All the numerical tests performed in this thesis comply with the condition of Equation 4.33.

The formulation of the Bézier like damage evolution law requires several input parameter (three control points per Bézier spline). Hence the parameters c_1^-, c_2^- and c_3^- are introduced in order to minimize the number of required input values. Those

factors are able to adjust the post peak part and avoid a specific definition of the post peak control points. Table 4.1 shows all required input values for the damage evolution in compression. The values marked in gray are the necessary ones for the correct law application thanks to the introduction of the c-factors. The computation of the remaining inputs of the Bézier like damage evolution law is attached to the appendix files of this thesis (Appendix B.1).

Table 4.1: Strain and stress properties needed for the Bézier damage law in compression

ϵ_0^-	ϵ_i^-	ϵ_p^-	ϵ_j^-	ϵ_k^-	ϵ_r^-	ϵ_u^-
f_0^-	f_i^-	f_p^-	f_j^-	f_k^-	f_r^-	f_u^-
c_1^-	c_2^-	c_3^-				

4.3.2 Tension behavior

4.3.2.1 Exponential softening

Figure 4.3 displays the uni-axial tension behavior of the material for post-peak exponential softening.

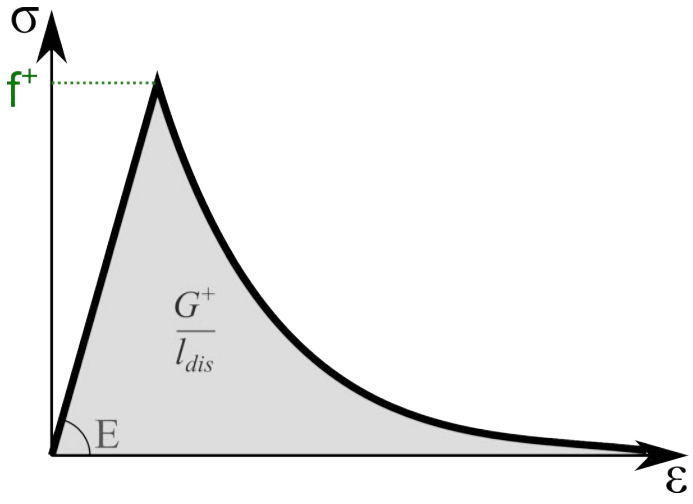

Figure 4.3: Uni-axial strain-stress curve for exponential softening of the material's tension behavior

According to an exponential softening behavior assumed in tension, the damage variable d^+ evolves as follows

$$d^+(r^+) = 1 - \frac{r_0^+}{r^+} exp\left[2H_{dis}\left(\frac{r_0^+ - r^+}{r_0^+}\right)\right] \tag{4.34}$$

Where H_{dis} is the discrete softening parameter, and can be calculated considering

$$H_{dis} = \frac{l_{dis}}{l_{mat} - l_{dis}} \tag{4.35}$$

Where $l_{mat} = 2EG^+/(f_t^+)^2$.

4.3.2.2 Extension of the tension damage behavior

The tension behavior of brittle materials is usually modeled as a combination of linear elastic behavior up to the tension peak and followed by an exponential softening as shown in Section 4.3.2.1. However, in order to better represent the pre peak hardening of masonry's tension behavior, this thesis considers a hardening part for the damage evolution in tension. Investigations performed in a later part of this thesis show that, while homogenizing the material masonry, pre-peak hardening occurs also in tension. Therefore, the Bézier like hardening and softening evolution law introduced in Section 4.3.1 is also implemented for the damage behavior in tension. Figure 4.4 shows the relation for the uni-axial tension damage evolution.

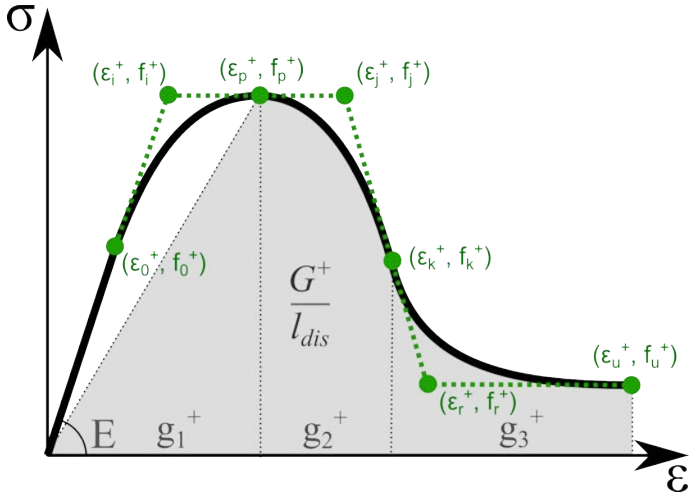

Figure 4.4: Uni-axial strain-stress curve for Bézier -like hardening and softening of the materials tension behavior

The computation is carried out analogously to the one presented for compression damage evolution. Substituting the corresponding tension parameters to the Equations 4.16 to 4.33, leads to the damage parameter in tension as follows

$$d^+(r^+) = 1 - \frac{\Upsilon(\xi^+)}{r^+} \tag{4.36}$$

with ξ^+ as the strain-like counterpart for tension behavior.

4.4 Available constitutive laws

This section presents the constitutive models available for the numerical analysis carried out in this thesis in terms of possible combinations of yield criteria and damage evolution laws. Two different yield criteria have been presented for tension behavior in order to compute the tension uni-axial equivalent stress. The first theory is based on the Lubliner yield criteria presented in Equation 4.8. The second is based on the classic Rankine criterion shown in Equation 4.13. For compression behavior the only criteria available is the modified Lubliner yield of Equation 4.9 and from here on named as Petracca yield criteria.

Two different damage evolution laws have been presented in this thesis. For compression behavior an advanced Bézier based damage evolution law has been presented in Equation 4.24. For tension behavior an exponential softening (Equation 4.34), which is typical for brittle materials such as masonry, has been chosen. This thesis considers also the formulations made for the Bézier based damage evolution law also for the tension damage behavior (Equation 4.36). Table 4.2 displays all the possible combinations included in the work of this thesis. Additionally an overview of all the required parameters is listed in Table 4.3.

4.5 Constitutive tensor

The constitutive tensor contains information about the actual state of the analysis (loading/unloading) and whether there has already occurred damage or not. The most important indicator therefore is the damage criteria Φ presented in Equation 4.15. If the damage criteria is positive or equal to 0, the constitutive tensor is

Table 4.2: Overview of the available constitutive law combinations of this thesis

	Tension				Compression	
	Yield		Damage		Yield	Damage
	Rankine	Lubliner	Expo	Bézier	Petracca	Bézier
TRECPB	✓		✓		✓	✓
TLECPB		✓	✓		✓	✓
TRBCPB	✓			✓	✓	✓
TLBCPB		✓		✓	✓	✓

Table 4.3: Required parameters for the model's integrity

	Tension									
	f_0^+	f_p^+	f_r^+	ϵ_p^+	G^+	c_1^+	c_2^+	c_3^+		
TRECPB / TLECPB		✓			✓					
TRBCPB / TLBCPB	✓	✓	✓	✓	✓	✓	✓	✓		
	Compression									
	f_0^-	f_p^-	f_r^-	f_{bi}^-	ϵ_p^-	G^-	κ_1	c_1^-	c_2^-	c_3^-
TRECPB / TLECPB / TRBCPB / TLBCPB	✓	✓	✓	✓	✓	✓	✓	✓	✓	✓

the tangent stiffness tensor. Otherwise, no proceeding damage is occurring during the analysis and the constitutive tensor is equal to the secant stiffness tensor. The following sections describe the implementation of the constitutive tensors to the above presented constitutive models.

4.5.1 Secant stiffness tensor

The constitutive law from Equation 4.2 can be rewritten in terms of the secant stiffness tensor $\boldsymbol{C}_s$ as follows

$$\boldsymbol{\sigma} = \underbrace{(\boldsymbol{I} - \boldsymbol{D}) : \boldsymbol{C}}_{\boldsymbol{C}_s} : \epsilon \tag{4.37}$$

where $\boldsymbol{D}$ is a fourth order tensor that contains the projection matrices $\boldsymbol{P}^{\pm}$ and the damage variables $d^{\pm}$ as follows (Pelà et al. (2011))

$$\boldsymbol{D} = d^{+}\boldsymbol{P}^{+} + d^{-}\boldsymbol{P}^{-} \tag{4.38}$$

4.5.2 Algorithmic tangent stiffness tensor

This thesis applies an algorithmic procedure of perturbations introduced by Martinez et al. (2011) in order to compute the tangent stiffness tensor $\boldsymbol{C}_t$. This method complies for isotropic and orthotropic material laws so that the tangent stiffness matrix can be written in matrix form with the following components

$$\boldsymbol{C}_t = \begin{bmatrix} c_{t,11} & \dots & c_{t,1n} \\ \vdots & \ddots & \vdots \\ c_{t,n1} & \dots & c_{t,nn} \end{bmatrix} \tag{4.39}$$

Where n is the rank of the matrix, e.g for 2D Voigt notation: $n = 3$. The computation of the entries is column based so that in total n calculations must be performed to obtain the entire tangent stiffness matrix. The column vectors $\boldsymbol{c}_{t,j}$, with $j = 1, \dots, n$ of $\boldsymbol{C}_t$ can then be calculated as follows:

$$\boldsymbol{c}_{t,j} = \frac{\delta_j \boldsymbol{\sigma}}{\chi_{pert}} \tag{4.40}$$

Where χ_{pert} is the perturbation factor, a small value (here $\chi_{pert} = 10^{-8}$) that is used to compute the perturbation strain vector $\boldsymbol{\epsilon}_{pert,j}$ by adding χ_{pert} to the j-th entry of $\boldsymbol{\epsilon}$. The perturbation strain $\boldsymbol{\epsilon}_{pert,j}$ can then be applied to the constitutive law, and the resulting stress vector is the perturbation stress vector $\boldsymbol{\sigma}_{pert,j}$ (following the procedure starting from Equation 4.1). $\delta_j \boldsymbol{\sigma}$ then defines the increment between the stress vector $\boldsymbol{\sigma}$ and $\boldsymbol{\sigma}_{pert,j}$ and is computed as follows

$$\delta_j \boldsymbol{\sigma} = \boldsymbol{\sigma}_{pert,j} - \boldsymbol{\sigma} \tag{4.41}$$

Where $\boldsymbol{\sigma}$ is the previously computed stress tensor by applying the constitutive model.

4.6 Numerical implementation

The constitutive model presented in the previous sections is implemented as a constitutive law available in the open source framework of KRATOS MULTIPHYSICS Dadvand et al. (2010). KRATOS is a multi-disciplinary simulation software that has been developed at the *CIMNE - International Centre for Numerical Methods in Engineering*. The coding language for the object oriented implementation of the constitutive law is C++. The constitutive model is strain driven, thus the model's input is the strain vector coming from the FE analysis results obtained at the KRATOS core stage. The outputs of the constitutive model are then returning the stress vector and the constitutive matrix. Both entities enable a further step computation at the FE analysis level. Algorithm 4.1 shows the numerical implementation of the constitutive law for the 2D plane stress condition and Voigt's notation.

Algorithm 4.1 Implementation of the presented constitutive law

input: *constitutive law parameters*
output: Cauchy stress tensor $\boldsymbol{\sigma}$, *constitutive matrix*

START

step $n = 0$
Initialize damage thresholds and damage variables, $r^{\pm}_{n+1} = r^{\pm}_{0}$ and $d^{\pm}_{n+1} = 0$
for $n \rightarrow n+1$ **do**
    Nonlinear FE iteration at Gauss point level starts
    Call strain vector $\boldsymbol{\epsilon}_{n+1}$ from the FE analysis level
    Compute effective stress vector $\bar{\boldsymbol{\sigma}}_{n+1}$ ▷ Eq.(4.1)
    Decompose effective stress vector to $\bar{\boldsymbol{\sigma}}^{+}_{n+1}$ and $\bar{\boldsymbol{\sigma}}^{-}_{n+1}$ ▷ Eq. (4.3),(4.4)
    Calculate equivalent stresses τ^{+}_{n+1} and τ^{-}_{n+1} ▷ Eq. (4.8),(4.9)
    Compute damage criteria Φ^{+} and Φ^{-} ▷ Eq. (4.15)
    if $\Phi^{\pm} > 0$ **then**
        Update thresholds $r^{\pm}_{n+1}$ and variables $d^{\pm}_{n+1}$ ▷ Eq. (4.14), (4.24), (4.34), (4.36)
    else
        $r^{\pm}_{n+1} = r^{\pm}_{n}$ and $d^{\pm}_{n+1} = d^{\pm}_{n}$
    Compute Cauchy stress vector $\boldsymbol{\sigma}_{n+1}$ ▷ Eq. (4.2)
    if Nonlinear FE iteration at Gauss point level has converged **then**
        Proceed with algorithm step 19
    else
        Reform the system and go back to algorithm step 5
    Pass results to FE analysis level
    if $\Phi^{\pm} > 0$ **then**
        Calculate tangent constitutive matrix $\boldsymbol{C}_t$ via perturbation ▷ Eq.(4.40)
        pass $\boldsymbol{\sigma}_{n+1}$, $\boldsymbol{C}_t$
    else
        Calculate secant constitutive matrix $\boldsymbol{C}_s$ ▷ Eq. (4.37)
        pass $\boldsymbol{\sigma}_{n+1}$, $\boldsymbol{C}_s$

END

4.7 Application examples

4.7.1 Cyclic loading analysis of a single element model

This section presents an example applying the above described constitutive model. The numerical model for this analysis is a 2D triangle element with a single Gauss point. The two base nodes of the triangle are fixed in all directions and a dis-

placement is applied to the top node of the triangle. Two cases are considered: a) stretching (pure tension state) and b) compressing (pure compression state) the triangle. This example applies for tension an exponential softening damage evolution and the Lubliner yield criteria and in compression the Petracca yield criteria with Bézier like hardening and softening. In both cases, the displacement is performed by alternating between increasing displacements (loading) and decreasing displacements (unloading) in order to show the functionality of the law under cyclic loading. Figure 4.5 depicts the boundary force - top displacement curves of both the cases.

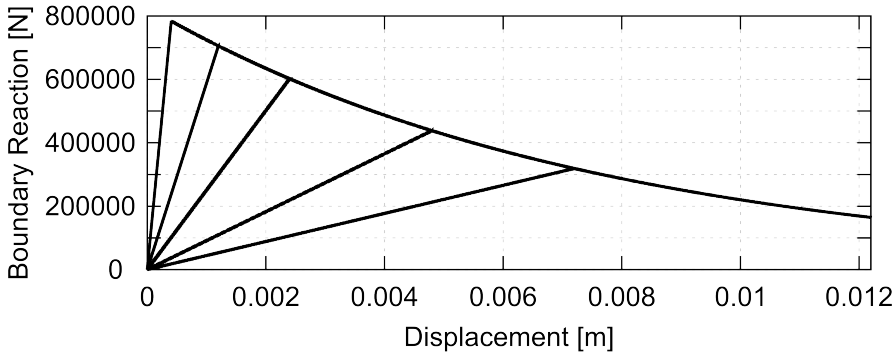

(a) Tension test

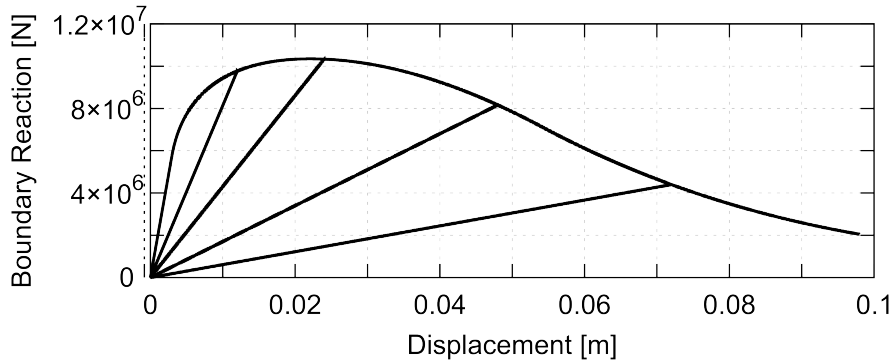

(b) Compression test

Figure 4.5: Force displacement results of numerical analyses of a single triangle element following the constitutive model described in Chapter 4 for two different deformations: (a) pure tension and (b) pure compression

4.7.2 Diagonal compression test of Flemish bond masonry wall

This section presents the application of the above described constitutive damage model to a Flemish bond masonry wall. A summary is presented of experimental tests performed at the Laboratory of Technology of Structures and Building Materials (LATEM) of the Technical University of Catalonia (UPC - BarcelonaTech), with emphasis on the diagonal compression tests. The description of the numerical micro model, the constitutive law parameters and the numerical analysis results are also presented.

This example follows two main objectives. First, the demonstration of the ability of the damage model to represent the experimental results of a diagonal compression test. Second, to show the calibration of the numerical model further utilized in this thesis, especially in the application example of Chapter 6.

4.7.2.1 Experimental program

The experimental program summarized in this thesis has been performed by Larisa Garcia-Ramonda and Jorge Segura Domingo (Garcia Ramonda (2020) and Segura Domingo (2020)). The author advises to read the presentation of the entire experimental campaign made in Garcia-Ramonda et al. (2020) and Segura et al. (2021) for further information, since a brief presentation is presented here.

Materials The masonry walls were built with handmade solid clay bricks and a low mechanical performance lime mortar. The dimensions of the bricks were $311 \times 145 \times 40\ mm^3$. The mortar utilized to bind the masonry bricks was based on a commercial premixed hydraulic lime mortar. In order to reduce its strength, the mortar was modified with limestone filler additions as explained in Segura et al. (2020).

Masonry wall The masonry wall built up in the laboratory had the nominal dimensions $1270 \times 1270 \times 311\ mm^3$ and consisted of two leafs. It was constructed in Flemish bond with 21 courses and a mortar thickness of 15 mm.

Testing setup and procedure Figure 4.6 shows the setup of the diagonal compression test performed in the laboratory. The wall was constructed on a metallic

bench and two robust steel braces were installed at two diagonally opposite corners of the wall. Both braces were connected by two Dywidag bars on each side. In order to introduce the diagonal load to the wall, two hydraulic jacks pulled these bars. Two orthogonal LVDTs were installed on each side of the wall. One was measuring the deformations in the diagonal loading direction (compression), i.e. in same direction as the bars, and the other the perpendicular one (tension).

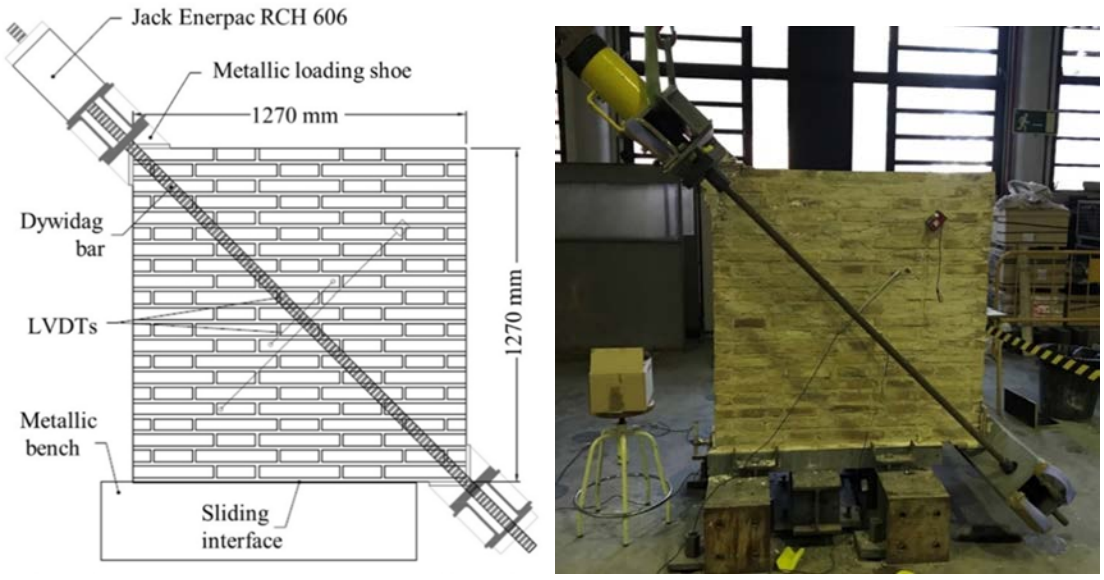

(a) (b)

Figure 4.6: Setup of the diagonal compression test as reported in Garcia-Ramonda et al. (2020) and Segura et al. (2021)

Results During the experimental analyses performed in the laboratory five unreinforced masonry walls (URM) were constructed. Each wall was loaded until failure. The deformations were measured in the LVDTs installed on each wall, and the applied force was measured at the jacks. Figure 4.7 shows the failure crack patterns of the walls after the experiments. Each case shows perfectly developed shear cracks by presenting cracking in the mortar joints and the bricks, respectively.

4.7.2.2 Numerical micro model analysis

This section reports the results of the numerical analysis of the diagonal compression test applied to a micro modeled masonry wall. Both materials, mortar and bricks, are modeled separately, each one following the continuum damage model introduced

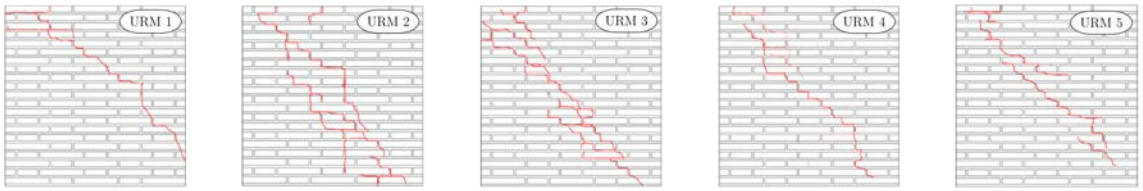

Figure 4.7: Crack patterns of the unreinforced masonry walls after having performed the diagonal compression experiments (Garcia-Ramonda et al. (2020) and Segura et al. (2021))

in this Chapter. For both the bricks and the mortar, an exponential softening behavior in tension and a Bézier-like hardening softening in compression are considered. Both the materials underlie the modified Lubliner (Petracca) damage surface model. Table 4.4 shows the material parameters applied in this numerical analysis. For both the materials the Bézier controllers are defined as follows: $c_1^- = 0.65$, $c_2^- = 0.5$ and ,$c_3^- = 1.5$.

Table 4.4: Material properties, brick unit and mortar joint, for the numerical analysis of the shear compression test applied to a Flemish bond masonry wall (Garcia-Ramonda et al. (2020) and Segura et al. (2021))

Brick unit

E	ν	f_p^+	G^+	f_0^-	f_p^-	f_r^-	ϵ_p^-	G^-	k_b	κ
7000.0	0.2	1.5	0.048	2.0	6.0	2.0	0.01	3.6	1.2	0.16
$[MPa]$	–	$[MPa]$	$[\frac{N}{mm}]$	$[MPa]$	$[MPa]$	$[MPa]$	–	$[\frac{N}{mm}]$	–	–

Mortar joint

E	ν	f_p^+	G^+	f_0^-	f_p^-	f_r^-	ϵ_p^-	G^-	k_b	κ
1800.0	0.2	0.15	0.020	2.0	6.0	2.0	0.01	3.6	1.2	0.16
$[MPa]$	–	$[MPa]$	$[\frac{N}{mm}]$	$[MPa]$	$[MPa]$	$[MPa]$	–	$[\frac{N}{mm}]$	–	–

The numerical simulation of the diagonal compression test was applied by monotonically increasing the diagonal displacements of the steel braces. Figure 4.8 depicts the force-displacement curves of the numerical and the experimental results. The numerical model was calibrated in order to be able to represent the experimental curves of the two walls with higher capacities (URM 1 and URM 4). The curves of Figure 4.8 show that these requirements of the numerical model could be fulfilled

with a very good agreement.

A short discussion about the results obtained during the non linear numerical analysis of the micro modeled Flemish bond wall is made. Figure 4.9 shows contour plots of the tension damage variable d^+ at various diagonal displacement values u_d of the analysis. After a displacement of $u_d = 0.68\ mm$ tension damage starts in the mortar joints, since the mortar's tension strength is less than the one of the bricks. After having increased the diagonal displacement up to $u_d = 1.39\ mm$, the mortar damage propagates and some brick units enter into damage. At a diagonal displacement of $u_d = 2.09mm$ first connected staircase cracks passing through mortar and bricks, respectively, appear. Further raising the diagonal displacements of the braces develops wide diagonal joined cracks. The crack pattern obtained from the numerical simulation matches to the diagonal cracks that occurred in the experimental test (Figure 4.7).

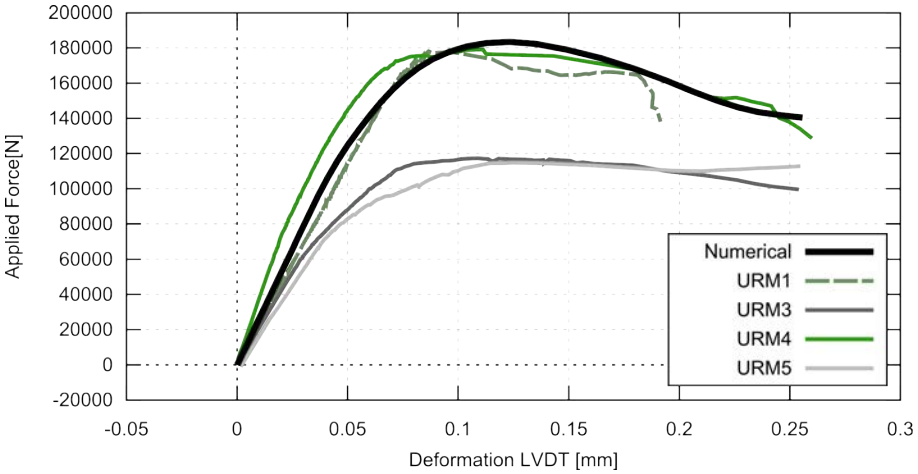

Figure 4.8: Force-displacement plots of the diagonal compression tests of unreinforced masonry walls developed by Garcia-Ramonda et al. (2020) and Segura et al. (2021), and the numerical simulation of the micro modeled wall

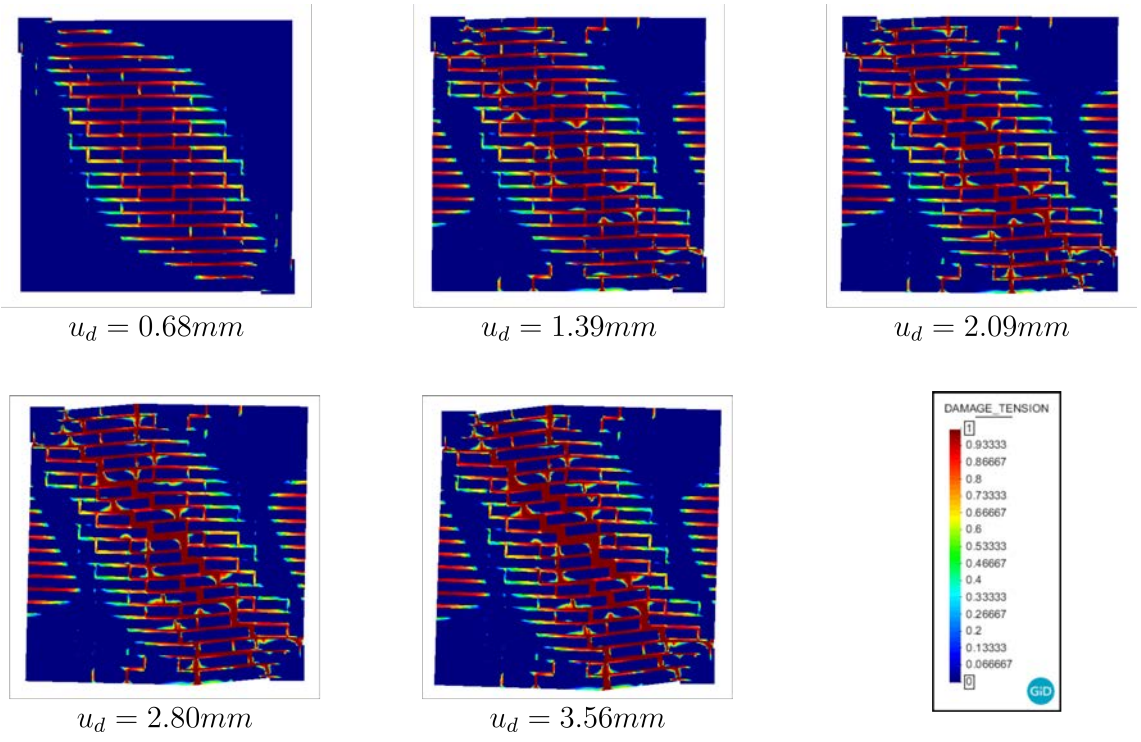

$u_d = 0.68mm$ $u_d = 1.39mm$ $u_d = 2.09mm$

$u_d = 2.80mm$ $u_d = 3.56mm$

Figure 4.9: Contour plots of the damage tension parameter and scaled total deformation of the model at different analysis stages

4.8 Summary

This chapter has presented the constitutive nonlinear damage model used in this thesis for the numerical simulation of masonry with micro and macro modeling. A strain-based constitutive model that aims to respect the brittle material behavior of masonry has been introduced. By splitting the effective stress tensor into a tension and a compression part, separate damage evolution laws can be implemented in order to differ between tension and compression damage. This strategy ensures an orthotropic material behavior that differs between tension and compression states. In order to define those damage variables, specific nonlinear functions have been introduced. An advanced damage evolution law elaborated by Petracca (2016) has been presented. The same research has also introduced a novel formulation for yield criteria that better represents the material response under shear. This model delivers highly accurate numerical results when compared with experimental results, as demonstrated in structural applications with micro and macro models of masonry by Petracca (2016). The present research has adopted the same constitutive model. An application example has shown to produce accurate results while applying the constitutive law to the numerical simulation of a diagonal shear compression test.

Micro modeling includes the complex interaction of units and joints. Cracking in masonry micro models appears first in the mortar joints, thus the total stiffness decreases, but the load can still be increased. This phenomenon produces a hardening behavior also in tension, that has been modeled by means of a uniaxial Bézier softening law. When masonry is considered as homogenized, this hardening behavior should also be considered in the nonlinear homogenized damage model prior to softening. Therefore, this chapter has presented a hardening- softening damage evolution for tension behavior applicable to brittle homogenized materials. The mathematical formulation has been adopted from the Bézier curves already applied for the compression uni-axial nonlinear damage behavior. Investigations made in a later part of this research (Chapter 6) further motivate these assumptions.

The constitutive model introduced in this chapter will also serve as the fundamental part of the machine learning homogenization technique explained in the following chapter. The model will be the substance of a variety of tests applied to micro models of masonry walls. Furthermore, the constitutive law will serve as the machine learning model in order to train the parameters of a macro model

constitutive law.

Chapter 5

Machine learning material homogenization

5.1 Introduction

Classical computational homogenization techniques, such as the first order computational homogenization presented by Petracca et al. (2016) and Petracca et al. (2017), still do not disconnect both the micro and the macro-scale at the solving stage. If applied in finite element analysis, the procedure transfers strains from a Gauss point of the macro-scale to a boundary value problem of a representative volume element (RVE) at the micro scale. Thus a boundary value problem of an entire RVE is solved in order to obtain stress results for only one Gauss point at the macro-scale. As a consequence, the microscopic behavior of the heterogeneous masonry material can be represented accurately at the macro-scale. However, the computational cost is very high, and increases further with the size of the model at macro scale.

Research made in Zaghi et al. (2018) introduces an off-line technique to avoid solving the RVE at each analysis step. The strains at the macro scales are not sent to a micro model RVE, but to a large database. The creation of this database includes the strain and stress results of previously performed analyses on the RVE. Thus the strains coming from the macro-scale can "choose" their corresponding stress state from the database by comparing the incoming strains with the ones of the database. The works made in Zaghi et al. (2018) contributed substantially to the approach, since a virtual laboratory was used to construct the database. However, the method

still implies jumping away from the macro-scale at the solving stage.

The idea of the present research is to avoid hopping around at multiple scales. The key issue is then finding a single homogeneous continuum damage model for the macro scale analysis of masonry that takes into account more realistically its anisotropic behavior due to material heterogeneity. This research focuses on utilizing a machine learning model to predict such a homogeneous continuum damage model for masonry structures.

Figure 5.1 shows the work flow of the homogenization technique. It includes the main idea of starting from data production in a virtual laboratory at the micro scale, goes further to the machine learning and finalizes in a post machine learning constitutive law applicable to macro analysis of masonry structures.

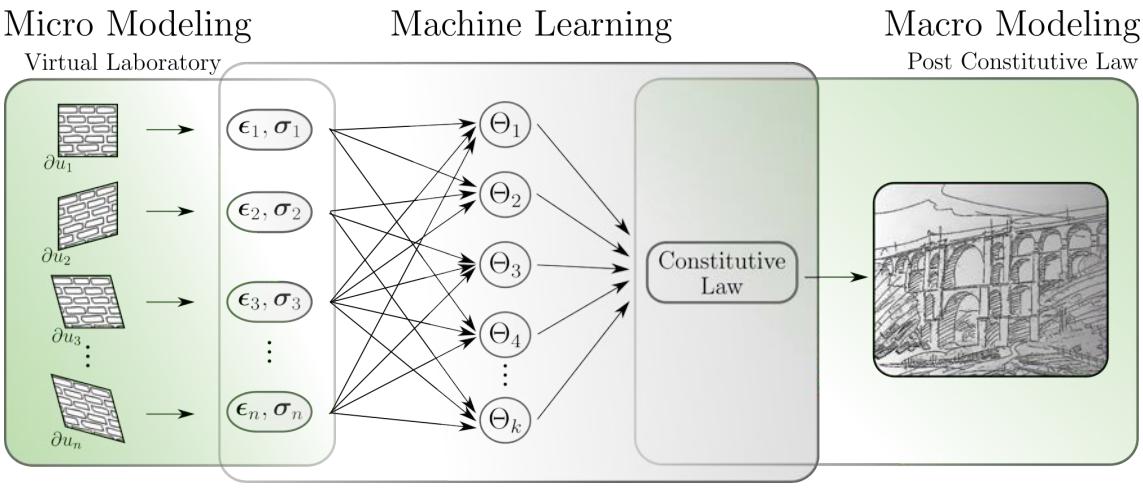

Figure 5.1: Overview of the machine learning homogenization technique, showing all included procedures at multiple scales and the machine learning technique as connector

This chapter presents all steps required for the construction of a machine learning model that is able to homogenize the masonry material. Section 5.2 introduces the machine learning model applied in this research. It serves as the connector of the analysis at the multiple scales. For this purpose, this section clarifies the integration of the constitutive model of Chapter 4 into the machine learning framework. Related tools, such as computation graphs - including the constitutive law - and training loops - essential for machine learning - are defined. This part is initially headed by giving a fundamental background of machine learning and the software as applied in this thesis.

Machine learning models learn from large amounts of data. Section 5.3 introduces a space, where relevant data can be produced: the *virtual laboratory*. Subject of this lab is a representative volume element modeled at the micro scale - a numerical model that contains clear information about the material's heterogeneity. A variety of nonlinear numerical experiments are carried out on the RVE in order to obtain a large amount of data that include the heterogeneous characteristics of the material.

Section 5.4 presents a method to isotropize the data obtained from the virtual laboratory, based on the works of Norris (2006) and Rossi et al. (2021). The presented procedure becomes necessary, since the data coming from the virtual laboratory are following an anisotropic elasticity rule, while the constitutive law integrated into the machine learning is based on the hypothesis of isotropic elasticity. In order to utilize the data for training of the isotropic model, a mapping procedure must be adopted, that allows working at both anisotropic and isotropic spaces (Oller et al. (2003), Pelà et al. (2011)).

After having isotropized the data, the machine learning model can be trained. Training results in an approximated model that is most suitable to represent the training data. Furthermore, this model can be stored and utilized in order to predict the masonry material behavior for macro scale analyses. Section 5.5 presents the so-called post machine learning constitutive law.

Section 5.6 terminates the chapter by giving a summary about the homogenization technique.

5.2 Machine learning technique

5.2.1 Fundamentals

When a certain task is extremely difficult to program, machine learning tools start to make sense. The general idea of machine learning is to collect data and utilize it to train a "black box" model how to solve a certain task by learning from them. This way of learning connects a set of inputs I_{true} and a set of outputs O_{true} by searching a function F so that

$$F(I_{true}) = O_{true} \tag{5.1}$$

This function aims to fit the inputs to the outputs. Thus a fundamental part of

a machine learning model is a mathematical formulation that is able to achieve this connection. Such a fitting can be attained by introducing adjustable parameters to the function F. This procedure of adjusting parameters in order to obtain a best possible fitting can be called optimization by learning.

Broadly spoken there exist two types of learning methods: *supervised* and *unsupervised learning*. It depends on the kind of data that are at disposal. While *supervised learning* considers coupled pairs of inputs and outputs, *unsupervised learning* only has access to some outputs of the input examples. In that case underlying patterns of the input data are analyzed. However, this research implies having coupled pairs of inputs and outputs that train the model by *supervised learning*.

The goal of supervised learning is to adjust the models parameters $\boldsymbol{\Theta}$ so that the given inputs I_{true} fit to the given outputs O_{true} as accurately as possible. The given outputs O_{true} are compared with predicted outputs O_{pred} in a loss function $\mathcal{L}(\boldsymbol{\Theta})$. If the loss function does not fulfill a predefined loss minimum, an adjustment of the model's parameters $\boldsymbol{\Theta}$ is carried out in order to approximate the outputs O_{pred} of the model to the given outputs O_{true}. The most popular algorithms to perform such optimization are gradient descent operators Ruder (2016).

5.2.1.1 Gradient descent operators

Gradient descent operations update the models parameters $\boldsymbol{\Theta}$ in the opposite direction of the gradient of the loss function $\nabla_{\boldsymbol{\Theta}}\mathcal{L}(\boldsymbol{\Theta})$ w.r.t. the parameters $\boldsymbol{\Theta}$, in order to minimize the loss function. A learning rate η defines the velocity the optimization heads towards the minimum. A classical gradient descent operation can be defined as follows:

$$\boldsymbol{\Theta}_n = \boldsymbol{\Theta}_{n-1} - \eta \cdot \nabla_{\boldsymbol{\Theta}}\mathcal{L}(\boldsymbol{\Theta}_{n-1}, I_{true}, O_{true}) \tag{5.2}$$

Where $\boldsymbol{\Theta}_n$ is the vector of the optimized variables at step n and $\boldsymbol{\Theta}_{n-1}$ at the previous step $n-1$. $\nabla_{\boldsymbol{\Theta}}\mathcal{L}(\boldsymbol{\Theta})$ is the gradient of the loss function w.r.t. the parameters. The gradient descent operator in Equation 5.2 considers a constant learning rate η for all the model's variables. As a consequence, the parameters are optimized to the same extent. However, some variables require smaller or larger learning rates than other parameters. Thus the procedure of Equation 5.2 may lead to problems while

optimizing a machine learning model with a large number of trainable variables.

Let a short example clarify the problem. Two parameters of a constitutive model are considered: f_p^-, the peak compression strength and f_p^+, the peak tension strength. If a brittle material is assumed, e.g. concrete or mortar, the ratio between f_p^- and f_p^+ approximately counts around 10.0. If both parameters are variables of an optimization procedure with a constant learning rate η, the smaller value, in this case f_p^+ would be modified faster than the larger value. This may lead to divergence problems during optimization and should be avoided.

As a consequence, proper and easily applicable gradient descent operations that enable adaptive and parameter individual learning rates must be considered for the present research and are summarized in Ruder (2016).

Adagrad optimizer A standard adaptive gradient descent optimizer is the Adagrad optimizer Ruder (2016). It optimizes while adapting learning rates for each specific parameter Θ_i of all parameters $\boldsymbol{\Theta}$. In a first step the gradient per i-th parameter must be considered as follows

$$g_{n,i} = \nabla_{\boldsymbol{\Theta}} \mathcal{L}(\Theta_i, I_{true}, O_{true}) \tag{5.3}$$

After having substituted the gradient into Equation 5.2 the update rule of the Adagrad optimizer does then modify the learning rate and the optimization as follows

$$\boldsymbol{\Theta}_n = \boldsymbol{\Theta}_{n-1} - \eta (G_{n,ii})^{-0.5} \cdot g_{n,i} \tag{5.4}$$

$G_{n,ii}$ is a diagonal matrix containing the sum of the squares of all the previous gradients $g_{n,i}$, Duchi et al. (2011). As a result, larger updates of the learning rate for more frequent appearing parameters and smaller updates for less frequent appearing parameters can be achieved. However, Adagrad optimizer decreases the learning rates monotonically, thus further improvements are required.

Adam optimizer A strong achievement to gradient descent optimization has been made by Kingma and Ba (2015). The introduction of the Adam (Adaptive Momen-

tum Estimator) optimizer enables to consider an exponentially decaying average of past linear and squared gradients $m_{n,i}$ and $v_{n,i}$. Equation 5.2 can then be adjusted as follows

$$\Theta_{n,i} = \Theta_{n-1,i} - \eta \cdot \frac{m_{n,i}}{\sqrt{v_{n,i}} + \chi_{adap}} \cdot \omega_t \tag{5.5}$$

$$m_{n,i} = \beta_1 m_{t-1,i} + (1 - \beta_1) g_{t,i} \tag{5.6}$$

$$v_{n,i} = \beta_2 v_{t-1,i} + (1 - \beta_2) g_{t,i}^2 \tag{5.7}$$

$$\omega_t = \frac{\sqrt{1 - \beta_2^t}}{1 - \beta_1^t} \tag{5.8}$$

With $\beta_1, \beta_2 \in [0, 1)$ as parameters to control the decay rate. A smoothing term χ_{adap} (usually a value around $1.0e-08$) ensures that the denominator cannot switch to zero.

The work done in this research applies the *Adam Optimizer*. As shown in the following Section the machine learning model contains several parameters that require different updates while optimizing. A great benefit of the Adam Optimizer is to be able to tune the learning rates per parameter automatically. Recommendations made in Ruder (2016) characterize it as the best overall choice. Due to the bias correction factor ω_t it performs better than other adaptive optimizers.

5.2.1.2 Batch sizing for training

Each optimization procedure requires to be fed by the inputs and outputs. The previously described procedure considers feeding the entire set of inputs I_{true} and outputs O_{true} to the gradient of the loss function as a batch. Thus the gradients are computed for all the values encountered in I_{true} and O_{true} before the parameters can be optimized. For large sets of training data this leads to an expensive computational process before the proper optimization takes place. This drawback can be avoided by breaking down the training data set into mini-batches as shown in the following

$$I_{true} = \left(I_{true}^{1:m}, I_{true}^{m+1:2m}, \dots, I_{true}^{(n-1)m:n} \right) \tag{5.9}$$

$$O_{true} = \left(O_{true}^{1:m}, O_{true}^{m+1:2m}, \dots, O_{true}^{(n-1)m:n} \right) \tag{5.10}$$

Where m is the number of sets per mini-batch. Feeding the mini-batch to the model decreases the computational effort of computing the gradients and optimizes the variables faster. In the present work mini-batches are applied to the machine learning model.

5.2.1.3 Loss function

Loss functions are used to count machine learning prediction errors. The error is a scalar value that indicates which stage the optimization process has reached: *Is the model already accurate enough or is there still a long way to go?* A classical computation of the loss function is the $\mathcal{L}_2$ loss function that computes a mean square error as follows

$$\mathcal{L}_2 = \frac{1}{n} \sum_{i=1}^{n} \left(O_{true} - O_{pred} \right)^2 \tag{5.11}$$

The entire loss function applied to the gradient descent optimization can then be written as follows

$$\mathcal{L}(\boldsymbol{\Theta}) = \frac{1}{m} \sum_{j=1}^{m} \frac{1}{n} \sum_{i=1}^{n} \left(O_{true} - O_{pred}(\boldsymbol{\Theta}, I_{true}) \right)^2 \tag{5.12}$$

Where m is the batch size of the inputs and outputs and n is the length of the vectors O_{true} and O_{pred}.

5.2.2 TensorFlow

For the numerical implementation of the here subjected machine learning model, the open source framework *TensorFlow* started by the Google Brain project is utilized (Abadi et al. (2015)). TensorFlow performs an optimization by constructing a graph

of mathematically connected nodes and running a session over the graph for multiple times until a certain criterion is reached. A basic graph for optimization problems consists of the following entities: *tensors*, *variables*, *operations* and *placeholders* (for TensorFlow 1 versions).

Tensors are multi-dimensional arrays containing integer, float or double types, complex numbers but also string elements. *Variables* are the parameters of the model that are modified during a graph session in order to obtain a trained machine learning model. In other words, they are trained after each session executed. *Operations* connect the nodes of an entire graph by defining abstract computations between them. Such computations are already implemented to the environment of TensorFlow, e.g. the operation add tensor of node 1 to tensor of node 2 and give the result to node 3. However, even more complex actions (e.g. matrix multiplication, gradient computation, optimizer construction) can directly be called. *Placeholders* are empty TensorFlow tensors that are essential for the graph. They define which data flows through. During a session the placeholders are fed with training input data in order to optimize the model.

Performing an optimization with TensorFlow consists of two substantial parts: the *graph construction* and running the graph in a *graph session*. In the step of constructing the computation graph the above described entities are connected. The connections are made according to the mathematical model one aims to optimize. This includes defining the tensors, the variables, the placeholders and the mathematical operations.

The second step is running the graph in order to perform the optimization. For this purpose, the inputs of the machine learning model are fed to the placeholders. These inputs do then run through the graph and define all the nodes numerically until the output of the graph is produced. If the aim of the TensorFlow model is optimization, the graph must be run multiple times in order to be able to modify the model's variables at the end of each graph running step.

Supported frontend languages to build machine learning models with TensorFlow are python or C++. They enable a user friendly construction of the machine learning models. In this research a python based application programming interface (API) is utilized.

In the following the described entities of Section 5.2.1 and Section 5.2.2 are mapped to the present problem in order to define the constitutive law machine

learning model. The computation graph for the machine learning homogenization technique implemented to TensorFlow is discussed and the examination of the graph session is described.

5.2.3 The constitutive law machine learning model

This Section presents the construction of the specific machine learning model as utilized in this thesis. In order to apply the machine learning approach the fundamentals explained in Section 5.2.1 must be mapped to the present scientific issue. Thus the fundamental questions are: Which are the coupled input and output items and which mathematical formulation connects them?

The function $F(I_{true})$ This research aims to find a correlation between strains and stresses for a homogenized material. For any material, constitutive laws can define such a correlation. Thus the here considered mathematical formulation for the machine learning model is derived from a constitutive law and is defined as function $\Psi(I_{true})$.

The input I_{true} **and output** O_{true} The constitutive law function Ψ considered in this thesis is based on strain equivalence. Thus the input I_{true} of the function Ψ is a set of strain states $\boldsymbol{\epsilon}_{true}$. In order to perform the supervised learning, the model requires the reference true output stresses $\boldsymbol{\sigma}_{true}$ as the output O_{true}.

The parameters $\boldsymbol{\Theta}$ In order to obtain the predicted output of the machine learning model, the strains $\boldsymbol{\epsilon}_{true}$ run through the model and are adjusted by the constitutive law material parameters in order to compute the predicted output.

The predicted output O_{pred} The predicted output O_{pred} of the machine learning model is the predicted stress $\boldsymbol{\sigma}_{pred}$ computed by the constitutive law function Ψ.

After having introduced the machine learning model's participating entities the general mathematical formulation of the optimization process can be stated as follows

$$\Psi\left(\boldsymbol{\epsilon}_{true}, \boldsymbol{\Theta}\right) \approx \boldsymbol{\sigma}_{true} \tag{5.13}$$

The model searches a modification of the parameters $\boldsymbol{\Theta}$ of the constitutive model Ψ, so that by inputting strain states $\boldsymbol{\epsilon}_{true}$ an accurate approximation to the reference stresses $\boldsymbol{\sigma}_{true}$ can be achieved. A predefined learning criterion checks the error value of the actual optimization state. If the error value is less or equal to the learning criterion, the optimization finishes and stores the actual modification of the parameters $\boldsymbol{\Theta}$ as the optimized model parameters $\boldsymbol{\Theta}^{\star}$. Then the model can be utilized to predict stresses $\tilde{\boldsymbol{\sigma}}_{pred}$ by entering any strain state $\tilde{\boldsymbol{\epsilon}}$. It follows

$$\Psi\left(\tilde{\boldsymbol{\epsilon}}, \boldsymbol{\Theta}^{\star}\right) = \tilde{\boldsymbol{\sigma}}_{pred} \tag{5.14}$$

5.2.3.1 Computation graph

Figure 5.2 shows the computation graph for the machine learning homogenization technique. It depicts an universal graph construction that can be utilized for any machine learning technique that aims to fit a strain driven constitutive law.

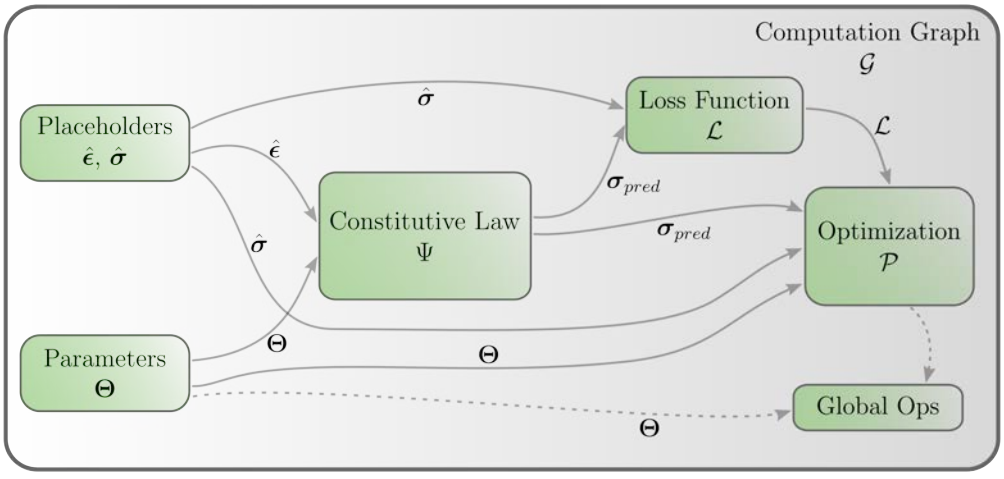

Figure 5.2: Overview of the computation graph $\mathcal{G}$ implemented to *TensorFlow* for the machine learning material homogenization technique

The starting node of the computation graph is the definition of the parameters

$\boldsymbol{\Theta}$. This node contains all the variables that are essential to define the constitutive law (e.g. compression strength, tension strength, etc.). The parameters of each constitutive law that are in the scope of this thesis are shown in Table 4.3. A specific command, able to specify if these parameters are trainable or not, can be called. All the variables are then send to the node of the constitutive law function Ψ. The variables associated as trainable are also send to the optimization procedure $\mathcal{P}$.

Another starting node is the placeholder node. It contains the empty tensors for the strains $\hat{\boldsymbol{\epsilon}}$ and the stresses $\hat{\boldsymbol{\sigma}}$. The placeholder entity $\hat{\boldsymbol{\epsilon}}$ is sent to the node of the constitutive law function as the strain input. And the placeholder $\hat{\boldsymbol{\sigma}}$ is passed to the node of the loss function $\mathcal{L}$.

The main node of the computation graph is the constitutive law function. Here the predicted stresses $\boldsymbol{\sigma}_{pred}$ are computed. The user of the machine learning homogenization technique must now define the constitutive law he wants to predict. The inputs are always the parameters $\boldsymbol{\Theta}$ of the chosen law and the placeholder $\hat{\boldsymbol{\epsilon}}$ as the input strains. Both these inputs are the dependencies for all the mathematical relations inside the constitutive law node. These mathematical operations result in the predicted stress outcome. Each of them is a function depending always on the two input entities $\boldsymbol{\Theta}$ and $\hat{\boldsymbol{\epsilon}}$ and can be described as follows

$$f_i(\boldsymbol{\Theta}, \hat{\boldsymbol{\epsilon}}) \tag{5.15}$$

Where i in this case is the i-th node inside the constitutive law node. Each node describes a function that enables the computation of the functions gradients w.r.t the parameters $\boldsymbol{\Theta}$. They are essential for the optimization procedure in node $\mathcal{P}$

$$\nabla_{\boldsymbol{\Theta}} f_i(\boldsymbol{\Theta}, \hat{\boldsymbol{\epsilon}}) \tag{5.16}$$

.

Apart from the graph's universality, namely to be applicable to any strain driven constitutive law, this thesis aims to investigate the predictability of an advanced constitutive law (Chapter 4) for the macro analysis of masonry structures. Thus the construction of this node must be specified. Figure 5.3 shows a zoom into the constitutive law function of Figure 5.2 and displays how the predicted stresses $\boldsymbol{\sigma}_{pred}$ are calculated. The function of each node shown in Figure 5.3 is sent to the

optimization node $\mathcal{P}$.

The computation shown in Figure 5.3 is capable to utilizing any of the constitutive laws summarized in Section 4.4 , since they are all implemented to the computation graph. This includes changing the yield criteria in order to compute the positive or negative equivalent stress on the one hand, but also the damage evolution law for positive or negative stresses on the other hand.

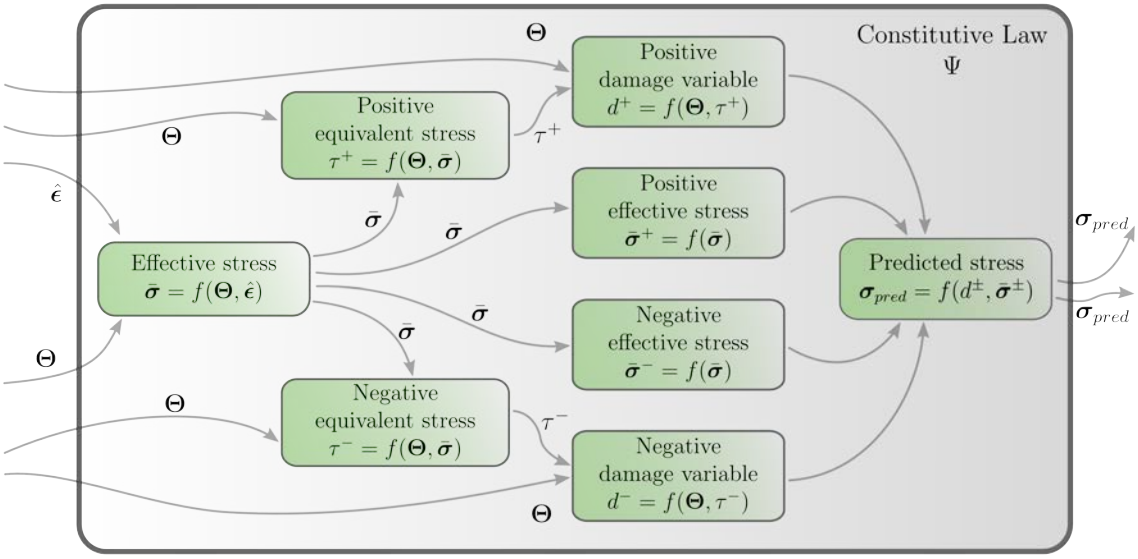

Figure 5.3: Zoom into the constitutive law implemented to the computation graph $\mathcal{G}$ of the machine learning material homogenization technique considered in this thesis. It shows the inputs and outputs of the model

The next node of the computation graph is the calculation of the loss function $\mathcal{L}$. Any loss function can be chosen. This research adopts the $\mathcal{L}_2$ loss as introduced in Equation 5.12. It can be adopted according to the present discussions as follows

$$\mathcal{L}(\boldsymbol{\Theta}) = \frac{1}{n} \sum_{i=1}^{n} \left(\hat{\boldsymbol{\sigma}} - \boldsymbol{\sigma}_{pred} \right)^2 \tag{5.17}$$

with n as the length of the stress vector in Voigt notation and i denotes the i-th component of both the vectors $\hat{\boldsymbol{\sigma}}$ and $\boldsymbol{\sigma}_{pred}$. The input to this node is the placeholder $\hat{\boldsymbol{\sigma}}$ on the one hand, and the predicted stress $\boldsymbol{\sigma}_{pred}$ from the constitutive law node on the other hand. The output is passed to the optimization node $\mathcal{P}$.

The final optimization of the machine learning problem is executed in the node $\mathcal{P}$. This includes the computation of the gradients of all the previously appearing

functions. The gradients are then passed to an optimizer. The work here utilize the Adam optimizer introduced in Equation 5.5 . Figure 5.4 shows an overview of the here adopted optimization node $\mathcal{P}$. The inputs are the entities of all the previous nodes and additionally the two scalars β_1 and β_2 (Equation 5.5) for the Adam optimizer.

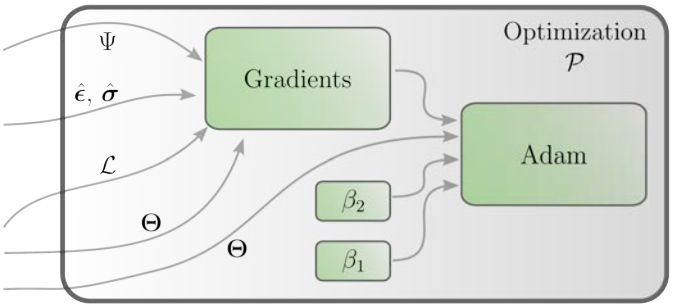

Figure 5.4: Zoom into the optimization procedure of the computation graph $\mathcal{G}$ of the the machine learning material homogenization technique considered in this thesis. It shows the computation of the gradients and the construction of the Adam optimizer

The here presented computation graph of the machine learning material homogenization procedure can be written as follows

$$\mathcal{G} = f\left(\hat{\boldsymbol{\epsilon}}, \hat{\boldsymbol{\sigma}}, \boldsymbol{\Theta}, \mathcal{L}, \mathcal{P}\right) \tag{5.18}$$

where $\mathcal{G}$ is a function that depends on the placeholders $\hat{\boldsymbol{\epsilon}}$ and $\hat{\boldsymbol{\sigma}}$, the constitutive law parameters Θ, the loss function $\mathcal{L}$ and the optimizer $\mathcal{P}$. After having carefully constructed the computation graph $\mathcal{G}$, the main part of the machine learning model can start by running $\mathcal{G}$ in a training loop.

5.2.3.2 Training loop

Machine learning models are based on multiple steps of training. As mentioned in Section 5.2.1, loss functions can only be minimized by repeatedly performing optimization procedures. Thus improvements in accuracy of the machine learning model inside the computation graph can only be achieved by running it in a repetitive operation: a training loop.

A training loop consists of a certain number of optimization steps, the so-called *epoch* steps. In each *epoch* step one iteration over the entire data set of training is executed. Consequently, the loop starts with an initial *epoch* step and ends, if a

learning criteria could be reached. An additional user defined maximum number of steps n_{epoch} can be utilized in order to stop the optimization at a certain point.

Before starting the training loop, several important steps must be carried out in order to initialize the computation graph $\mathcal{G}$ and to be able to evaluate the training accuracy during learning. The initialization of the variables or parameters $\boldsymbol{\Theta}$ can be achieved by setting them to predefined values. Then a vector of initialized parameters $\boldsymbol{\Theta}_{init}$ is introduced. It serves as the variable configuration in the first *epoch* iteration step of the loop. The evaluation of training accuracy can be achieved by splitting the entire input set of data into a set for training and a set for evaluation so that

$$\langle \bullet \rangle_{train} = \zeta \cdot \langle \bullet \rangle_{true} \tag{5.19}$$

$$\langle \bullet \rangle_{eval} = (1 - \zeta) \cdot \langle \bullet \rangle_{true} \tag{5.20}$$

where $\langle \bullet \rangle$ may either denote the input strains or the input stresses of the machine learning model. ζ is a value ranging from 0 to 1 that defines the participation of the input data set in the training procedure. Here, the data set $\langle \bullet \rangle_{train}$ is utilized for the training part in each epoch iteration and $\langle \bullet \rangle_{eval}$ is taken to evaluate the error after each iteration. It assesses the accuracy of the machine learning model online, so to say during the actual optimization by using a data set that is not touched while training.

As mentioned in Section 5.2.1.2 batch sizing facilitates the learning process since small sets decrease the number of gradients that must be computed. In this research a batch size m of a single entry is chosen. Thus training is performed by taking one strain state and its corresponding stress state from the training set per optimization. Thus a second loop inside the actual i-th *epoch* iteration unzips the training set and optimizes the variables.

Machine learning models learn better the more random the training data enter to the model. Therefore, a previous randomization of the coupled training set is performed at the beginning of each *epoch* step. This procedure is able to avoid repeatedly feeding the coupled input sets to the computation graph in the same order. This randomization can be performed without doubts regarding path dependence, since the training data of this thesis is produced by monotonically increasing the

deformations so that loading/unloading cases do not appear.

Inside the second loop - at mini batch level - the actual training starts by feeding the training inputs $\boldsymbol{\epsilon}_{train}$ and $\boldsymbol{\sigma}_{train}$ to the graph's placeholders $\hat{\boldsymbol{\epsilon}}$ and $\hat{\boldsymbol{\sigma}}$, respectively. Accessing the command

$$\mathcal{G}\left(\hat{\boldsymbol{\epsilon}} = \boldsymbol{\epsilon}_{train}, \hat{\boldsymbol{\sigma}} = \boldsymbol{\sigma}_{train}, \boldsymbol{\Theta}, \mathcal{L}, \mathcal{P}\right).\texttt{optimize} \tag{5.21}$$

leads to the start of the optimization procedure.

After having executed the optimization step, a learning rate ω_{learn} is calculated. It is the absolute value of the difference between the loss error computed with the optimized variables of the actual *epoch* step and the loss error computed with the previous variable configuration. If ω_{learn} is less than a initially defined learning criteria ω_{crit} the optimization ends. Else the optimization continues with a further *epoch* iteration. Figure 5.5 shows a flowchart of the here applied training loop.

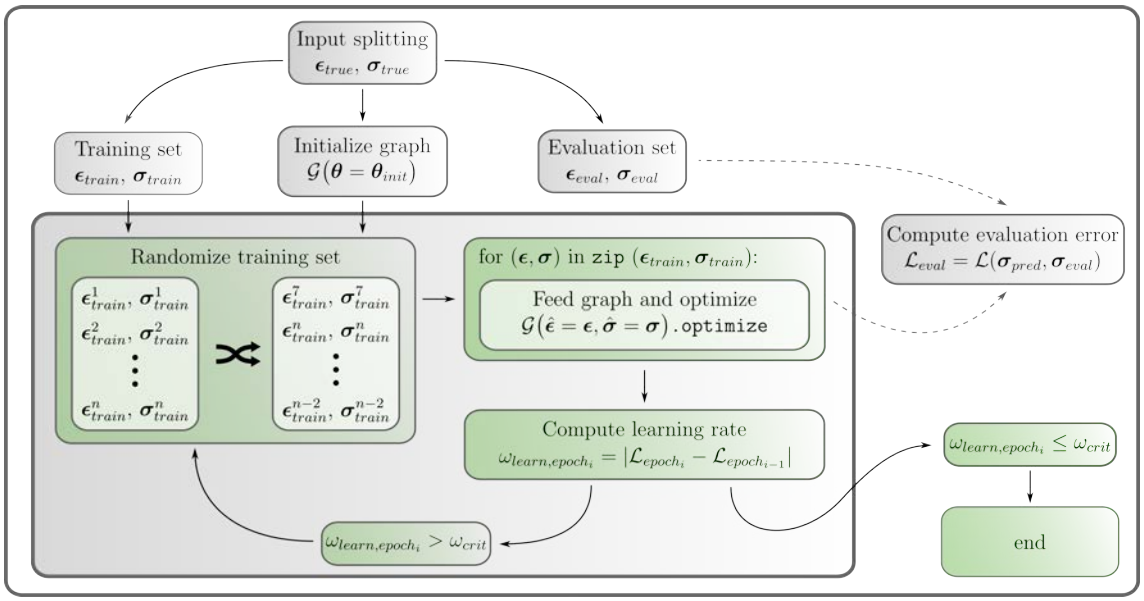

Figure 5.5: Flowchart of the training loop of the computation graph for the machine learning homogenization technique

5.2.3.3 Numerical implementation

Algorithm 5.2 presents the numerical implementation of the optimization procedure of the machine learning homogenization technique. It includes the construction of the computation graph and the loop over the graph session execution.

Algorithm 5.2 Find $\boldsymbol{\Theta}^{\star}$ so that $\boldsymbol{\Psi}\left(\boldsymbol{\epsilon}_{true}, \boldsymbol{\Theta}^{\star}\right) \approx \boldsymbol{\sigma}_{true}$

input: $\boldsymbol{\epsilon}_{true}$, $\boldsymbol{\sigma}_{true}$, $\boldsymbol{\Theta}_{init}$, η, $\mathtt{n}_{epoch}$, ω_{crit}
output: $\boldsymbol{\Theta}^{\star}$

CONSTRUCT COMPUTATION GRAPH $\mathcal{G}$

Build placeholders $\hat{\boldsymbol{\epsilon}}$, $\hat{\boldsymbol{\sigma}}$
Build variable list $\boldsymbol{\Theta}$
Compute the effective stress vector $\bar{\boldsymbol{\sigma}} = f(\boldsymbol{\Theta}, \hat{\boldsymbol{\epsilon}})$ ▷ Eq. (4.1)
Decompose effective stress vector to $\bar{\boldsymbol{\sigma}}^{\pm} = f(\bar{\boldsymbol{\sigma}})$ ▷ Eqs. (4.3)and (4.4)
Compute equivalent stresses $\tau^{\pm} = f(\boldsymbol{\Theta}, \bar{\boldsymbol{\sigma}}^{\pm})$ ▷ Eqs. (4.8) and (4.9)
Calculate the damage thresholds $r^{\pm} = f(\boldsymbol{\Theta}, \tau^{\pm})$ ▷ Eq. (4.14)
Compute the damage variables $d^{\pm} = f(\boldsymbol{\Theta}, r^{\pm})$ ▷ Eqs. (4.24), (4.34), (4.36)
Compute the predicted stress $\boldsymbol{\sigma}_{pred} = f(\bar{\boldsymbol{\sigma}}, d^{\pm})$ ▷ Eq. (4.2)
Define the error loss $\mathcal{L} = f(\hat{\boldsymbol{\sigma}}, \boldsymbol{\sigma}_{pred})$ ▷ Eq. (5.17)
Build the optimizer $\mathcal{P} = f(\mathcal{L}, \eta, \nabla f(\bullet))$
Store the graph $\mathcal{G} = f(\hat{\boldsymbol{\epsilon}}, \hat{\boldsymbol{\sigma}}, \boldsymbol{\Theta}, \mathcal{L}, \mathcal{P})$

PREPARE THE TRAINING LOOP

Extract training set $(\boldsymbol{\epsilon}_{train}, \boldsymbol{\sigma}_{train})$ from $(\boldsymbol{\epsilon}_{true}, \boldsymbol{\sigma}_{true})$
Initialize the graph $\mathcal{G}(\mathcal{P}, \hat{\boldsymbol{\epsilon}}, \hat{\boldsymbol{\sigma}}, \boldsymbol{\Theta} = \boldsymbol{\Theta}_{init})$

RUN GRAPH IN TRAINING LOOP

$epoch_i = 1$
for $epoch_i < \mathtt{n}_{epoch}$ **do**
    Randomize order of training set $(\boldsymbol{\epsilon}_{train}, \boldsymbol{\sigma}_{train})$, but keep couples
    for $(\boldsymbol{\epsilon}, \boldsymbol{\sigma})$ **in** `zip` $(\boldsymbol{\epsilon}_{train}, \boldsymbol{\sigma}_{train})$ **do**
        $\mathcal{G}(\hat{\boldsymbol{\epsilon}} = \boldsymbol{\epsilon}, \hat{\boldsymbol{\sigma}} = \boldsymbol{\sigma}, \boldsymbol{\Theta}, \mathcal{L}, \mathcal{P})$`.optimize`
    Compute the learning rate ω_{learn}
    if $\omega_{learn} < \omega_{crit}$ **then**
        end
    else
        $epoch_i \rightarrow epoch_i + 1$

5.3 Virtual laboratory

This research presents a technique that targets the homogenization of a heterogeneous material. Thus the material's heterogeneity must be represented in a carefully constructed micro-model. Such a model takes into account the constitutive behaviors of the material's components. It is called a representative volume element (RVE). RVEs can be exposed to different boundary conditions producing different

strain states, in order to analyze the anisotropic material's behavior. Catching this behavior is essential for any homogenization technique.

The here investigated technique necessitates a space where boundary conditions can be applied to a properly micro-modeled RVE in order to determinate its behavior. This space is called virtual laboratory (VL). Laboratories exist in order to perform physical experiments on real structures and to analyze the structure's material behavior. Applying the amount of experiments necessary to obtain enough training data for the machine learning model, would be detrimental for a real laboratory from both the economical and technical points of view. However, performing the experiments numerically in a virtual space would enable a reasonable data production for the machine learning model.

The accuracy of the machine learning homogenization technique is based on several operational needs. Two of them can be influenced by the virtual laboratory: a) a large amount of data, and b) a broad data representation. Need a) is crucial for any machine learning model: the more input data in learning, the bigger is the scope of representative data that was considered during training. Thus, the prediction is also more representative. Need b) is crucial for the homogenization technique: the data should represent the nonlinear behavior of the RVE in order to be able to respect it in the homogenization technique. Also the heterogeneous and anisotropic behavior of the RVE must be respected. Both requirements can be achieved by performing the virtual experiment up to failure and at the same time by carrying out a large amount of experiments on the same RVE, each of them taking into account the application of different boundary conditions. Then, each analysis of the RVE material runs through its entire nonlinear response and result data can be stored including all this information.

This section explains the fundamental idea of the virtual laboratory. Its main parts are the construction of the RVE, the application of multiple varying boundary conditions producing different deformation states, and the solution of each of the multiple boundary value problems. The procedure is explained by showing examples of 2D RVE models of masonry. However, it can be applied similar to the analysis of 3D models.

5.3.1 Representative volume element

As firstly described by Hill (1963) in the field of continuum mechanics, a RVE is a sample of a heterogeneous material that is, on average, structurally typical of the whole material. Thus one can find an RVE of the composite material that can represent the material constitutive response of a comparable model at a macroscopic homogeneous scale by only neglecting an insignificant small difference in the RVE surface deformation and traction.

The subject of the here presented virtual laboratory is a micro model of a masonry wall. In order to be able to utilize this micro model as an RVE, it must comply with the definition above. Hence, the micro model must a) be able to represent both the homogeneous components of the masonry and b) consider the geometrical allocation of the components to each other - known as the masonry bond. Thus, a carefully designed geometrical model of the RVE has to be elaborated. At the same time, the composite components require being modeled by specific damage constitutive laws that are able to represent the component's behavior, respectively.

Figure 5.6 shows the schematic view of a micro model RVE of a masonry structure as it is considered in this research. Where Ω_{RVE} is the volume of the RVE and $\delta\Omega_{RVE}$ describes the boundary where the external forces or deformations are applied. Both homogeneous components, brick units and mortar joints, are modeled by nonlinear continuum damage models.

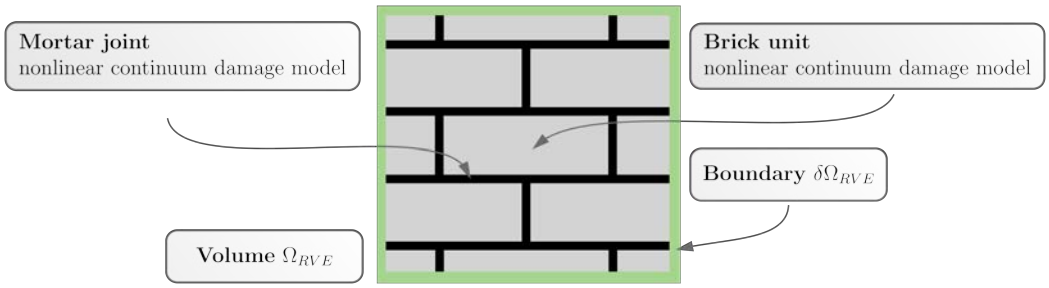

Figure 5.6: Example of micro-scale modeled representative volume element for the virtual laboratory. The volume Ω_{RVE} consists of brick units and mortar joints, both numerically modeled as nonlinear homogeneous continuum materials, and the RVE's boundary $\delta\Omega_{RVE}$

5.3.2 The boundary value problem

A boundary value problem consists of the volume or the region of the considered problem and its boundaries. On the boundary an entity of deformation or traction is applied. The research done in Petracca et al. (2016) summarize several boundary displacement fluctuations that can be applied to RVEs:

There exists the concept of *zero displacement fluctuation*, where the displacement fluctuations vanish in every point of the entire volume Ω_{RVE}. Another method of applying boundary conditions are *zero boundary displacement fluctuations*. The displacement fluctuations then only disappear on the RVE's boundary $\delta\Omega_{RVE}$. Moreover there exists the idea of applying *periodic boundary displacement fluctuations*, where the displacements of two opposite points on the boundary are equal.

This work adopts the concept of *zero boundary displacement fluctuations*. The boundary condition is then applied as a displacement of the boundary $\delta\Omega_{RVE}$ by monotonically increasing the boundary values at each analysis step. For the 2D analysis of the RVE the boundary conditions of a single virtual experiment are defined as follows

$$d_x = (\epsilon_{xx} \cdot x + \epsilon_{xy} \cdot y) \cdot t \tag{5.22}$$

$$d_y = (\epsilon_{yy} \cdot y + \epsilon_{xy} \cdot x) \cdot t \tag{5.23}$$

Where d_x and d_y are the displacements applied to all points of the RVE boundary $\delta\Omega_{RVE}$ in x- and y-direction, respectively. t is the actual analysis time instance, so that $t \in [t_0, t_e]$, with t_0 as the start time instance and t_e the end time instance of the analysis. After each step n of the analysis a scalar Δt is added to the previous t. The scalar values ϵ_{xx}, ϵ_{yy} and ϵ_{xy} are the components of a previously defined strain vector in Voigt's notation. The strain vector then defines the displacement shape of the RVE.

A determination of the boundary conditions in terms of a strain vector allows performing a variety of virtual experiments. A modification of the strain vector in Equations 5.22 and 5.23 results in a specific boundary condition that deforms the RVE. A further modification of these values causes a novel boundary condition and a different displacement shape. Therefore, the strain vector can then be chosen as the modification tool for the virtual laboratory in order to be able to run a variety

of different virtual experiments. However, the choice of the strain vector is not arbitrary. As mentioned, the virtually produced data should cover a wide range of possible deformations of the RVE. A well defined database of different strain vectors possibly ensures a wide scope of the input data for the machine learning model.

Investigations made by Zaghi et al. (2018) show that all possible two dimensional strain states can be defined as the coordinates of a three dimensional sphere in a coordinate system where the components ϵ_{xx}, ϵ_{yy} and ϵ_{xy} of the strain vector are the axes. The strain vector can then be defined as follows

$$\boldsymbol{\epsilon} = \begin{pmatrix} \epsilon_{xx} \\ \epsilon_{yy} \\ \epsilon_{xy} \end{pmatrix} = \lambda \begin{pmatrix} \cos\theta \\ \sin\theta\cos\phi \\ \sin\theta\sin\phi \end{pmatrix} \tag{5.24}$$

Where θ, ϕ and λ are the three parameters that define the coordinates of the sphere. The components of the strain vector depend on periodic sine and cosine functions. Thus all possible strain configurations can be obtained by modifying the angles θ and ϕ in the interval $[-\pi, \pi]$. The scalar λ is the norm of the strain vector so that

$$\lambda = ||\boldsymbol{\epsilon}|| = \sqrt{\epsilon_{xx}^2 + \epsilon_{yy}^2 + \epsilon_{xy}^2} \tag{5.25}$$

Figure 5.7 shows the three dimensional strain space and a variation of 26 combinations of the two angles in order to define the set of strain vectors. The norm of each strain vector is equal to 1. Figure 5.8 depicts the RVE exposed to four different boundary conditions caused by varying the strain vector of Equation 5.24. It also shows the difference of the deformation shapes.

5.3.3 Solution of the boundary value problem

The solution of each boundary value problem of the virtual laboratory is searched numerically. A non-linear finite element analysis is performed for each virtual experiment. The number n_{vl} of analysis in the virtual laboratory depends on the number of variations of the strain vector $\boldsymbol{\epsilon}$ of Equation 5.24. Hence all strain states are stored in a matrix $\boldsymbol{\epsilon}_d$ consisting of n_{vl} column vectors as follows

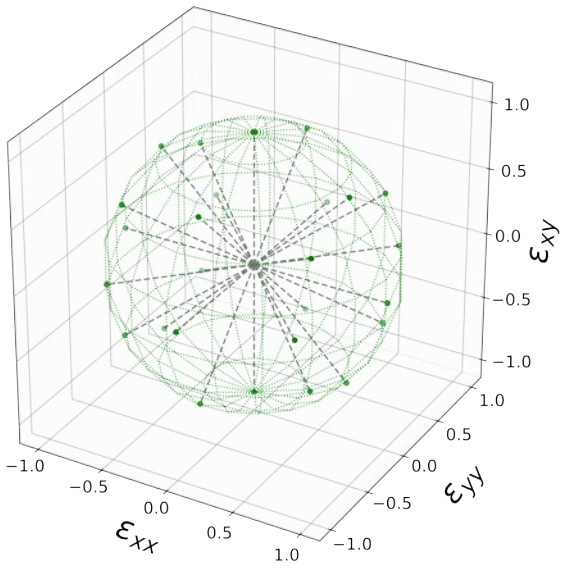

Figure 5.7: Three dimensional strain space for the 26 variation of the angles θ and ϕ in Equation 5.24.

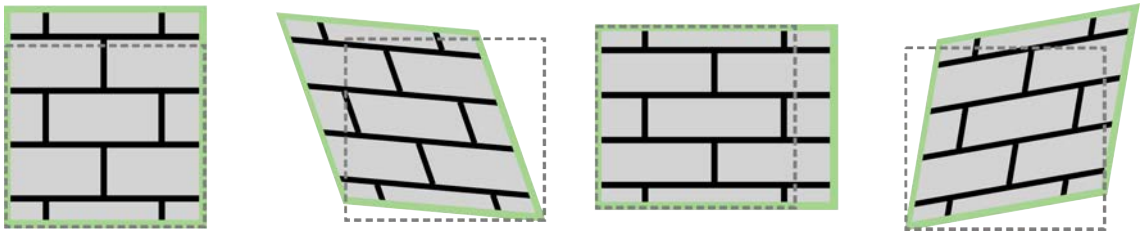

Figure 5.8: Four deformed RVEs by applying a variation of boundary conditions

$$\boldsymbol{\epsilon}_d = \begin{bmatrix} \boldsymbol{\epsilon}_1 & \boldsymbol{\epsilon}_2 & \dots & \boldsymbol{\epsilon}_{n_{vl}} \end{bmatrix} \tag{5.26}$$

Each finite element analysis does then take its corresponding entry of the matrix $\boldsymbol{\epsilon}_d$ in order to define the boundary conditions and runs until complete failure of the micro model can be achieved.

For the finite element analyses, this research utilizes the open source framework KRATOS MULTIPHYSICS Dadvand et al. (2010). It offers the possibility to run the n_{vl} analyses of the virtual laboratory by a user defined loop. So that all n_{vl} analyses can be run automatically by a single command file. Moreover, KRATOS includes the constitutive laws introduced in Chapter 4, so that the material components of the masonry RVE can be numerically modeled by an appropriate law for brittle materials. The modularity of KRATOS also allows to write user specific python files,

that have access to the data structure while FE solving, e.g. writing user specific output files automatically. Being able to write such specific files is a great advantage for the preparation of the machine learning training data. The stresses appearing during the analyses of the RVE must be up-scaled to a macro scale level in order to serve as training input for the prediction of a homogenized constitutive model. The following section describes the procedure of up-scaling the stresses.

5.3.4 Up-scaling of strain and stress states

The finite element solution delivers the local deformations at all the Gauss points of the micro model RVE. The strains and stresses of the micro scale must then be transformed to a macro level by up-scaling each entity in order to use the coupled strain and stress pairs for training. For this purpose, a single representative entity must be defined that considers all the solution values of each Gauss point of the RVE.

This transition takes place by computing an average of all the saved RVE stresses. Thus, this research presents a procedure, written in a user specified python file, that accesses to the solving stage of KRATOS and computes a mean volume over all the Gauss points. The implemented procedure that computes the up-scaled stresses is defined as follows and is valid for 2D elements only

$$\tilde{\sigma}_i = \frac{1}{A_{RVE}} \sum_{j=1}^{n} \left[\frac{A_j}{k_j} \sum_{l=1}^{k_j} \sigma_{i,jl} \right] \tag{5.27}$$

Where $\tilde{\sigma}_i$ is the i-th component of the mean stress vector $\tilde{\boldsymbol{\sigma}}$. n is the total number of finite elements of the RVE, A_{RVE} is the total area of the RVE. A_j is the area of the j-th element of the RVE, k_j is the total number of Gauss points of the i-th element. And $\sigma_{i,jl}$ is the i-th component of the stress vector $\boldsymbol{\sigma}$ of the j-th element at the l-th Gauss point. Figure 5.9 shows the entities of Equation 5.27 for a masonry RVE finite element model with four node quadrilateral elements each having $k_j = 4$ Gauss integration points.

The corresponding up-scaled strains can be derived by transforming the applied boundary strains $\boldsymbol{\epsilon}$ from Equation 5.24 to the engineering notation as follows

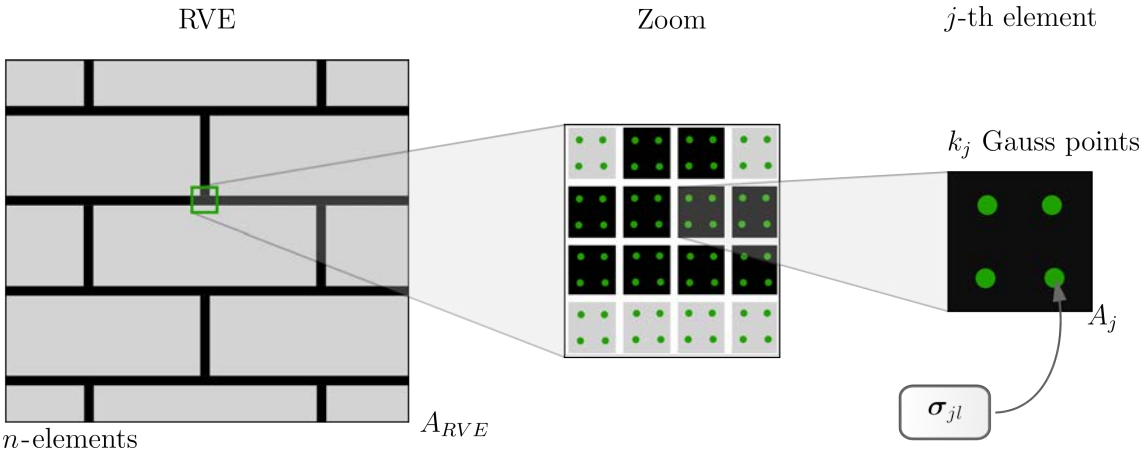

Figure 5.9: Example showing the entities of Equation 5.27 for the up-scaling procedure of a masonry RVE finite element model with 4 node quadrilateral elements each having $k_j = 4$ Gauss integration points

$$\tilde{\boldsymbol{\epsilon}} = \begin{pmatrix} \epsilon_{xx} \\ \epsilon_{yy} \\ 2\epsilon_{xy} \end{pmatrix} \tag{5.28}$$

Where ϵ_{xx}, ϵ_{yy} and ϵ_{xy} are the components of the strain vector $\boldsymbol{\epsilon}$ applied to the boundary of the RVE during the analysis. It has to be taken into account, that $\tilde{\boldsymbol{\epsilon}}$ contains values for each analysis step n amplified by the actual time instance t explained in Equation 5.22 and 5.23. Thus consistency of coupled pairs of $\tilde{\boldsymbol{\epsilon}}$ and $\tilde{\boldsymbol{\sigma}}$ can be guaranteed.

This procedure of constructing a mean over the stresses and the strains to one single vector, respectively, results in values belonging to a representative single element (RSE). Thus this single element contains both the averaged vectors and is representative for the RVE. It has the characteristic element size $l_{ch,RSE}$. The element size $l_{ch,RSE}$ is computed as the average value of all the characteristic element sizes of the RVE.

5.3.5 Numerical implementation

The virtual laboratory is programmed as a loop over n_{vl} analysis which depend on the parameters chosen to define the strain vector $\boldsymbol{\epsilon}_d$ of Equation 5.26. Each numerical experiment of the virtual laboratory has a total analysis step number of

n by monotonically increasing the analysis time instance t. Algorithm 5.3 shows the numerical implementation of the automated loop of the virtual laboratory.

Algorithm 5.3 Automated procedure of the virtual laboratory

input: n, n_{vl}
output: $\tilde{\boldsymbol{\epsilon}}$, $\tilde{\boldsymbol{\sigma}}$

START

Build the finite element model of the RVE
Set up the boundary strain vector $\boldsymbol{\epsilon}_d$ ▷ Eq. (5.26)
Initialize the lists of the averaged strains $\tilde{\boldsymbol{\epsilon}}$ and stresses $\tilde{\boldsymbol{\sigma}}$
Initialize virtual laboratory loop $i = 1$
while $i \leq n_{vl}$ **do**
    Define the i-th boundary condition $d_{x/y} = f(\boldsymbol{\epsilon}_{d,i}, t)$ ▷ Eqs. (5.22), (5.23)
    procedure KRATOS SOLVING STAGE
        for each analysis step $j \in n$ **do**
            Apply boundary condition and solve the boundary value problem
            Compute up-scaled strains $\tilde{\boldsymbol{\epsilon}}_j$ and stresses $\tilde{\boldsymbol{\sigma}}_j$ ▷ Eqs. (5.27), (5.28)
            Append upscaled entities: $\tilde{\boldsymbol{\epsilon}}$`.append(`$\tilde{\boldsymbol{\epsilon}}_j$`)` and $\tilde{\boldsymbol{\sigma}}$`.append(`$\tilde{\boldsymbol{\sigma}}_j$`)`
    $i \rightarrow i + 1$ ▷ Go to next virtual experiment

END

5.4 Data isotropization

5.4.1 The problem

The data produced in the virtual laboratory serves as the training data of the machine learning model previously described in Section 5.2. The model behind this technique is a constitutive nonlinear model based on linear elastic isotropy. It assumes an isotropic relation between the input strains $\boldsymbol{\epsilon}_{true}$ and the input stresses $\boldsymbol{\sigma}_{true}$. Thus the data coming from the virtual laboratory should also follow an isotropic strain stress relation. The possible predictions made by an isotropic model can then be improved. This section presents a mapping procedure that is able to isotropize the data coming from virtual laboratory.

The masonry RVE introduced in the previous section consists of two materials. Each of them following an isotropic nonlinear damage constitutive law, respectively. But when put together into a heterogeneous material, isotropic behavior of the composite cannot be assumed directly. Due to the spatial organization and the complex

brick-mortar interaction, it exhibits different behavior in different directions.

This section shows, that the raw data coming from the virtual laboratory and the masonry RVE does not follow an isotropic elasticity relation. This means that the up-scaled stresses of the RVE are related to the applied boundary strains by an anisotropic condition. Thus a procedure is presented in this section that is able to isotropize the relation between both mentioned entities. This method is called *data isotropization*. It is basically a preparation of the input data for the machine learning model in order to ensure consistent input output flow at an isotropic level. All the necessary steps of the method are clarified in the following. An accompanying example illustrates the problem at a linear elastic level.

The method is based on a transformation between an anisotropic and an isotropic space. It requires a transformation tensor that is capable of modifying between both the spaces. This tensor can be computed from the raw elastictity tensor at the anisotropic level and the isotropic elasticity at the isotropic level. Thus Section 5.4.2 presents a computation method that is able to obtain both these matrices from the results of the virtual laboratory. Once the raw and the isotropic elasticity matrices are defined, the transformation procedure can be applied as described in Section 5.4.3.

5.4.2 Linear elastic properties

This section presents the computation of the raw linear elasticity tensor from strain and stress states computed in a virtual laboratory. Furthermore, it presents a procedure that is able to find the closest isotropic tensor to the raw elasticity tensor. The computation takes place in the linear elastic range and holds for two dimensional problems in Voigt notation.

In order to compute both the linear elastic matrices, values of the strain vector $\tilde{\boldsymbol{\epsilon}}$ and the stress vector $\tilde{\boldsymbol{\sigma}}$ must be extracted that are still in the linear elastic range. It is then satisfactory to gather the first entry of the i-th virtual experiment of all n_{vl} analyses and store them in a matrix so that

$$\breve{\boldsymbol{\sigma}} = \left[\tilde{\boldsymbol{\sigma}}_1 \;\; \tilde{\boldsymbol{\sigma}}_{1+n_1} \;\; \tilde{\boldsymbol{\sigma}}_{1+n_1+n_2} \;\; \dots \;\; \tilde{\boldsymbol{\sigma}}_{1+n_1+n_2+\dots+n_{n_{vl}-1}}\right] \tag{5.29}$$

Where $\breve{\boldsymbol{\sigma}}$ is a matrix of rank $3 \times n_{vl}$ that includes the analysis results of the first analysis step of each virtual experiment extracted from the up scaled stresses $\tilde{\boldsymbol{\sigma}}$. The

subscript denotes the position of the first result value of each virtual experiment in the entire set of $\tilde{\boldsymbol{\sigma}}$. Where $n_1, n_2, \ldots, n_{vl}$ are the scalar entries of a vector $\boldsymbol{n}$ that contains the number of analysis steps per analysis, e.g. n_1 is the total number of analysis steps of the first virtual experiment, and so on. The vector $\boldsymbol{n}$ then holds n_{vl} entries. The computation of the corresponding strain vector $\breve{\boldsymbol{\epsilon}}$ containing only the first strains of each analysis can be constructed from $\tilde{\boldsymbol{\epsilon}}$, accordingly.

5.4.2.1 Raw elasticity tensor

Given the set of stresses and the set of strains in the linear elastic range of all the virtual experiments, the raw elasticity tensor can be computed starting from linear elasticity

$$\underbrace{\breve{\boldsymbol{\sigma}}}_{3\times n_{vl}} = \underbrace{\boldsymbol{C}_{raw}}_{3\times 3} : \underbrace{\breve{\boldsymbol{\epsilon}}}_{3\times n_{vl}} \tag{5.30}$$

Rearranging Equation 5.30 leads to the computation of the raw elasticity tensor as a least squares problem

$$\boldsymbol{C}_{raw} = \underbrace{\breve{\boldsymbol{\sigma}}}_{3\times n_{vl}} : \underbrace{\breve{\boldsymbol{\epsilon}}^{+}}_{n_{vl}\times 3} \tag{5.31}$$

Where $\breve{\boldsymbol{\epsilon}}^{+}$ denotes the *Moore-Penrose* inverse of $\breve{\boldsymbol{\epsilon}}$ that has a common use in solving least square problems (also known as *pseudoinverse*). It is a generalization of the inverse matrix used for non symmetric matrices. So that $\boldsymbol{A}\boldsymbol{A}^{+} = \boldsymbol{I}$ for a $(n \times k)$ matrix $\boldsymbol{A}$ $(n \neq k)$.

Example 5.1 shows the application of the above described procedure to a masonry RVE. It also gives suggestions for the further procedure of the data isotropization for masonry RVEs.

Example 5.1. *Computation of the linear elastic properties of a small masonry RVE - raw elasticity tensor*

Subject of this example is a two dimensional micro model of a small masonry wall specimen. The model consists of four horizontal brick layers. The vertical offset of one layer to the other is half the size of the brick's length. The dimensions width $\times$ height of the wall specimen count 0.31 m $\times$0.23 m, while each brick unit measures

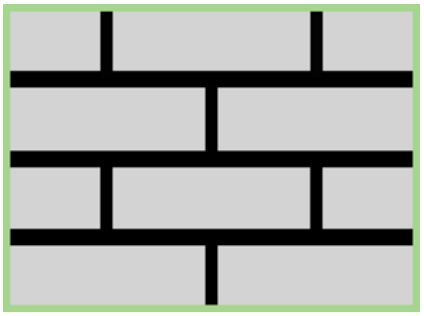

Figure 5.10: RVE of the virtual laboratory for a small masonry wall specimen of Example 5.1

Table 5.1: Linear elastic properties chosen for Example 5.1

	Young's modulus E	Poisson ratio ν
Bricks	5.0 GPa	0.2
Mortar	2.0 GPa	0.2

$0.15m \times 0.044m$. The thicknesses of the mortar joints are, $1.55cm$ for the horizontal and $1.1cm$ for the vertical joints, respectively. Figure 5.10 shows the RVE of the micro model. For the finite element analysis a mesh with quadrilateral elements each having four Gauss integration points was chosen. The average element is squared with an edge length of $3mm$. Each material is provided with a linear elastic plane stress elasticity law defined by the isotropic elasticity matrix with the properties of the Young's modulus E and the Poisson ratio ν. Table 5.1 shows the material properties of the virtual laboratory campaign.

In order to perform the virtual laboratory, the total number of virtual experiments is chosen to be $n_{vl} = 26$. Different strain vectors are computed according to Equation 5.24 by utilizing different values of the angles cos and θ. These boundary strain vectors are then applied as boundary conditions to the RVE in separate analysis. The stress results of each analysis are up-scaled and the first result of each analysis is extracted according to the procedure described in Section 5.3, in order to obtain the matrices $\breve{\boldsymbol{\sigma}}$ and $\breve{\boldsymbol{\epsilon}}$.

Given these results, the raw elasticity tensor $\boldsymbol{C}_{raw}$ can be computed according to Equation 5.31. For the here considered example the following tensor can be obtained.

$$\boldsymbol{C}_{raw} = \begin{bmatrix} 4.26 & 0.77 & 0.70 \cdot 10^{-6} \\ 0.77 & 3.90 & 0.06 \cdot 10^{-6} \\ 0.17 \cdot 10^{-6} & 0.22 \cdot 10^{-6} & 1.56 \end{bmatrix} GPa \tag{5.32}$$

The result shows a matrix structure close to that of an orthotropic elasticity matrix. Thus, the following paragraph holds a discussion about how to obtain a

totally orthotropic tensor out of the raw elasticity tensor $\boldsymbol{C}_{raw}$.

5.4.2.2 Orthotropic elasticity tensor

Masonry structures, when composed of uniform brick layers and constant mortar joint thicknesses exhibit a different elastic response in the layer direction than in its perpendicular one. Substance of this thesis are such uniform masonry bonds. Example 5.1 has shown that the structure of the raw elasticity tensor $\boldsymbol{C}_{raw}$ is really close to the ideal orthotropic one. This shall be highlighted in the following by performing a transformation of the raw elasticity tensor to the orthotropic one and by evaluating its error.

The general orthotropic linear elastic tensor for two-dimensional problems in the plane stress condition reads as follows

$$\boldsymbol{C} = \frac{1}{1 - \nu_{12}\nu_{21}} \begin{bmatrix} E_1 & \nu_{21}E_1 & 0 \\ \nu_{12}E_2 & E_2 & 0 \\ 0 & 0 & G \end{bmatrix} \tag{5.33}$$

Here $E_{1/2}$ is the Young's modulus of the material in the 1- and the 2-direction, respectively, where such directions are perpendicular to each other. The same holds for the Poisson ratios $\nu_{12/21}$. G is the shear modulus of the linear elastic material. The identification of the directions 1 and 2 is not required since the orthotropic matrix is utilized only for the computation of the closest isotropic matrix.

The orthotropic linear elasticity matrix is symmetric and has zero entries in the first two entries of the third column and of the third row. As can be observed in Example 5.1, these entries are not equal to zero, however, they seem negligible small when compared with the other entries. Anyway, these values must be equalized to zero, in order to obtain an orthotropic matrix, as follows

$$c_{raw,ij} = 0.0 \text{ , with } i,j = (1,3),(2,3),(3,1),(3,2) \tag{5.34}$$

Where $c_{raw,ij}$ is the entry of the raw elasticity matrix at the i-th row and the j-th column. Moreover must be ensured that the orthotropic elasticity matrix is symmetric. This can be achieved as follows

$$\boldsymbol{C}_{ortho} = 0.5 \cdot \left(\boldsymbol{C}_{raw} + \boldsymbol{C}_{raw}^T \right) \tag{5.35}$$

After having performed the transformation from the raw elasticity tensor to the orthotropic tensor an error evaluation utilizing the Frobenius norm must be considered. The Frobenius norm is defined as follows

$$\|\boldsymbol{A}\|_F = \sqrt{\sum_{i=1}^{m}\sum_{j=1}^{n} a_{ij}^2} \tag{5.36}$$

Where $\boldsymbol{A}$ is a matrix of rank $m \times n$ with the components a_{ij}. After having calculated the Frobenius norm of the initial raw elasticity matrix $\boldsymbol{C}_{raw}$ and of $\boldsymbol{C}_{ortho}$ the error of the orthotropic transformation can be computed as follows

$$\chi = \left\| \frac{1}{\|\boldsymbol{C}_{raw}\|_F} \cdot \boldsymbol{C}_{raw} - \frac{1}{\|\boldsymbol{C}_{ortho}\|_F} \cdot \boldsymbol{C}_{ortho} \right\|_F \tag{5.37}$$

This procedure computes the Frobenius norm of the difference between the norms of the raw elasticity matrix and the orthotropic matrix. This error states the accuracy of the orthotropic matrix. In the following, Example 5.1 will be continued by applying the above stated procedure.

Example 5.1 (continued)**.** *Computation of the linear elastic properties of a small masonry RVE - orthotropic elasticity matrix*

The computation of the orthotropic elasticity matrix according to Equation 5.35 results in

$$\boldsymbol{C}_{ortho} = \begin{bmatrix} 4.26 & 0.77 & 0.0 \\ 0.77 & 3.90 & 0.0 \\ 0.0 & 0.0 & 1.56 \end{bmatrix} GPa \tag{5.38}$$

Comparing the orthotropic matrix with the raw matrix as shown in Equation 5.37 gives an error of $\chi = 3.06 \cdot 10^{-7}$. This value is negligible small, thus "cleaning" the raw elasticity matrix as shown in Equation 5.35 can be applied to the procedure of evaluating the linear elastic properties of an averaged RVE, without large error values χ.

The above continuation of Example 5.1 has shown that the up-scaled linear elastic material behavior of the considered masonry RVE is extremely close to orthotropic behavior. As explained, this is typical for masonry structures. For any

RVE considered in this work, the RVEs are geometrically similar to the RVE shown in Example 5.1. It is obvious, that the error between the raw and the orthotropic elasticity matrix must always be discussed for any RVE considered in the virtual laboratory.

5.4.2.3 Closest isotropic elasticity matrix

In order to apply the previously mentioned transformation procedure between the real and the isotropic scale an isotropic elasticity matrix is required. Thus this paragraph presents an optimization procedure that finds an isotropic elasticity matrix closest to an anisotropic one. The method is described in the following and an application example, as continuation of Example 5.1, is carried out. A closed form procedure has been presented in Norris (2006) and further improved in the work of Rossi et al. (2021). The research defines the closest isotropic matrix to an anisotropic one. The procedure is also applied here, in order to show that the optimization delivers equal results.

An isotropic elasticity matrix is defined by two parameters, e.g. the Young's modulus E and the Poisson ratio ν. Both theses parameters can then be utilized as the trainable variables of an optimization algorithm. The goal of this algorithm is to find a variable constellation of E and ν, so that an error function $\mathcal{L}$ reaches its minimum. The error computation considers the raw elasticity matrix $\boldsymbol{C}_{raw}$ and the wanted isotropic elasticity matrix $\boldsymbol{C}_{iso}$ as inputs. $\boldsymbol{C}_{iso}$ is the isotropic plane stress linear elastic matrix that here depends on the trainable variables E and ν as follows

$$\boldsymbol{C}_{iso} = \frac{E}{1-\nu^2} \begin{bmatrix} 1 & \nu & 0 \\ \nu & 1 & 0 \\ 0 & 0 & \frac{1-\nu}{2} \end{bmatrix} \tag{5.39}$$

The error function $\mathcal{L}$ itself is then defined as the Frobenius norm of the difference between $\boldsymbol{C}_{raw}$ and $\boldsymbol{C}_{iso}$. It follows

$$\mathcal{L} = \|\boldsymbol{C}_{raw} - \boldsymbol{C}_{iso}\|_F \tag{5.40}$$

The Adam optimizer (Section 5.2.1.1) then calculates all gradients w.r.t. the variables E and ν of the linear elastic isotropic matrix and searches the minimum

of the error $\mathcal{L}$. Once arrived at the minimum, the isotropic elasticity matrix $\boldsymbol{C}_{iso}$ closest to the raw elasticity matrix is defined. The optimization procedure can either be applied by taking the raw or the orthotropic elasticity matrix. However, the error value χ between the raw and the orthotopric matrix should then be negligible small. Since this is the case in Example 5.1 its continuation is performed with the orthotropic matrix.

Before continuing the example, let the alternative closed form definition of the closest isotropic matrix for the two-dimensional case be introduced. Considering an anisotropic elasticity matrix, here named as $\boldsymbol{C}_{raw}$, the works presented in Norris (2006) and Rossi et al. (2021) define a closed form for the computation of the closest isotropic matrix $\boldsymbol{C}_{iso}$ according to the following steps.

$$\boldsymbol{C}_{iso} = 3\Big(\frac{\alpha^\star}{3}\kappa^\star\Big)\boldsymbol{J} + 2\mu^\star\boldsymbol{K} \tag{5.41}$$

Where the coefficient $\alpha^\star = 2$, the matrix $\boldsymbol{J} = \boldsymbol{t}\boldsymbol{t}^T$, with $\boldsymbol{t}^T = (2^{-0.5}, 2^{-0.5}, 0)$, the matrix $\boldsymbol{K} = \boldsymbol{I_4} - \boldsymbol{J}$. Where $\boldsymbol{I_4} = diag\big(1.0, 1.0, 0.5\big)$. The values $\kappa^\star$ and $\mu^\star$ depend on the original anisotropic matrix in the following way

$$\mu^\star = 0.2(c_{00} - 2c_{01} + c_{11} + c_{22}) \tag{5.42}$$

$$\kappa^\star = \frac{\boldsymbol{m}^T\boldsymbol{C}_{aniso}\boldsymbol{m}}{\alpha^2} \tag{5.43}$$

Where $\boldsymbol{m} = \big(1, 1, 0\big)^T$ and the c_{ij} define the corresponding entry of the anisotropic matrix. The definition of the closest isotropic matrix is based on the Frobenius norm $||\boldsymbol{C}_{raw} - \boldsymbol{C}_{iso}||_F$. Thus, this procedure follows the same conceptual idea as the optimization procedure of finding the closest isotropic matrix. The continuation of Example 5.1 shows the application of both methods. Equal results can be observed.

Example 5.1 (continued)**.** *Computation of the linear elastic properties of a small masonry RVE - closest isotropic elasticity matrix*

In order to obtain $\boldsymbol{C}_{iso}$ as the closest matrix to $\boldsymbol{C}_{ortho}$, the optimization procedure to train the variables E and ν is carried out. Figure 5.11 shows the results along the whole optimization. The curves depict the progression of E, ν and the ratio of the actual loss and the initial loss. All curves show a horizontal tangent at the end.

This indicates that a closest constellation is achieved. The final values are $E = 3.91$ GPa and $\nu = 0.194$.

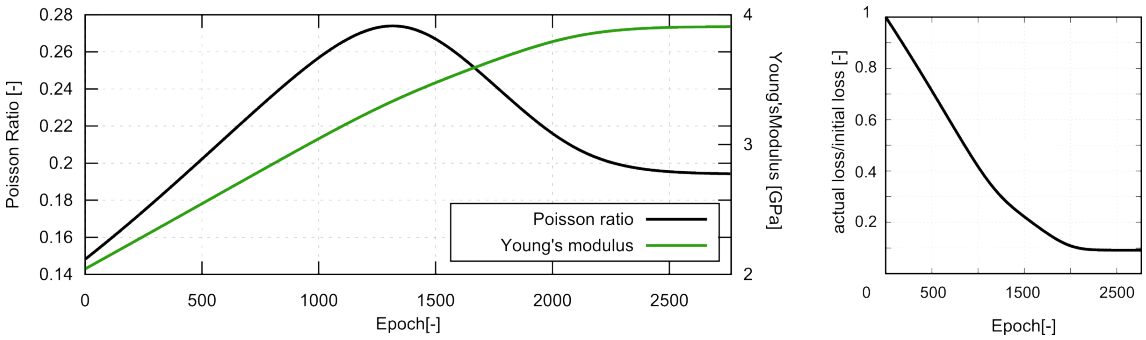

Figure 5.11: Example 5.1: results of the optimization procedure to find the closest isotropic linear elasticity matrix to an orthotropic one. Showing the progression of the parameters E and ν and the ratio of the actual loss to the initial loss

The alternative closed form procedure shown in Equation 5.41 results in the following isotropic matrix

$$\boldsymbol{C}_{iso} = \begin{bmatrix} 4.061 & 0.789 & 0 \\ 0.789 & 4.061 & 0 \\ 0 & 0 & 1.636 \end{bmatrix} GPa \tag{5.44}$$

The equal matrix is obtained by substituting the values E and ν obtained above in the plane stress elasticity matrix of Equation 5.39.

This section has shown that the orthotropic linear elasticity parameters can be directly derived from the virtual laboratory results in the linear range. Furthermore, a procedure that finds an isotropic linear elastic material closest to the raw or orthotropic behavior, has been presented. Thus the linear elastic properties of the masonry RVEs can be computed apart from the optimization of the nonlinear damage constitutive law. Anyway, in order to perform the entire machine learning optimization, results following an isotropic material behavior are required. Thus, the entire linear and nonlinear range of the up-scaled raw RVE results must be mapped to isotropic results. This can be done in a consistent transformation from an anisotropic to an isotropic space as shown in the following.

5.4.3 Isotropic mapping of up-scaled stresses

Previous works have introduced and applied the concept of mapping stresses and strains from orthotropic to isotropic formulations. Oller et al. (2003) define an orthotropic yield criteria that uses an isotropic formulation in a mapped space to then transform it back to an orthotropic formulation in the real space. This method includes a transformation from an orthotropic stress and strain space to an isotropic one by introducing transformation tensors. The transformation tensors are defined so to enable a consistency while transforming and back-transforming. The presented mapping procedure in Oller et al. (2003) can be applied for the transformation from an anisotropic to an isotropic space analogously.

The transformations between the spaces can be obtained by introducing the transformations from the real orthotropic stress and strain spaces to the mapped isotropic spaces, respectively. For two dimensional problems in Voigt notation it is defined as follows

$$\boldsymbol{\sigma}_{iso} = \boldsymbol{A}_{\sigma} : \boldsymbol{\sigma}_{ortho} \tag{5.45}$$

$$\boldsymbol{\epsilon}_{iso} = \boldsymbol{A}_{\epsilon} : \boldsymbol{\epsilon}_{ortho} \tag{5.46}$$

Where $\boldsymbol{\sigma}_{iso}$ and $\boldsymbol{\epsilon}_{iso}$ are the stress tensor and the strain tensor in the isotropic space. The respectively linked entities in the orthotropic space are $\boldsymbol{\sigma}_{ortho}$ and $\boldsymbol{\epsilon}_{ortho}$. The $\boldsymbol{A}_{\sigma}$ is the stress transformation tensor and $\boldsymbol{A}_{\epsilon}$ is the strain transformation tensor.

The stresses at both spaces underlie constitutive models based on strain equivalence and the concept of effective stresses. Thus they can be computed in terms of the corresponding strain tensor and the linear elasticity tensor, so that

$$\boldsymbol{\sigma}_{iso} = \boldsymbol{C}_{iso} : \boldsymbol{\epsilon}_{iso} \tag{5.47}$$

$$\boldsymbol{\sigma}_{ortho} = \boldsymbol{C}_{ortho} : \boldsymbol{\epsilon}_{ortho} \tag{5.48}$$

Considering the formulations made in Equations 5.45, 5.46, 5.47 and 5.48 a symmetric transformation condition $(\boldsymbol{A}_{\sigma}^{-1} = \boldsymbol{A}_{\epsilon})^T$ between the orthotropic and isotropic elasticity tensor can be made

$$\boldsymbol{C}_{ortho} = \boldsymbol{A}_{\sigma}^{-1} : \boldsymbol{C}_{iso} : \boldsymbol{A}_{\epsilon} \tag{5.49}$$

Figure 5.12 shows an overview of the consistent mathematical connections made between the real orthotropic and the mapped isotropic spaces.

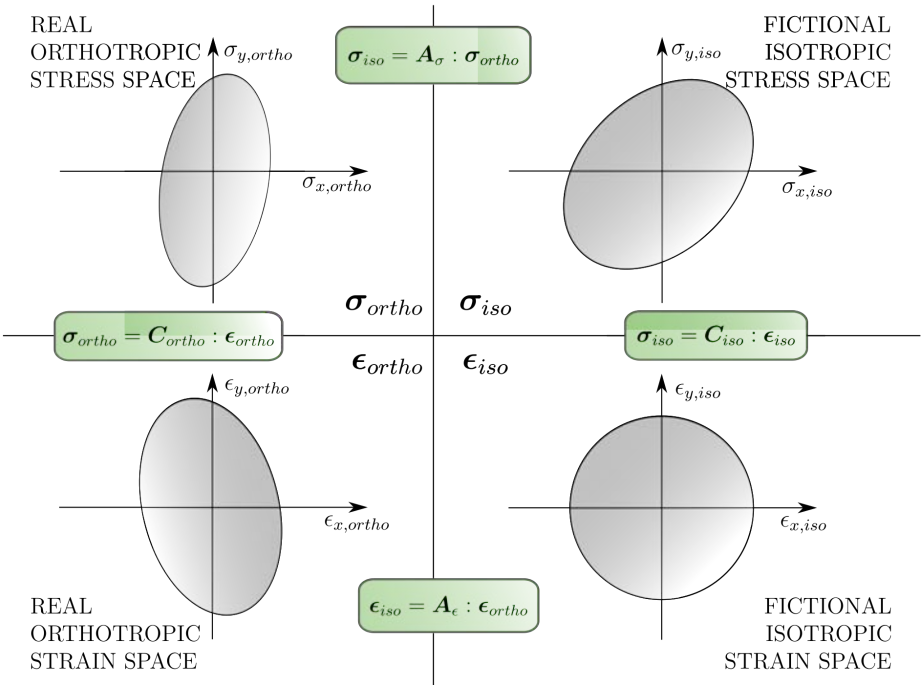

Figure 5.12: Overview of the different spaces considered in the mapping procedure

The choice of the transformation tensors in general is arbitrary, but consistency of the transformation procedure must be ensured. The works made in Pelà et al. (2011), Pelà et al. (2013) and Pelà et al. (2014) go further and propose that the transformation tensors should embody the anisotropic properties of the material. For orthotropic materials they assume the stress transformation tensor to be a diagonal matrix with each diagonal's component depending on the orthotropic material strength in the respective direction. This specific definition supposes to previously define the material strengths in each orthogonal direction by running uniaxial experiments. The strain transformation tensor in Pelà et al. (2013) can be chosen arbitrarily, but consistency must be guaranteed.

However, the work done in this thesis follows a different approach. As introduced in the previous sections, both the orthotropic and isotropic tensors are already defined. Thus, this research utilizes a method, that defines the transformation

tensors $\boldsymbol{A}_\sigma$ and $\boldsymbol{A}_\epsilon$ by considering a classical transformation of tensors as follows

$$\boldsymbol{C}_{ortho} = \boldsymbol{T}^T : \boldsymbol{C}_{iso} : \boldsymbol{T} \tag{5.50}$$

Here $\boldsymbol{T}$ is a transformation tensor that still needs to be defined. In order to do so, let the square roots $\sqrt{\boldsymbol{C}_{ortho}}$ and $\sqrt{\boldsymbol{C}_{iso}}$ of both $\boldsymbol{C}_{ortho}$ and $\boldsymbol{C}_{iso}$ be considered. Such square roots exist, since $\boldsymbol{C}_{ortho}$ and $\boldsymbol{C}_{iso}$ are symmetric positive definite (SPD). Then Equation 5.50 can be rearranged by utilizing the symmetric square roots as follows

$$\sqrt{\boldsymbol{C}_{ortho}} : \sqrt{\boldsymbol{C}_{ortho}} = \boldsymbol{T}^T : \sqrt{\boldsymbol{C}_{iso}} : \sqrt{\boldsymbol{C}_{iso}} : \boldsymbol{T} \tag{5.51}$$

Originating from this definition one can compute the transformation tensor according to

$$\boldsymbol{T} = \left(\sqrt{\boldsymbol{C}_{iso}}\right)^{-1} : \sqrt{\boldsymbol{C}_{ortho}} \tag{5.52}$$

Once the transformation tensor $\boldsymbol{T}$ is defined, it can be transferred to the concept of mapped spaces so that, $\boldsymbol{A}_\epsilon = \boldsymbol{T}$ and $\boldsymbol{A}_\sigma = \boldsymbol{T}^{-T}$. The method of mapping strains and stresses to an isotropic space must be applied to the entire set of up-scaled strains and stresses coming from the virtual laboratory. Then the isotropic up-scaled stresses and strains read

$$\tilde{\boldsymbol{\epsilon}}_{iso} = \boldsymbol{T} : \tilde{\boldsymbol{\epsilon}} \tag{5.53}$$

$$\tilde{\boldsymbol{\sigma}}_{iso} = \boldsymbol{T}^{-T} : \tilde{\boldsymbol{\sigma}} \tag{5.54}$$

Where $\tilde{\boldsymbol{\epsilon}}$ and $\tilde{\boldsymbol{\sigma}}$ are all the coupled strains and stresses coming from the virtual laboratory.

5.4.4 Equivalent damage computation

In order to obtain isotropic training data that follow a bi-dissipative d^+/d^- damage law, the input data of the machine learning model can be further modified. This method is optional and follows the idea of using the isotropic strains and stresses from equation 5.53 and 5.54 in order to calculate two equivalent damage variables

$d_{eq}^{\pm}$. Both equivalent damage variables can then be used in order to compute adjusted stresses according to Equation 4.2. The adjusted stresses serve as the input of the machine learning model. The following explanation utilizes the stresses and strains of the mapped isotropic space. The method is applied to the entire set of n_{vl} virtual experiment results in order to obtain a positive and a negative equivalent damage variable for each coupled strain-stress pair, respectively.

In a first step the effective isotropic stress is computed based on the isotropic strains and the isotropic elasticity tensor as follows

$$\tilde{\boldsymbol{\sigma}}_{iso,eff} = \boldsymbol{C}_{iso} : \tilde{\boldsymbol{\epsilon}}_{iso} \tag{5.55}$$

In order to enable the computation of a positive and a negative equivalent damage variable, the following tensors of the mapped isotropic space must be split into their positive and negative parts according to Equations 4.3 and 4.4: the effective isotropic stress tensor $\tilde{\boldsymbol{\sigma}}_{iso,eff}$, the isotropic stress tensor $\tilde{\boldsymbol{\sigma}}_{iso}$ and the isotropic strain tensor $\tilde{\boldsymbol{\epsilon}}_{iso}$. These entities and the equivalent damage variables can then be placed in Equation 4.2 and the following equation can be obtained

$$\tilde{\boldsymbol{\sigma}}_{iso} = \underbrace{(1-d^{+}) \cdot \tilde{\boldsymbol{\sigma}}_{iso,eff}^{+}}_{\tilde{\boldsymbol{\sigma}}_{iso}^{+}} + \underbrace{(1-d^{-}) \cdot \tilde{\boldsymbol{\sigma}}_{iso,eff}^{-}}_{\tilde{\boldsymbol{\sigma}}_{iso}^{-}} \tag{5.56}$$

Splitting Equation 5.56 into two terms, one with the positive and the other with the negative isotropic stresses $\tilde{\boldsymbol{\sigma}}_{iso}^{\pm}$, allows the computation of the equivalent damage variables $d_{eq}^{\pm}$ separately. Each equation is then multiplied by the positive and negative part of the isotropic mapped strains $\tilde{\boldsymbol{\epsilon}}_{iso}^{\pm}$, respectively. Then the following equation to compute the equivalent damage variables can be obtained

$$d_{eq}^{\pm} = 1 - \frac{\tilde{\boldsymbol{\sigma}}_{iso}^{\pm} : \tilde{\boldsymbol{\epsilon}}_{iso}^{\pm}}{\tilde{\boldsymbol{\sigma}}_{iso,eff}^{\pm} : \tilde{\boldsymbol{\epsilon}}_{iso}^{\pm}} \tag{5.57}$$

Now, adjusted isotropic stresses can be computed by utilizing the equivalent damage variables as follows.

$$\tilde{\boldsymbol{\sigma}}_{iso,adj} = (1-d_{eq}^{+}) \cdot \tilde{\boldsymbol{\sigma}}_{iso,eff}^{+} + (1-d_{eq}^{-}) \cdot \tilde{\boldsymbol{\sigma}}_{iso,eff}^{-} \tag{5.58}$$

Where now $\tilde{\boldsymbol{\sigma}}_{iso,adj} \approx \tilde{\boldsymbol{\sigma}}_{iso}$, except of the latest part of the non linear range. The application of the damage equivalent stress adjustment is optional and depends on

the quality of the virtual laboratory data. Hence the user of the machine learning model, after having analyzed the stresses, can choose if the procedure is applied. Further insights will be given in the application example of Chapter 6 where the damage equivalent adjustment is applied.

5.5 Post machine learning constitutive model

The definition of the post machine learning constitutive model finalizes the machine learning homogenization technique. During the definition of the preceding procedure several assumptions have been made which also must be taken into account for the application of the post machine learning constitutive model. Thus a consistent constitutive model must be presented that can be utilized during the finite element analysis of a masonry structure at macro scale.

This section presents the procedure and the implementation that enables to use the result of the machine learning homogenization technique. The principal parts of the post machine learning constitutive model are based on the definitions made in Chapter 4. This section gives an overview of the necessary modifications to the model as described in Chapter 4 in order to include energy regularization and the space transformation procedure. It starts with a general operation flowchart showing how the post machine learning constitutive law is included to the analysis of homogeneous masonry at a macro scale. In a second part energy regularization is tackled. Mesh independence must be guaranteed while using the optimized constitutive law at the macro scale. This section introduces a proper approach.

Finally, this section includes the mapping procedure that is utilized in data isotropization of Section 5.4 in order to transform from an anisotropic to an isotropic space. The transformation ensures compatibility between the optimized machine learning model trained at the mapped isotropic space and the real anisotropic space.

The post machine learning model presented in this section is implemented as an available constitutive model of the finite element program KRATOS MULTIPHYSICS.

5.5.1 General operation flow

Figure 5.13 shows a flowchart of how the post-machine-learning constitutive law is extracted from the machine learning procedure by considering all analyses at the

multiple scales.

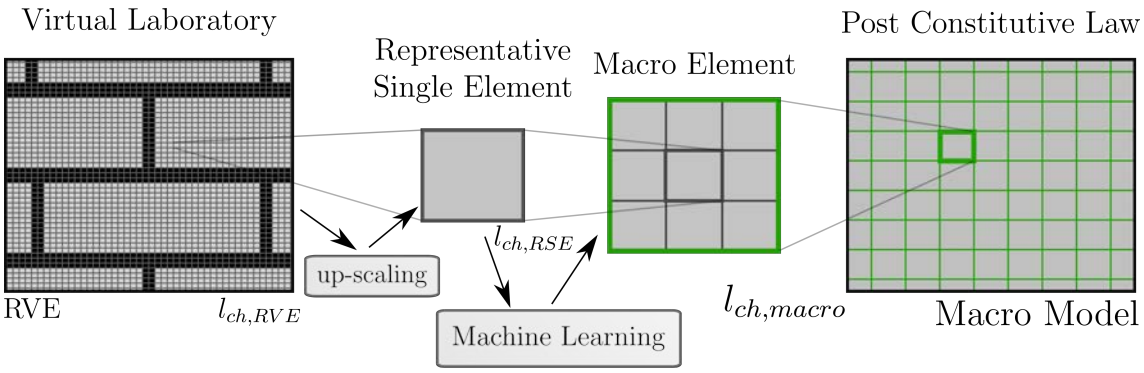

Figure 5.13: Chart of the operational flow in order to obtain the post-machine-learning constitutive model. Showing the fictitious position of the representative single element in a macro model

In order to obtain a consistent post machine learning constitutive law, the explanation of the general operation flow starts from the analysis of the virtual laboratory. Then the procedure moves forward to an up-scaled procedure, that averages the stresses and strains of the RVE in a representative single element (RSE). These stresses are then send to the machine learning technique and train a constitutive model, that represents a homogeneous damage constitutive model for the RSE. The RSE is then multiple times fictitiously positioned in the element of a homogeneous macro model. In this way the constitutive model trained at the RSE level can be reflected and utilized for the analysis at macro scale. A factor ω_{ch} can be introduced, that counts the number of multiple positions of the RSE in the macro element. It is important for the energy regularization and mesh independent results during the homogenization technique and is defined as follows

$$\omega_{ch} = \frac{l_{ch,macro}}{l_{ch,RSE}} \tag{5.59}$$

Where $l_{ch,RSE}$ is the mean value of all the characteristic lengths l_{RVE} of the RVE and $l_{ch,macro}$ is the characteristic length of the element at macro scale.

The parameters of the post-machine-learning constitutive law have been obtained during the machine learning procedure and are stored as optimized parameters in $\boldsymbol{\Theta}^{\star}$. Most of the parameters included in $\boldsymbol{\Theta}^{\star}$ can be directly used for the post-

machine-learning constitutive law. Anyway, especially the fracture energies, that contribute to mesh independent results, are substance of further discussions.

5.5.2 Energy regularization

As shown in Figure 5.13 two different scales of mesh sizes are present. On the one hand there is the characteristic length $l_{ch,RSE}$ of the RSE and on the other there is the characteristic length of the element at macro scale.

The same problem occurs for two different micro models with different finite element meshes. Then an energy regularization must be performed in order to obtain mesh independent results. For both the damage evolution laws present in this thesis, namely the exponential softening and the Bézier like hardening softening behavior, the energy is regularized. This procedure has been introduced in Section 4.3. It is simple and straight forward, since the energy regularization is based on the user input of the fracture energy G^- or G^+. Both values are divided by the characteristic element length l_{ch} in order to compute a specific fracture energy g^- or g^+. These specific values then regularize the energy of the element. The flow of energy regularization for classical application (Chapter 4) is as follows

$$G^{\pm} \longrightarrow g^{\pm} = \frac{G^{\pm}}{l_{ch}} \tag{5.60}$$

However, this flow is not necessary for the post machine learning constitutive law, since the specific fracture energies $g^{\pm}$ can be directly computed from the optimized constitutive law parameters $\boldsymbol{\Theta}^{\star}$ and the known characteristic element length $l_{ch,RSE}$ of the RSE. However, it has been shown in Figure 5.13 that the element sizes of the RSE and the macro model are unequal. Thus it must be shown that the fracture energy $G_{c/t}$ of the post machine learning constitutive law is computed in a consistent way. It all depends on the elemental size. The difference in elemental size of the both scales is measured by the factor ω_{ch} as introduced in Equation 5.59. The following calculations prove the approach.

Giving the specific fracture energy g_{RSE} of the RSE by the parameters $\Theta^{\star}$, one can compute the fracture energy G_{RSE} by applying Equation 4.32 as follows

$$G_{RSE} = g_{RSE} \cdot l_{ch,RSE} \tag{5.61}$$

As already explained, the RSE is fictitiously placed in the macro element. The counter for this is ω_{ch}. If $l_{ch,RSE}$ is smaller than $l_{ch,macro}$, than $\omega_{ch} > 1$. Thus ω_{ch} is a multiplier that defines the amount of fracture energy G_{RSE} that is placed in the macro element. Thus the fracture energy G_{macro} can be computed as follows:

$$G_{macro} = G_{RSE} \cdot \omega_{ch} \tag{5.62}$$

By now substituting Equations 5.59 and 5.61 into 5.62 the following equation can be obtained

$$G_{macro} = g_{RSE} \cdot l_{macro} \tag{5.63}$$

Equation 5.63 proofs that the specific fracture energy g_{RSE} obtained by the machine learning model can directly enter into the post machine learning constitutive law. The energy regularization takes place in the opposite direction as shown for regular application in Equation 5.60 as follows

$$g^{\pm} \longrightarrow G^{\pm} = g^{\pm} \cdot l_{macro} \tag{5.64}$$

The following example shows the performance for two tests with different FE mesh refinements.

Example 5.2. *Numerical tests of the post machine learning constitutive model in terms of FE mesh independence.*

Subject to this example is a rectangle material model with lateral lengths of $0.5m \times 0.25m$. Two different FE models have been developed. Model 1 contains 16×8 elements (128 total) and model 2 contains 26×14 elements (364 total). Only four node quadrilateral elements have been considered. Figure 5.14 shows the two models and the FE mesh refinement. For both the tests the post machine learning constitutive model with Bézier like hardening and softening in tension and

compression is chosen with equal material properties.

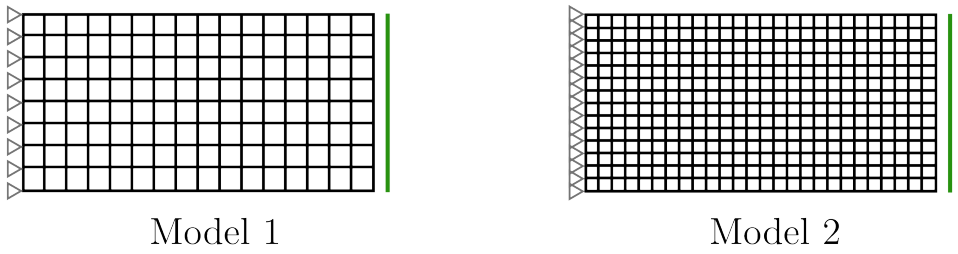

Figure 5.14: Two FE models with different mesh refinements to demonstrate energy regularization

Both models are fixed on one of the short edges, this can be obtained by constraining displacement of the nodes of that specific boundary in x and y direction. Two different load applications are applied to the models, in order to obtain a compression and a shear case. Load case 1 (compression) is applied by monotonically increasing the displacements of the second short edge in negative x-direction. Load case 2 (shear) is applied by monotonically increasing the displacements of the second short edge in negative y-direction.

Figure 5.15 shows the results in terms of boundary force - displacement curves of both the models for load case 1 and 2. Equal results of both the models and analyses have been obtained for this compression and shear examples, respectively.

5.5.3 Space transformation

The constitutive model subjected in this thesis (Chapter 4) and implemented to the machine learning technique is based on an isotropic strain stress relation as shown in Equation 4.1. That is why the strains and stresses, coming from the virtual laboratory and contributing as inputs of the machine learning model, have been transformed into an isotropic relation, as introduced in Section 5.4. Without transforming, their real relation, would be an orthotopic or even an anisotropic one and would not serve for the constitutive model implemented into the machine learning procedure of this thesis.

This mapping procedure of transforming between multiple spaces (anisotropic - isotropic - anisotropic) must also be included to the post machine learning constitutive model for the finite element analysis of macro scale masonry structures.

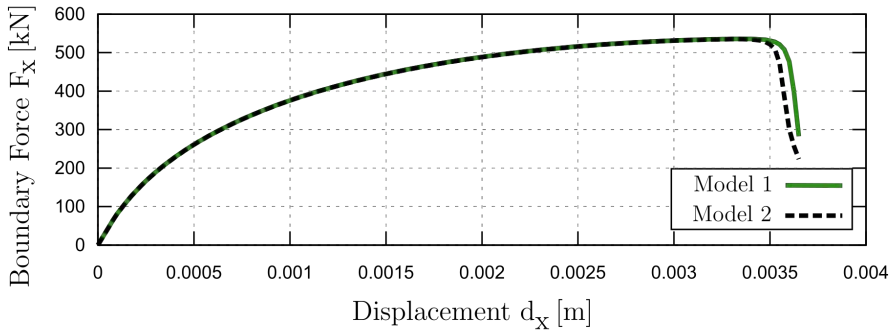

(a) Load 1: Compression

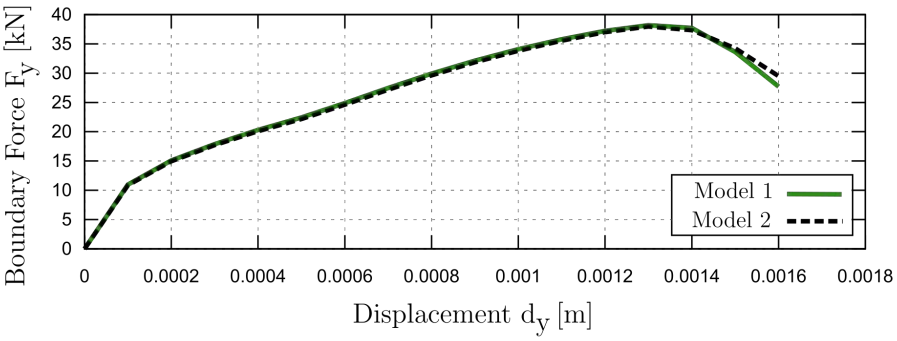

(b) Load 2: Shear

Figure 5.15: Force - Displacement curves of model 1 and model 2 of (a) compression and (b) shear load examples, respectively. The models differ in the number of FE elements, the similar results illustrate mesh independence

The input strains $\tilde{\boldsymbol{\epsilon}}$ and the predicted stresses $\tilde{\boldsymbol{\sigma}}_{pred}$ coming from the machine learning model are defined in an isotropic space. Hence, the trained constitutive law is not directly applicable to the macro modeling approach of masonry, since it does not include the anisotropy of masonry. Thus, during the macro scale analysis, the strains coming from the finite element solving stage are defined in the anisotropic space and must be transformed to an isotropic space, in order to apply the optimized constitutive law. The strain state at the isotropic space can then be obtained by applying the mapping procedure as follows

$$\tilde{\boldsymbol{\epsilon}}_{iso} = \boldsymbol{T} : \tilde{\boldsymbol{\epsilon}} \tag{5.65}$$

Where $\tilde{\boldsymbol{\epsilon}}$ is the anisotropic strain state coming from the finite element solving stage. The transformation tensor $\boldsymbol{T}$ has been obtained previously, while trans-

forming the input training data for the optimization procedure at machine learning level. $\tilde{\boldsymbol{\epsilon}}_{iso}$ is the strain state at the isotropic space and is ready to run through the procedure described in Algorithm 4.1. This results in $\tilde{\boldsymbol{\sigma}}_{iso}$, the stress state at the isotropic space. In order to finalize the post machine learning constitutive law, the stress state at isotropic level must be transformed back to the initial space by applying a transformation as follows

$$\tilde{\boldsymbol{\sigma}} = \boldsymbol{T}^T : \tilde{\boldsymbol{\sigma}}_{iso} \tag{5.66}$$

Where $\tilde{\boldsymbol{\sigma}}$ is the computed stress at the anisotropic space obtained by applying the post-machine-learning constitutive model. Figure 5.16 shows an overview of the mapping procedure and its implementation to the constitutive law at an isotropic space.

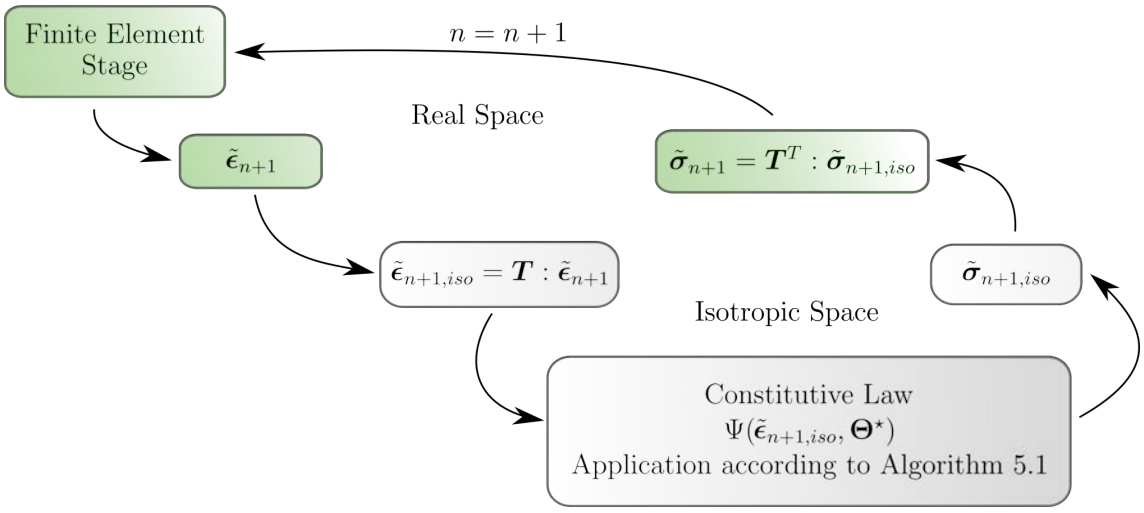

Figure 5.16: Overview of general application procedure of the post-machine-learning constitutive law for the analysis of structures at the macro scale including Algorithm 4.1

Table 4.2 shows the available constitutive laws presented in this thesis at the isotropic scale. All these laws are also implemented to the machine learning procedure and can be used for the macro model analysis after an optimization result has been found. The parameters that define these laws are summarized in Table 4.3 but must be completed or substituted as the present section has shown. In a first step, the transformation tensor must be included to the parameters of the post-

machine-learning constitutive law. The tensor was obtained during the machine learning homogenization technique and is essential for the correct and consistent application. The discussion held about the energy regularization has shown, that it is not necessary to define the fracture energies G^+ and G^-, but the specific fracture energies g^+ and g^-.

5.6 Summary

This chapter has presented in detail a procedure in order to homogenize the heterogeneous material masonry by utilizing machine learning. The machine learning model optimizes the parameters of a homogeneous nonlinear damage constitutive model until a modification of the parameters is obtained that represents training data as best as possible.

This Chapter has started with the introduction of the fundamentals of machine learning and how it is applied in this thesis. A supervised learning procedure has been chosen in order to train a mathematical model by inputting coupled sets of inputs and outputs. The mathematical model is assumed to be a strain driven constitutive law. The available laws have been introduced in the previous Chapter 4. The implementation of these laws to a machine learning model has been narrowly presented in this chapter. A computation graph has been constructed, that includes all the mathematical operations of the constitutive model. In order to train the computation graph, a batch sized training loop has been elaborated.

Strain and stress states serve as the training data inputs and outputs of the computation graph. The data inputs must be capable of representing the heterogeneous behavior of masonry structures. For this purpose, a virtual laboratory has been introduced. This laboratory is able to perform a large amount of numerical nonlinear analysis at the micro scale of masonry. The results of each virtual experiment are then averaged and stored in representative vectors of stresses and strains.

Masonry is an anisotropic material thus the stored data also follow an anisotropic elasticity relation. In contrast, the constitutive laws implemented to the machine learning procedure are based on isotropic elasticity. Thus, a procedure has been introduced in this section that has shown to make the data, coming from the virtual laboratory, compatible to the machine learning model. This approach has been called *data isotropization*. It enables the transformation from an anisotropic space

to an isotropic one. The calculation of the closest isotropic tensor to an anisotropic one allows to define a transformation tensor. It furthermore allows the back transformation to the anisotropic real space.

After having introduced the machine learning model and its training data, a closed training procedure can be started. The result is an optimized modification of constitutive law parameters that can be used for a post machine learning application at the macro scale. Therefore, this chapter has given an overview explaining the correct use of the post machine learning constitutive model. The overview includes a consistent use of the model by correctly relating the machine learning results to the post constitutive model.

The following chapter presents the application of the entire procedure to a masonry wall. It includes the performance of the virtual laboratory, the definition of homogenized linear elastic properties and the execution of the machine learning procedure in order to define a homogenized nonlinear constitutive model. Homogenization results and a post machine learning application will be discussed.

Part III

Application examples

Chapter 6

Machine learning homogenization of Flemish bond masonry wall

6.1 Introduction

This chapter presents an application example of the proposed novel machine learning homogenization technique for masonry structures. It demonstrates that a unique optimized constitutive law can be found by machine learning that is able to represent the behavior of masonry, thanks to training data derived from RVE micro models. Macro models for the numerical modeling of masonry are usually not as accurate as micro models. However, this application example shows that there exists a single homogenized constitutive model that is able to reproduce accurate results comparable with those obtained by micro modeling. The applied technique extremely facilitates the modeling of masonry structures at a macro scale without loosing accuracy by smearing from heterogeneous to homogeneous properties.

The numerical micro model of a masonry wall built in Flemish bond is subject of the homogenization technique. The geometry and the material properties of the here considered masonry wall model have been introduced in the application example of Chapter 4. A numerical analysis of a diagonal compression test has shown that the finite element micro model is able to accurately reproduce experimental results (Section 4.7.2). This application example then represents a calibrated numerical micro model, which can be utilized for the micro scale analysis in the virtual laboratory of the homogenization method.

This chapter is separated into several sections. Section 6.2 summarizes the vir-

tual laboratory campaign. It introduces the representative volume element used for the numerical analyses and presents the results. Section 6.3 observes the data obtained from the virtual laboratory, and presents the preparation for their application to the machine learning model. Section 6.4 gives an overview of the considered machine learning model. An evaluation example demonstrates the accuracy of the obtained model, and shows good prediction results of the optimized models also for an additionally performed virtual laboratory. Section 6.5 presents the post machine learning application of the macro scale laws. Very accurate results of numerical macro analyses can be obtained when compared with the results of equivalent micro scale analyses. A discussion and a summary closes this chapter.

6.2 Micro scale virtual laboratory campaign

This section presents the numerical analysis at the micro scale in order to obtain input data for the machine learning model. The data are produced in a virtual laboratory campaign. The framework of this campaign includes the definition of the considered RVE, the background information of the numerical finite element analysis, the performance of a number of n_{vl} virtual experiments and the presentation of the results.

6.2.1 The representative volume element

The representative volume element of the here presented virtual laboratory campaign is based on the analyses made in Section 4.7.2. This section has treated the numerical analysis of a diagonal compression test of a Flemish bond masonry wall. The material properties and the constitutive models of each material of the micro model have been calibrated in order to be able to reproduce the results of real experimental tests. Thus, the material properties of the calibrated numerical model of the diagonal compression test can be adopted for the micro model of the RVE. However, the dimensions of the diagonal compression test model are considered to be too large for the RVE analysis of the virtual laboratory. Hence, a smaller geometrical model is extracted from the numerical model subjected in Section 4.7.2. The RVE is a squared rectangle with an edge size of 0.53 m. The total number of finite elements counts 6160, of which 1624 follow the material properties of the

mortar joint and 4536 the brick unit. Figure 6.1 shows the numerical model of the RVE considered for this virtual laboratory, with the mortar and the brick elements, respectively, and the finite element mesh discretization.

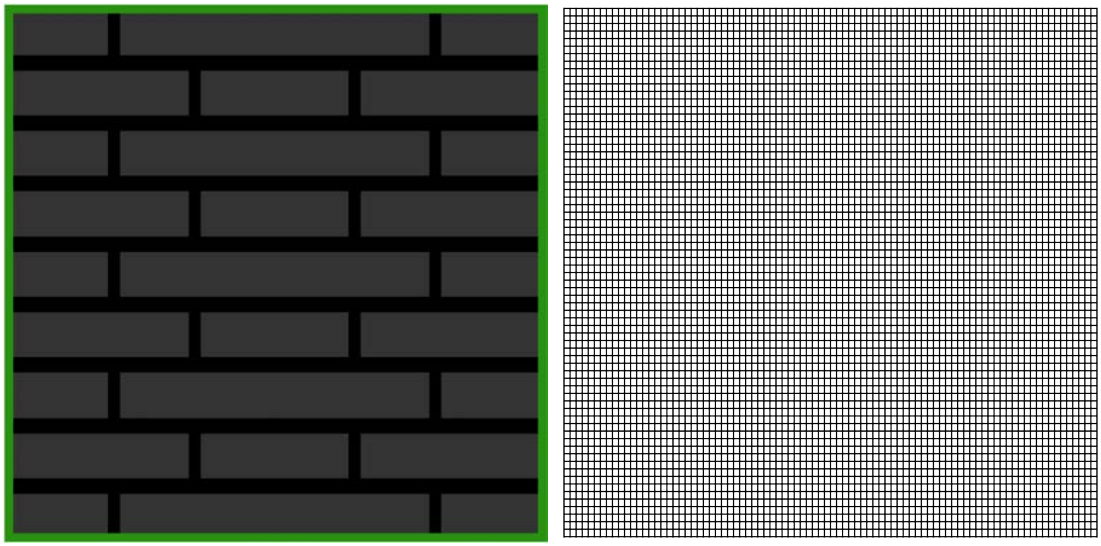

(a) RVE micro model (b) FE discretization

Figure 6.1: Virtual laboratory: representative volume element of the micro scale finite element analysis, showing a) the micro model and b) the finite element mesh discretization

Both materials, either the mortar joints or the brick units, follow an isotropic d^+/d^- damage law as introduced in Chapter 4. The material properties of the constitutive laws are summarized in Table 4.4. The damage criteria assumed are the Petracca yield criteria as shown in Equations 4.8 and 4.9. The damage evolution law in tension follows an exponential softening and a Bézier like hardening softening behavior in compression.

6.2.2 Numerical analyses and results

The virtual laboratory campaign consists of $n_{vl} = 26$ numerical analyses. Each analysis applies a different deformation condition on the boundary of the RVE. The analyses are performed until complete failure of the RVE is obtained. The 26 cases have been generated automatically according to the procedure described in Section 5.3.2. The angles θ and ϕ that define the boundary applied strain vector ϵ of Equation 5.24 are varied by utilizing a step size of $\pi/4$ in order to modify the

angles that generated each strain case. The intervals of the angles for the generation of the 26 cases are defined as follows

$$\theta \in \left[-\pi, \pi \right] \tag{6.1}$$

$$\phi \in \left[-\pi/2, \pi/2 \right] \tag{6.2}$$

By considering a variation of 26 cases, different combinations of tension and compression states can be assured. This large set of training data covers a wide scope of different deformation states, thus it is able to catch the anistropic behavior of the masonry RVE.

The results of the virtual experiments are discussed and stored according to the up-scaling procedure introduced in Section 5.3.4. Thus, the corresponding strain and stress vectors of a representative single element (RSE) are obtained (Equations 5.28 and 5.27 , respectively). The size of the characteristic element length of the RSE counts $l_{ch,RSE} = 0.006\ m$.

Table 6.1 shows a summary of the results obtained by each case. It includes the unit vector of the boundary applied strain state $\tilde{\boldsymbol{\epsilon}}$ that demonstrates the multi directional deformations of the masonry RVE. Column 3 shows the stress state caused by the applied boundary conditions. While C stands for compression and T for tension. In total there are 5 compression/compression, 5 tension/tension and 16 mixed tension/compression states. Since the strength in tension is far less than the strength in compression for both the brick units and the mortar joints, respectively, the models with tension/compression states fail in tension. Column 4 demonstrates the peak principal stresses calculated from the up-scaled stresses $\tilde{\boldsymbol{\sigma}}$ that causes the corresponding failure of each case (compression or tension stress). While the deviation of the compression peak stresses per case does not vary that much, the tension peak stresses cover a range from 0.07 MPa to 0.66 MPa. This is an evidence for anisotropic behavior, since the tension peak stress of the model strongly depends on the "direction" of the imposed deformation.

Figure 6.2 shows an overview of the damage patterns at an ultimate state of each case analyzed in the virtual laboratory. It demonstrates the variety of different crack patterns and failure mechanisms. The patterns of each case are indicated whether

Table 6.1: Virtual laboratory: summary showing the unit vectors of the applied boundary strains in engineering notation, the corresponding stress state (C = Compression, T = Tension), the peak principal stress leading to the corresponding damage and the indication whether damage in tension or compression is significant

Case	Unit boundary strain (ϵ_{xx}, ϵ_{yy}, γ_{xy})	Stress state (σ_1/σ_2)	Principal peak stress $[MPa]$	Damage in
1	(−1.0, 0.0, 0.0)	C/C	−6.87	C
2	(−0.71, −0.71, 0.0)	C/C	−7.18	C
3	(−0.53, −0.38, −0.76)	C/C	−7.19	C
4	(−0.53, −0.38, 0.76)	C/C	−7.19	C
5	(−0.45, 0.0, −0.89)	T/C	0.07	T
6	(−0.45, 0.0, 0.89)	T/C	0.07	T
7	(−0.53, 0.38, −0.76)	T/C	0.13	T
8	(−0.53, 0.38, 0.76)	T/C	0.13	T
9	(−0.71, 0.71, 0.0)	T/C	0.17	T
10	(0.0, −1.0, 0.0)	C/C	−6.87	C
11	(0.0, −0.45, −0.89)	T/C	0.19	T
12	(0.0, −0.45, 0.89)	T/C	0.19	T
13	(0.0, 0.0, −1.0)	T/C	0.25	T
14	(0.0, 0.0, 1.0)	T/C	0.25	T
15	(0.0, 0.45, −0.89)	T/C	0.21	T
16	(0.0, 0.45, 0.89)	T/C	0.21	T
17	(0.0, 1.0, 0.0)	T/T	0.17	T
18	(0.71, −0.71, 0.0)	T/C	0.66	T
19	(0.53, −0.38, −0.76)	T/C	0.57	T
20	(0.53, −0.38, 0.76)	T/C	0.57	T
21	(0.45, 0.0, −0.89)	T/C	0.49	T
22	(0.45, 0.0, 0.89)	T/C	0.49	T
23	(0.53, 0.38, −0.76)	T/T	0.46	T
24	(0.53, 0.38, 0.76)	T/T	0.45	T
25	(0.71, 0.71, 0.0)	T/T	0.43	T
26	(1.0, 0.0, 0.0)	T/T	0.65	T

the damage variable d^+ or d^- leads to failure of the RVE masonry wall.

The virtual laboratory is terminated and serves as the data production part of the machine learning homogenization technique. The outcomes are the coupled sets of strains $\tilde{\boldsymbol{\epsilon}}$ and stresses $\tilde{\boldsymbol{\sigma}}$ of each analysis step for all the considered virtual experiments. These data require further preparation as shown in the following.

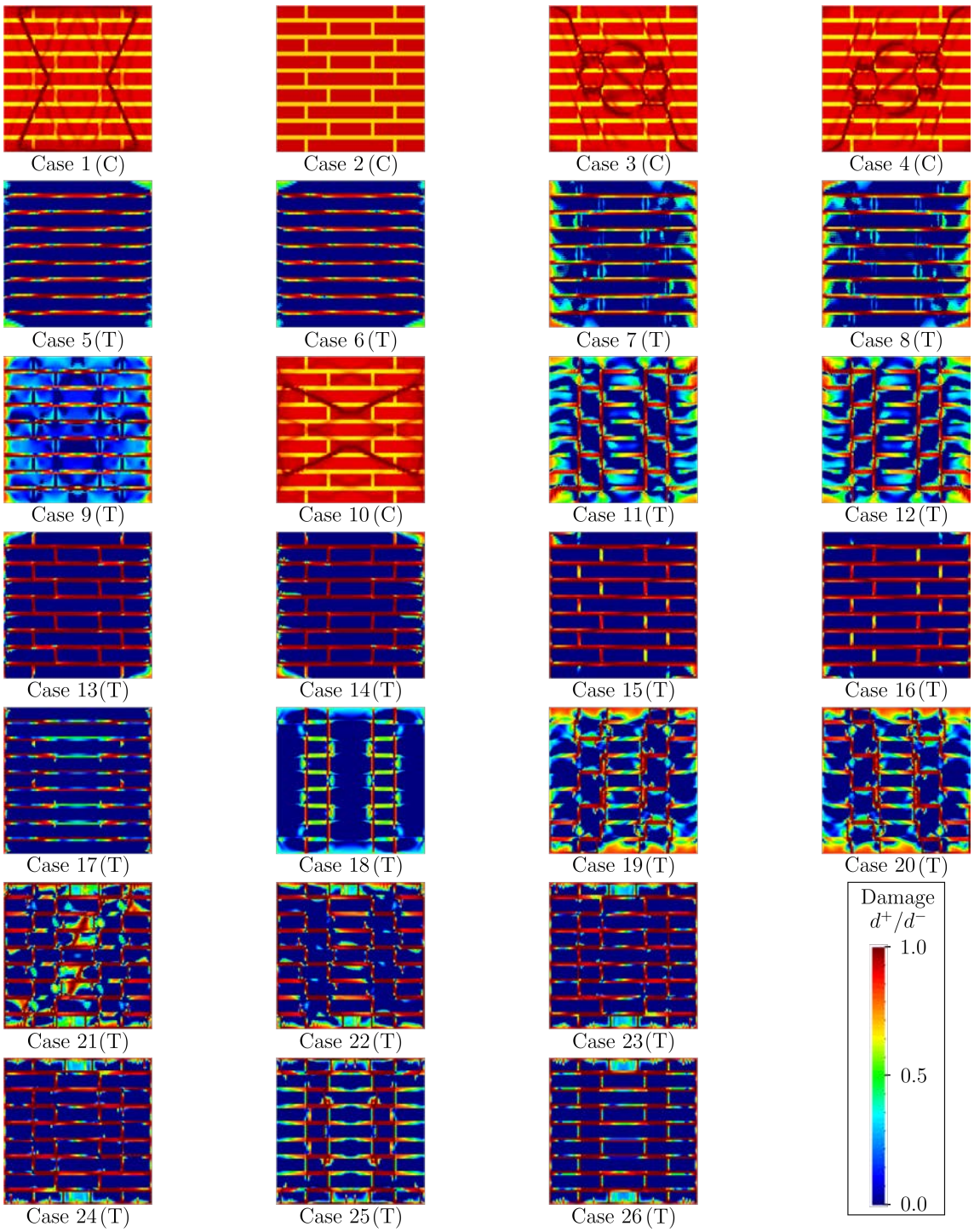

Figure 6.2: Flemish bond RVE virtual laboratory: damage contour plots of the 26 cases considered in the virtual laboratory, showing the damage variables d^+/d^- depending on the significant damage (T for tension, C for compression)

6.3 Data preparation and isotropization

This section performs the data isotropization of the representative strains $\tilde{\boldsymbol{\epsilon}}$ and stresses $\tilde{\boldsymbol{\sigma}}$ from the virtual laboratory. This procedure consists of the following steps. Firstly, the matrices $\breve{\boldsymbol{\epsilon}}$ and $\breve{\boldsymbol{\sigma}}$, only containing the first result of each virtual experiment, must be extracted from $\tilde{\boldsymbol{\epsilon}}$ and $\tilde{\boldsymbol{\sigma}}$ according to Equation 5.29. These matrices of strain and stress states represent the linear elastic behavior of the RVE under different boundary conditions. Both can then be utilized in order to compute the raw linear elasticity matrix $\boldsymbol{C}_{raw}$ as presented in Equation 5.31. The following matrix is obtained for the presented application example

$$\boldsymbol{C}_{raw} = \begin{bmatrix} 5.44 & 0.83 & 0.25 \cdot 10^{-6} \\ 0.83 & 4.29 & 0.01 \cdot 10^{-6} \\ 0.03 \cdot 10^{-6} & 0.04 \cdot 10^{-6} & 1.71 \end{bmatrix} GPa \tag{6.3}$$

In a second step, the closest isotropic matrix must be found. Thus the optimization procedure as introduced in Section 5.4.2.3 is applied. A machine learning model is trained in order to minimize a loss function that takes into account the Frobenius norm of the difference between C_{raw} and C_{iso}. (Equation 5.40). The machine learning model variables are the Young's modulus E on the one side and the Poisson's ratio ν on the other side. These variables define the isotropic linear elastic plane stress matrix.

The procedure terminates with a value of $E = 4.64\ GPa$ and $\nu = 0.187$. Figure 6.3 shows the evolution of both the variables during optimization. The computation of the normed error χ as introduced in Equation 5.37 is calculated to be $\chi = 0.12$ for the obtained isotropic elasticity matrix. This value is the smallest error that can be achieved while searching the closest isotropic matrix to the raw anisotropic one of this example.

The isotropic elasticity matrix for the application example then reads

$$\boldsymbol{C}_{iso} = \begin{bmatrix} 4.80 & 0.90 & 0.0 \\ 0.90 & 4.80 & 0.0 \\ 0.0 & 0.0 & 1.95 \end{bmatrix} GPa \tag{6.4}$$

In order to now transform the entire set of raw strains and stresses coming from the virtual laboratory, the transformation matrix $\boldsymbol{T}$ must be defined. Substituting

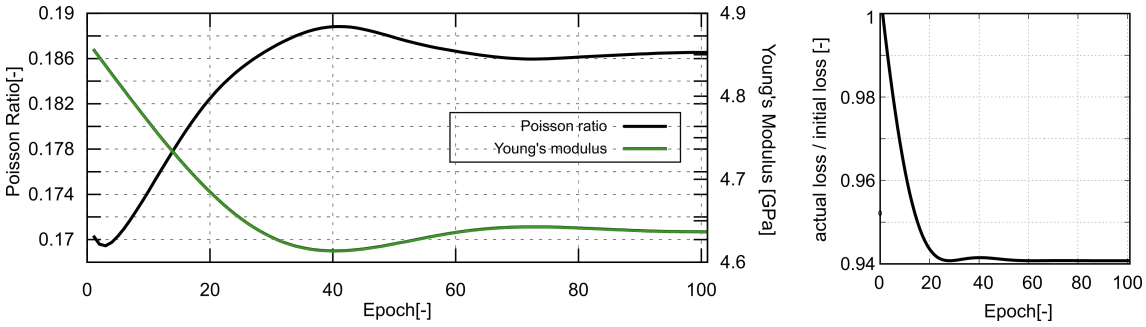

Figure 6.3: Variable results of the optimization procedure in order to find the closest isotropic matrix to an anisotropic one, showing the evolution of the variables E and ν and the ratio of the actual and initial loss

the actual modifications of the isotropic elasticity matrix and the raw anisotropic matrices into Equation 5.52, leads to the following transformation matrix

$$\boldsymbol{T} = \begin{bmatrix} 1.06 & -0.01 & 0.0 \\ 0.0 & 0.95 & 0.0 \\ 0.0 & 0.0 & 0.93 \end{bmatrix} \tag{6.5}$$

Applying the transformation matrix $\boldsymbol{T}$ to Equation 5.53 and 5.54 results in an entire isotropized set of training data consisting of the isotropized strains $\tilde{\boldsymbol{\epsilon}}_{iso}$ and the isotropizd stresses $\tilde{\boldsymbol{\sigma}}_{iso}$. The isotropic data set can now be utilized for training of the machine learning model. However, this application example applies the damage equivalent stress computation introduced in Section 5.4.4. The reasons are explained in the following.

The constitutive model implemented to the machine learning technique is based on strain equivalence. This implies that the principal direction of the strain vector that enters the model is equal to the principal direction of the outgoing stress vector. Thus the coupled input pairs (strain and stress states) of the machine learning model should also comply with this requirement. Hence an investigation of the principal directions of the isotropized strains $\tilde{\boldsymbol{\epsilon}}_{iso}$ and stresses $\tilde{\boldsymbol{\sigma}}_{iso}$ must be made.

Figure 6.4 shows the evolution of the principal directions during the analysis for selected cases analyzed in the virtual laboratory. The values are related to the principal directions of the isotropized strains $\tilde{\boldsymbol{\epsilon}}_{iso}$ and the isotropized stresses $\tilde{\boldsymbol{\sigma}}_{iso}$. It demonstrates that there exist analysis results that do not conform with the above

mentioned requirement. While the principal direction of the isotropized strains remains constant during the entire analysis of a case, the principal directions of the isotropized stresses are changing and deviate from the one of the strains.

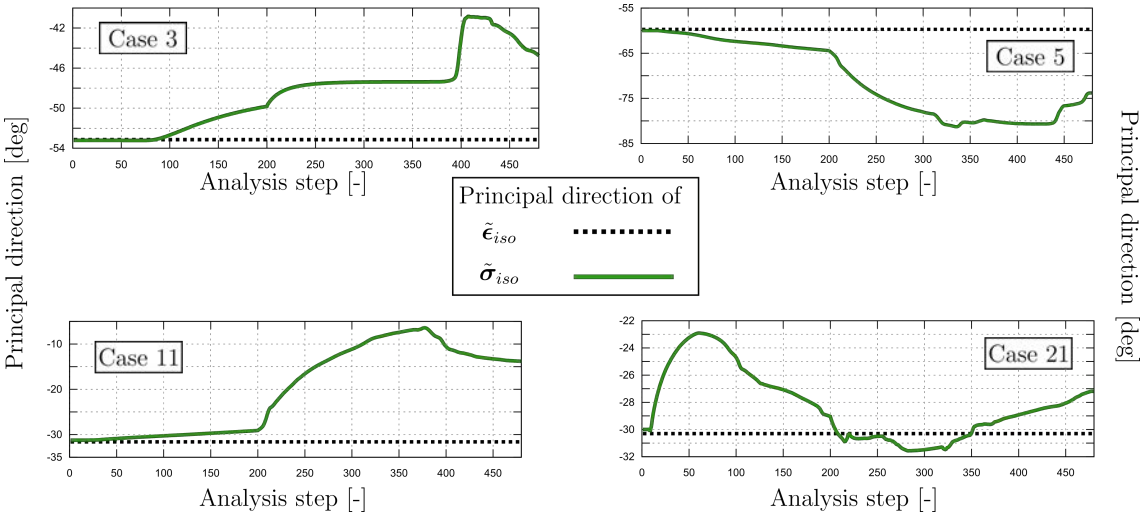

Figure 6.4: Demonstration of the deviation of the principal directions of the isotropized strain and stress vectors, respectively. Exemplary the principal direction evolution of the virtual laboratory cases 3, 5, 11 and 21 are shown.

An equivalent damage computation as shown in Section 5.4.4 can solve this problem. The procedure includes computing equivalent damage variables d_{eq}^{+} and d_{eq}^{-} based on the isotropic strains $\tilde{\boldsymbol{\epsilon}}_{iso}$, the elasticity matrix C_{iso} and the isotropic stresses $\tilde{\boldsymbol{\sigma}}_{iso}$. Then a modified damage equivalent isotropic stress $\tilde{\boldsymbol{\sigma}}_{iso,adj}$ can be computed by only taking into account the isotropic strains, the equivalent damage variables and the isotropic elasticity matrix (Equation 5.58). The principal directions of the damage equivalent stresses do then remain constant and are equal to the ones of the isotropic strains.

The data preparation is finished and the training data can be passed to the machine learning model. The machine learning inputs are $\epsilon_{true} = \tilde{\boldsymbol{\epsilon}}_{iso}$ and $\sigma_{true} = \tilde{\boldsymbol{\sigma}}_{iso,adj}$.

6.4 Machine learning homogenization

6.4.1 The computation graph

The computation graph $\mathcal{G}$ considered for model training includes the constitutive model presented in Chapter 4. The damage evolution law for both tension and compression behavior then follows a Bézier like hardening softening function. The yield criteria in tension is assumed to be the Rankine and in compression the Petracca criterion. The constitutive model for the graph $\mathcal{G}$ is called Ψ.

The set of trainable parameters is called $\boldsymbol{\Theta}$. Table 6.2 shows the entries of both the parameter sets and indicates the corresponding trainable variables of the machine learning model.

Table 6.2: Overview of the trainable variables for the considered machine learning model as applied in the application example of the novel masonry homogenization technique

Constitutive Model Ψ									
Tension	f_0^+	f_p^+	f_k^+	f_r^+		ϵ_p^+	ϵ_j^+	ϵ_k^+	ϵ_u^+
Compression	f_0^-	f_p^-	f_k^-	f_r^-	f_{bi}^-	ϵ_p^-	ϵ_j^-	ϵ_k^-	ϵ_u^-

6.4.2 Model training and results

Training the constitutive law machine learning model includes optimizing a large number of variables during the training procedure. Table 6.2 shows that for the computation graph $\mathcal{G}$ a number of 17 variables must be adjusted in order to define the constitutive model. In order to facilitate and improve the optimization, these variables are trained by several different coupled input sets $\epsilon_{true,i}$ and $\sigma_{true,i}$, with i as the number of sets. These sets can be obtained by separating the entire input set ϵ_{true} and σ_{true}. Such a separation depends on the strain stress curves of each considered case of the virtual laboratory as explained as follows.

Figure 6.5 shows a plot of the principal stresses of $\tilde{\boldsymbol{\sigma}}_{iso,adj}$ of the analysis of the virtual experiment case 18. It demonstrates a separation of the two curves into three sets. The boundaries of the sets are defined by the peak values of the principal stresses $\sigma_{1/2}$, respectively. They indicate when hardening of the material

ends and softening starts. Consequently three sets are obtained. The first contains the coupled strains and stresses up to the $\sigma_{1,peak}$. The second set includes the coupled pairs of strains and stresses going from the $\sigma_{1,peak}$ to the $\sigma_{2,peak}$ and the third contains the remaining pairs.

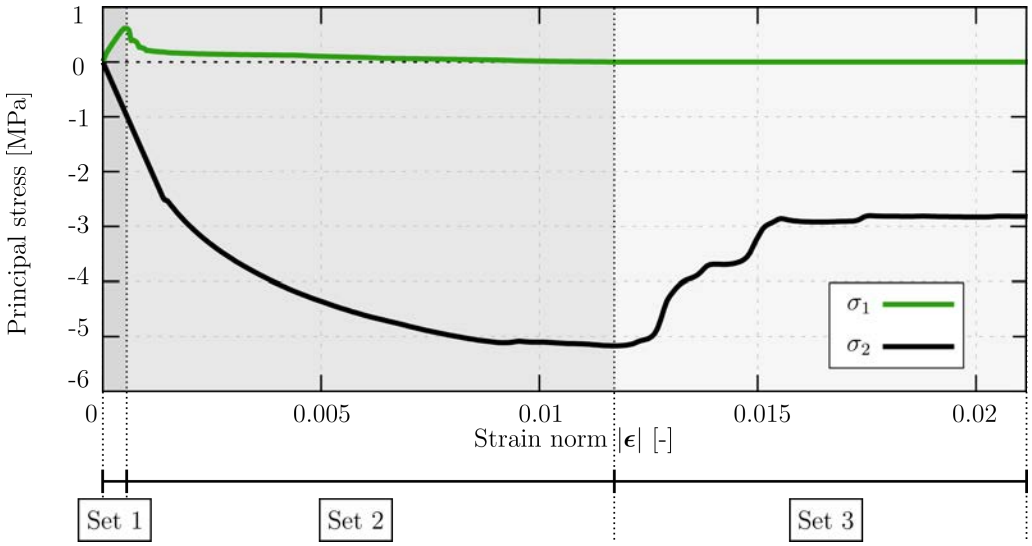

Figure 6.5: Principal stress values of the isotropized stresses $\tilde{\boldsymbol{\sigma}}_{iso,adj}$ of the virtual experiment 18 plotted over the norm of the strain vector $\tilde{\boldsymbol{\epsilon}}_{iso}$. A separation of the curves into three sets is shown, depicting the borders of the sets as the peaks of the principal stresses σ_1 and σ_2, respectively.

The obtained sets are then fed to separated training loops. Each loop training a proportion of the entire set of trainable variables, namely the ones that are defined in the range of a set.

Let a short example clarify this approach: training the residual compression strength while inputting set 1 into the training loop is pointless, since the coupled pairs of set 1 do not represent the post peak behavior nor the residual compression strength. Thus the variables not affected in the range of the corresponding set can be switched to non-trainable. Consequently, the optimization procedure can be facilitated tremendously. At least three optimization procedures are performed in order to train a portion of the variables shown in Table 6.2 .

In case the virtual experiment is exposing a tension/ tension or compression/ compression state, the sets are divided analogously. However, the curves are only separated into two sets. Each appended to the corresponding set out of the three original sets.

Table 6.3 shows the distribution of the trainable variables according to the introduced sets for the constitutive model Ψ. It clarifies which variable is kept constant during the optimization and which is trained. Once an optimum has been reached for a variable, the value is frozen for the following training loop. The number of runs for the optimization of model Ψ is six. That is because the number of trainable variables of this model is large and several more optimization runs are performed with set 2.

Table 6.3: Overview showing the training procedure for constitutive model Ψ indicating the variables that are trained during the feeding of the sets Set 1, Set 2 and Set 3. Showing also the multiple runs with different variables training

Constitutive law Ψ

		Tension parameters						Compression parameters				
		f_0^+	f_p^+	f_r^+	ϵ_p^+	ϵ_j^+	ϵ_u^+	f_0^-	f_p^-	f_{bi}^-	ϵ_p^-	ϵ_j^-
Set 1	R1	✓	✓	x	x	x	x	x	x	x	x	x
Set 2	R1	x	x	x	✓	✓	x	x	x	x	x	x
	R2	x	x	✓	x	x	✓	x	x	x	x	x
	R3	x	x	x	x	x	x	✓	x	x	✓	x
	R4	x	x	x	x	x	x	x	✓	✓	✓	x
Set 3	R1	x	x	x	x	x	x	x	x	x	x	✓

Figure 6.6 shows the optimization results depending on each run. The figure shows the results of each training run introduced in Table 6.3. On the left of the figure, the ratio of the actual loss and the initial loss is shown. This ratio is an indicator for training improvement. The flatter the curve, the closer is the optimization to the minimum and no further improvement can be obtained. For all the training runs of the constitutive model Ψ a flat curve evolves after a certain amount of epoch steps.

The constitutive models of the Bézier like damage evolution laws have been introduced in Chapter 4 by considering factors $c_i^{\pm}$ with $i = [1, 2, 3]$. These have been introduced in order to define dependencies between the control nodes of the Bézier curves in the softening range. The machine learning model did not utilize these factors, since the control nodes of the curves have been all defined as variables of the optimization procedure. A back calculation in order to obtain the factors $c_i^{\pm}$

can be performed. Table 6.4 shows the optimized variables in terms of the factors c_i for the model Ψ.

Table 6.4: Optimization results of the parameters of the machine learning model Ψ in terms of the Bézier regulators

Tension Parameters

	f_0^+	f_p^+	f_r^+	e_p^+	c_1^+	c_2^+	c_3^+
	$[Mpa]$	$[Mpa]$	$[Mpa]$	$[-]$	$[-]$	$[-]$	$[-]$
Model Ψ	0.21	0.32	0.01	0.0007	0.5	0.135	5.68

Compression Parameters

	f_0^-	f_p^-	f_{bi}^-	f_r^-	e_p^-	c_1^-	c_2^-	c_3^-
	$[Mpa]$	$[Mpa]$	$[Mpa]$	$[Mpa]$	$[-]$	$[-]$	$[-]$	$[-]$
Model Ψ	0.65	6.44	6.77	1.06	0.0081	0.5	0.20	1.86

Figure 6.7 depicts plots of the strain norm $|\bar{\boldsymbol{\epsilon}}|$ versus principal stresses of selected compression/ compression and tension/ tension cases from the virtual laboratory. It compares the anisotropic stress results $\bar{\boldsymbol{\sigma}}_{aniso,adj}$ of the numerical experiments (real curve) with the stresses $\boldsymbol{\sigma}_{aniso,pred}$ calculated by applying the trained constitutive model (predicted curve). Both stresses are computed as follows

$$\bar{\boldsymbol{\sigma}}_{aniso,adj} = \boldsymbol{T}^T : \bar{\boldsymbol{\sigma}}_{iso,adj} \tag{6.6}$$

$$\boldsymbol{\sigma}_{aniso,pred} = \boldsymbol{T}^T : \underbrace{\Psi(\boldsymbol{\epsilon}_{iso}, \Theta^\star)}_{\boldsymbol{\sigma}_{iso,pred}} \tag{6.7}$$

6.4.3 Model evaluation

A substantial step of machine learning is evaluating the results. Such en evaluation can be obtained by testing the prediction accuracy of the model for data which was not part of training. As introduced in Chapter 5 the data input set of the machine learning model is split into a training set and a testing/evaluation set (Figure 5.5). After each epoch training step a testing step is performed. This

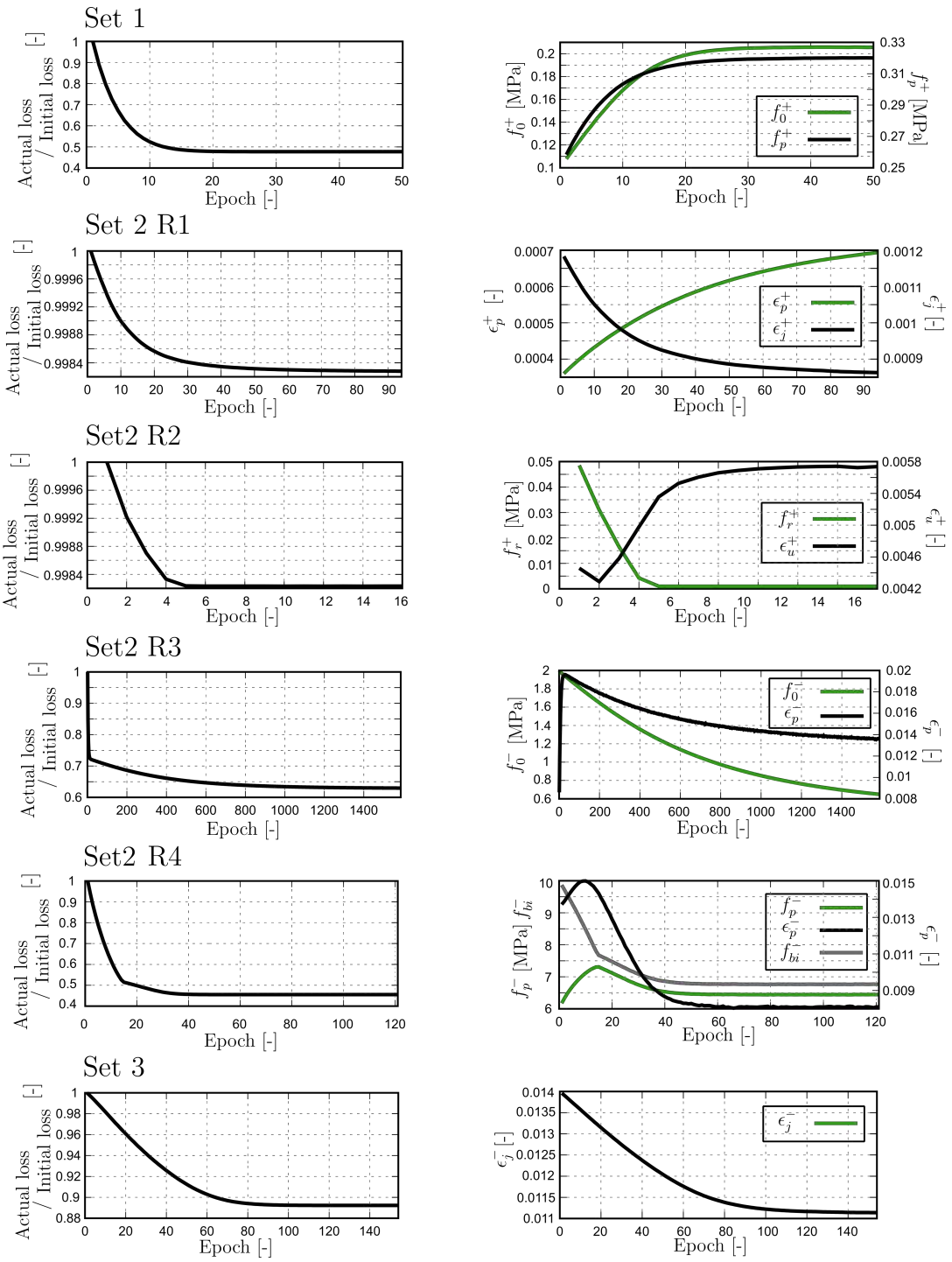

Figure 6.6: Results of the machine learning optimization procedure for the constitutive law Ψ. Showing the separation into the six training runs each depicting the evolution of the corresponding variable and the ratio of the actual training cost and the initial training cost during optimization

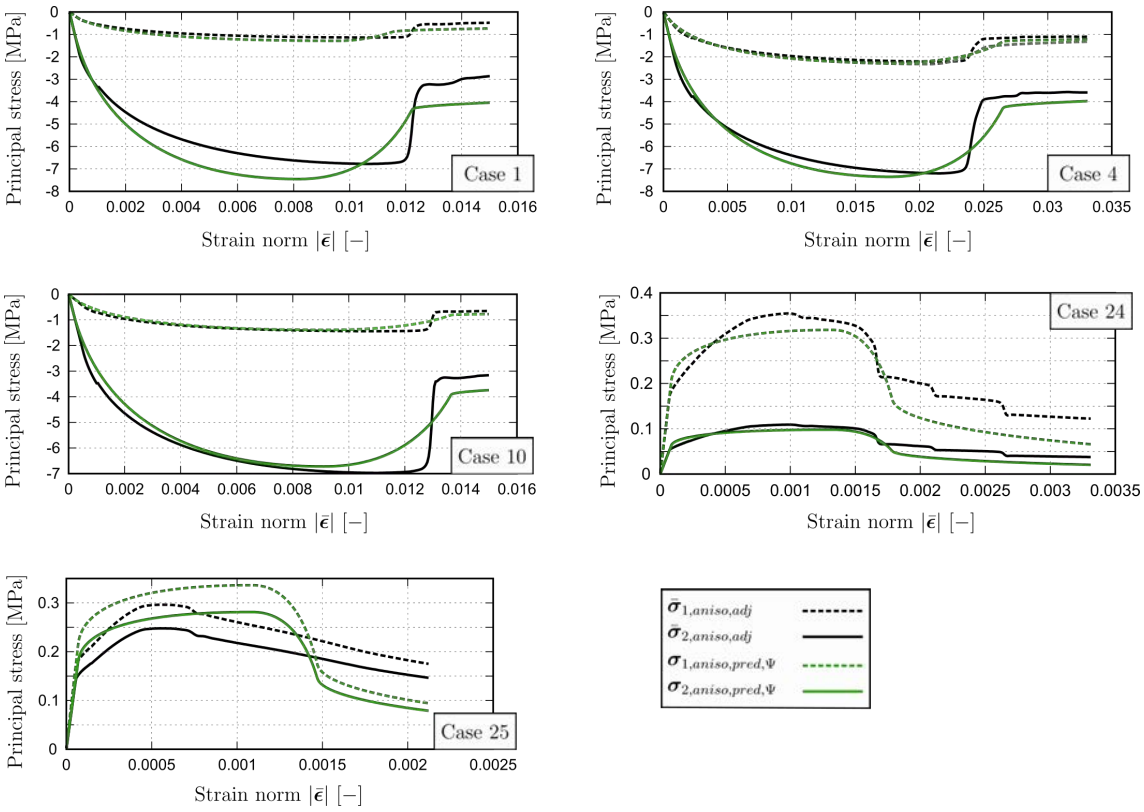

Figure 6.7: Comparison of the prediction results obtained by the trained constitutive model Ψ. Showing the principal stress values of the anisotropic results of the damage equivalent adjusted stresses from the virtual laboratory and the predicted stresses plotted versus the norm of the boundary applied strain vector.

procedure ensures that an online check of the model accuracy during training is made. However, the testing and training sets are subsets of the same input set. Thus, both sets contain results obtained from the same deformation states and they are never completely independent from each other. In order to avoid this, a new virtual laboratory campaign is performed. It applies novel and different boundary applied strains on the same masonry RVE. Consequently, a set of evaluation data evolves which is completely disconnected to the data used for training. This virtual campaign is called new virtual laboratory in the following.

The new virtual laboratory performed for this evaluation example consists of 58 different cases. The results of the new campaign pass through the same data isotropization procedure as the previous virtual laboratory results did. This results in a coupled set of anisotropic strains and anisotropic adjusted stresses (equivalent damage).

In order to now evaluate the trained model Ψ, predicted stresses must be computed. The anisotropic strains from the new virtual laboratory must then be mapped to the isotropic space. They serve as the input of the two trained constitutive models. Their outputs are the isotropic predicted stresses, which are back-transformed to the anisotropic space. Then three stress sets are obtained. The first is the vector of true stresses coming from the new virtual laboratory and the two remaining are vectors of the predicted stresses. Their results are shown in terms of peak values of the principal stresses. Figure 6.8 shows these maximum values for the evaluation set (58 cases) from the new virtual laboratory on the right. On the left of the same figure, the analogous results from the training set (26 cases) are depicted. All results are shown at the anisotropic level.

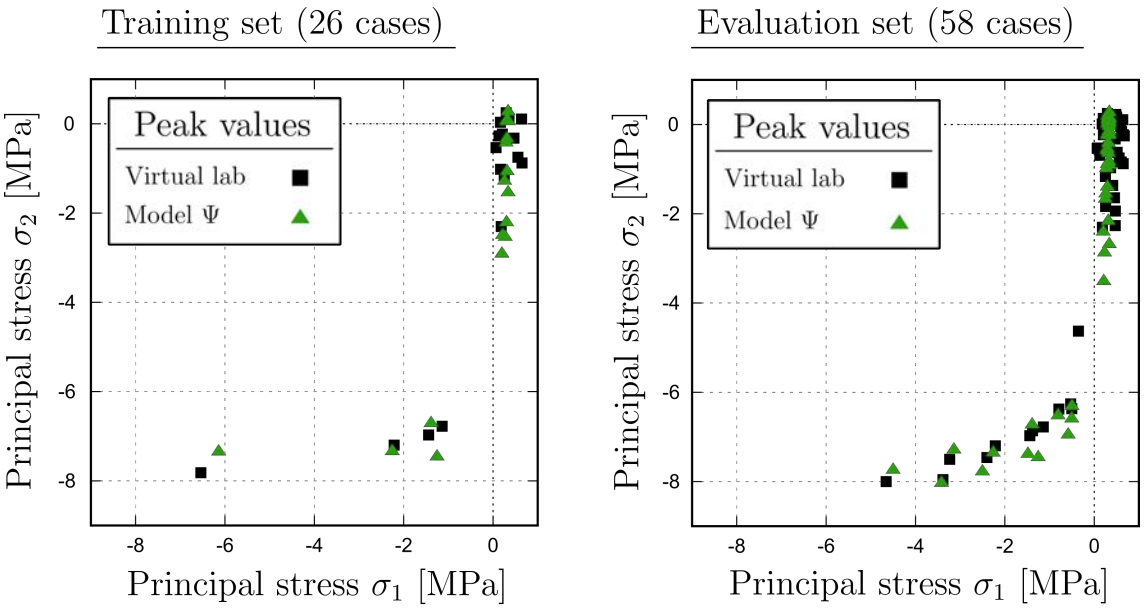

Figure 6.8: Comparison of the maximum principal stress values of the virtual laboratory results for the data used in training (26 cases) and the data used for evaluation (58 cases) and the predictions of the machine learning model Ψ. The results are shown at the anisotropic scale

The achieved results present a very good fitting for the machine learning model Ψ. On the one hand, the model fits the virtual laboratory training set results (Figure 6.8 left). On the other hand, it predicts the results that have been obtained by the new virtual laboratory.

The very accurate prediction results shown here, represent the performance of the trained model for a direct comparison of strains and stresses. However, the models

are going to be used as the constitutive laws inside a finite element analysis of a macro modeled masonry wall. Thus, the following section evaluates the performance of the trained model at the finite element analysis level.

6.5 Post homogenization application

The main goal of the machine learning homogenization technique is to utilize the trained constitutive law for the application at the macro scale analysis. Hence, this section presents the application of the trained model Ψ to the analysis of two different in plane tests performed on a masonry wall. The results obtained from both the macro scale analyses are compared with the results of a numerical micro model. The micro model has exactly the same geometrical masonry bond allocation as the RVE used in the virtual laboratory. The section is structured by firstly explaining the two numerical tests, followed by a discussion about the results from the micro and macro models.

6.5.1 Numerical analyses

Subject of the numerical analyses are two 2D micro and a macro models of the same masonry wall. The micro model wall respects the same geometrical allocation of the bricks (Flemish bond) as utilized for the RVE of the virtual laboratory. However, the dimensions of the wall measure $1.27 \times 1.27\ m^2$, which is larger than the dimensions of the RVE. Each of the two walls is subjected to two different boundary conditions. The first analysis is a compression test and the second one is a shear compression test. The walls are loaded by incrementally applying displacements on top of the wall until failure. Figure 6.9 shows the concepts for both the numerical tests.

Compression test The finite element nodes of the base of the wall are fixed for displacements in any direction. The load is applied by monotonically increasing a vertical displacement to the top nodes of the wall's finite element model in order to perform the compression test.

Shear compression test The finite element model of the shear compression test is subjected to two loading sets. The first is an incrementally increasing vertical

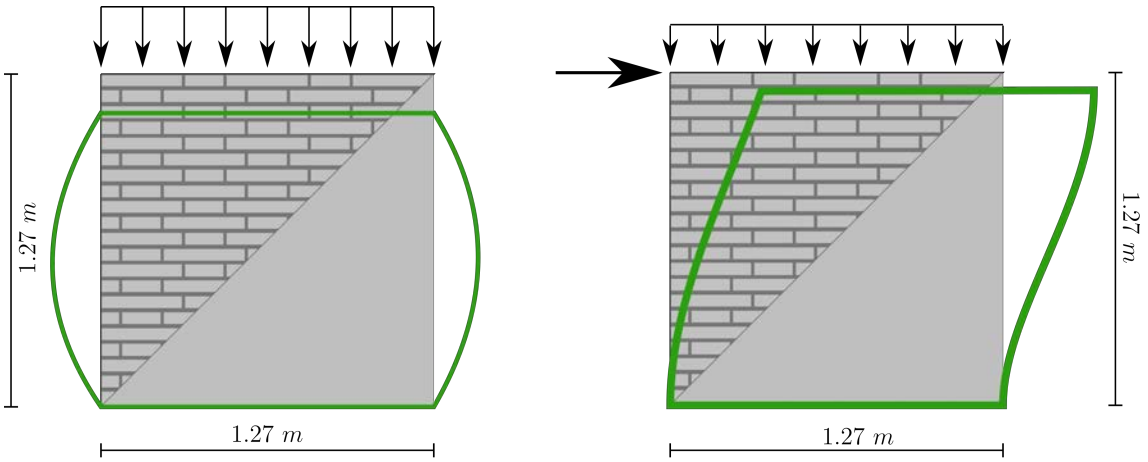

Figure 6.9: Schematic views of the micro and macro models of the compression and the shear compression tests.

displacement similar to the model of the compression test. This vertical displacement moves up to a predefined value of $d_y = 0.09\ mm$ where no failure of the wall is caused. This vertical displacement is kept constant during the second step of the analysis and equals a vertical load of $\sigma_0 \approx 0.30\ MPa$. After having reached the vertical displacement, a monotonic increasing horizontal top displacement is applied in order to burden the wall in shear. The horizontal displacement is then applied until ultimate failure of the model.

A total number of four numerical analyses is performed in this example. Two of them are the micro model analyses of the compression and the shear compression test, respectively. The material properties of the micro model components have been introduced in Table 4.4 and are also applied here. The remaining two analyses are the macro model analysis of both the compression and the shear compression test. The smeared material properties of the macro models have been predicted in the previous sections in terms of optimal fitting of the parameters $\boldsymbol{\Theta}$ of the constitutive model Ψ. The properties applied are shown in Table 6.4.

All the analysis are calculated by utilizing the finite element program KRATOS MULTIPHYSICS. The analyses at macro scale utilize the novel implemented constitutive law introduced in Section 5.5. It applies the transformation matrix $\boldsymbol{T}$ in order to map the strains and stresses from the anisotropic to the isotropic scale (and vice

versa).

6.5.2 Analyses results and comparison

Compression test The vertical reaction force of the two analyses was measured during the boundary application in order to compare the results. Figure 6.10 shows this force plotted against the applied vertical top displacement for the micro and the macro model analyses, respectively. The two tests remain in the linear range up to a top displacement of $d_y \approx 0.8\ mm$. The initial stiffness of the tests is approximately equal. After having reached the damage onset, material hardening starts for the analyses. The hardening progress can also be seen as approximately equal up to a top displacement of $d_y \approx 6.0\ mm$. Table 6.5 shows the maximum vertical reaction forces and the corresponding top displacements of the two models. The capacity of the macro model Ψ is slightly larger than the capacity of the micro model. A deviation of the peak value from the macro scale analyses with respect to the peak of the micro model counts 6.6 %.

Table 6.5: Compression test: peak values of the micro and the macro models.

	Vertical force $F_y\ [MN]$	Displacement at peak $d_{y,peak}\ [mm]$
Micro Model	2.18	6.5
Macro model Ψ	2.33	7.5

Figure 6.11 shows the crack patterns of the compression tests in terms of the contour plots of the maximum principal strains and total displacements. All plots are taken at a top displacement of $d_y = 10.0\ mm$. The crack pattern of the micro model analysis exhibits the hourglass shape which is typical for compression tests on brittle materials such as masonry. The macro model analyses is able to produce an overall crack pattern very similar to the one of the micro model. The results of the compression test have shown that the trained macro model is an appropriate model when compared with the compression test analysis of a micro model.

Shear compression test The comparison of the shear compression test applied to the micro and the macro model is based on the measurements of the horizontal

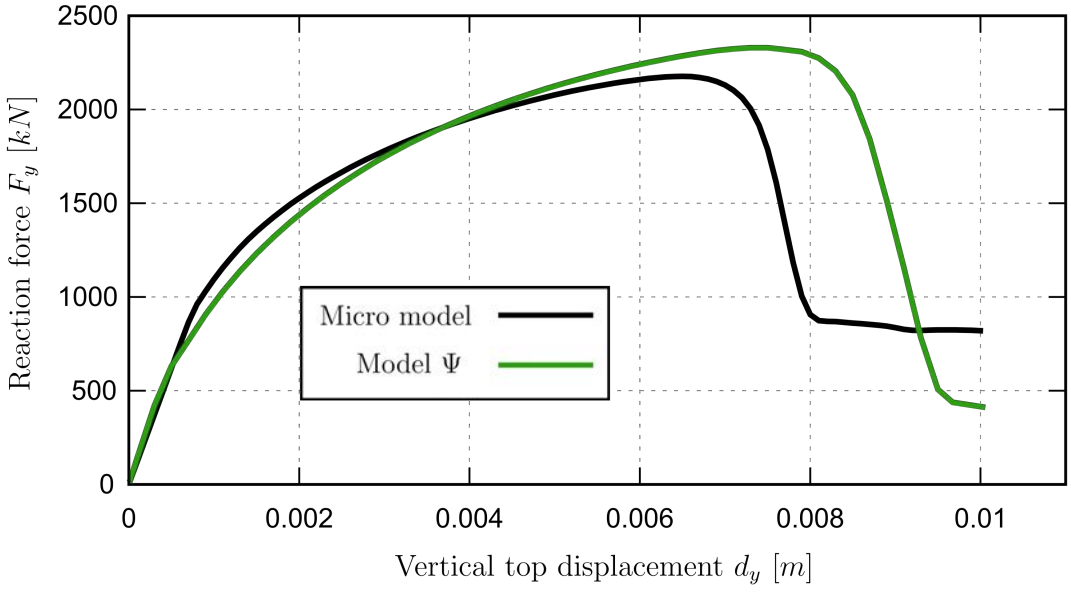

Figure 6.10: Compression test: vertical reaction force vs. vertical displacement curves of the micro and the macro models.

reaction force F_x. Figure 6.12 depicts the curves of the force plotted against the horizontal top displacement d_x for the two analyses, respectively. The initial stiffness demonstrates an equal linear elastic behavior for both the models. A damage onset starts at a horizontal top displacement of $d_x \approx 0.03\ mm$. Further increasing of the deformation leads to similar behavior of the models up to a reaction force of $F_x \approx 180.0\ kN$. From there on, the curve of the macro model Ψ rises flatter than the micro model curve until both the analyses reach their peak.

Table 6.6 shows the peak values of the horizontal reaction forces for both the analyses and the corresponding horizontal top displacements at the peak. A deviation of 9.7 % between the force peaks can be observed.

Figure 6.13 shows the contour plots of the maximum principal strain and the global displacement at a horizontal top displacement of $d_x = 3.8\ mm$ for the results

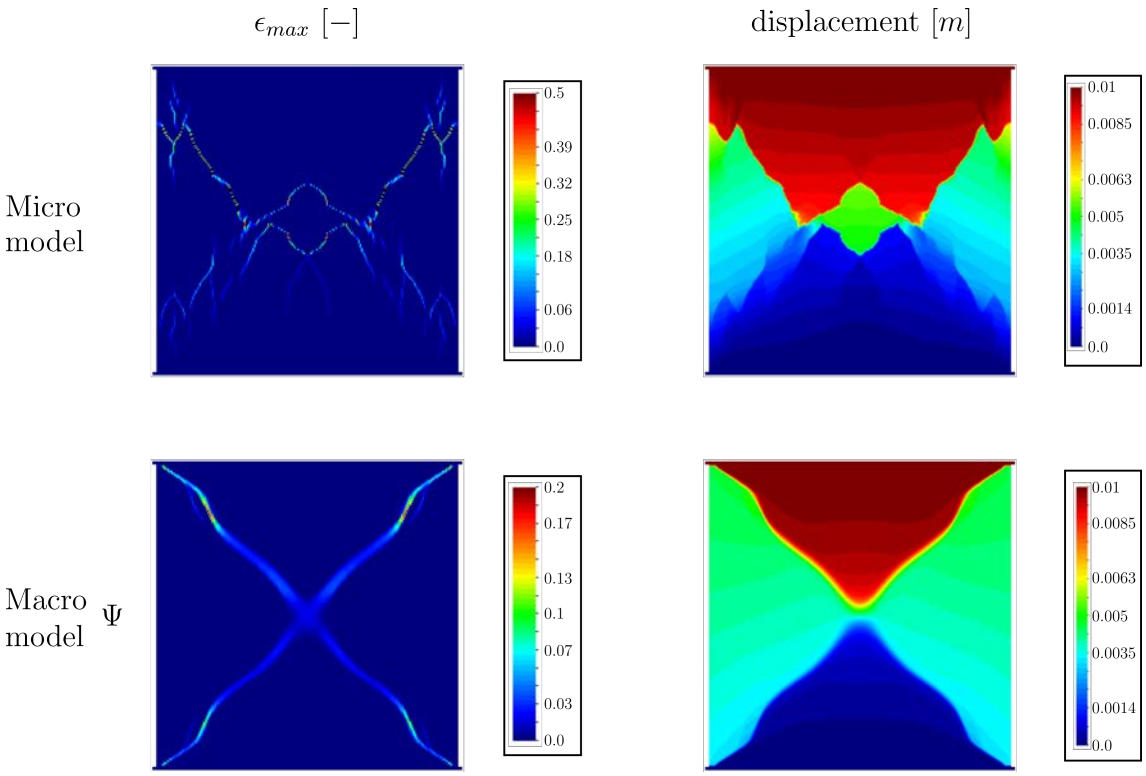

Figure 6.11: Compression test: crack patterns of the micro model and the macro model Ψ, and the contour plots of the maximum principal strain ϵ_{max} and the displacement at a vertical top displacement of $d_y = 10.0\ mm$.

of the micro model and the macro model analyses, respectively. The maximum strain contour plot of the micro model demonstrates a diagonal crack that passes through the mortar joints and the brick units. Such a pattern is typical for shear compression tests of masonry walls (Petracca (2016)). This single diagonal crack leads to ultimate failure of the micro model.

The crack pattern of macro model Ψ, shown in the contour plot of the maximum strain, demonstrates a single diagonal crack. This crack leads to failure of the model at a horizontal top displacement very similar to the one of the micro model.

The numerical analysis results of the compression and the shear compression tests show that the macro model Ψ is able to represent the micro model results very accurately. This is shown in the comparison of the force displacement curves on the one hand and in the evolution of cracks on the other hand.

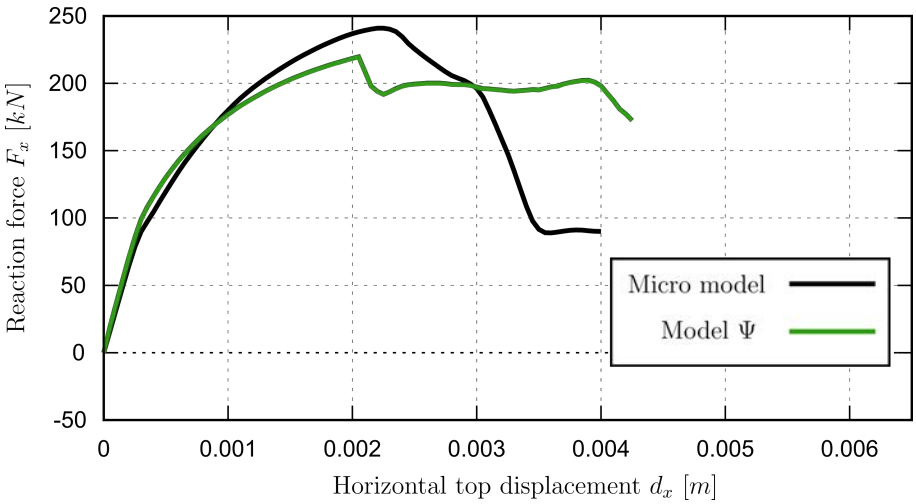

Figure 6.12: Shear compression test: curves showing the horizontal reaction force vs. horizontal displacement of the micro model and the macro model Ψ.

Table 6.6: Shear compression test: peak values of the micro and the macro models.

	Horizontal force F_x $[MN]$	Displacement at peak $d_{x,peak}$ $[mm]$
Micro Model	0.24	2.2
Macro model Ψ	0.22	2.1

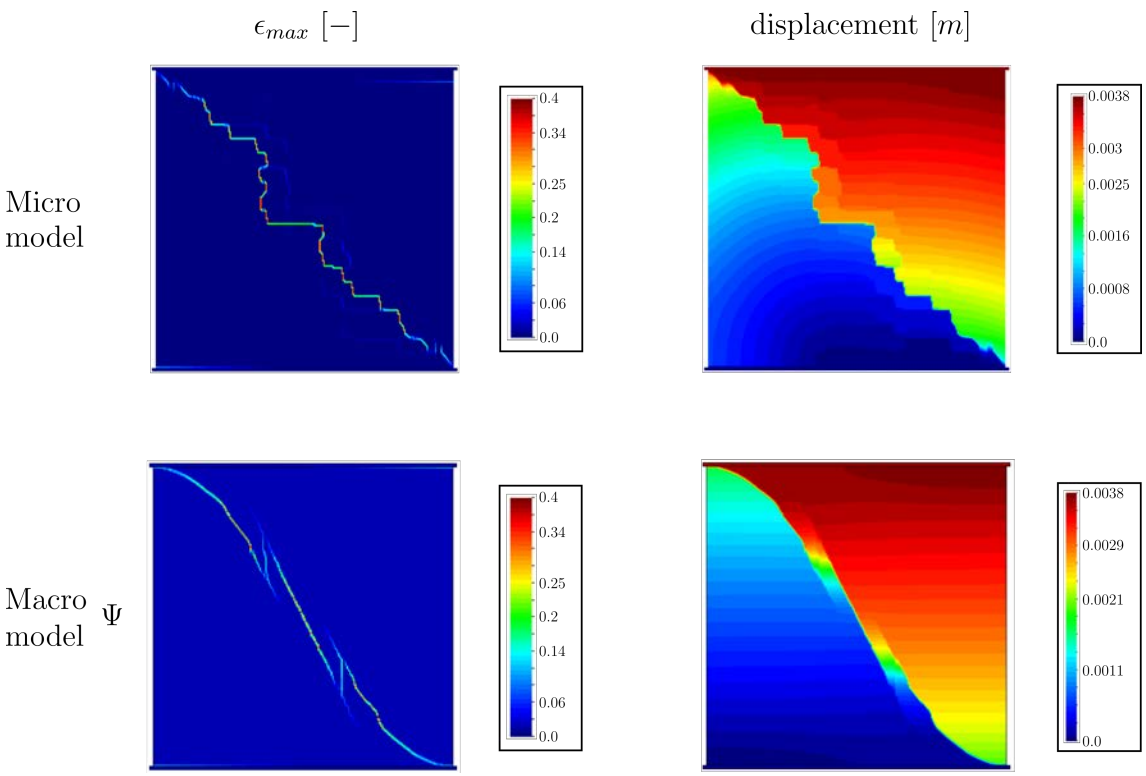

Figure 6.13: Shear compression test: crack patterns of the micro model and the macro model Ψ, and the contour plots of the maximum principal strain ϵ_{max} and the displacement at a horizontal top displacement of $d_x = 3.8\ mm$.

6.6 Summary

This chapter has presented the application of the machine learning homogenization technique to the numerical analysis of a Flemish bond masonry wall. Chapter 5 has presented the theoretical background and the steps of the homogenization procedure. The present chapter has adopted the necessary tasks and furthermore clarified their application.

In the first step, the virtual laboratory has been build up, by including the micro modeling of a masonry RVE in Flemish bond, and the calibration of the brick and mortar material properties. The RVE has been subjected to a number of virtual experiments. A total of 26 boundary conditions have been created in order to cover a wide range of different deformations of the RVE. The results of the 26 cases have been presented in this chapter in terms of plots of the damage contours, and peak values of principal stresses. It has been shown that the results exhibit the typical anisotropy of masonry micro models. For this purpose, the virtual laboratory results have been made compatible with the isotropic constitutive laws implemented in the machine learning model by applying the transformation procedure presented in Chapter 5 to the entire set of the virtual laboratory results. Furthermore, it has been shown that the computation of damage equivalent stresses has become necessary. This is due to equality of the principal direction angle of the strain and stress vectors.

In a second step of the application example, the essential part of the homogenization technique has been carried out, i.e. the machine learning. Its actual purpose has been to find a single constitutive law, that can be applied to the macro scale analysis of masonry, without loosing the accuracy of micro modeling. Therefore, the computation graph of the machine learning model has been introduced. This example has considered a constitutive model that utilizes advanced yield criteria and damage evolution laws. The graph has been defined by these assumptions and its corresponding set of trainable variables.

Once the model has been set up, the actual training procedure has been executed. In order to minimize the computational cost of the training loops, the data input coming from the virtual laboratory has been split into a number of sets. As a result, the procedure of variable training has also been split up to the number of obtained sets. An overview showing the trainable variables of the model and each set has been given. The results of the training loop have been presented in terms of evolution of

the training loss and the variable modifications per set and per model.

A table has been drawn that summarizes the final variable results of the model. These results have been taken in order to evaluate the machine learning prediction. In order to evaluate the predictions offline, a second new virtual laboratory campaign has been carried out. Its results have been compared with the prediction results made by the model. The predictions have shown to be very accurate and the trained model is able to represent the virtual laboratory results.

The last step of the machine learning homogenization technique has been the evaluation of the results at a finite element analysis level. Thus, a post machine learning application of the trained constitutive model has been performed. Two numerical tests, a compression and a shear compression test, have been carried out.

The analyses have been carried out at two scales, micro and macro scale, in order to be able to compare the macro scale results with the micro scale results. Thus, two models have been built up. The micro model properties have been chosen to be equal to the ones of the RVE, and the macro model properties have been assumed to be those predicted by the machine learning. Force-displacement curves and crack patterns of the micro and macro model analyses have been investigated in order to compare the analysis results. It has been shown that the macro models are able to represent the micro model results very accurately.

Chapter 7

Seismic Analysis of Palacio Pereira using Machine Learning based Homogenization

7.1 Introduction

The previous Chapters have introduced a machine learning based homogenization technique that results in a homogeneous constitutive law that can be used for the macro scale analysis of masonry structures. This Chapter investigates its applicability on real scale structures and discusses its results when compared to conventional macro scale analyses.

The structure chosen for this application example, is the Palacio Pereira already introduced in Chapter 3. Subject will be multiple numerical pushover analyses of the buildings facades within a two-dimensional macro scale approach. Both facades of the Palacio Pereira (Southern and Eastern) are charged during each analysis with monotonically increasing horizontal accelerations. Such an analysis is known as mass proportional pushover analysis.

Section 7.2 shows the conventional approach of applying nonlinear pushover analysis to masonry structures. Therefore a geometrical FE model of the two facades is build up within the commercial FE software DIANA FEA TNO (2017). The macro material properties are calibrated by adjusting them in order to be able to represent the results of an in-situ experiment. The experiment has been performed by Sandoval et al. (2017) and its results will be presented here together with the DIANA

FEA macro model calibration.

After having demonstrated the conventional approach of defining macro model material properties, Section 7.3 shows the application of the novel approach for material homogenization based on machine learning. The nonlinear pushover analyses of the facades are then numerically performed within the open source software KRATOS MULTIPHYSICS Dadvand et al. (2010). The post machine learning constitutive model is implemented in its framework.

Unlike the conventional approach, the machine learning based homogenization requires the calibration of a micro model, training data production and the machine learning. Each respective step has been demonstrated in the detailed application example of Chapter 6. An analogous procedure is utilized here in order to carry out the machine learning based homogenization of the Palacio Pereira.

Section 7.4 presents and discusses the results of the pushover macro scale analyses of the facades carried out in DIANA FEA and KRATOS MULTIPHYSICS, respectively. The final Section 7.5 gives a summary of this Chapter.

7.2 Conventional macro scale seismic analysis

7.2.1 Macro model calibration

Numerical analysis of entire masonry buildings is a challenging task, since the heterogeneous material of masonry must be simplified to a smeared macro model approach. Therefore, a conventional technique is the calibration of a numerical macro model that aims to fit appropriately the results of an experimental test. In case of the Palacio Pereira, an in-situ experiment has been performed by Sandoval et al. (2017). The test setup and the final crack pattern are shown in Figure 3.6a and 3.6b.

The calibration of this experiment has been performed in DIANA FEA. Therefore, a numerical FE model of the in-situ experiment has been built up by using symmetry. The nodes of the upper boundary are fixed in horizontal and vertical direction. However, in order to apply the weight acting on this wall, a fixed vertical displacement is applied that is equal to a load of 0.14 MPa (also assumed by Sandoval et al. (2017)). The nodes of the lower boundary are fixed only in vertical direction. An incrementally increasing horizontal load, simulating the force induced

by the hydraulic jack, is applied by displacing the lower boundary nodes in horizontal direction. Non linearity of the material is included to the model by utilizing the total strain based rotating crack model implemented in DIANA FEA. A parabolic softening behavior in compression and an exponential softening behavior in tension is assumed. The analysis is carried out until failure.

Figure 7.1 depicts the crack pattern of the numerical analysis by showing the crack width distribution. A consistent single shear crack is evolving during the numerical analysis. Moreover, Figure 7.1 shows the plots of the horizontal force over the angular strain curves of the in-situ experiment and the numerical calibration analysis, respectively. The curve of the numerical analysis is in a very good agreement with the curves of the experiment.

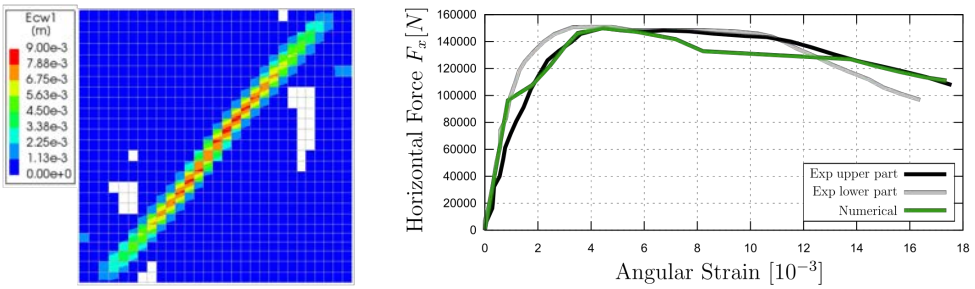

a) b)

Figure 7.1: Macro model calibration results for conventional macro model analysis of large scale structures. Showing a) the crack width distribution of the numerical calculation at failure, and b) the numerical results compared with the experiment (Sandoval et al. (2017)) in terms of angular strain versus horizontal reaction force curve.

The conventional approach of calibrating macro model material properties for large scale analysis applications, based on reproduction of one physical experimental test, is completed. Table 7.1 shows the material properties obtained during macro model calibration. These properties are from now on utilized for the macro model large scale pushover analyses of the Palacio Pereira in DIANA FEA.

7.2.2 Macro scale pushover analysis

Figure 7.2 shows the two dimensional FE models of the Southern and Eastern facade of the Palacio Pereira as modeled in DIANA FEA. Four noded quadrilateral elements have been used for the numerical FE models with an average size of approximately

Table 7.1: Material properties of the macro crack model for the finite element model of the *Palacio Pereira* in DIANA FEA of Chapter 7

Material property	**Symbol**	**Value**	**Unit**
Density	ρ	1800	kg/m^3
Young's modulus	E	775.0	MPa
Poisson's ratio	ν	0.2	-
Compressive strength	f_p^-	1.65	MPa
Compressive fracture energy	G^-	5.0	kN/m
Tensile strength	f_p^+	0.095	MPA
Tensile fracture energy	G^+	0.05	kN/m
Residual compressive strength	f_r^-	0.5	MPa
Residual tensile strength	f_r^+	0.005	MPa

0.22 m. In both the models all base nodes of the FE element mesh are fixed in x and y direction, respectively. The material parameters have been adopted from the previous calibration and are summarized in Table 7.1. The weights of the first floor and the roof are added as point mass to the respective nodes of the mesh.

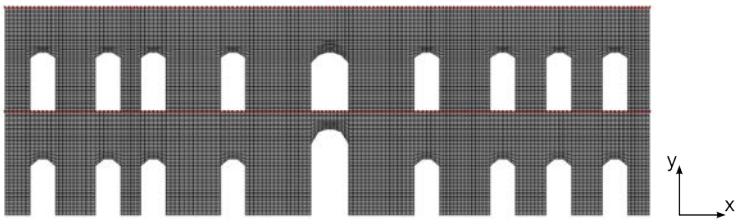

(a) South facade

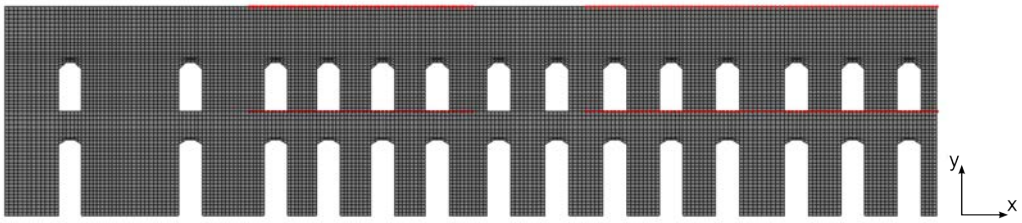

(b) East facade

Figure 7.2: Two dimensional FE models of the facades of the Palacio Pereira for the numerical analyses in DIANA FEA

The nonlinear mass proportional pushover analysis is applied to both the facades. Each analysis is performed in two steps. Firstly, the self weight of the structure is applied in gravity direction (y-direction). Secondly, the monotonically increasing

lateral pushover acceleration is applied horizontally. The numerical problem is solved using an arc length control and the Newton-Raphson method.

The results are going to be discussed in Section 7.4 by comparing them with the novel machine learning based homogenization approach.

7.3 Machine learning based homogenization approach for seismic analysis

7.3.1 Micro model calibration

The machine learning based homogenization technique rests upon the performance of a virtual laboratory in order to produce the training data. The virtual laboratory requires a micro model RVE in order to run the multiple numerical experiments. However, the material properties of the RVE must be calibrated previously. Therefore, a proper micro model analysis of the experimental in-situ test shown in Section 7.2.1 is performed.

The real brick/mortar allocation of the Palacio Pereira for the micro model has been taken from pictures made during the in-situ experiment and the size of the bricks used for the construction. Figure 7.3 shows the FE model with brick mortar distinction and shows the dimensions of the brick. The mortar thickness is assumed to be approximately 20 mm. The average element size counts 10×10 mm^2 so that the mortar is modeled by two elements in its thickness direction. The total number of elements counts 10300.

As for the calibration of the macro model in DIANA FEA the boundaries are chosen as follows. The top nodes of the FE model are constrained in horizontal and vertical direction. Whereas the bottom nodes are constrained only in vertical direction so that the monotonically increasing load can be applied in horizontal direction.

Both the components, brick unit and mortar joint, are modeled by continuous elements with d^+/d^- damage models (Chapter 4). Both yield criteria, in tension and compression, are the Petracca modified Lubliner yield criteria that better controls the damage effects under shear loading. In compression the damage evolution follows the Bézier like hardening softening behavior as introduced in Chapter 4 and in tension an exponential softening is assumed. A calibrated micro model can be

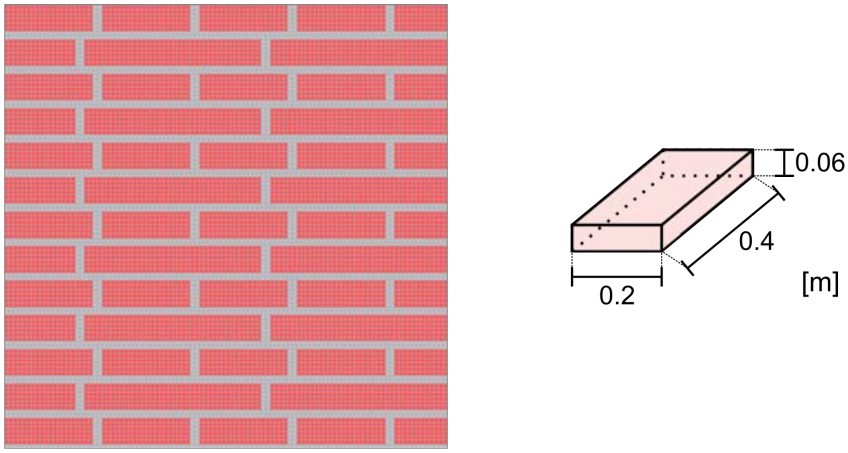

Figure 7.3: Micro model FE mesh for the numerical calibration of the Palacio Pereira in-situ experiment and a schematic three dimensional display of the Palacio Pereira brick size

obtained when using the material properties, as shown in Table 7.2 .

Table 7.2: Material properties, brick unit and mortar joint, for the numerical analysis of the in-situ shear compression test applied to an inner wall of the Palacio Pereira

Brick unit

E	ν	f_p^+	G^+	f_0^-	f_p^-	f_r^-	ϵ_p^-	G^-	k_b	κ
1400.0	0.2	0.6	0.12	2.0	6.7	1.0	0.03	35.0	1.2	0.16
$[MPa]$	–	$[MPa]$	$[\frac{N}{mm}]$	$[MPa]$	$[MPa]$	$[MPa]$	–	$[\frac{N}{mm}]$	–	–

Mortar joint

E	ν	f_p^+	G^+	f_0^-	f_p^-	f_r^-	ϵ_p^-	G^-	k_b	κ
200.0	0.2	0.3	1.5	0.5	2.0	0.1	0.03	35.0	1.2	0.16
$[MPa]$	–	$[MPa]$	$[\frac{N}{mm}]$	$[MPa]$	$[MPa]$	$[MPa]$	–	$[\frac{N}{mm}]$	–	–

Figure 7.4 shows the results of the numerical analysis when compared with the experimentally recorded strain - force curve. Figure 7.5 shows the evolution of the diagonal shear crack for different analysis steps.

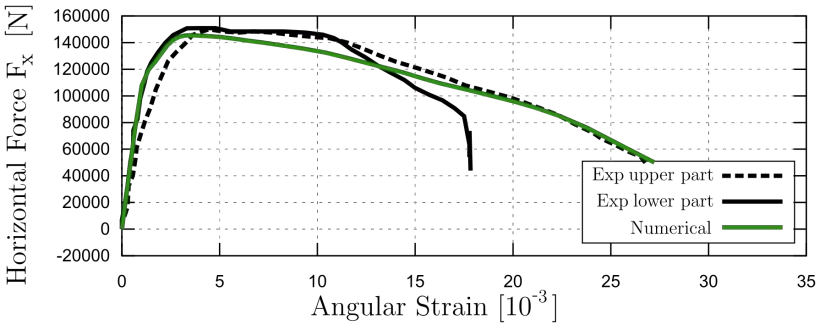

Figure 7.4: Micro model calibration results of the Palacio Pereira in-situ shear test in terms of angular strain - horizontal force curve. Comparison of the experimental results (Sandoval et al. (2017)) with the numerical micro model results

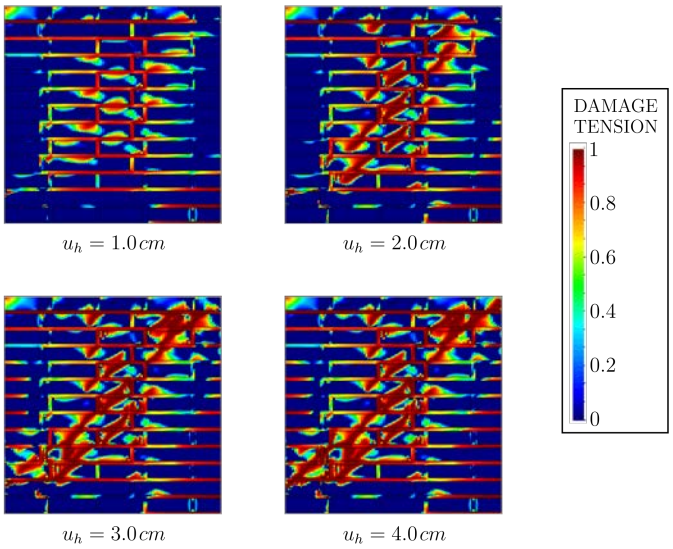

Figure 7.5: Contour plots of the the damage tension parameter d^+ for the micro model analysis of the Palacio Pereira in-situ experiment for four different horizontal displacements

7.3.2 Virtual laboratory performance

Proceeding from the calibrated model of the previous Section, a micro model RVE is constructed. Figure 7.6 shows the micro model considered for the virtual laboratory of the Palacio Pereira homogenization. It is assigned with the material parameters of the previous calibration (Table 7.2). The geometry of the RVE is obtained by

extracting a cut from the micro model used for calibration. The edge size of the FE model is 0.76 m and counts 5928 elements.

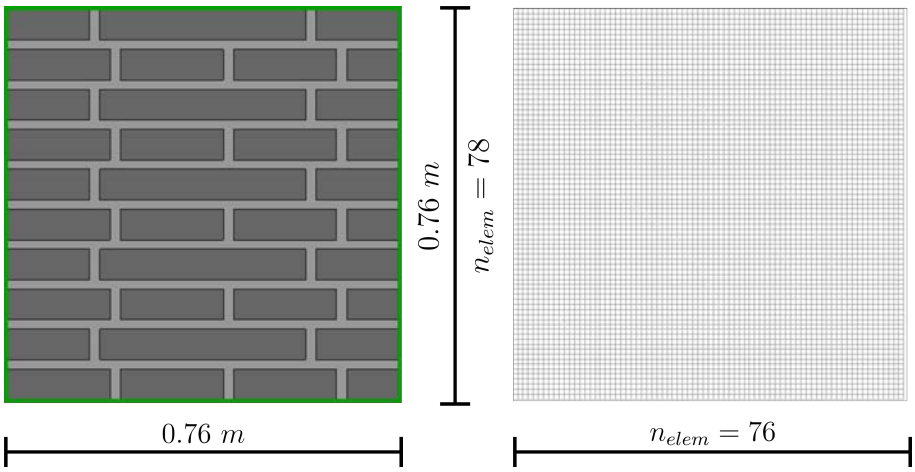

Figure 7.6: The representative volume element of the Palacio Pereira virtual laboratory showing the brick mortar allocation, the model size and the FE mesh

The virtual laboratory is carried out in the same way as already presented in the application example of Chapter 6. A number of $n_{VL} = 26$ different boundary conditions are applied to the RVE so that 26 different strain/stress conditions are represented in the training data set. Each respective analysis is carried out until failure. Figure 7.7 depicts the ultimate damages of each virtual experiment, respectively. The entire set of stored coupled strain and stress states counts 30160. All of them serve as input for model training.

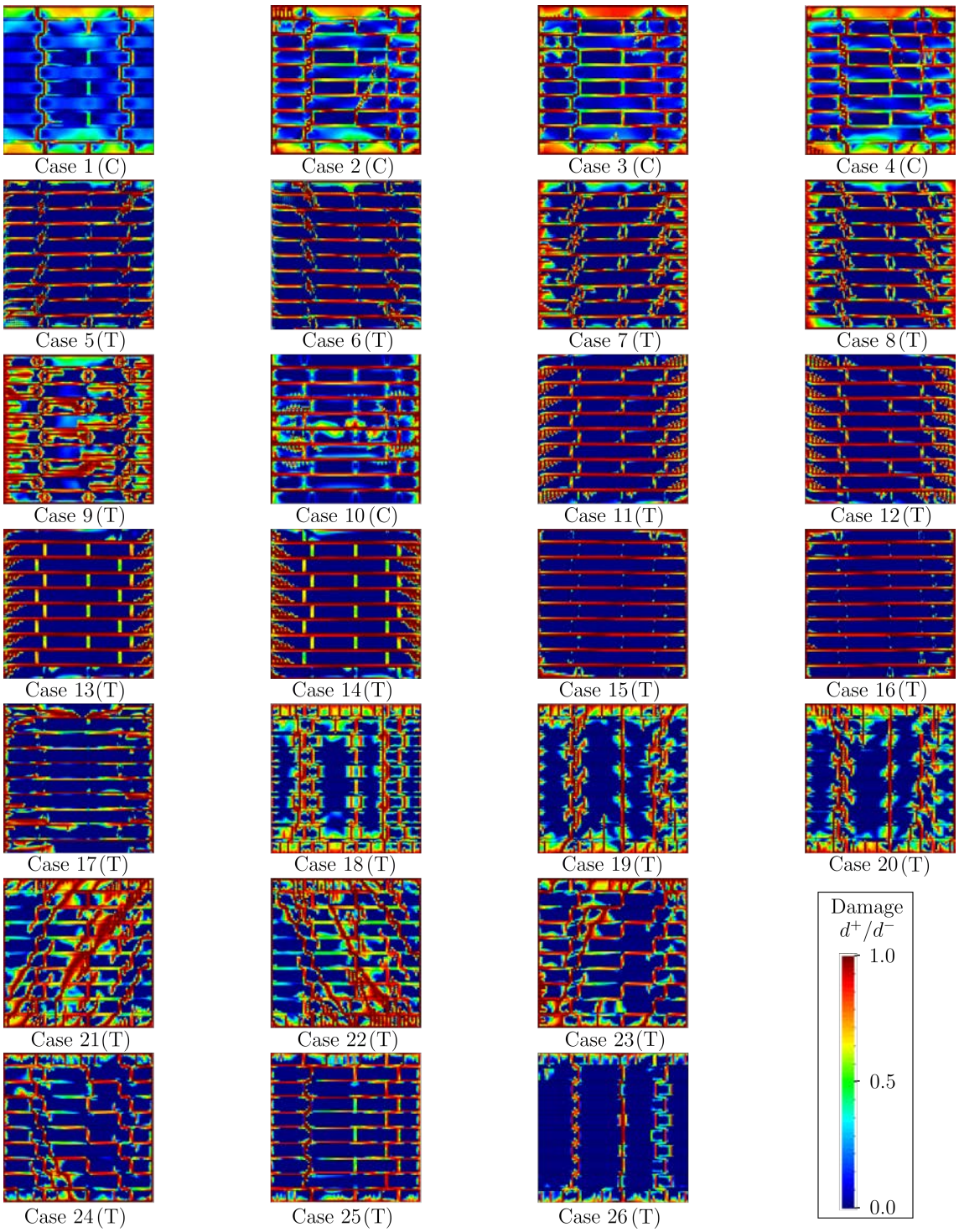

Figure 7.7: Palacio Pereira RVE virtual laboratory: damage contour plots of the 26 cases considered in the virtual laboratory, showing the damage variables d^+/d^- depending on the significant damage (T for tension, C for compression)

7.3.3 Constitutive model determination

7.3.3.1 Linear elastic parameters

The determination of the anisotropic and the corresponding closest isotropic matrix is performed analogously as done in Section 6.3. The following raw (anisotropic) elasticity matrix $\boldsymbol{C}_{raw}$, the closest isotropic elasticity matrix $\boldsymbol{C}_{iso}$ and the transformation matrix $\boldsymbol{T}$ can be obtained after applying the procedure described in Section 5.4 as follows

$$\boldsymbol{C}_{raw} = \begin{bmatrix} 921.9 & 116.4 & -0.428 \\ 116.4 & 635.3 & -0.145 \\ -0.429 & -0.145 & 250.5 \end{bmatrix} MPa \tag{7.1}$$

$$\boldsymbol{C}_{iso} = \begin{bmatrix} 762.4 & 132.6 & 0.0 \\ 132.6 & 762.4 & 0.00 \\ 0.0 & 0.0 & 314.9 \end{bmatrix} MPa \tag{7.2}$$

$$\boldsymbol{T} = \begin{bmatrix} 1.1 & -0.02 & -0.0005 \\ 0.0 & 0.92 & -0.0001 \\ 0.0 & 0.0 & 0.89 \end{bmatrix} [-] \tag{7.3}$$

The isotropic linear parameters assumed in the following machine learning procedure are then $E = 739.3\ MPa$ and $\nu = 0.174$.

7.3.3.2 Damage model parameters

The computation graph of the TENSORFLOW Abadi et al. (2015) application contains the constitutive damage model introduced in Chapter 4. It considers the bi-dissipative $d^+ \backslash d^-$ damage law with the Bézier like damage evolution both in tension and compression behavior. Furthermore, a Rankine yield criteria is considered for tension behavior. Whereas for the compression behavior the Petracca yield criterion is chosen. These assumptions are based on the application example of Chapter 6. Where the Graph $\mathcal{G}$ has shown to be able to train a very accurate macro model damage law. Therefore, the same model modifications are chosen for the Palacio Pereira application.

These assumptions lead to a machine learning model with 17 trainable variables. In order to separately train tension and compression parameters the training input

set is divided into three different sets. Each set does then serve as input for six training steps (see procedure description in Chapter 6).

Table 7.3 shows the optimization results of the machine learning procedure. The values are then stored together with the transformation matrix $\boldsymbol{T}$ (Equation 7.3) and the isotropic elasticity parameters E and ν in a separate file that serves as material property file for the post machine learning application.

Table 7.3: Optimization results of the parameters of the machine learning model for the homogenization of the Palacio Pereira in terms of the Bézier regulators

Tension Parameters

f_0^+	f_p^+	f_r^+	e_p^+	c_1^+	c_2^+	c_3^+
$[Mpa]$	$[Mpa]$	$[Mpa]$	$[-]$	$[-]$	$[-]$	$[-]$
0.15	0.37	0.012	0.0008	0.5	0.82	16.7

Compression Parameters

f_0^-	f_p^-	f_{bi}^-	f_r^-	e_p^-	c_1^-	c_2^-	c_3^-
$[Mpa]$	$[Mpa]$	$[Mpa]$	$[Mpa]$	$[-]$	$[-]$	$[-]$	$[-]$
0.88	4.58	4.81	0.57	0.069	0.5	0.04	1.09

7.3.4 Model evaluation by in-situ shear test analysis

The previous machine learning based homogenization of the masonry properties of the Palacio Pereira is going to be evaluated here. Therefore, a numerical macro analysis, taking into account the machine learning based macro constitutive law, of the in-situ experiment is carried out.

Figure 7.8 depicts the FE mesh of the model. The average element size is approximately $35 \times 35\ mm^2$. It also shows the results of the first principal strain at the ultimate analysis stage reproduces accurately the diagonal shear crack of the in-situ experiment. Figure 7.8 plots also the horizontal reaction force over the angular strain. The numerical results present the same initial stiffness behavior as the results from the experimental curve. Also the ductility can be reproduced very properly.

However, the peak value of approximately 150.0 kN cannot be reached by the numerical macro model analysis. Nonetheless, this material model is considered to be on the safe side, since the peak value is less than the value reached in the experiment. One must also have in mind, that the virtual laboratory takes into account distinct deformation cases that serve for the model calibration. A discussion about this behavior in connection with the application to the large scale structure is following in this chapter.

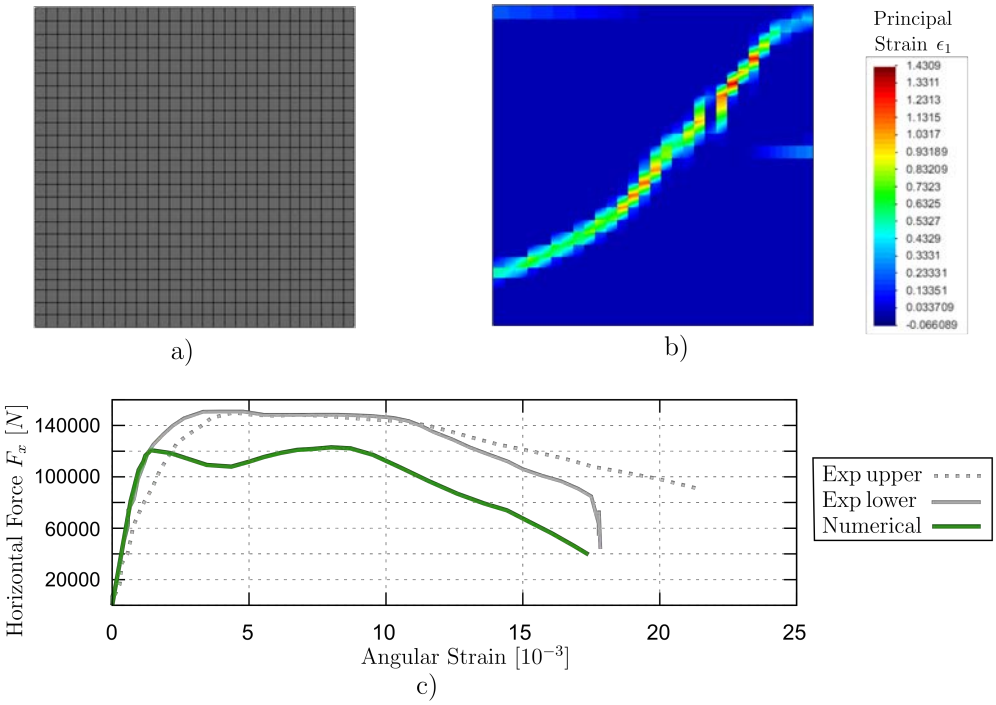

Figure 7.8: Post machine learning macro model analysis of the Palacio Pereira in-situ shear test. Showing a) the FE mesh, b) the first principal strains at the ultimate analysis stage, and c) the horizontal reaction force plotted against the angular strain for the numerical macro analysis and the recorded values during the experiment

7.3.5 Macro scale pushover analysis of Palacio Pereira

The mass proportional pushover analyses in KRATOS MULTIPHYSICS are carried out by utilizing the machine learning based homogenized material damage law elaborated in the previous sections. In this context, the orthotropic approach, applying the previously defined transformation procedure (with $\boldsymbol{T}$ from Eq. 7.3) is considered. In addition an isotropic approach is applied, where the transformation matrix

$\boldsymbol{T}$ is equalized to the identity matrix $\boldsymbol{I}$.

The aim of this analyses is to compare the results with the ones obtained by the conventional approach applied in DIANA FEA, where the material is considered isotropic. Therefore, the equal FE mesh discretization of the South and East facade used in DIANA FEA of the Palacio Pereira is elaborated for the KRATOS MULTIPHYSICS analyses. Figure 7.9 shows both the FE models.

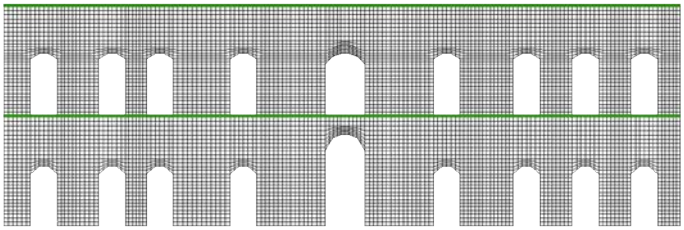

(a) South facade

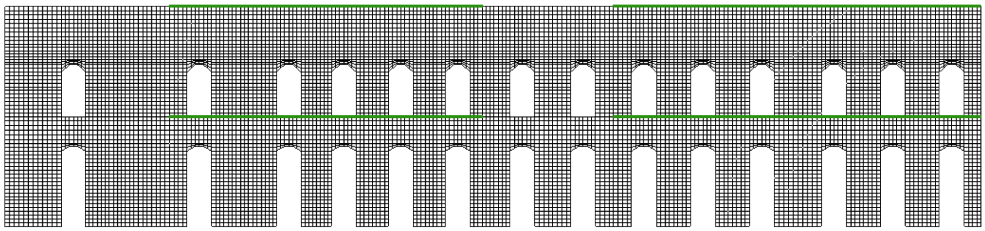

(b) East facade

Figure 7.9: Two dimensional FE models of the facades of the Palacio Pereira for the numerical analyses in KRATOS MULTIPHYSICS

Each analysis is carried out analogously to the pushover analysis performed in DIANA FEA. In a first step the selfweight is applied by activating gravity acceleration. Secondly, monotonically increasing horizontal accelerations are applied to the model. Each one is preformed until failure. Section 7.4 presents the results and compares them with the ones obtained in the DIANA FEA analyses.

7.4 Results and discussion

This Section presents the results of the pushover analyses of the Palacio Pereira. It gives a comparison of the conventional macro scale and the machine learning based homogenization approach for the application of smeared damage models. Firstly, a short discussion about the linear elastic parameters is given. In a second step,

the control node displacements, the damage patterns and the failure modes of the seismic pushover analyses will be presented and discussed.

7.4.1 Linear parameters

Equation 7.4 shows the plane stress linear elasticity matrix $\boldsymbol{C}_{conv}$ of the DIANA FEA macro model analysis. With the Young's modulus and the Poisson's ratio being $E = 775.0\ MPa$ and $\nu = 0.2$.

$$\boldsymbol{C}_{conv} = \begin{bmatrix} 807.29 & 161.46 & 0.0 \\ 161.46 & 807.29 & 0.0 \\ 0.0 & 0.0 & 322.92 \end{bmatrix} MPa \tag{7.4}$$

When comparing this matrix with the elasticity matrix of the machine learning approach at isotropic scale (Equation 7.2) a slightly stiffer, but almost negligible difference in linear behavior at isotropic scale of both the approaches is expected. The following Section clarifies this statement.

7.4.2 Nonlinear analyses

7.4.2.1 Comparison of in-situ analysis results

Figure 7.10 shows the results of the macro model analysis performed in DIANA FEA and the micro model analysis carried out in KRATOS MULTIPHYSICS that has been utilized to calibrate the respective damage material models. The models parameters were adjusted in order to be able to numerically represent the results of an experimental in-situ test carried out in the Palacio Pereira. Figure 7.10 also presents the results of the post machine learning application of the trained macro model law.

7.4.2.2 South facade

Conventional macro approach Figure 7.11a shows the ultimate displacement of the pushover analysis carried out with DIANA FEA. First cracks appear at a base shear force of around $F_x \approx 1.2\ MN$ in the centered and the right neighbored spandrel at the first floor. These shear cracks evolve with increasing lateral acceleration. At a base shear force of approximately $F_x \approx 1.5\ MN$ shear cracks also appear in the spandrels of the base floor. While the lateral force is increasing further, the cracks

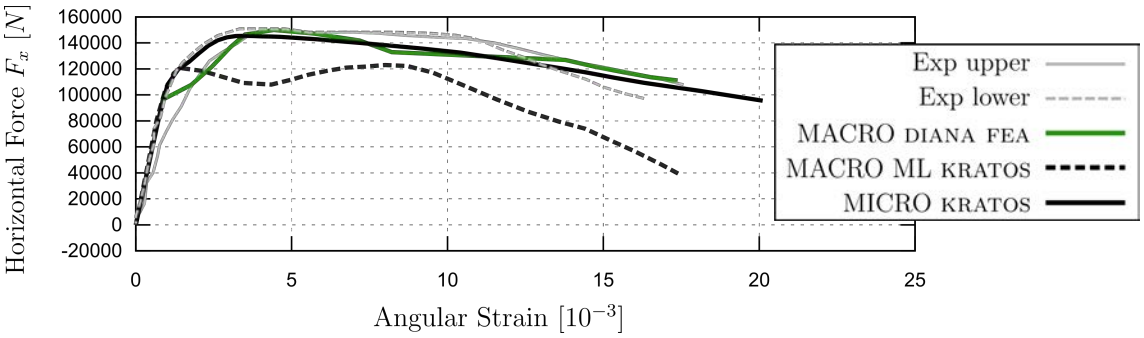

Figure 7.10: Numerical and experimental results of the Palacio Pereira in-situ experiment, showing the horizontal force plotted over the angular strain for the experiment and the numerical analyses carried out in DIANA FEA and KRATOS MULTIPHYSICS by considering a conventional macro model, a micro model and a machine learning based macro model calibration.

grow and at a maximum base shear force of $F_{x,max} \approx 1.8\ MN$ they completely disconnect the right part of the south facade from its left part. The final crack goes from the third opening at the base floor towards the fourth opening at the first floor and from there a diagonal shear crack going upwards further divides the facade. All locations are indicated from the right edge of the facade. Figure 7.12a shows the ultimate crack pattern of the south facade analysis by plotting the contours of the crack widths.

Machine learning based homogenization approach Figure 7.11b shows the ultimate displacement of the pushover analysis performed with KRATOS MULTIPHYSICS and the orthotropic law. The first damages appear at a base shear force $F_x \approx 1.5\ MN$ above both the biggest openings in the center of the facade. With increasing lateral acceleration the cracks start growing and further cracks appear in the remaining spandrels. While further increasing the load up to $F_x \approx 2.5\ MN$, two main shear cracks start to develop. One of them starting at the spandrel of the biggest opening in the first floor and the other expanding in the base floor from the opening right to the biggest one. At a maximum base shear of $F_{x,max} \approx 2.7\ MN$ both these cracks are connecting to a single crack entirely disconnecting the right part of the facade from the left part so that total failure occurs. This mechanism can be further investigated by considering Figure 7.12b. It shows the crack patterns of the pushover analysis at ultimate stage by plotting the contour of the tension damage parameter d^+.

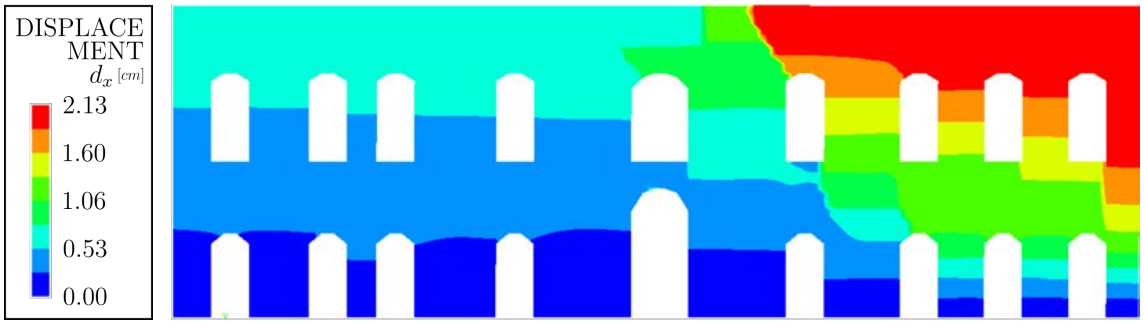

(a) Conventional approach DIANA FEA

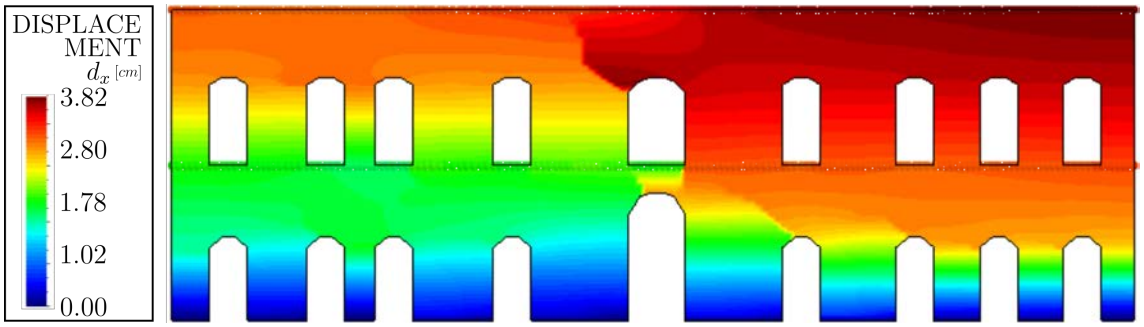

(b) Machine learning approach KRATOS MULTIPHYSICS (orthotropic)

Figure 7.11: South facade Palacio Pereira: contour plots of the horizontal displacement at failure of the structures, showing the results for the analysis in DIANA FEA and KRATOS MULTIPHYSICS

Pushover curves Figure 7.13 shows the pushover curves for the conventional (DIANA FEA) and the novel machine learning approach (KRATOS MULTIPHYSICS) in terms of isotropic and orthotropic analysis approach, respectively. It plots the recorded base shear force F_x versus the horizontal control node displacement d_x. The control node is located at the most upper right corner of the model for both the analyses.

Both the curves of the conventional and the isotropic machine learning based approach show an equal linear elastic behavior and thus outline a similar rigidity of both the models. This is in a very good agreement with the discussion already held in Section 7.4.1. When considering the orthotropic machine learning based approach, a slight decrease of stiffness can be observed.

However, a difference can be detected when comparing the maximum base shear forces. The conventional macro scale analysis performed in DIANA FEA has a maximum force of $F_{x,max} = 1.8MN$. This value undercuts the capacity of the machine learning based homogenization approach, as well as for the isotropic and the or-

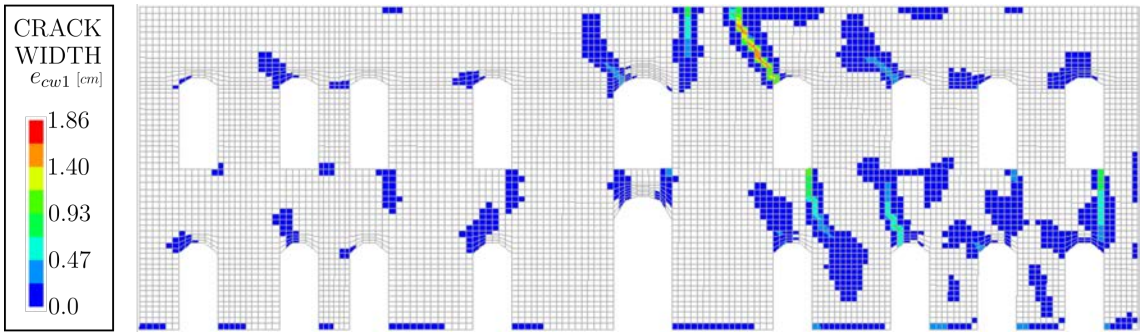

(a) Conventional approach DIANA FEA

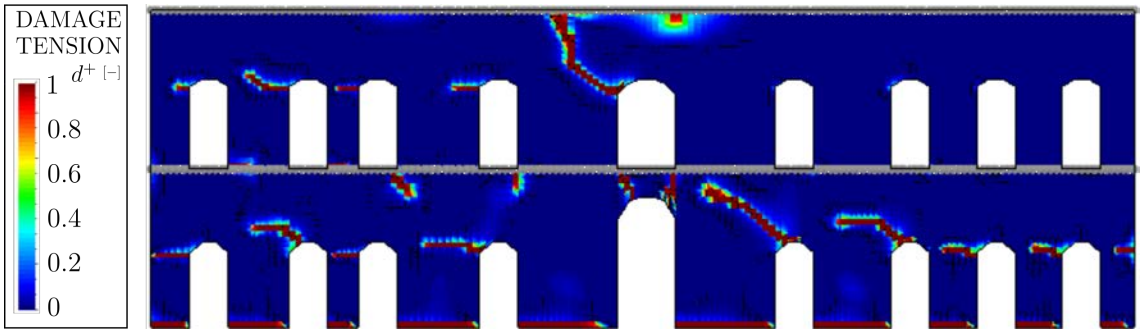

(b) Machine learning approach KRATOS MULTIPHYSICS (orthotropic)

Figure 7.12: South facade Palacio Pereira: contour plots of the cracks at failure of the structures, showing the results for the analysis in DIANA FEA and KRATOS MULTIPHYSICS

thotropic approach, significantly. Since both the maximum values lie at approximately $F_{x,max} = 2.7MN$.

Comparison with real earthquake damage Figure 7.14 shows two photos of the south facade in the damaged state captured after the 2010 Santiago de Chile earthquake. Shear cracks can be found in the spandrels of the building. A large crack is present in the spandrel at the center of the building which has been also detected by the numerical analyses. Furthermore Figure 7.14 also shows the cracks above the openings of the base floor that have been a result of the numerical analyses, too.

7.4.2.3 East facade

Conventional macro approach The horizontal displacement at an significantly damaged state of the pushover analysis performed in DIANA FEA is shown in Figure 7.15a by presenting a displacement contour plot. The damage mechanism develops

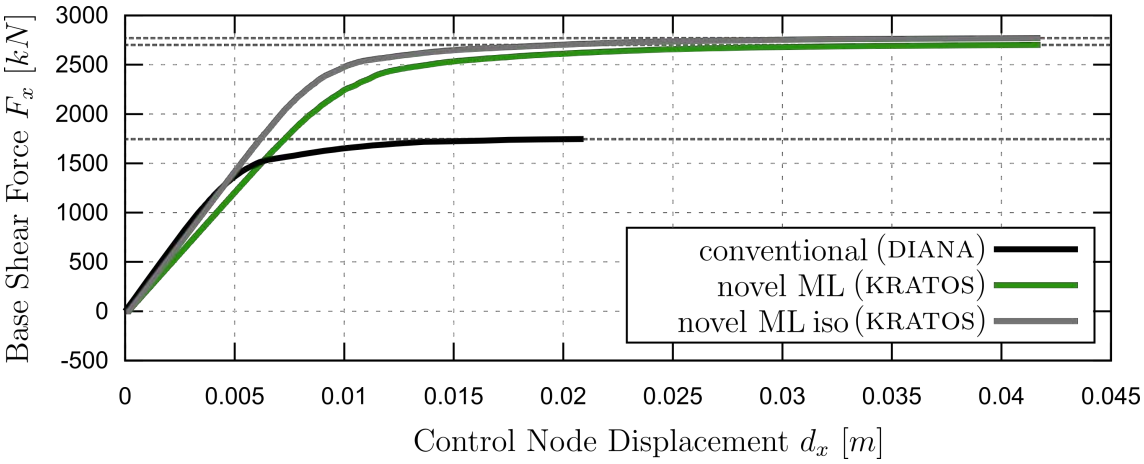

Figure 7.13: South facade Palacio Pereira: pushover curves showing the base shear force F_x plotted against the control node displacement d_x of the most upper right node of the FE models for the conventional DIANA FEA and the isotropic and orthotropic machine learning KRATOS MULTIPHYSICS approaches

as follows. The first small cracks initiate at a base shear force of approximately $F_x \approx 1.4\ MN$. Those cracks are located above almost all the openings spread over the facade. Further increasing the horizontal load up to $F_x \approx 1.7\ MN$ leads to the development of the two principal cracks located at the spandrels of the southern part (left) of the east facade. At a maximum base shear force of $F_{x,max} \approx 2.2\ MN$ the principal cracks are further expanding so that the right part of the facade is disconnected completely from the left part. Total failure has been reached. This mechanism is also clarified in Figure 7.16a. It demonstrates the crack pattern of the pushover analysis for the east facade by showing the contour plot of the crack widths.

Machine learning based homogenzation approach Figure 7.15b depicts the horizontal displacement of the pushover analysis carried out in KRATOS MULTIPHYSICS considering the orthotropic approach at the ultimate stage. The failure has developed as follows. First damage starts with a base shear force of $F_x \approx 1.8\ MN$. Cracks initiate above almost all the spandrels of the facade. While further increasing the load up to $F_x \approx 2.5\ MN$, two main cracks at the openings of the southern part (left) of the east facade evolve. Within an increase of $0.3MN$ these cracks are expanding so that the facade is separated completely. The total failure mechanism occurs at a shear base force of $F_{x,max} \approx 2.8\ MN$. Figure 7.16b also

(a) (b)

Figure 7.14: South facade Palacio Pereira: Photos of damages present in the facade after the 2010 Santiago de Chile earthquake, showing large shear cracks in and above the spandrels of the window openings

illustrates the corresponding failure mechanism by showing the contour plot of the tension damage parameter d^+.

Pushover curves Figure 7.17 plots the pushover curves for the numerical analyses of the Palacio Pereira east facade. It has been evaluated analogously to the curves of the south facade.

Again, the curves of the conventional DIANA and the isotropic machine learning based KRATOS approach show a similar linear elastic behavior, while considering orthotropic behavior a slight decrease of stiffness can be observed.

However, the maximum shear forces, differ significantly. While the conventional approach has a force limit of $F_{x,max} = 2.2\ MN$, the capacity of the machine learning based homogenization approaches is greater. It counts for the isotropic approach $F_{x,max} \approx 3.0\ MN$ and for the orthotropic one $F_{x,max} \approx 2.8\ MN$.

Comparison with real earthquake damage Figure 7.18 shows a photo of the east facade of the Palacio Pereira. It depicts damaged areas at the most left part of the facade. A crack can be found at the upper floor close to the second opening. This crack has also been presented by both the numerical analyses.

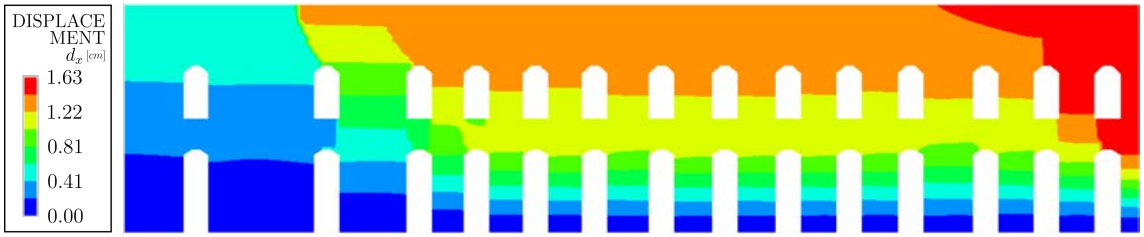

(a) Conventional approach DIANA FEA

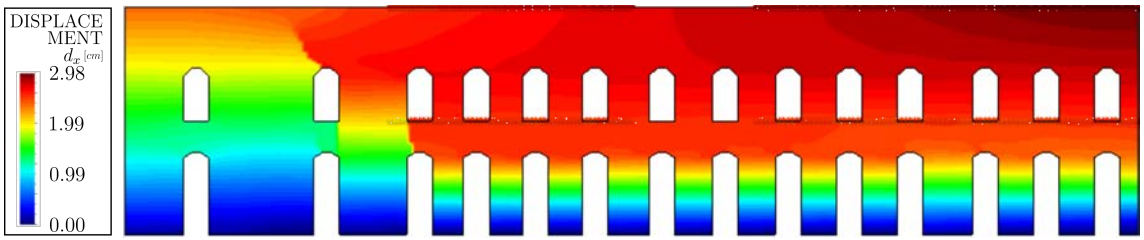

(b) Machine learning approach KRATOS MULTIPHYSICS (orthotropic)

Figure 7.15: East facade Palacio Pereira: contour plots of the horizontal displacement at failure of the structures, showing the results for the analysis in DIANA FEA and KRATOS MULTIPHYSICS

7.4.3 Discussion

The presented numerical analyses of the Palacio Pereira facades has utilized a conventional and a novel approach of defining the macro model material damage laws. It has been shown that on the isotropic level both the techniques show similar elastic behavior. Whereas a decrease of stiffness is observed when applying the orthotropic transformation. A discussion about the linear elastic parameters has been carried out in Section 7.4.1. And the seismic pushover analyses have underlined this.

Furthermore it has been shown that the capacity of the novel machine learning based approach is significantly greater than the one obtained by applying the conventional approach. However, this is only true for the comparison of the results from the large scale structures. When discussing the results of the numerical in-situ experiment, the capacity of the conventional material model is greater than the one of the machine learning based model.

These differences may lie in the assumptions made during the conventional model calibration. This approach has just taken into account one specific calibration experiment, namely the in situ shear test. The analyses carried out in this chapter have shown that this hypothesis is not a limitation but results in more conservative results on the safe side. On the other hand, the novel machine learning approach

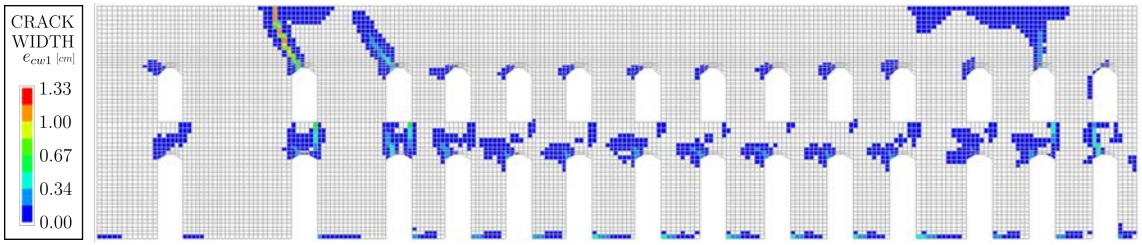

(a) Conventional approach DIANA FEA

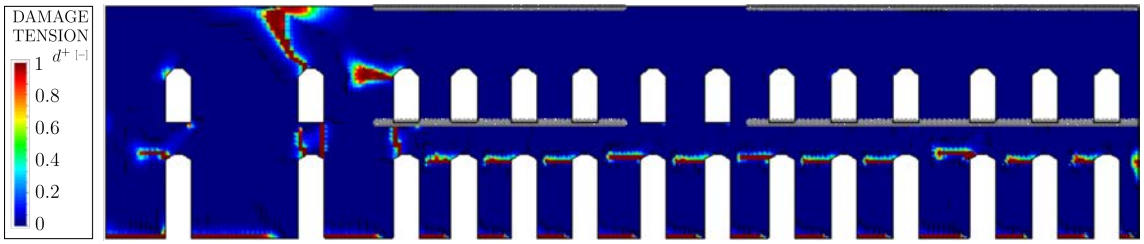

(b) Machine learning approach KRATOS MULTIPHYSICS (orthotropic)

Figure 7.16: East facade Palacio Pereira: contour plots of the cracks at failure of the structures, showing the results for the analysis in DIANA FEA and KRATOS MULTIPHYSICS

has utilized the same experiment only for the calibration of the virtual laboratory micro model RVE. While performing the virtual laboratory, multiple different strain-stress relations have been numerically tested and later used for macro model training. Hence the trained model considers a wider scope of possible damage mechanisms and accompanying nonlinear behavior in a more complete model calibration set. For the seismic analyses of the Palacio Pereira facades this leads to larger model capacities.

Furthermore, the conventional macro model constitutive law does not consider orthotropic behavior. It applies a smeared isotropic approach. However, masonry is not an isotropic material. In contrast, the machine learnig based model applies the transformation process from orthotropic to isotropic scales in order to take into account the masonry's orthotropy. Applying this approach to the here presented Palacio Pereira has shown a signifcant decrease in stiffness when including the orthotropic behavior to the constitutive model.

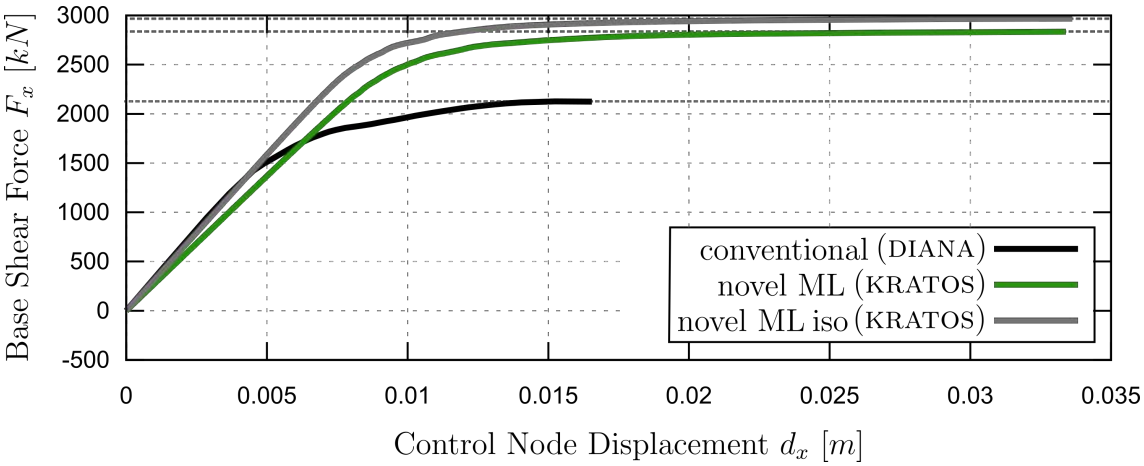

Figure 7.17: East facade Palacio Pereira: Pushover curves showing the base shear force F_x plotted against the control node displacement d_x of the most upper right node of the conventional DIANA FEA and the isotropic and orthotropic machine learning KRATOS approaches.

7.5 Summary

This chapter has shown an application example of the machine learning based material homogenization procedure to the seismic analysis of a large scale masonry structure. The case study considered in this chapter has been the Palacio Pereira that was also investigated in Chapter 3 of this thesis. The chapter has presented a comparison of this novel material homogenization approach with an approach conventionally used for large scale analysis of masonry buildings. In this context, two dimensional nonlinear pushover analyses have been applied to the south and the east facade of the building. These analyses have been carried out by means of conventional macro scale analysis, and a machine learning based macro scale analysis.

In a first step, the conventional approach of defining macro model material properties for large scale analysis of masonry structures has been carried out. The facade macro models have been calibrated by considering a single in-situ shear experiment carried out in the Palacio Pereira. It has been shown that there exists a proper homogeneous macro model that is able to numerically model the nonlinear cracking behavior of the real experiment. This has been shown by comparing the results in terms of force - strain curve. Very good results could be achieved. The tool used for this conventional approach has been the FE software DIANA FEA. The calibrated FE macro model has then been utilized for the large scale analyses of the Palacio

Figure 7.18: Photo of damages in the Palacio Pereira east facade after the 2010 Santiago de Chile earthquake, showing shear cracks over the openings at the most southern part of the facade

Pereira facades. The obtained results of both the in situ test calibration and the Palacio Pereira pushover analyses perfomed in DIANA FEA have then served in order to compare the results with the novel homogenization approach.

In a second step, the machine learning based approach has been presented. Therefore, a micro model, that distinguishes between brick units and mortar joints and considers the correct masonry bond of the Palacio Pereira, has been calibrated. The result data of the in-situ experiment have been also utilized for micro model calibration. In this context, a material model has been found for the brick units and mortar joints, respectively. The results have been shown to be in a very good agreement with the experimentally obtained results. Proceeding with the calibrated micro model, the virtual laboratory has been performed by using the RVE, having carried out the multiple virtual experiments and having stored the representative strain stress states as training data. With these data, the material parameters of a proper constitutive model have been elaborated. The linear elastic properties have been computed by having applied the procedure of anisotropic to isotropic

scale mapping. The nonlinear material law parameters have been obtained by the machine learning based approach. The homogenized macro constitutive model has been evaluated by performing a numerical macro scale analysis of the in-situ shear experiment. An equal linear elastic behavior and a similar ductility could have been observed. It has also been observed that the peak value of the macro analysis shows a slightly smaller value than the in-situ, i.e. on the safe side.

The comparison of the results derived from the conventional macromodel and the novel machine learning based approach has shown the following outcomes:

- The novel machine learning based homogenization approach is able to reproduce the orthotropic behaviour of masonry in the elastic range, beside the conventional isotropic hypothesis. The linear elastic behaviors of the conventional and the novel machine learning based homogenization approach are equal at the isotropic level, and differ when the machine learning model considers orthotropic behavior for the large scale structure analysis.

- The crack evolution and the failure mechanisms are very similar for the numerical macro analyses of the in-situ experiment and the facades.

- The crack patterns of both the analyses comply with the cracks observed in the Palacio Pereira after the 2010 Santiago de Chile earthquake.

- The peak value of the conventional macro model analysis is larger than the one obtained by the corresponding machine learning based approach when comparing the in-situ shear analysis.

- The capacity of the models utilizing the novel machine learning approach is larger than the conventional macro model analysis when comparing the results of the pushover analyses of the facades.

Novel achievements have been obtained by representing the anisotropy in the masonry macro model by means of the machine learning based homogenization approach. A first example at a small-scale structure, i.e. the in-situ experiment, has shown a similar linear elastic behavior when comparing with the machine learning based macro model, where orthotropy is applied to the macro model approach thanks to the implementation of the transformation mapping procedure. This example has

served as an evaluation test of the machine learning based model, and has presented a good agreement between the different linear behaviors.

The second macro model analysis has been carried out for the large-scale structure. The results have shown a significant difference in the linear elastic behavior of the machine learning based macro model when compared with that of the conventional macro model one of commercial software. These outcomes are once again a direct result of the implementation of the transformation mapping procedure within the machine learning based macro model, which allows the representation of material's anistropy. It is worth noticing that the geometry of large masonry models of entire building facades is much more complex than that of small single masonry walls, due to the presence of openings and spandrels. This fact leads to more complex stress/strain conditions during the analysis of complex masonry facades, and the anisotropic behavior embedded into the macro model can exhibit a greater influence on the analysis results. The anisotropic response of the material to multiple stress/strain conditions is directly considered in the machine learning based macro model, since data coming from multiple virtual experiments, each one considering different stress/strain conditions, are considered for model calibration. The observations of this large-scale application example have shown the significant influence of the anisotropic behavior during numerical analysis of existing masonry buildings. These effects become more apparent the larger the analyzed structure is. The machine learning based macro model has shown a better representation of this behavior than conventional macro model techniques in commercial software, where the calibration of model parameters is challenging and often based on approximate hypotheses.

Part IV

Conclusions

Chapter 8

Conclusions

8.1 Summary

The principal aim of this research has been the development of a homogenization technique for masonry by using machine learning tools. The main motivation of the thesis has been to define a homogenized material model that improves the conventional approaches of defining the macro scale material properties of masonry. Masonry is a heterogeneous material composed of units and joints and homogenizing its material properties comes along with simplifications that often tend to neglect the material's anisotropy. From a structural engineering point of view, modeling such composite materials is a challenging task.

Recent investigations respected the heterogeneity of masonry by studying the mechanical behavior by means of micro models. This approach carefully distinguishes between the material components by modeling separately their nonlinear material responses. Results obtained from micro modeling have shown to represent the damage patterns and failure mechanisms of masonry very accurately. However, these approaches are restricted to small scale masonry structures since their computational effort is very high.

Therefore, special attention was given to techniques that average the heterogeneous material behavior and consider continuous continuum models. These approaches are known as macro scale models, able to afford the analysis of large-scale structures with a minimum of computational effort. Both linear and advanced nonlinear static and dynamic analysis procedures could be applied to entire masonry buildings. However, defining a strong tool that is able to determine robustly the

macro mechanical material properties is still a pending task in the field. In order to tackle this problem, the multi scale or homogenization techniques have received great interest in the last decades, as their aim is to connect both modeling accuracy of micro modeling and computational efficiency of macro modeling. These approaches have shown to be very accurate. However, they still produce high computational costs. Chapter 2 has pointed out these three modeling techniques (micro, macro and multi scale) and their main contributions to the field in order to illustrate the main tasks of the present research.

Chapter 2 has introduced machine learning and its possible inclusion as a modern tool for the homogenization of the masonry material. A short presentation of machine learning history and its original application has been made. Explicit insight on the use of machine learning in structural engineering have demonstrated its ascending position in the current research.

As mentioned above, the macro modeling technique has opened new doors for the numerical simulation of masonry structures. Masonry structures are able to bear large compression loads, while masonry's weakness lies in the low tension and shear resistance. This issue makes masonry structures vulnerable to horizontal loads, such as wind or seismic actions. In order to assess the vulnerability of complex and large masonry structures, the macro modeling approach has shown to be one of the most useful one. Chapter 3 has presented an advanced numerical earthquake simulation technique for masonry structures. It has demonstrated the wide ranging possibilities of macro modeling, and its positive effects on assessing the masonry structures. A multi directional nonlinear static analysis procedure for irregular masonry structures without box behavior has been developed. The application to a case study has shown that the novel approach performs better than conventional pushover analyses, and that the results are in very good agreement with nonlinear dynamic analysis results. Furthermore, the limitations of macro modeling concerning the material property definition have been presented by discussing a conventional approach of homogenizing the macro model material properties. Chapter 3 has shown the importance of macro modeling for the numerical analysis of masonry on the one hand, but also its strong dependency on the assumptions made during the process of choosing the input material parameters on the other hand.

The use of macro modeling for masonry in commercial engineering has demonstrated a general acceptance of using assumption-based macro material property

definition. Therefore, this thesis has presented a machine learning technique that trains the parameters of a unique constitutive law available for macro scale analysis with a more rigorous approach than in conventional practice. The presented technique utilizes data from micro model analyses in order to optimize macro model parameters. This procedure has been called *machine learning homogenization technique* in the present research. It consists of performing analyses at two stages: an experimental campaign in a *virtual laboratory*, followed by and the actual *constitutive model training*. The virtual laboratory covers the scope of training data production. Those data, derived from a large amount of virtual experiments, have provided a complete representation of the heterogeneous mechanical behavior of masonry micro models when subjected to different stress/strain states. The second stage - constitutive model training - includes the construction of the machine learning model and its parameters' training by being fed with the data from the virtual laboratory.

Both stages, the virtual laboratory campaign and the model training, have required the formulation of proper constitutive damage models. On the one hand, these models must be able to represent the brittle behavior of the masonry components for the micro scale analysis in the virtual laboratory. On the other hand, their applicability to smeared macro scale approaches must be ensured. In the last years, several detailed micro modeling techniques have been presented that utilize continuum damage models for each component of masonry. Therefore, the present research has considered a strain driven bi-dissipative damage constitutive model that has been utilized successfully for the micro model analysis of masonry walls. Chapter 4 has presented this constitutive model in detail, including the description of yield criteria and damage evolution laws. An application example has demonstrated the model's capability of representing the correct failure mechanisms and material responses when compared with experimental tests. The accuracy of the application example has also justified the use of the constitutive model for the micro mechanical analyses in the virtual laboratory.

Chapter 5 has presented the definition of the machine learning homogenization technique and its implementation. Fundamentals on gradient descent optimization and loss functions have been presented in order to detail the applied machine learning technique. The python based application programming interface (API) TENSORFLOW has been introduced. This API utilizes the concept of computation graphs. A computation graph is based on sequentially performed mathematical operations

by taking an input and calculating the corresponding output. This concept has shown to be suitable for the implementation of strain driven constitutive models, since they are based on the same input-output principle (strains-stresses). Chapter 5 has presented the numerical implementation of the constitutive laws introduced in Chapter 4 to a machine learning model.

The concept of the virtual laboratory has been introduced as a general tool for the production of training data. The virtual laboratory is necessary since the prediction accuracy of a machine learning model strongly depends on the quality of the training data. In the present research, the data must have been able to represent accurately the heterogeneous material behavior of masonry. Therefore, a well defined micro model representative volume element (RVE) of the considered masonry material has been the subject of this laboratory. The application of different boundary conditions in multiple virtual experiments and the storage of their results (coupled strain and stress states) have shown to be able to create a database that can be utilized for model training. These sets contain information about the anisotropic damage behavior of the micro modeled masonry RVE.

Chapter 5 has also clarified that the data coming from the virtual laboratory has to undergo a modification in order to serve as correct training input for the machine learning model. On the one hand, the selected constitutive model is defined in an isotropic space. On the other hand, the real material behavior of masonry is anisotropic. Consequently, the *data isotropization* procedure has been introduced to connect both spaces. This approach includes the prediction of isotropic linear elastic results, and the application of a transformation procedure.

Chapter 5 has been finalized with the definition of an anisotropic constitutive damage model, based on the isotropic constitutive damage models presented in Chapter 4 that have also been implemented as the machine learning models. The optimization of these models has been obtained by utilizing the isotropized training data. These optimized models still do not represent the anisotropic behavior of masonry. Therefore, the research has also implemented the transformation procedure (utilized in data isotropization) to the post machine learning constitutive model.

In Chapter 6, the machine learning based homogenization techniques for masonry has been evaluated within an application example. A Flemish bond masonry has been chosen in order to define a homogenized constitutive model for macro scale analysis. The first step of the application has been the calibration of the material

properties of a micro modeled wall. A numerical micro model of a diagonal compression test has been constructed and the material properties of each component have been modified in order to be able to represent the real experimental results. The calibration results have also been used in order to demonstrate the accuracy of the applied constitutive model.

Starting from the calibrated micro model, a RVE of the Flemish masonry bond wall has been constructed. A virtual laboratory campaign has been performed by applying a large variety of boundary conditions to the RVE. The stored results have been passed through the data isotropization procedure in order to define the linear elastic properties and the transformation requisites, and to prepare the data set for model training.

A constitutive law has been implemented into the machine learning model, by utilizing the law presented in Chapter 4 that better determines the macro model behavior in tension and shear. The machine learning results have been evaluated by running a second virtual laboratory. These results have been compared with the predictions made by the trained model. The model has shown to be able to accurately predict the peak values of the virtual laboratory results.

A final application of the post machine learning constitutive law has been performed. Two numerical tests have been considered, i.e. a compression test and a shear compression test. Having considered multiple tests demonstrates the performance of the homogenized constitutive models when exposed to different stress/strain conditions. Both tests were modeled at the micro and macro scale in order to compare the results of the homogenized constitutive model and the micro model. The obtained outcomes have shown that the macro model is able to represent results similar of those derived from micro modeling.

After the application example of the Flemish bond masonry, the machine learning based homogenization has been applied to a large scale structure. The investigated case study has been the seismic nonlinear analysis of the main facades (south and east) of the Palacio Pereira by means of mass proportional pushover analyses at the macro scale. The analyses have been carried out by considering two different approaches, i.e. a conventional procedure of macro modeling and the machine learning based macro modeling approach. The latter has been formulated both under the hypotheses of isotropy and orthotropy. The constitutive law of the novel machine learning based macro modeling approach has been elaborated in the same way as

for the nonlinear model of the Flemish bond masonry of Chapter 6.

The analyses have been carried out by considering two different approaches of homogenizing the masonry material of the Palacio Pereira. Firstly all the analyses have been performed by utilizing a conventional procedure of macro modeling. In a further step the same pushover analyses have been performed using the machine learning based macro modeling approach on an isotropic and an orthotropic level. The constitutive law of the novel approach has been elaborated equally as the nonlinear material damage law of the Flemish bond masonry.

The research has shown that both the conventional and the novel approach are able to detect the real damage observed in the Palacio Pereira facades after the 2010 earthquake. When comparing the results of both the approaches, similar linear elastic behaviors are observed on the isotropic level. The novel approach has also shown to present a larger capacity than the conventional one.

The research presented in this thesis has shown to be able to calibrate a numerical macro constitutive model for masonry, bay considering a significantly larger number of experiments (on a virtual scale) than conventional macro model calibration procedures. This new approach gives a more versatile alternative than the ones provided by commercial software.

8.2 Main contributions

The main novelties presented in this research lie in the following original contributions:

- The development of a novel pushover method for the seismic analysis of masonry structures at the macro scale. The so-called multi directional pushover analysis has shown to be able to better represent the possible failure mechanisms than conventional pushover techniques.

- The formulation of an anisotropic continuum damage model for nonlinear analysis of masonry structures based on a bi-dissipative d^+/d^- damage model for masonry that better represents the tension damage evolution. A transformation procedure able to map from an anisotropic to an isotropic space has been included into the model.

- The definition of a machine learning technique able to homogenize a composite material like masonry. The smeared properties are presented in a single damage constitutive model. In comparison to conventional homogenization techniques, the novel procedure disconnects micro and macro analysis scale while homogenizing the material, with important benefits in terms of computational efficiency.

- The elaboration of a virtual laboratory instrument able to numerically produce data that can be utilized for big data analysis tools, such as machine learning or artificial intelligence. This approach is clearly promoting the idea of assessing the mechanical behavior of material by the use of directly processed data. In this regard, an experimental campaign performed in the virtual laboratory produced data that accurately represent the anisotropic behavior of masonry and could be used for training of a specific machine learning model.

- The definition of a numerical transformation procedure that is able to find the closest isotropic linear elastic properties to a given anisotropic material. This method includes linear least square fitting, machine learning prediction and the concept of space transformation. The procedure has been compared with analytic procedures.

- The application and discussion of the developed homogenization tool to a Flemish bond masonry wall. The proposed technique has shown to present results that are in very good agreement with those obtained from micro modeling.

- The application and discussion of the developed tool to a large scale masonry structure. The case study of the Palacio Pereira, a heritage building located in Santiago de Chile, has been investigated. The results obtained by the novel tool have been compared with the ones of a conventional tool, as well as with the damage patterns observed after the 2010 earthquake suffered by the structure. The results have shown the possibility of exhibiting different linear elastic behaviors (isotropic and anisotropic) and greater capacities of the novel homogenization method.

8.3 Suggestions for future works

The proposed machine learning homogenization technique has shown to result in a damage constitutive model for the macro scale analysis of masonry that is able to predict accurately the complex mechanical behavior of masonry. This concluding section presents some possible ideas for future works, as potential continuation of the present research.

- A larger amount of physical laboratory tests could be performed in order to obtain an optimal matching between experimental and numerical behavior. This contribution would improve the robustness of the developed methodology.

- The presented homogenization technique has shown to represent very accurately the complex behavior of in-plane loaded masonry walls. However, masonry has shown to be very vulnerable when exposed to out-of-plane deformations, too. Therefore, a very interesting supplement to the present research would be the investigation of machine learning homogenization techniques for out-of-plane loaded masonry walls. This research would consist in considering shell elements for the RVE model, since those are able to represent the out-of-plane deformations. Moreover, extended boundary conditions for the virtual laboratory must be defined that are able to also expose the RVE to out-of-plane displacements.

- The research has shown an application example of the homogenization technique to a two-dimensional Flemish bond masonry wall. The results are in good agreement with those obtained by micro modeling. Further work may address the extension to different bond patterns for masonry, and different properties of materials contituents.

- The proposed method has been applied to the analysis of a real case study. A future research may address the same activity by considering a complete multidisciplinary approach, combining both experimental and numerical tasks. Possible stages of the investigation could be: i) execution of an experimental campaign in order to evaluate the mechanical response of masonry both in-plane and out-of-plane; ii) calibration of a RVE able to represent accurately the experimentally observed material behavior; iii) execution of the machine learning homogenization technique, by including the virtual laboratory campaign

and model training with extension to out-of-plane behavior; iv) application of the post machine learning constitutive model to the macro analysis of the three dimensional large scale structure.

- The massive research field of big data analysis offers many different machine learning approaches. This work has considered the optimization of a predefined mathematical model in terms of a constitutive law. Such laws are coherently defined in a mathematical way and may restrict the intuitiveness of machine learning. Therefore a proposal for future works could be the analysis of less restricted machine learning models in order to homogenize heterogeneous materials. Starting from more flexible constitutive models and passing on to complete data pattern analysis as done in artificial intelligence, e.g. regression trees, deep neural networks etc.

- The present research has elaborated a method that is able to define the averaged material properties of masonry for the application in nonlinear macro scale analysis. There are also investigations that contributed strongly to the improvement of macro scale analysis in general (e.g. crack tracking technologies, that are able to predict crack localization patterns more accurately). Therefore, an overarching research for macro scale analysis could be investigated by combining such techniques with the here presented machine learning homogenization technique.

- The application of the machine learning homogenization technique to other heterogeneous materials. The challenges of structural engineering for the 21st century lie in the development of sustainable materials. The use of these materials should support the construction field in order to reach well-defined climate change goals. Numerical techniques should facilitate the structural assessment of buildings constructed with sustainable materials. Such materials are for example: masonry from upcycled bricks, fiber-reinforced concrete, cross-laminated timber, etc. Therefore, a suggestion for future works is to investigate and apply the machine learning homogenization techniques to these types of new materials.

Appendices

Appendix A

Seismic analysis of the Palacio Pereira

A.1 Linear Seismic Analysis

A.1.1 Modal Analysis

The modal analysis of the *Palacio Pereira* is performed to obtain the modal shapes, their eigenfrequencies and participating masses. Figure A.1 shows the trend of variation of the cumulative effective mass at each direction with the increasing number of modes of vibration. For the x- and y-directions, a value around 70% seems to be the maximum value that can be reached after considering 500 eigenmodes. This result suggests to combine 500 modes in the response spectrum analysis to get the most accurate results.

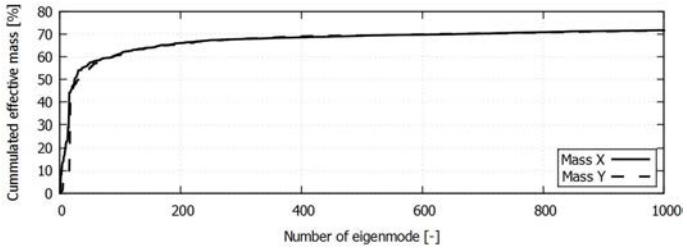

Figure A.1: Modal analysis: cumulative effective mass from the eigenvalue analysis depending on the number of eigenmodes

Table A.1 shows the most important vibration modes derived from the eigenvalue analysis, i.e. those with effective mass participation higher than 4%.

Table A.1: Main vibration modes of the *Palacio Pereira*

	Mode number [−]	**Period** [s]	**Frequency** [Hz]	**Effective mass** [%]
X	2	0.267	3.75	6.61
	14	0.177	5.66	5.69
	16	0.170	5.87	15.23
Y	6	0.238	4.20	4.22
	17	0.161	6.21	14.40
	18	0.156	6.40	18.28

Figure A.2 shows that the vibration modes reported in Table A.1 are local ones and involve just small percentage of the mass of the whole structure. This result is typical in irregular masonry buildings without box behavior.

A.1.2 Response spectrum analysis

The response spectrum analysis (RSA) of the *Palacio Pereira* is performed by using four different spectra, shown in Figure A.3. The elastic spectra of the 2010 earthquake are the same used by Sandoval et al. (Sandoval et al., 2017; Valledor et al., 2015). The other two spectra are calculated following the Chilean standards NCh433 (Instituto Nacional de Normalización, 2009) for a building with a soil type III and a maximum ground acceleration $A_0 = 0.3\,g$, according to the location of the building.

The reduction factor R^*, suggested by the Chilean standards for the reduction of the elastic spectra in the RSA, is calculated as follows:

$$R^* = 1 + \frac{T^*}{0.1T_0 + \frac{T^*}{R_0}} \tag{A.1}$$

where T^* is the vibration period with the highest translational mass in the direction of the analysis, T_0 is a parameter depending on the foundation soil, R_0 is the factor of modification of the response according to the structural typology. Since the RSA is executed along the two perpendicular directions x and y, two different reduction factors are calculated. The parameter $T^* = 0.170\ s$ in the x direction, and $T^* = 0.156\ s$ in the y direction, being the modes 16 and 18 those with the highest translational masses in the two directions of the analysis, see Table A.1. The pa-

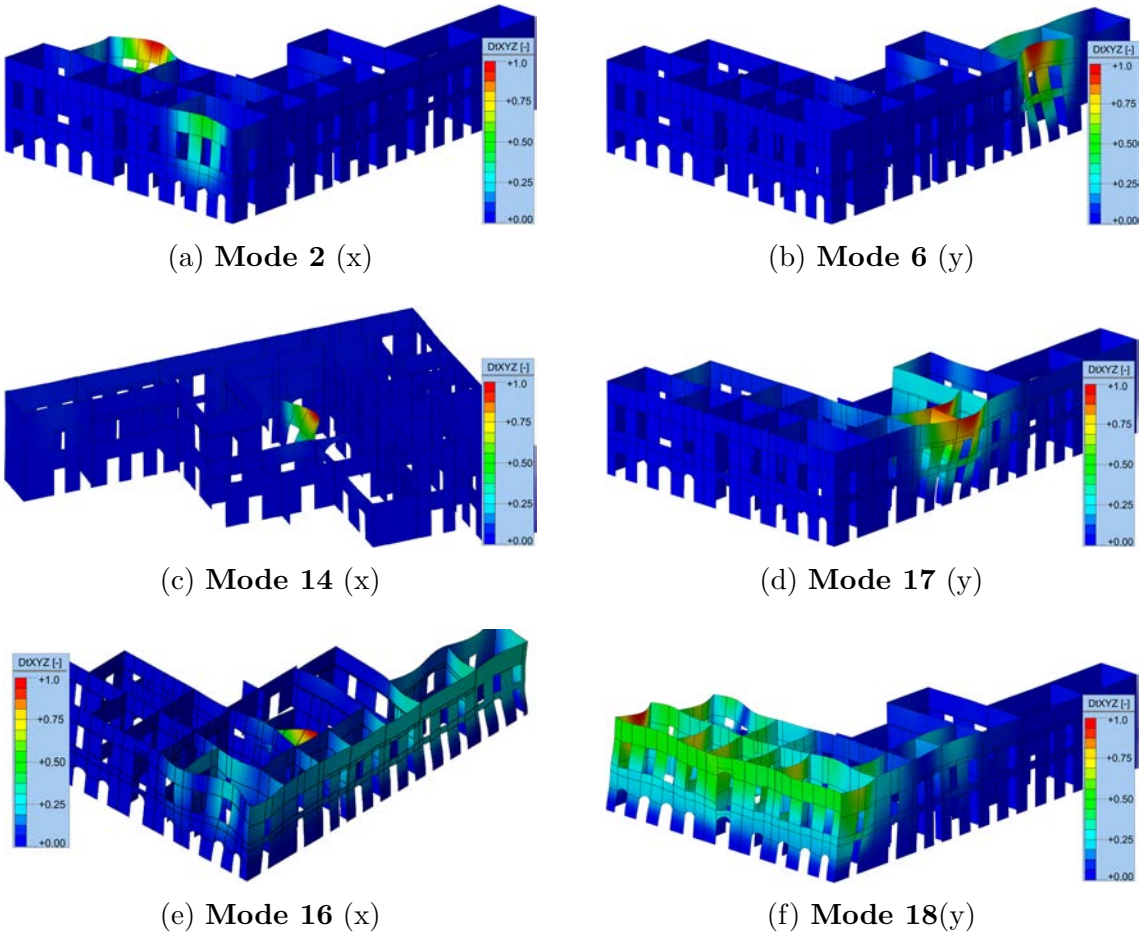

(a) **Mode 2** (x)

(b) **Mode 6** (y)

(c) **Mode 14** (x)

(d) **Mode 17** (y)

(e) **Mode 16** (x)

(f) **Mode 18**(y)

Figure A.2: Normalized mode shapes with mass participation higher than 5 % in the x-direction and higher than 4 % in the y-direction

rameter $T_0 = 0.3$ for a type II soil, and $R_0 = 2$ for unreinforced masonry buildings. Therefore, the reduction factors $R^* = 2.48$ in the x direction and $R^* = 2.44$ in the y direction.

The inelastic spectra of the 2010 earthquake record is evaluated by using the same reduction factors R^*. Two different combination rules, the SRSS and the CQC, are adopted. As mentioned in Section A.1.1, 500 eigenmodes are considered.

Figure A.4 shows the principal stress contours for major modes in the x-direction (2, 14, 16) and in the y-direction (6, 17, 18) derived from the RSA with the 2010 earthquake inelastic spectra. The red contour indicates the regions in the building where the tensile principal stress exceeds the tensile strength of the material of 0.12 MPa. These regions may be interpreted as cracks corresponding to the activation

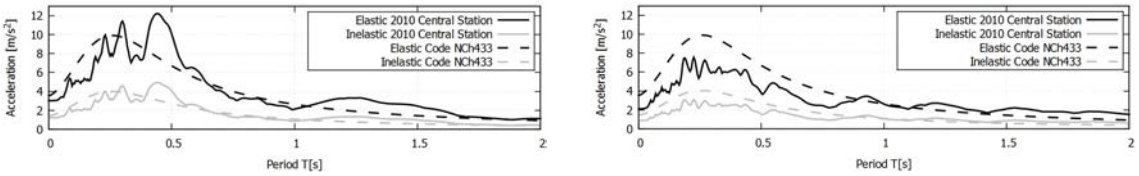

(a) Component in x direction (b) Component in y direction

Figure A.3: Acceleration spectra considered in the seismic assessment of the *Palacio Pereira*

of local out-of-plane mechanisms (modes 2, 14, 6, 17), and in-plane failures in the east facade (mode 16) and south facade (mode 18).

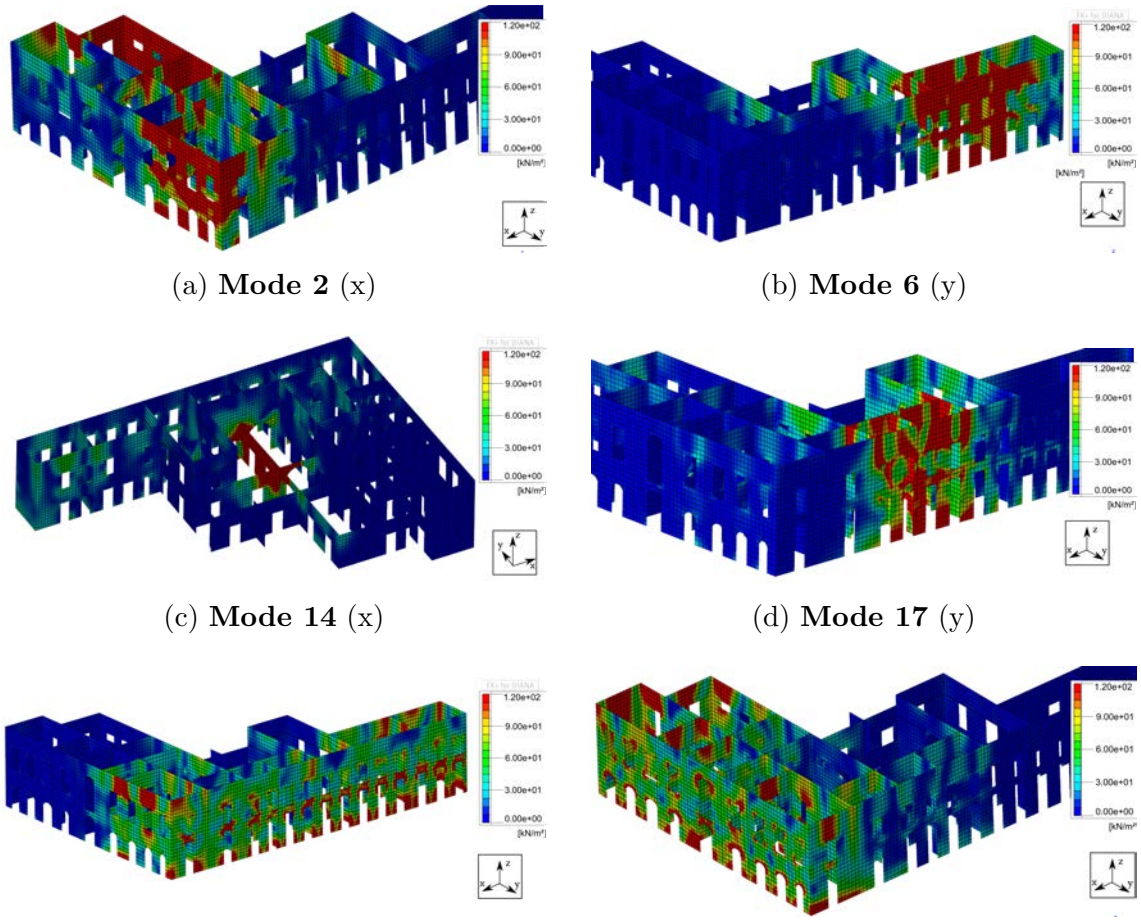

(a) **Mode 2** (x) (b) **Mode 6** (y)

(c) **Mode 14** (x) (d) **Mode 17** (y)

(e) **Mode 16** (x) (f) **Mode 18** (y)

Figure A.4: Response spectrum analysis with inelastic spectra of 2010 earthquake: principal stress contours for major vibration modes in the x-direction.

Appendix B

Machine learning homogenization technique

B.1 Bézier regulators

In Section 4.3.1 three regulators to facilitate the post peak part definition of the Bézier like damage evolution are introduced. The dependencies for the remaining variables are then

$$
\begin{aligned}
f_{c,i} &= f_{c,j} = f_{c,p} \\
f_{c,k} &= f_{c,r} + c_{c,1} \cdot (f_{c,p} - f_{c,r}) \\
\epsilon_j &= \epsilon_p + \alpha \cdot c_{c,2} \\
\epsilon_k &= \epsilon_p + \alpha \\
\epsilon_r &= \frac{(\epsilon_k - \epsilon_j) \cdot (f_{c,p} - f_{c,r})}{f_{c,p} - f_{c,k}} + \epsilon_j \\
\epsilon_u &= c_{c,3} \cdot \epsilon_r \\
\epsilon_0 &= \frac{f_{c,0}}{E} \\
\epsilon_i &= \frac{f_{c,p}}{E} \\
\alpha &= 2(\epsilon_p - \frac{f_{c,p}}{E})
\end{aligned}
\tag{B.1}
$$

Where above equation presents the computation of the missing variables for

the Bézier like damage evolution in compression. In order to compute the missing variables for the damage evolution in tension, a substitution of the corresponding values must be carried out. As shown in Equation 4.18 the factor A of the Bézier definition may not be equal to 0. Hence the numerical implementation must ensure this by customizing factor x_2 as follows

$$x_2 = \begin{cases} x_2 + 1.0E-06 \cdot (x_3 - x_1), & if A \leq 1.0E-12 \\ x_2, & else \end{cases} \tag{B.2}$$

References

Bibliography

Abadi, M., Agarwal, A., Barham, P., Brevdo, E., Chen, Z., Citro, C., Corrado, G. S., Davis, A., Dean, J., Devin, M., Ghemawat, S., Goodfellow, I., Harp, A., Irving, G., Isard, M., Jia, Y., Jozefowicz, R., Kaiser, L., Kudlur, M., Levenberg, J., Mané, D., Monga, R., Moore, S., Murray, D., Olah, C., Schuster, M., Shlens, J., Steiner, B., Sutskever, I., Talwar, K., Tucker, P., Vanhoucke, V., Vasudevan, V., Viégas, F., Vinyals, O., Warden, P., Wattenberg, M., Wicke, M., Yu, Y., and Zheng, X. (2015). TensorFlow: Large-scale machine learning on heterogeneous systems. https://www.tensorflow.org/.

Adeli, H. (2001). Neural Networks in Civil Engineering : 1988-2000. *Computer-Aided Civil and Infrastructure Engineering*, 16:126–142.

Adeli, H. and Yeh, C. (1989). Perceptron Learning in Engineering Design. *Microcomputers in Civil Engineering*, 4:247–256.

Aguilar, V., Sandoval, C., Adam, J. M., Garzón-Roca, J., and Valdebenito, G. (2016). Prediction of the shear strength of reinforced masonry walls using a large experimental database and artificial neural networks. *Structure and Infrastructure Engineering*, March 2016(March).

Almac, U., Schweizerhof, K., Blankenhorn, G., Duppel, C., and Wenzel, F. (2013). Structural behaviour of Hagia Sophia under dynamic loads. In *Vienna Congress on Recent Advances in Earthquake Engineering and Structural Dynamics 2013 (VEESD2013)*, page 475. VEESD2013.

Amezquita-Sanchez, J. P., Valtierra-Rodriguez, M., and Adeli, H. (2020). Machine learning in structural engineering. *Scientia Iranica A: Civil Engineering*, 27:2645–2656.

Amezquita-Sanchez, J. P., Valtierra-Rodriguez, M., Aldwaik, M., and Adeli, H. (2016). Neurocomputing in civil infrastructure. *Scientia Iranica A: Civil Engineering*, 23:2417–2428.

ASCE (2007). *Seismic Rehabilitation of Existing Buildings*. American Society of Civil Engineers, asce/sei 41-06 edition.

Asteris, P. G. (2019). Artificial bee colony-based neural network for the prediction of the fundamental period of infilled frame structures. *Neural Computing and Applications*, 1.

Asteris, P. G. and Plevris, V. (2017). Anisotropic masonry failure criterion using artificial neural networks. *Neural Computing and Applications*, 28:2207–2229.

Avila, L., Vasconcelos, G., and Lourenço, P. B. (2018). Experimental seismic performance assessment of asymmetric masonry buildings. *Engineering Structures*, 155:298–314.

Barbosa, C. S., Lourenço, P. B., and Hanai, J. B. (2010). On the compressive strength prediction for concrete masonry prisms. *Materials and Structures*, 43:331–344.

Berto, L., Saetta, A., Scotta, R., and Vitaliani, R. (2004). Shear behaviour of masonry panel: parametric FE analyses. *International Journal of Solids and Structures*, 41:4383–4405.

Bhele, S. G. and Mankar, V. H. (2012). A Review Paper on Face Recognition Techniques. *International Journal of Advanced Research in Computer Engineering and Technology*, 1(8):339–346.

Boroschek, R., Soto, P., and Leon, R. (2010). Registros del Terremoto del Maule Mw = 8.8 de 27 de Febrero de 2010. *Informe RENADIC 10/05 Rev. 1, Departamento de Ingeniería Civil, Facultad de Ciencias Físicas y Matemáticas, Universidad de Chile (in Spanish)*.

Brunelli, A., de Silva, F., Piro, A., Parisi, F., Sica, S., Silvestri, F., and Cattari, S. (2021). Numerical simulation of the seismic response and soil–structure interaction for a monitored masonry school building damaged by the 2016 Central Italy earthquake. *Bulletin of Earthquake Engineering*, 19(2):1181–1211.

Camara, A. and Astiz, M. A. (2012). Pushover analysis for the seismic response prediction of cable-stayed bridges under multi-directional excitation. *Engineering Structures*, 41:444–455.

Cannizzaro, F., Pantò, B., Lepidi, M., Caddemi, S., and Caliò, I. (2017). Multi-directional seismic assessment of historical masonry buildings by means of macro-element modelling: Application to a building damaged during the L'Aquila earthquake (Italy). *Buildings*, 7(4):106.

Cattari, S., Marino, S., and Lagomarsino, S. (2015). Seismic assessment of plan irregular masonry buildings with flexible diaphragms. In *Proceedings of the Tenth Pacific Conference on Earthquake Engineering*, pages 90–98.

Cervera, M., Oliver, J., and Faria, R. (1995). Seismic evaluation of concrete dams via continuum damage models. *Earthquake Engineering and Structural Dynamics*, 24(9):1225–1245.

Chácara, C., Lourenço, P. B., Cannizzaro, F., Pantò, B., and Caliò, I. (2019). Assessment of the seismic vulnerability of an unreinforced masonry structure based on discrete-macro dynamic analyses. In Aguilar, R., Torrealva, D., Moreira, S., Pando, M. A., and Ramos, L. F., editors, *Structural Analysis of Historical Constructions*, pages 1210–1218. RILEM Bookseries 18.

Chisari, C., Macorini, L., Amadio, C., and Izzuddin, B. A. (2018). International Journal of Solids and Structures Identification of mesoscale model parameters for brick-masonry. *International Journal of Solids and Structures*, 146:224–240.

Chopra, A. K. (1995). *Dynamics of Structures: Theory and Applications to Earthquake Engineering*. Prentice-Hall.

Chopra, A. K. and Goel, R. K. (2004). A modal pushover analysis procedure to estimate seismic demands for unsymmetric-plan buildings. *Earthquake Engineering and Structural Dynamics*, 33(8):903–927.

Dadvand, P., Rossi, R., and Oñate, E. (2010). An object-oriented environment for developing finite element codes for multi-disciplinary applications. *Archives of Computational Methods in Engineering*, 17:253–297.

D'Altri, A. M., Vasilis, S., Milane, G., Rots, J. G., Cattari, S., Lagomarsino, S., Sacco, E., Tralli, A., Castellazzi, G., and de Miranda, S. (2019). Modeling Strategies for the Computational Analysis of Unreinforced Masonry Structures : Review and Classification. *Archives of Computational Methods in Engineering*.

De Stefano, M. and Mariani, V. (2014). Pushover analysis for plan irregular building structures. *Perspectives on European Earthquake Engineering and Seismology*, pages 429–448.

Degli Abbati, S., D'Altri, A. M., Ottonelli, D., Castellazzi, G., Cattari, S., de Miranda, S., and Lagomarsino, S. (2019). Seismic assessment of interacting structural units in complex historic masonry constructions by nonlinear static analyses. *Computers & Structures*, 213:51–71.

Drougkas, A., Roca, P., and Molins, C. (2015). Analytical micro-modeling of masonry periodic unit cells - Elastic properties. *International Journal of Solids and Structures*, 69-70:169–188.

Drougkas, A., Verstrynge, E., Hayen, R., and Van Balen, K. (2019). The confinement of mortar in masonry under compression: Experimental data and micromechanical analysis. *International Journal of Solids and Structures*, 162:105–120.

Duchi, J., Hazan, E., and Singer, Y. (2011). Adaptive subgradient methods for online learning and stochastic optimization. *Journal of Machine Learning Research*, 12:2121–2159.

Endo, Y., Pelà, L., and Roca, P. (2017). Review of different pushover analysis methods applied to masonry buildings and comparison with nonlinear dynamic analysis. *Journal of Earthquake Engineering*, 21(8):1234–1255.

Endo, Y., Pelà, L., Roca, P., da Porto, F., and Modena, C. (2015). Comparison of seismic analysis methods applied to a historical church struck by 2009 L'Aquila earthquake. *Bulletin of Earthquake Engineering*, 13:3749–3778.

European Committee for Standardization (2004). Eurocode 8: Design provisions for earthquake resistance of structures, Part 1: General rules, seismic actions and rules for buildings. Brussels. *CEN, 2004*.

European Committee for Standardization (2005). Eurocode 8: Design provisions for earthquake resistance of structures, Part 3: Assessment and retrofitting of buildings. Brussels. *CEN, 2005*.

Fajfar, P. (2000). A nonlinear analysis method for performance-based seismic design. *Earthquake Spectra*, 16(3):573–592.

Fajfar, P., Marušić, D., and Peruš, I. (2005). Torsional effects in the pushover-based seismic analysis of buildings. *Journal of Earthquake Engineering*, 9(6):831–854.

Faria, R., Oliver, J., and Cervera, M. (1998). A strain-based plastic viscous-damage model for massive concrete structures. *International Journal of Solids and Structures*, 35(14):1533–1558.

Faria, R., Oliver, J., and Cervera, M. (2000). On isotropic scalar damage models for the numerical analysis of concrete structures on isotropic scalar damage models for the numerical analysis of concrete structures. *CIMNE Monograph*, 198(December).

Ferreira, T. M., Estêvão, J., and Vicente, R. (2020). The use of Artificial Neural Networks to estimate seismic damage and derive vulnerability functions for traditional masonry. *Frontiers of Structural and Civil Engineering*, 14(3):609–622.

Gambarotta, L. and Lagomarsino, S. (1997). Damage Models for the Seismic Response of Brick Masonry Shear Walls: Part I: The Mortar Joint Model and its Applications. *Earthquake Engineering and Structural Dynamics*, 26(March 1996):423–439.

Garcia Ramonda, L. (2020). *Seismic retrofit of masonry with innovative materials for strengthening and repair*. PhD thesis, Universitat Politècnica de Catalunya, http://hdl.handle.net/10803/670566.

Garcia-Ramonda, L., Pelá, L., Roca, P., and Camata, G. (2020). In-plane shear behaviour by diagonal compression testing of brick masonry walls strengthened with basalt and steel textile reinforced mortars. *Construction and Building Materials*, 240:117905.

Garzón-Roca, J., Adam, J. M., Sandoval, C., and Roca, P. (2013). Estimation of the axial behaviour of masonry walls based on Artificial Neural Networks. *Computers and Structures*, 125:145–152.

Gorji, M. B., Mozaffar, M., Heidenreich, J. N., Cao, J., and Mohr, D. (2020). Journal of the Mechanics and Physics of Solids On the potential of recurrent neural networks for modeling path dependent plasticity. *Journal of Mechanics and Physics of Solids*, 143.

G.P. Cimellaro, T. Giovine , D. Lopez-Garcia (2014). Bidirectional Pushover Analysis of Irregular Structures. *Journal of Structural Engineering, ASCE*, 140(9):04014059–1 – 04014059–13.

Greco, A., Cannizzaro, F., and Pluchino, A. (2017). Seismic collapse prediction of frame structures by means of genetic algorithms. *Engineering Structures*, 143:152–168.

Gupta, B. and Kunnath, S. K. (2000). Adaptive spectra-based pushover procedure for seismic evaluation of structures. *Earthquake Spectra*, 16(2):367–392.

Hill, R. (1963). Elastic properties of reinforced solids: Some theoretical principles. *Journal of the Mechanics and Physics of Solids*, 11(Hill 1962):357–372.

Huang, D., Fuhg, J. N., Weißenfels, C., and Wriggers, P. (2020a). A machine learning based plasticity model using proper orthogonal decomposition. *Computer Methods in Applied Mechanics and Engineering*, 365:113008.

Huang, H., Zhao, L., Huang, H., and Guo, S. (2020b). Machine Fault Detection for Intelligent Self-Driving Networks. *Data Science and Artificial Intelligence for Communications*, January(January):40–46.

Huang, W. and Gould, P. L. (2007). 3-D pushover analysis of a collapsed reinforced concrete chimney. *Finite Elements in Analysis and Design*, 43:879–887.

Ibrahim, A., Eltawil, A., Na, Y., and El-Tawil, S. (2019). A Machine Learning Approach for Structural Health Monitoring Using Noisy Data Sets. *IEEE Transactions on Automation Science and Engineering*, pages 1–9.

Instituto Nacional de Normalización (2009). NCh 433 Diseño sísmico de edificios - Earthquake resistant design of buildings (in Spanish). *INN-Chile; Santiago, 2009.*

Jiang, X., Mahadevan, S., and Yuan, Y. (2016). Fuzzy stochastic neural network model for structural system identification. *Mechanical Systems and Signal Processing*, pages 1–18.

Kalkbrenner, P., Pelà, L., and Sandoval, C. (2019). Multi directional pushover analysis of irregular masonry buildings without box behavior. *Engineering Structures*, 201.

Kingma, D. P. and Ba, J. (2015). Adam: A method for stochastic optimization. In Bengio, Y. and LeCun, Y., editors, *3rd International Conference on Learning Representations, ICLR 2015, San Diego, CA, USA, May 7-9, 2015, Conference Track Proceedings*.

Kostić, B. and Gül, M. (2017). Vibration-Based Damage Detection of Bridges under Varying Temperature Effects Using Time-Series Analysis and Artificial Neural Networks. *Journal for Bridge Engineering*, 22(10).

Kumar, N. and Barbato, M. (2019). New Constitutive Model for Interface Elements in Finite-Element Modeling of Masonry. *Journal of Engineering Mechanics*, 145(5):1–15.

L. Luzi, F. Pacor, R. Puglia (2017). Italian Accelerometric Archive v 2.3. *Istituto Nazionale di Geofisica e Vulcanologia, Dipartimento della Protezione Civile Nazionale.*

Lagomarsino, S., Camilletti, D., and Cattari, S. (2018). Seismic assessment of existing irregular masonry buildings by nonlinear static and dynamic analyses. In *Pitilakis K. (eds) Recent Advances in Earthquake Engineering in Europe. ECEE 2018. Geotechnical, Geological and Earthquake Engineering, vol 46*, pages 123–151. Springer, Cham.

Lagomarsino, S. and Cattari, S. (2015). Seismic performance of historical masonry structures through pushover and nonlinear dynamic analyses. In *Perspectives on European Earthquake Engineering and Seismology*, pages 265–292. Springer, Cham.

Liu, X., Tian, S., Tao, F., Du, H., and Yu, W. (2020). How machine learning can help the design and analysis of composite materials and structures? *arXiv: 2010.09438v1*, pages 1–21.

Logarzo, H. J., Capuano, G., and Rimoli, J. J. (2021). ScienceDirect Smart constitutive laws : Inelastic homogenization through machine learning. *Computer Methods in Applied Mechanics and Engineering*, 373:113482.

Lotfi, H. R. and Shing, P. B. (1994). Interface model applied to fracture of masonry structures. *Journal of structural engineering*, 120(1):63–80.

Lourenço, P. B. (1995). An Orthotropic Continuum Model for Masonry. *TNO Building and Construction Research*, TNO-95-NM-R0712(03).

Lourenço, P. B. (1996). *Computational strategies for masonry structures*. PhD thesis, Delft University of Technology.

Lourenço, P. B. (2002). Computations on historic masonry structures. *Progress in Structural Engineering and Materials*, 4(July):301–319.

Lourenço, P. B., Mendes, N., Ramos, L. F., and Oliveira, D. V. (2011). Analysis of masonry structures without box behavior. *International Journal of Architectural Heritage*, 5(4-5):369–382.

Lourenço, P. B. and Rots, J. G. (1993). On the use of micromodels for the analysis of masonry shear walls. *Proceeding of the 2nd International Symposium on Computer Methods in Structural Masonry*, pages 14–26.

Lourenço, P. B. and Rots, J. G. (1997). Multisurface interface model for analysis of masonry structures. *Journal of Engineering Mechanics*, 123(7):660–668.

Lubliner, J., Oliver, J., Oller, S., and Oñate, E. (1989). A plastic-damage model for concrete. *International Journal of Solids and Structures*, 25(3):299 – 326.

Ma, L. and Sun, B. (2020). Machine learning and AI in marketing – Connecting computing power to human insights. *International Journal of Research in Marketing*, 37(3):481–504.

Ma, W. J. and Peters, B. (2020). A neural network walks into a lab : towards using deep nets as models for human behavior. *arXiv: 2010.09438v1*, pages 1–39.

Macorini, L. and Izzuddin, B. A. (2011). A non-linear interface element for 3D mesoscale analysis of brick-masonry structures. *International journal for numerical methods in engineering*, 85(October 2010):1584–1608.

Mallardo, V., Malvezzi, R., Milani, E., and Milani, G. (2008). Seismic vulnerability of historical masonry buildings: A case study in Ferrara. *Engineering Structures*, 30(8):2223–2241.

Martinez, X., Oller, S., and Barbero, E. (2011). Caracterización de la delaminación en materiales compuestos mediante la teoría de mezclas serie / paralelo. *Revista Internacional de Métodos Numéricos para Cálculo y Diseño en Ingeniería*, 27(3):189–199.

Massart, T. J. (2003). *Multi-scale modeling of damage in masonry structures*. PhD thesis, Technische Universiteit Eindhoven.

Massart, T. J., Mercatoris, B. C. N., Piezel, B., Berke, P., Laiarinandrasana, L., and Thionnet, A. (2011). Multi-scale modelling of heterogeneous shell structures. *Computer Assisted Mechanics and Engineering Sciences*, 18:53–71.

Massart, T. J., Peerlings, R. H. J., and Geers, M. G. D. (2007a). An enhanced multi-scale approach for masonry wall computations with localization of damage. *international jouranl for numerical methods in engineering*, 69(July 2006):1022–1059.

Massart, T. J., Peerlings, R. H. J., and Geers, M. G. D. (2007b). Structural Damage Analysis of Masonry Walls using Computational Homogenization. *International Journal of Damage Mechanics*, 16(April):199–226.

Mendes, N. and Lourenço, P. B. (2009). Seismic assessment of masonry "Gaioleiro" buildings in Lisbon, Portugal. *Journal of Earthquake Engineering*, 14(1):80–101.

Mendes, N. and Lourenço, P. B. (2014). Sensitivity analysis of the seismic performance of existing masonry buildings. *Engineering Structures*, 80:137–146.

Mercatoris, B. C. N., Bouillard, P., and Massart, T. J. (2009). Multi-scale detection of failure in planar masonry thin shells using computational homogenisation. *Engineering Fracture Mechanics*, 76(4):479–499.

Mercatoris, B. C. N. and Massart, T. J. (2011). A coupled two-scale computational scheme for the failure of periodic quasi-brittle thin planar shells and its application to masonry. *International Journal for Numerical Methods in Engineering*, 85(September 2010):1177–1206.

Micelli, F. and Cascardi, A. (2019). Structural assessment and seismic analysis of a 14th century masonry tower. *Engineering Failure Analysis*, 107:104198.

Milani, G. and Clementi, F. (2021). Advanced Seismic Assessment of Four Masonry Bell Towers in Italy after Operational Modal Analysis (OMA) Identification. *International Journal of Architectural Heritage*, 15(1):157–186.

Milani, G. and Valente, M. (2015). Failure analysis of seven masonry churches severely damaged during the 2012 Emilia-Romagna (Italy) earthquake: Non-linear dynamic analyses vs conventional static approaches. *Engineering Failure Analysis*, 54:13–56.

Minga, E., Macorini, L., and Izzuddin, B. A. (2018). Enhanced mesoscale partitioned modelling of heterogeneous masonry structures. *International Journal for Numerical Methods in Engineering*, 113(May 2017):1950–1971.

Ministero delle Infrastrutture e dei Trasporti. Circolare 21 gennaio 2019 (2019). 7. C.S.LL.PP. Istruzioni per l'applicazione dell' ≪Norme tecniche per le costruzioni≫ di cui al decreto ministeriale 17 gennaio 2018 (in Italian). *Rome*.

Mishra, M. (2021). Machine learning techniques for structural health monitoring of heritage buildings : A state-of-the-art review and case studies. *Journal of Cultural Heritage*, 47:227–245.

Nakamura, Y., Derakhshan, H., Griffith, M. C., Magenes, G., and Sheikh, A. H. (2017). Applicability of nonlinear static procedures for low-rise unreinforced masonry buildings with flexible diaphragms. *Engineering Structures*, 137:1–18.

Naranjo-Pérez, J., Infantes, M., Jiménez-Alonso, J. F., and Sáez, A. (2020). A collaborative machine learning-optimization algorithm to improve the finite element model updating of civil engineering structures. *Engineering Structures*, 225.

Norris, A. N. (2006). The isotropic material closest to a given anisotropic material. *Journal of Mechanics of Materials and Structures*, 1(February):223–238.

Oller, S., Car, E., and Lubliner, J. (2003). Definition of a general implicit orthotropic yield criterion. *Computer methods in applied mechanics and engineering*, 192:895–912.

Page, A. (1978). Finite element model for masonry. *ASCE J Struct Div*, 104:1267–1285.

Page, A. (1979). A non-linear analysis of the composite action of masonry walls on beams. *Proceedings of the Institution of Civil Engineers*, Part 2(67):93–110.

Page, A. (1988). Finite Elmeent Model for Masonry Subhected concentrated loads. *Journal of Structural Engineering*, 114:1761–1784.

Palazzi, N. C., Rovero, L., De La Llera, J. C., and Sandoval, C. (2019). Preliminary assessment on seismic vulnerability of masonry churches in central chile. *International Journal of Architectural Heritage*.

Panteleev, J., Gao, H., and Jia, L. (2018). Recent applications of machine learning in medicinal chemistry. *Bioorganic and Medicinal Chemistry Letters*, 28:2807–2815.

Parisi, F., Lignola, G. P., Augenti, N., Prota, A., and Manfredi, G. (2011). Nonlinear Behavior of a Masonry Subassemblage Before and After Strengthening with Inorganic Matrix-Grid Composites. *Journal of composites for construction*, 15(September-October):821–832.

Pelà, L., Aprile, A., and Benedetti, A. (2009). Seismic assessment of masonry arch bridges. *Engineering Structures*, 31(8):1777–1788.

Pelà, L., Benedetti, A., Aprile, A., and Mangoni, E. (2013). Seismic assessment of the Milano Centrale railway station. *International Journal of Architectural Heritage*, 7:609–627.

Pelà, L., Cervera, M., Oller, S., and Chiumenti, M. (2014). A localized mapped damage model for orthotropic materials. *Engineering Fracture Mechanics*, 124.

Pelà, L., Cervera, M., and Roca, P. (2011). Continuum damage model for orthotropic materials: Application to masonry. *Computer Methods in Applied Mechanics and Engineering*, 200(9):917–930.

Pelà, L., Cervera, M., and Roca, P. (2013). An orthotropic damage model for the analysis of masonry structures. *Construction and Building Materials*, 41:957–967.

Petracca, M. (2016). *Computational Multiscale Analysis of Masonry Structures*. PhD thesis, Universita' Degli Studi di Chieti Pescara, Universitat Politècnica de Catalunya.

Petracca, M., Pelà, L., Rossi, R., Oller, S., Camata, G., and Spacone, E. (2016). Regularization of first order computational homogenization for multiscale analysis of masonry structures. *Computational Mechanics*, 57(2):257–276.

Petracca, M., Pelà, L., Rossi, R., Zaghi, S., Camata, G., and Spacone, E. (2017). Micro-scale continuous and discrete numerical models for nonlinear analysis of masonry shear walls. *Construction and Building Materials*, 149:296–314.

Plevris, V. and Asteris, P. G. (2014). Modeling of masonry failure surface under biaxial compressive stress using Neural Networks. *Construction and Building Materials*, 55:447–461.

Prakash, P. R., Azenha, M., Pereira, J. M., and Lourenço, P. B. (2020). Finite element based micro modelling of masonry walls subjected to fire exposure: Framework validation and structural implications. *Engineering Structures*, 213(February):110545.

Raijmakers, T. and Vermeltfoort, A. (1992). Deformation controlled tests in masonry shear walls: report b-92-1156. Technical report, TU Eindhoven.

Reyes, J. C. and Chopra, A. K. (2011). Three-dimensional modal pushover analysis of buildings subjected to two components of ground motion, including its evaluation for tall buildings. *Earthquake Engineering & Structural Dynamics*, 40(7):789–806.

Roca, P., Cervera, M., Gariup, G., and Pelà, L. (2010). Structural analysis of masonry historical constructions. classical and advanced approaches. *Archives of Computational Methods in Engineering*, 17:299–325.

Roca, P., Cervera, M., Pelà, L., Clemente, R., and Chiumenti, M. (2013). Continuum FE models for the analysis of Mallorca Cathedral. *Engineering Structures*, 46:653–670.

Rossi, R., Zorrilla, R., and Codina, R. (2021). A stabilised displacement – volumetric strain formulation for nearly incompressible and anisotropic materials. *Computer Methods in Applied Mechanics and Engineering*, 377.

Ruder, S. (2016). An overview of gradient descent optimization algorithms. *arXiv: 1609.04747*, pages 1–12.

Saloustros, S., Pelà, L., Roca, P., and Portal, J. (2015). Numerical analysis of structural damage in the church of the Poblet Monastery. *Engineering Failure Analysis*, 48:41–61.

Sandoval, C., Valledor, R., and Lopez-Garcia, D. (2017). Numerical assessment of accumulated seismic damage in a historic masonry building. A case study. *International Journal of Architectural Heritage*, 11(8):1177–1194.

Schröder, J. and Hackl, K. (2014). *Plasticity and Beyond - Microstructures, Crystal-Plasticity and Phase Transitions*. Springer.

Segura, J., Aponte, D., Pelá, L., and Roca, P. (2020). Influence of recycled limestone filler additions on the mechanical behaviour of commercial premixed hydraulic lime based mortars. *Construction and Building Materials*, 238:117722.

Segura, J., Pelà, L., Saloustros, S., and Roca, P. (2021). Experimental and numerical insights on the diagonal compression test for the shear characterisation of masonry. *Construction and Building Materials*, 287:122964.

Segura Domingo, J. (2020). *Laboratory experimental procedures for the compression and shear characterisation of historical brick masonry*. PhD thesis, Universitat Politècnica de Catalunya, http://hdl.handle.net/10803/670897.

Sidey-Gibbons, J. A. M. and Sidey-Gibbons, C. J. (2019). Machine learning in medicine : a practical introduction. *BMC Medical Research Methodology*, 4:1–18.

Singh, S. P., Kunar, A., Darbari, H., Singh, L., Rastogi, A., and Jain, S. (2017). Machine Translation using Deep Learning: An Overview. In *International Conference on Computer, Communications and Electronics*. Comptelix.

Smarsly, K., Dragos, K., and Wiggenbrock, J. (2016). Machine learning techniques for structural health monitoring. In *8th European Workshop On Structural Health Monitoring*. EWSHM2016.

Theodossopoulos, D. and Sinha, B. (2013). A review of analytical methods in the current design processes and assessment of performance of masonry structures. *Construction and Building Materials*, 41:990–1001.

TNO (2017). *DIANA - finite element analysis, User's manual, Release 10.2*.

Torelli, G., D'Ayala, D., Betti, M., and Bartoli, G. (2019). *Analytical and numerical seismic assessment of heritage masonry towers*, volume 18. Springer Netherlands.

Torres, W., Almazan, J. L., Sandoval, C., and Peña, F. (2018). Fragility analysis of the nave macro-element of the Cathedral of Santiago, Chile. *Bulletin of Earthquake Engineering*, 16(7):3031–3056.

Valledor, R., López-García, D., and Sandoval, C. (2015). Linearly elastic seismic evaluation of masonry historical buildings in Santiago , Chile : The case of the Pereira Palace. In *3rd International Conference on Mechanical Models in Structural Engineering*, pages 281–299. CMMoST.

Woody Ju, J.-W., Chaboche, J.-L., and Voyiadjis, G. Z. (1998). *Damage Mechanics in Engineering Materials*. Elsevier.

Wu, J. Y., Li, J., and Faria, R. (2006). An energy release rate-based plastic-damage model for concrete. *International Journal of Solids and Structures*, 43(3-4):583–612.

Yongding, T. and Zhang, J. (2018). Rapid Impact Testing and System Identification of Footbridges Using Particle Image Velocimetry. *Computer-aided Civil and Infrastructure Engineering*, 0:1–16.

Yuen, K.-v., Sin-shi, K., and Dong, L. (2019). Self-calibrating Bayesian real-time system identification. *Computer-aided Civil and Infrastructure Engineering*, pages 1–16.

Zaghi, S., Martinez, X., Rossi, R., and Petracca, M. (2018). Adaptive and off -line techniques for non-linear multiscale analysis. *Composite Structures*, 206(August):215–233.